EPFL

Thesis n° 11 866

Beam Dynamics Limitations for Future Ions in the CERN Injector Complex

Presented on 29th September 2025

School of Basic Sciences
Particle Accelerator Physics Laboratory
Doctoral program in Physics

for the award of the degree of Docteur ès Sciences (PhD)

by

Elias Walter WAAGAARD

Accepted on the jury's recommendation

Prof. G. Carleo, jury president
Prof. M. Seidel, Dr H. Bartosik, thesis directors
Dr A. Adelmann, examiner
Dr K. S. B. Li, examiner
Prof. R. Marchevski, examiner

École
polytechnique
fédérale
de Lausanne

2025

But why, some say, the Moon?
Why choose this as our goal?
And they may well ask,
why climb the highest mountain?
Why, 35 years ago, fly the Atlantic?
...
We choose to go to the Moon in this decade
and do the other things,
not because they are easy,
but because they are hard ...
— John F. Kennedy, 1962

To Sveva, my co-sailor of the cosmos,
and to all my family members across the globe...

Acknowledgements

From the femtoscale interactions to particle detectors larger than cathedrals, from the quark-gluon plasma that reigned in the microseconds following the Big Bang to ... today, *Anthropocene*. If there is one place that encapsulates all these temporal and spatial dimensions, it is *CERN*: the heart of European and global research efforts in particle and accelerator physics. We humans make this feat possible, with technology. Working in this highly international and interdisciplinary environment has been a privilege like no other. Studying ion beams, present and future, across the whole CERN injector chain is a wide PhD topic, translating into tinkering at many scales simultaneously. It meant running several projects in parallel over three years: theoretical, numerical, experimental. Overwhelming at first, not knowing where to start the research puzzle: an aggregation of seemingly uncorrelated information. Tear the models down, start again. Measure yet again. An endurance test, a marathon. Like an apprentice building a sand castle between each wave that crushes it, finally learning how to construct the mental image fast enough, solid enough, to withstand the erosion of time. After each iteration, slightly better. This thesis represents the condensed end result. But it only shows the tip of the learning iceberg. The compounding effect of technological progress, elegantly phrased by Ray Kurzweil as “the Law of Accelerating Returns" — the observation that as technology evolves, it builds upon itself and develops even faster — applies equally well to the PhD learning curve, which for me was rather exponential than linear. My hope is that this thesis work sheds a small ray of light on previously dark areas. Even more important: I feel proud of what I learned in this process, even in fields I could never have anticipated. The list of world-class experts to thank is long, sharing their knowledge and time with me.

First, I want to express my gratitude to my thesis director Mike Seidel (EPFL) and my thesis co-director Hannes Bartosik (CERN) for offering me this unique opportunity. I also want to thank Nicolo’ Biancacci for accepting me into this project and for his initial supervision. My Uppsala University supervisor and mentor, Volker Ziemann, deserves to be mentioned as the one who sparked my first interest in accelerator physics and encouraged me into embarking upon this PhD journey. I would also like to thank my thesis committee Giuseppe Carleo, Radoslav Marchevski, Andreas Adelmann, and Kevin Li for their useful thesis comments and diverse discussions during the oral examination.

The fruits of this thesis work are the result of diverse collaborations with many colleagues, all worth thanking deeply (without any particular order): Roderik Bruce for our advances on the Injector Model and LHC ion luminosity production models; Reyes Alemany Fernández, Jose So-

moza, Jakob Olsen, Fenna Ukena and Günter Weber for our PS gas injection experiments and semi-empirical model development; Felix Soubelet, Michail Zampetakis, Szymon Lopaciuk, Sofia Kostoglou, and Giovanni Iadarola for all development and benchmarking efforts for space charge and intra-beam scattering models in Xsuite; Alexandre Lasheen, Theodoros Argyropoulos, Thomas Bohl, Maciej Slupecki, Heiko Damerau, Giulia Papotti, Leandro Intelisano, Konstantinos Paraschou, Ivan Karpov, Panos Zisopoulos, Ingrid Mases Sole, Elena De La Fuente Garcia, Michael Schenk, Verena Kain as well as the LINAC3, LEIR, PS and SPS operations teams for all their help during measurements in the CERN Control Center (CCC). Research does require its attentive proofreaders, for which I want to thank Edgar Mahner, Christian Carli, Davide Gamba, Detlef Küchler, Rhodri Jones, and Richard Scrivens for all their manuscript feedback. I also want to thank Adrian Russell and Witek Krasny for many fruitful high-level discussions on physics and its role for society. My office mates Peter Kruyt, John Patrick Salvesen, Tuuli Nissinen, Satya Jagabathuni, and Frank Schmidt were always there for uplifting chats and technical help. I thank my colleagues from the BE-ABP group and EPFL-LPAP for contributing to a cheerful environment with coffee breaks, social events and lunches together. My outreach efforts to promote physics among the youth started at CERN but went far beyond its walls, much thanks to Catarina Sahlberg, Fredrik Engelmark, Amelie Hallin and the whole team at Big Science Sweden. Vilken outreachturné genom Sverige!

This journey went far beyond physics. To the EPFL-ETH Sciencepreneurship Community for organizing an unforgettable week, building our European network. To all the inspirational thinkers who through their words gave me new eyes: Marcus Aurelius, Epictetus, Seneca, Plato, Andy Grove, Clayton Christensen, Eric Ries, Bent Flyvbjerg, Tony Fadell, Geoffrey Moore.

Long is the list of friends who supported me in this process. To Xavier and Álvaro for our Bains des Pâquis sauna tradition, for our endless hikes and ski outings. To Mohit, Ningning, Eirini, Miguel, Zeta, Vangelis, Léa and Andréa for all our picnics and apéros. To Laura and Max, for all our travels. To the YCC club members for igniting my passion for dinghies and catamarans, always with such a welcoming blissful atmosphere. À Genève, qui nous a tenu dans sa main avec les mots eternels écrits à *La Perle du Lac*, “Heureux celui qui sur ces bords peut longtemps reposer / Heureux celui qui les revoit s’il a dû les quitter”. On se reverra bientôt.

Along this curved path, family meant everything to me. Ett enormt tack till mamma Viktoria, pappa Frank, syster Lovisa, morfar Sven-Erik och hela bästa släkten för ert villkorslösa stöd. Grazie a Lula, Dario, Fulvio, Sergio e a tutta la famiglia italiana per farmi sentire a casa. À Sophie, Guillaume, et ma famille québécoise pour les cent mille horizons partagés ensemble. Sist men inte minst: to my co-sailor of the cosmos Sveva. We walked this thesis path hand-in-hand with laptops across all possible corners of this planet, you gave me the sandcastle metaphor. These words are for you: *vi klarade det.* Adesso, altre avventure ci aspettano...

One curve finishes here, another commences. Hopefully we stand at the start of the next exponential.

E. W. W. *Geneva, September 5, 2025*

Abstract

To achieve higher integrated nucleon-nucleon luminosity at the Large Hadron Collider (LHC) with lighter ions, as proposed by the ALICE detector collaboration, the CERN ion injector chain must deliver significantly higher beam intensities than for present lead (Pb) beams. Currently, the performance of Pb beams is limited by losses, the origin of which are not yet fully understood. In addition, the limitations for future lighter ions are largely unknown. This thesis addresses these challenges by quantifying key beam dynamics effects, developing predictive simulation models, and identifying optimal production schemes to maximize LHC luminosity production. The modelling efforts focus on understanding the main performance bottlenecks. First, a semi-empirical model for beam lifetime reduction caused by residual gas interactions was benchmarked via dedicated neutral gas injection experiments in the Proton Synchrotron (PS). Second, a detailed tracking model for the Super Proton Synchrotron (SPS) was developed to investigate the combined effect of space charge, intra-beam scattering (IBS), and power converter ripple inducing tune modulation. This model, validated against dedicated experiments, correctly predicted that a combination of these effects drives losses. These experiments, coupled with a newly implemented 50 Hz tune ripple compensation scheme, resulted in extracted Pb beam intensity exceeding the present operational goals by more than 40%. These findings were integrated into a semi-empirical Injector Model that propagates bunch intensities for any ion species through the accelerator complex. The model reveals that different ion species are limited by different effects in each machine. In an optimized production scenario, these studies predict that oxygen beams have the potential to increase the one-month integrated nucleon-nucleon luminosity by up to a factor of 4 compared to the baseline Pb case.

Keywords: Large Hadron Collider (LHC), light ions, beam dynamics, electron cooling, residual gas interactions, space charge, intra-beam scattering (IBS), luminosity modelling

Résumé

Pour atteindre une luminosité intégrée nucléon-nucléon plus élevée au Grand collisionneur de hadrons (LHC) avec des ions plus légers, comme proposé par la collaboration du détecteur ALICE, la chaîne d'injecteurs d'ions du CERN doit fournir des intensités de faisceau significativement plus élevées que pour les faisceaux de plomb (Pb) actuels. Actuellement, la performance du Pb est limitée par des pertes de faisceau dont l'origine n'est pas encore entièrement comprise, et les limites des futurs ions plus légers sont largement inconnues. Cette thèse aborde ces défis en quantifiant les effets clés de la dynamique du faisceau, en développant des modèles de simulation prédictifs et en identifiant des schémas de production optimaux pour maximiser la production de luminosité du LHC. Les efforts de modélisation se concentrent sur les principaux goulots d'étranglement de performance. Tout d'abord, un modèle semi-empirique pour la durée de vie du faisceau réduite par les interactions avec le gaz résiduel a été validé par des expériences dédiées d'injection de gaz neutre dans le synchrotron à protons (PS). Deuxièmement, un modèle de tracking détaillé pour le Super Synchrotron à Protons (SPS) a été développé pour étudier l'effet combiné de la charge d'espace, de la diffusion intra-faisceau (IBS) et de l'ondulation des convertisseurs de puissance induisant une modulation de tune. Ce modèle, validé par des expériences dédiées, a correctement prédit qu'une combinaison de ces effets entraîne des pertes. Ces expériences, couplées à un nouveau schéma de compensation d'ondulation de tune à 50 Hz, ont permis d'obtenir une intensité de faisceau de Pb extrait dépassant les objectifs opérationnels actuels de plus de 40%. Ces résultats ont été intégrés dans un modèle d'injecteur semi-empirique qui propage les intensités de paquets pour toute espèce d'ion à travers le complexe d'accélérateurs. Le modèle révèle que différentes espèces d'ions sont limitées par différents effets dans chaque machine. Dans un scénario de production optimisé, ces études prédisent que les faisceaux d'oxygène ont le potentiel d'augmenter la luminosité nucléon-nucléon intégrée sur un mois d'un facteur allant jusqu'à 4 par rapport au cas de référence du Pb.

Mots-clés : Le Grand collisionneur de hadrons (LHC), ions légers, dynamique du faisceau, refroidissement par électrons, interactions avec le gaz résiduel, charge d'espace, diffusion intra-faisceau (IBS), modélisation de la luminosité

List of publications

This thesis work is largely based on the following papers:

- Waagaard, E., Bruce, R., Bartosik, H., Alemany Fernández, R., Jowett, J. M., and Triantafyllou, N. (2025). Charting the luminosity capabilities of the CERN Large Hadron Collider with various nuclear species. *Nuclear Instruments and Methods in Physics Research Section A* (submitted). *arXiv preprint arXiv:2508.19653*. https://doi.org/10.48550/arXiv.2508.19653

- Waagaard, E., Ukena, F., Olsen, J., Alemany Fernández, R., Somoza, J., and Weber, G. (2025). Beam-gas interactions in the CERN Proton Synchrotron: Cross section measurements and lifetime modelling. *arXiv preprint arXiv:2506.02928*. https://doi.org/10.48550/arXiv.2506.02928

- Waagaard, E., Bartosik, H., Soubelet, F., and Paraschou, K. (2025). Investigating ion beam loss mechanisms at the SPS flat bottom. In *Proc. 16th Int. Particle Accelerator Conf. (IPAC'25)*, Taipei, Taiwan, ID: WEPM092. JACoW Publishing, Geneva, Switzerland.

- Waagaard, E., Alemany Fernandez, R., Bartosik, H., Bruce, R., and Soubelet, F. (2024). Expanding the CERN ion injector chain capabilities: new beam dynamics simulation tools for future ion species. In *Proc. 15th Int. Particle Accelerator Conf. (IPAC'24)*, Nashville, USA, ID: MOPC08. https://cds.cern.ch/record/2904667. JACoW Publishing, Geneva, Switzerland

- Waagaard, E. and Bartosik, H. (2024). Exploring space charge and intra-beam scattering effects in the CERN ion injector chain. In *Proc. of the 68th ICFA Advanced Beam Dynamics Workshop on High-Intensity and High-Brightness Hadron Beams (HB'23)*, Geneva, Switzerland, pages 515–518. https://doi.org/10.18429/JACoW-HB2023-THBP23

Contents

Acknowledgements i

Abstract (English/Français) iii

List of publications vii

1 Introduction 1

2 The CERN ion injector chain 5
2.1 Present Pb beam production in the injectors 5
2.2 Future ion species in the injector chain 8

3 Electron cooling studies in LEIR 11
3.1 Electron cooling formalisms 11
3.2 Previous LEIR electron cooling studies 13
3.3 Numerical electron cooling simulation studies 14
3.4 Conclusions 17

4 Studies of beam interactions with residual gas in the PS 19
4.1 Lifetime studies of atomic charge-changing interactions 19
4.1.1 Theoretical description of atomic beam-gas interactions 19
4.1.2 Experimental set-up and PS pressure profile reconstruction 27
4.1.3 Pb^{54+} lifetime experiment with injected Ar gas 30
4.1.4 Mg^{7+} lifetime experiment with injected Ar gas 32
4.1.5 Pb^{54+} lifetime experiment with injected He gas 33
4.1.6 Experimental cross sections from beam lifetime measurements 34
4.1.7 Beam lifetime estimates for future ion species at CERN 35
4.2 Beam degradation from inelastic and elastic collisions 39
4.2.1 Inelastic nuclear collisions 39
4.2.2 Elastic nuclear Coulomb scattering 40
4.3 Conclusions 42

5 Space charge, tune ripple and IBS effects for ions at the SPS flat bottom 43
5.1 Introduction: beam degradation mechanisms in the SPS 43
5.2 Theoretical background 43

5.2.1 Space charge . . . 44
5.2.2 Impact of resonances and tune modulation . . . 46
5.2.3 Intra-beam scattering . . . 49
5.2.4 Small note on statistical moments, beam distributions and q-Gaussians 58
5.3 Characterization of the SPS tune ripple . . . 60
5.4 Development of a predictive SPS ion tracking model . . . 69
5.4.1 Rationale and simulation framework . . . 69
5.4.2 SPS machine model . . . 69
5.4.3 Space charge implementation . . . 74
5.4.4 IBS model implementation . . . 76
5.4.5 Tune ripple implementation . . . 78
5.5 Benchmarking simulations against measurements . . . 78
5.5.1 Bunch intensity scan . . . 78
5.5.2 50 Hz noise amplitude scan . . . 83
5.5.3 Transverse tune scans with short cycles . . . 86
5.5.4 Ripple frequency scan in simulations . . . 90
5.6 Oxygen beams in the SPS . . . 91
5.6.1 Space charge limit and projections for oxygen . . . 91
5.6.2 Simulation benchmarking against preliminary oxygen measurements . 93
5.7 Achievements in SPS Pb ion operation . . . 98
5.8 Conclusions . . . 99

6 The Injector Model and future LHC ion luminosity production 101
6.1 Injector Model description . . . 101
6.2 Injector model results . . . 107
6.2.1 Injector model baseline predictions . . . 107
6.2.2 Possible ion production scheme improvements . . . 107
6.2.3 Comparison with 2025 oxygen pilot run data . . . 109
6.2.4 Charge state and isotope scan . . . 112
6.3 Studies of LHC ion luminosity production . . . 117
6.4 Conclusions . . . 120

7 Main conclusions and outlook 123
7.1 Study synthesis . . . 123
7.2 Major contributions of thesis work . . . 124
7.3 Future work . . . 125

Bibliography 127

Curriculum Vitae 143

1 Introduction

The Large Hadron Collider (LHC) [1] is a two-ring superconducting synchrotron collider, presently the world's largest with a circumference of 27 km. The machine is designed to store and collide 7 TeV protons, or fully stripped ion nuclei of equal magnetic rigidity. The main purpose of these collisions is to study rare physics events at high energies. In addition to the two high-luminosity experiments ATLAS [2] and CMS [3], the LHC has one dedicated ion experiment, ALICE [4]. These ion collisions are of particular importance investigating the physics of strongly interacting matter and studying the quark-gluon plasma at extreme energy densities and temperatures. The number of events per second dN_{event}/dt generated in the LHC collisions is expressed as

$$\frac{dN_{\text{event}}}{dt} = \mathscr{L}\sigma_{\text{event}}, \tag{1.1}$$

where $\mathscr{L}$ is the machine luminosity and σ_{event} is the cross section of the event under study. The luminosity is the key metric to describe the collider performance of producing such events. Ultimately, the LHC performance depends on the beam quality provided by its injectors, in particular, the particles per bunch N_b and transverse emittances ε. For round particle beams with Gaussian distributions, the machine luminosity for head-on collisions (without any geometric reduction factors) is

$$\mathscr{L} = \frac{N_b^2 n_b f_{\text{rev}} \beta_r \gamma_r}{4\pi\varepsilon^n \beta^*}, \tag{1.2}$$

where N_b denotes the bunch intensity, n_b the number of bunches, f_{rev} the revolution frequency, β_r the normalized velocity, γ_r the Lorentz factor, $\varepsilon^n = \beta_r\gamma_r\varepsilon$ the normalized transverse emittance and β^* the beta function at the collision point.

So far, the LHC has typically operated with $^{208}\text{Pb}^{82+}$heavy-ion beams for about one month per year during Run 1 (2010–2013) and Run 2 (2015–2018). These so-called "Runs" are multi-year operating periods between long shutdowns. So far, three annual campaigns have also been carried out in Run 3 (starting from 2022). In addition to colliding Pb-Pb, the LHC has provided proton-nucleus collisions (two one-month campaigns with p-Pb after an initial pilot campaign) [5, 6, 7, 8], a short productive campaign of Xe-Xe collisions [9, 10], and a

test of partially stripped $^{208}Pb^{81+}$ nuclei [11, 12]. A short pilot campaign with O-O and p-O collisions during 2025 uses beams with lower bunch numbers [13]. At the time of writing, the heavy-ion operation is expected to continue throughout Run 3 and Run 4 (presently scheduled for 2029–2032), with yearly campaigns of either Pb-Pb or p-Pb collisions, after which the presently approved heavy-ion program ends. However, there are ongoing studies to extend the heavy-ion operation to Run 5 and beyond [14], to reach a significantly higher integrated nucleon-nucleon luminosity than in Run 3–4. This could potentially be achieved with lighter ion species, mentioned by the ALICE detector upgrade study (ALICE3) as important to investigate the properties of quark-gluon plasma and of strongly interacting matter [15].

The LHC ion physics program relies on the upstream injectors in order to deliver dense high-intensity $^{208}Pb^{82+}$beams for collisions [16]. Before reaching the LHC, the ion beams pass through a sequence of accelerators, whose path in the CERN complex is illustrated in Fig. 1.1. This sequence is collectively denoted *the ion injector chain*, and consists of Linac3, LEIR, the PS, and the SPS.

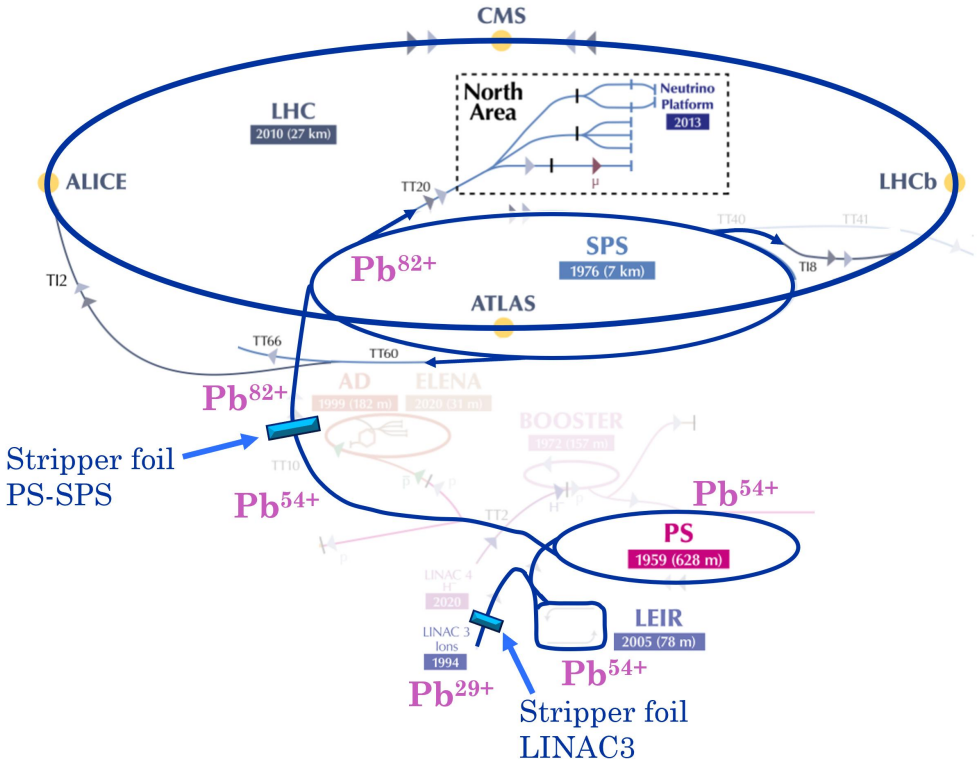


Figure 1.1: The present CERN ion injector chain, based on graphics from [17].

Numerous improvements of the injectors in recent years within the LHC Injector Upgrade (LIU) project [18] have almost doubled the number of Pb bunches in the LHC while also enhancing the intensity per bunch. Beyond these, no obvious large factors of improved Pb-Pb luminosity are within reach. To achieve this requested LHC nucleon-nucleon luminosity increase for the lighter ions, the CERN ion injector chain will need to provide significantly

higher beam intensities as compared to the Pb ion beams, the performance of which is limited by beam losses and emittance blow-up along the injector chain.

Before 2025, the operational experience with lighter ion beams in the injector chain was limited to the short 2017 Xe run and some low-intensity ion beam tests for fixed-target experiments [19]. This makes it difficult to understand light ion beam dynamics limitations and make intensity predictions for the injector complex. Some first estimates of the achievable luminosity for a range of different ion species between O and Xe were presented by the Working Group 5 of the HL/HE-LHC workshop [14] (or simply "WG5"), postulating a simple empirical power-law scaling of bunch intensity N_b, from Pb beams to any ion species with a given mass number A and atomic number Z

$$N_b(Z,A) = N_b(82,208)\left(\frac{Z}{82}\right)^{-p}, \tag{1.3}$$

with the fitting parameter $1.5 \geq p \geq 1.9$ obtained empirically from the limited experience with the ion beams for the SPS fixed target experiments. This study indicated a potentially high gain in integrated luminosity for the lightest ion species, in particular O. However, these projections appear too optimistic, since realistic injector brightness limitations were not accounted for, and the LHC luminosity model was simplified. Better models are necessary to refine the estimates.

In this light, this PhD thesis work addresses **three key questions**:

- Which beam dynamics effects currently limit Pb ion beam quality in the CERN ion injector chain?
- How will these effects impact future lighter ion species in the injector chain?
- What is the optimal beam production scheme for future ion species to maximize nucleon-nucleon luminosity in the LHC?

This thesis is structured to *follow the beam across the CERN ion injector chain*:

- Chapter 2 provides an overview of the present Pb beam production scheme in the CERN injector complex, and discusses assumed parameters for future ion species.
- Chapter 3 presents studies on the LEIR electron cooler performance in the context of future ions.
- Chapter 4 features ion beam lifetimes studies due to residual gas interactions in the PS.
- Chapter 5 presents recent experimental performance optimization studies of Pb beams at the SPS flat bottom, followed by theoretical studies to understand the impact of tune ripple, space charge, and intra-beam scattering effects with the development of a new

tracking simulation model. A benchmarking comparison between measurements and the SPS tracking simulation model results is also discussed.

- Chapter 6 condenses all these insights into the numerical developments of a semi-empirical Injector Model. This model aims to realistically propagate bunch intensities through the injector chain to LHC injection for any ion species. This is followed by detailed simulations to estimate the achievable integrated ion luminosity in the LHC for various ion species and beam production schemes.
- Finally, Chapter 7 highlights the main conclusions and the major contributions of this thesis work, also discussing ideas for future studies.

This thesis assumes that the reader is familiar with basics accelerator physics concepts, described in detail in for example Ref. [20].

2 The CERN ion injector chain

This chapter provides an experimental introduction to the ion injector chain, mainly addressing the following questions:

- *How are lead ion beams produced today for the LHC?*
- *Which are the expected beam parameters for future ion species?*

2.1 Present Pb beam production in the injectors

A detailed $^{208}Pb^{82+}$ production scheme is given by [18], but here an overview is provided for context within this thesis. The Pb ion beam production of the Pb starts at the electron cyclotron resonance ion source (ECRIS), which delivers partially stripped $^{208}Pb^{29+}$ ions — isotopically enriched with a purity of 99.6% — to the radio-frequency (RF) quadrupole and the Linear Accelerator 3 (Linac3), accelerating the ions up to a kinetic energy of E_k = 4.2 MeV/u.

At the exit of Linac3, a stripper foil produces the resulting charge state $^{208}Pb^{54+}$ before delivery to the Low-Energy Ion Ring (LEIR). Two operational LEIR modes and beam types are currently available: either single-injection low-intensity (EARLY) or multiple-injection high-intensity (NOMINAL). A typical $^{208}Pb^{54+}$ NOMINAL cycle is showcased in Fig. 2.1.

In the NOMINAL cycle, LEIR accumulates up to seven or eight 300-μs-long pulses from Linac3 for LHC-type beams. During this injection process, an electron cooler is active (explained in detail in Chapter 3) to enhance the phase space density of the beam. The beam is then captured into two dense bunches before acceleration up to E_k = 72 MeV/u. The whole cycle lasts 3.6 s. The two 200-ns-long bunches from LEIR are sent to the Proton Synchrotron (PS), where each bunch is split into two bunches through RF manipulations (changing the harmonic h), creating a total of four bunches with a bunch spacing of 100 ns in the nominal scheme [21]. This bunch splitting happens at an intermediate energy plateau (intermediate flat-top) before the final acceleration to E_k = 5.9 GeV/u. A waterfall plot of the bunch profile evolution (generated with a tomoscope [22]) during the RF manipulations for bunch splitting is shown in

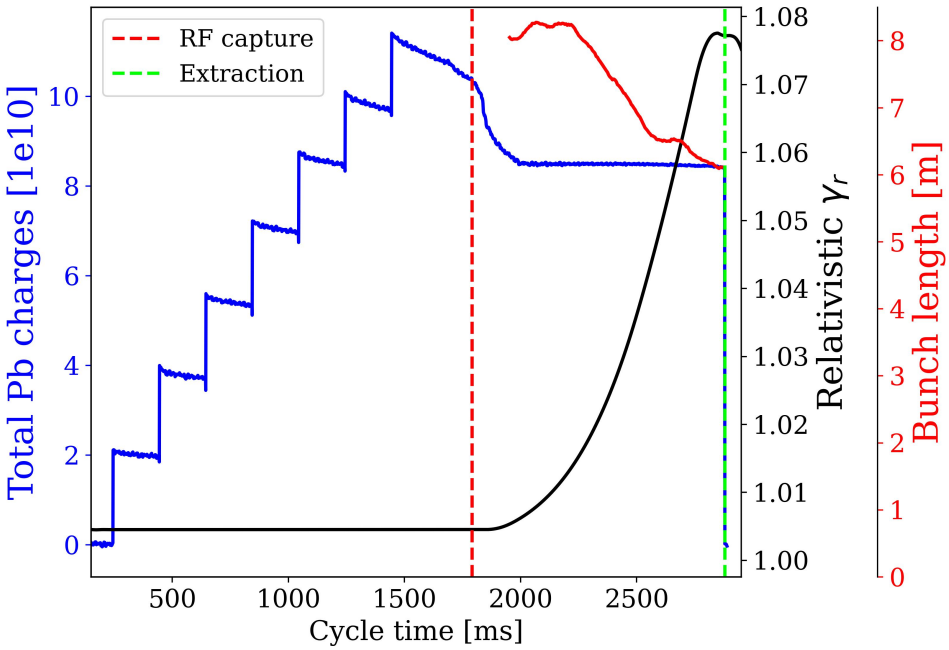


Figure 2.1: NOMINAL $^{208}Pb^{54+}$ cycle in LEIR, with total charges from the Beam Current Transformer (BCT), relativistic Lorentz factor γ_r, and fitted bunch length from tomoscope data.

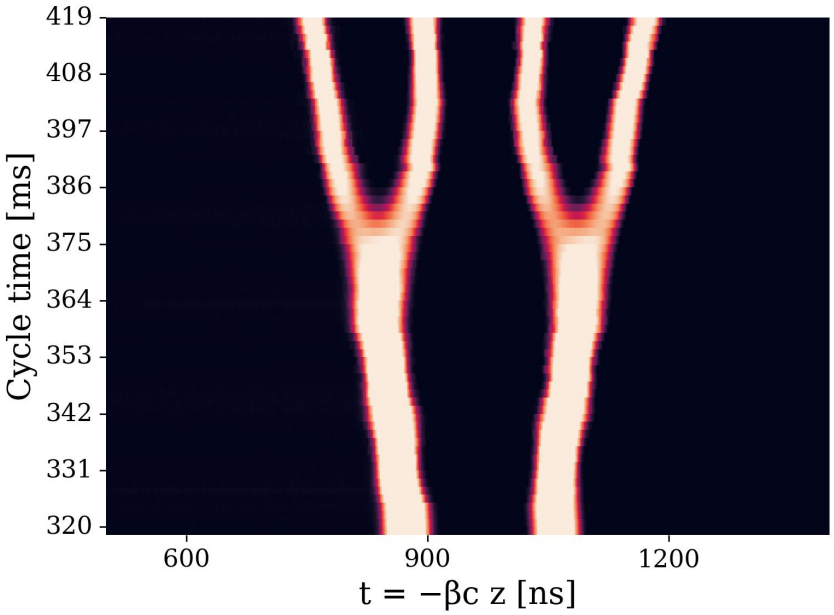


Figure 2.2: Longitudinal PS waterfall plot of bunch splitting during the $^{208}Pb^{54+}$ cycle.

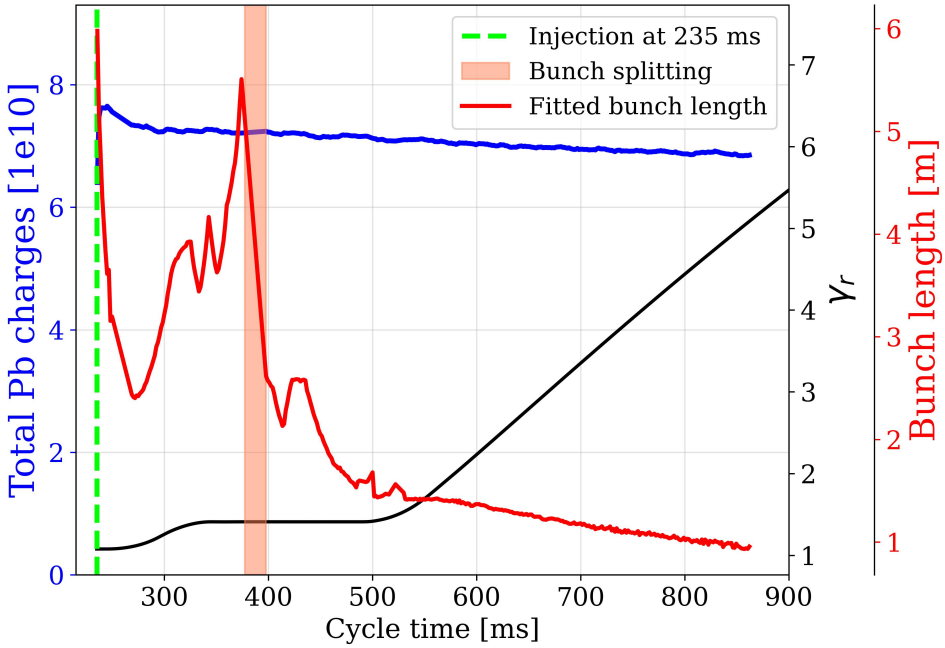


Figure 2.3: Parts of the operational PS cycle for LHC-type $^{208}Pb^{54+}$beams, with BCT intensity, relativistic γ_r and fitted 4σ bunch length from tomoscope data. During the bunch splitting, the two injected PS bunches are split into four bunches.

Fig. 2.2, where the two 200-ns-long bunches are split into four 100-ns-long bunches. Figure 2.3 shows parts of the operational PS ion cycle, in which the beam typically spends around 1.2 s in the machine.

The bunch splitting happens at around t_{cycle} = 380 ms at the intermediate flat top, where bunch intensity is halved as the two bunches split in four. The main purpose behind the PS bunch splitting process is to optimize the beam performance in the LHC by producing longer bunch trains and thus being more efficient in filling the LHC, while at the same time mitigating detrimental space charge effects at SPS injection by reducing the particle density per bunch. Compared to LEIR, total beam losses during the whole PS cycle are relatively small, in the order of a few percent.

The batch of four bunches is extracted from the PS into the TT2-TT10 transfer line to the SPS, where any remaining electron is stripped off to achieve the fully-stripped $^{208}Pb^{82+}$charge state. The SPS accumulates 14 injections from the PS during the long injection segment, also denoted flat bottom (FB), before the energy ramp. The total intensity evolution (as measured with the DC Beam Current Transformer, DCBCT) and momentum for a typical operational SPS $^{208}Pb^{82+}$cycle (from the early 2024 Pb beam commissioning) is shown in Fig. 2.4. Following an SPS RF system upgrade for Run 3, the so-called momentum slip-stacking process interleaves pairs of the four-bunch batches through RF manipulations to form eight-bunch batches, reducing the bunch spacing from 100 ns to 50 ns. The accumulated SPS injections form longer trains and define the final LHC bunch train structure, resulting in a final structure of

consecutive 8-bunch 50-ns batches with a 100 ns batch spacing.

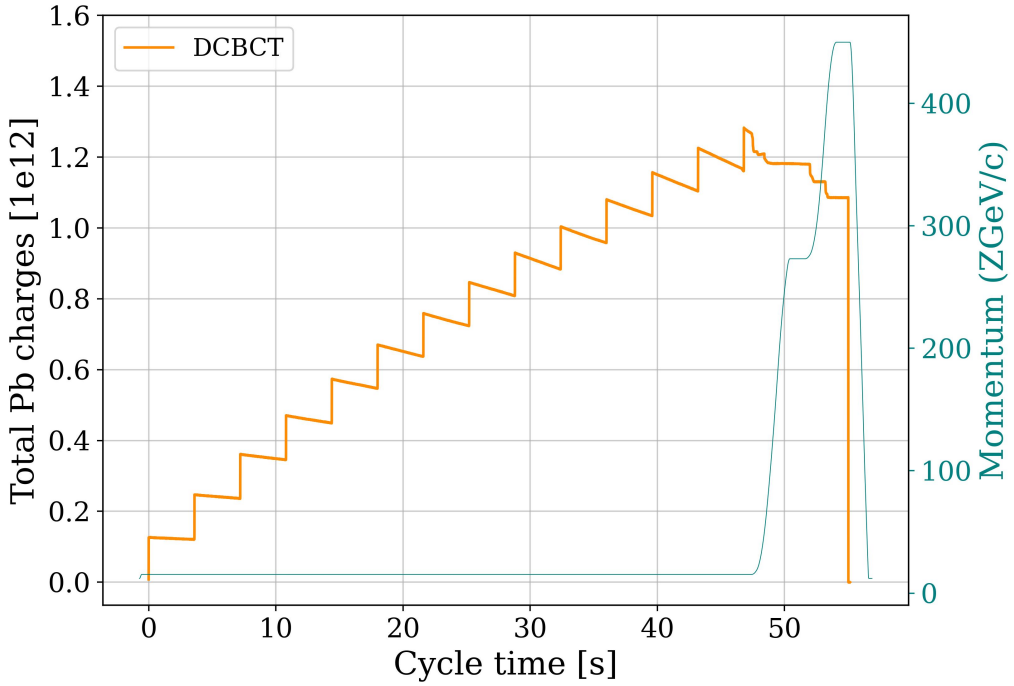


Figure 2.4: SPS nominal $^{208}Pb^{82+}$ cycle for LHC-type beams, with 14 injections.

After acceleration and slip-stacking, the bunch train is extracted at E = 177 GeV/u (corresponding to 450 Z GeV, with u being the unified atomic mass unit and Z the charge number). After transfer from the SPS, the LHC accumulates several SPS bunch trains up to 1240 bunches to form the full beam for the nominal filling scheme, which involves a combination 54 and 40 bunches in the SPS trains [23]. The current ion bunch train structure throughout the CERN ion injector chain is illustrated in Fig. 2.5.

2.2 Future ion species in the injector chain

The motivation behind lighter ion species was already discussed in Chapter 1. Here, the assumed parameters for the source and Linac3 within the context of new ion species are discussed, which will be used as input for experimental and theoretical loss studies in subsequent chapters.

Little operational experience exists with ion species other than protons and $^{208}Pb^{82+}$ in the CERN ion injectors, let alone what their performance limits. On limited occasions, other ion species have been used for the SPS fixed target experiments: In (2003), Ar (2015), and Xe (2017). A short but productive 2017 LHC pilot run tested Xe-Xe collisions [9, 10]. Further upstream, oxygen was first tested briefly during the LEIR commissioning in 2005. In 2025, a short single-bunch oxygen pilot campaign took place in the ion injectors until LHC collisions [13], which constitutes a central part in this thesis work. A short Mg pilot test run was also conducted

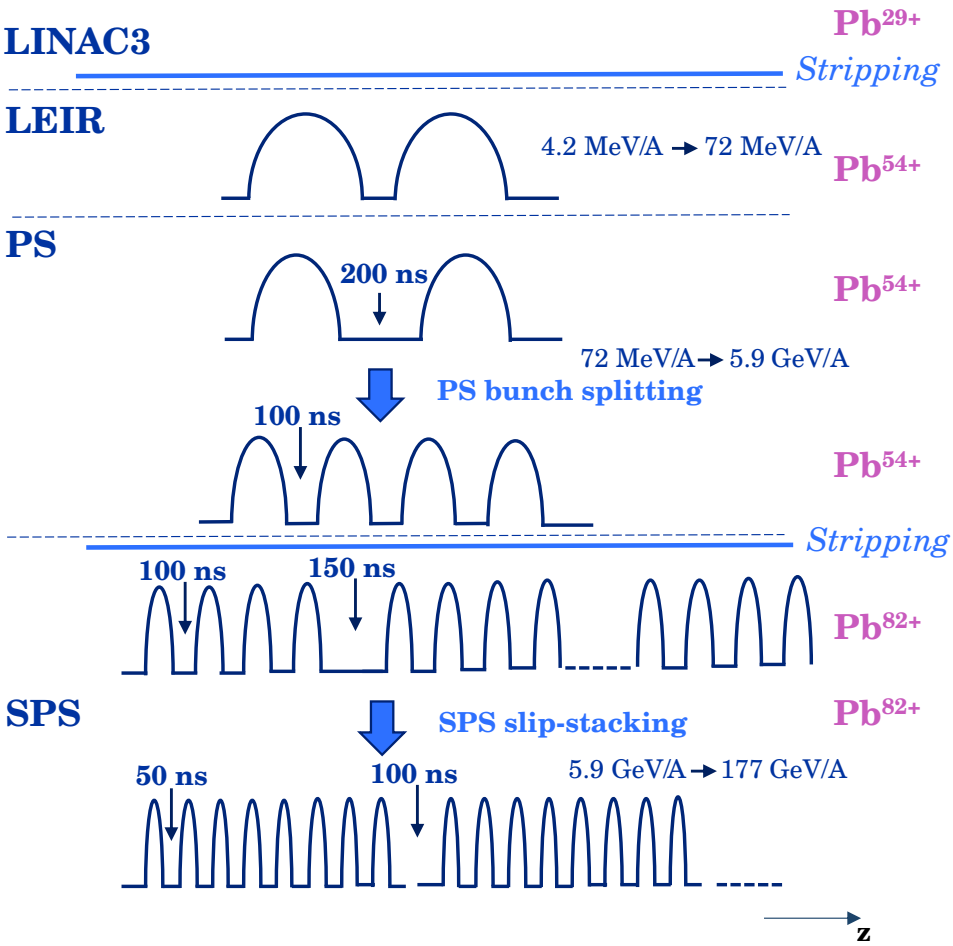


Figure 2.5: Present configuration of $^{208}Pb^{82+}$ beam production scheme at CERN: stripping splitting, charge states and bunch train structure.

in 2024 up to LEIR and PS. These instances combined with previous source tests of new ion species provide empirical input for parameters such as charge state and Linac3 current [24, 25, 26], as shown in Table 2.1.

The choice of Kr charge state is twofold: Kr^{22+} or Kr^{29+}. Previous scenarios assumed Kr^{29+} at 25 μA deliverable Linac3 current with stripping [27]. However, recent source tests revealed currents up to 40 μA for Kr^{22+}, produced directly from the source without any stripping. Proposed but untested ion species in Table 2.1 include Ca, highlighted by the Gamma-Factory design [12, 28] for a novel type of light source with partially stripped beams of heavy ions. As this species has never been tested, 25 μA — the lowest observed experimental value — is conservatively assumed. This table with charge states and Linac3 currents represents the expected parameters for future ions. Until further detail beam profile measurements have been made, identical geometric $\varepsilon_{x,y}$ and σ_z from Pb operation are assumed.

To assess the impact of the various effects limiting the performance across the injector chain,

Table 2.1: Assumed properties of future ion species: charge state and Linac3 current. Values from [24] are marked by †, from [25] by ‡, from [26] by ⋆, and achieved in 2025 by ⋄. The symbol ⊙ indicates an untested current, for which 25 μA is conservatively assumed.

Ion	Z	A	charge in LEIR-PS	mass [GeV/c^2]	Linac3 current [μA]
He	2	4	1	3.73	$160^{\dagger}$
O	8	16	4	14.86	$90^{\diamond}$
Mg	12	24	7	22.36	$20^{\star}$
Ar	18	40	11	37.22	$60^{\dagger}$
Ca	20	40	17	37.22	$25^{\odot}$
Kr	36	86	22 (29)	80.03	$40^{\ddagger}$ ($25^{\odot}$)
In	49	115	37	107.01	$25^{\dagger}$
Xe	54	129	39	120.05	$30^{\dagger}$
Pb	82	208	54	193.69	$30^{\dagger}$

it is important to evaluate the injection and extraction energy for the different ion species. For each machine, the kinetic energy E_k, momentum p and γ_r can be calculated at injection and extraction for from the magnetic rigidity $B\rho$

$$B\rho = \frac{p}{q}, \tag{2.1}$$

where q is the charge state. If no stripping occurs, $B\rho$ remains identical from one accelerator to the next. Instead of stripping in the PS-SPS transfer line, as presently done for $^{208}Pb^{82+}$, an alternative stripper foil after LEIR has also been discussed as an alternative for different ion species. Upon stripping and changed charge state, a new $B\rho$ is calculated assuming unchanged γ_r. The Linac3 structure implies a fixed γ_r and kinetic energy, 4.2 MeV/u for all species. Another important aspect to consider is whether the proton-equivalent momentum p/q is sufficiently high to be within the acceptable range of the dipole magnets, and has to be calculated for all charge states. In particular, the tolerable PS magnetic dipole field range spans from $B_{\text{min}} = 0.0383$ T to $B_{\text{max}} = 1.26$ T.

3 Electron cooling studies in LEIR

Electron cooling is a method to decrease the beam emittance for a given distribution of particles, an important step in LEIR for the ion beam production. The main question of this chapter is:

- *How will the LEIR electron cooler affect the performance of future ions species?*

The method of electron cooling was first proposed by Budker [29] in 1967 as a way to increase the luminosity of p-p and p-$\bar{p}$ colliders. Electron cooling has been widely implemented in accelerators worldwide over the years, with at least 20 facilities having operated electron cooling to date [30]. Three of these are located at CERN: Low Energy Ion Ring (LEIR) [31], the Extra Low Energy Antiproton ring (ELENA) [32] and the Antiproton Decelerator (AD) [33]. In the context of ions, it is worth noting that the LEIR electron cooler system — state-of-the-art when installed in 2006, with adiabatic expansion, electrostatic bend, and variable density electron beam — was used routinely for the LEIR ring commissioning with O^{4+} and Pb^{54+} ions before the first LHC ion run in 2008 [31]. The LEIR electron cooler was designed to stack Pb^{54+} ion injections from Linac3 for the LHC ion beams, where the number of injections is limited by how quickly each pulse can be cooled and merged into the circulating stack before the next injection. Ultimately, the electron cooling time τ_{cool} determines the number of injections one can stack in LEIR for a given cycle length.

One of the main challenges with electron cooling is that the cooling time heavily scales with the particle energy, effectively limiting its operational regime to low-energy ion, proton, or anti-proton beams. From simplified relations, the transverse cooling time approximately scales as $\tau_{\text{e}} \sim \beta^4\gamma^5$ [34], whereas in the longitudinal plane $\tau_{\text{e}} \sim \gamma^2$ [30].

3.1 Electron cooling formalisms

The main principle of electron cooling consists of cooling a circulating ion beam with the aid of a co-propagating electron beam, moving with the same average velocity as the beam to be

cooled. The electron beam originates from an electron gun and propagates parallel to the ion beam until diverted to an electron collector. Energy is transferred from the hotter circulating beam to the cooler electron beam through Coulomb interactions, effectively reducing the temperature and hence the emittance of the circulating beam. On a theoretical level, the building block needed for predicting electron cooling performance consists of calculating the friction ("drag") force experienced by a heavy particle moving in an electron gas either in the absence or presence of an external magnetic field. These scenarios represent the *un-magnetized* and *magnetized* cases. The friction force can then be used to estimate the cooling time τ_{cool}, defined as the time needed to decrease the beam emittance (or momentum spread) by $1/e$, i.e. assuming an exponential decay $\varepsilon(t) = \varepsilon_0 e^{-t/\tau}$. A broad overview on the fundamentals of electron cooling theory is given in [35]. In the simplest un-magnetized case, a particle with charge Ze transfers to the electron a momentum kick

$$\Delta p_{\perp} = \frac{2Ze^2}{\rho V} \tag{3.1}$$

when surpassing an electron with mass m_e at an impact parameter ρ with velocity V. In the case of intermediate impact parameters, the mean energy loss of a charged particle moving in an electron gas is obtained from

$$\frac{dE}{dt} = \mathbf{F}\cdot\mathbf{V} = -\int_{\rho_{\min}}^{\rho_{\max}} \frac{\Delta p_{\perp}}{2m_e} n_e V \cdot 2\pi\rho\, d\rho = \frac{4\pi Z^2 e^4 n_e}{m_e V} \ln\frac{\rho_{\min}}{\rho_{\max}}, \tag{3.2}$$

where n_e is the density of the electron beam. If the proper thermal motion of the electrons in the beam has to be considered, one has to average the drag force over the electron velocity distribution $f_e(\mathbf{V}_e)$. In the magnetized case, the drag force is altered significantly by the longitudinal magnetic field B in the cooling zone. The influence of the magnetic field becomes important when the ion-electron interaction duration exceeds the Larmor oscillation period, i.e. impact parameters ρ smaller than the Larmor gyration radius

$$\rho_L = \frac{m_e V_{e,\perp} c}{eB}. \tag{3.3}$$

If the impact parameters are large and the ion velocities are small compared to the electron velocities, the ion effectively interacts only with a "Larmor circle" moving only along the magnetic field, which can lead to a cooling force enhancement up to an order of magnitude stronger [30]. As the magnetic field B increases, the range of impact parameters within which there exist noticeable momentum transfers decreases rapidly.

Different electron cooling models exist to calculate drag forces:

- The **Budker** model [36] neglects the influence of the accompanying longitudinal magnetic field, making it unsuitable to describe the magnetized electron cooling in LEIR.
- The **Debrenev-Skrinsky-Meshkov** formalism [37, 38] assumes three collision types: fast,

adiabatic, and magnetized. The regime depends on the value of impact parameter ρ with respect to the Larmor radius ρ_L, where the relative contributions of the aforementioned interactions depend on the relative electron and ion velocities.

- The **Parkhomchuk** formalism [39] is comparatively the simplest and commonly used drag force model based on a semi-empirical formula, which includes an effective velocity V_{eff} parameter. The advantage of this tuning parameter is that magnetic field line perturbations and other imperfections can be taken into account, to better relate the formula to realistic situations for experiments.

The simplicity, widespread use and experimental comparability of the Parkhomchuk model make it the most suitable to study the LEIR electron cooler performance for future ions. To analytically describe the drag force in experiments in the magnetized case, Parkhomchuk [35] proposed in conjunction with numerical studies the following drag force formula

$$F = \frac{4Z^2e^4n_eV}{m_e(V^2+V_{\text{eff}}^2)^{3/2}}\ln\left(\frac{\rho_{\max}+\rho_L+\rho_{\min}}{\rho_L+\rho_{\min}}\right), \tag{3.4}$$

where V_{eff} is the effective Larmor velocity of the electrons due to longitudinal motion and transverse drift motions caused by other electromagnetic fields such as space charge. In the simplest case, the cooling force in Eq.(3.4) ultimately leads to nonphysical point-like emittance and no momentum spread. In reality, the electron cooling of the ion beam only continues until an equilibrium is established between the cooling (energy extraction) and “heating" (energy supply) from the diffusion of kicks from thermal electron motion. The total heat balance leads to a simple condition for theoretical temperature equalization between the ions and electrons:

$$\langle V^2\rangle = \frac{m_e}{m_{\text{ion}}}V_{\text{eff}}^2, \qquad T = T_e. \tag{3.5}$$

An even more realistic heat balance requires additional kicks from other heating sources such as space charge or intra-beam scattering, and cannot be modeled without detailed particle tracking simulations. However, the drag force formula in Eq.(3.4) is typically sufficient for smaller time scales (such as the < 2 seconds of active cooling time in LEIR) to estimate cooling times before other heating sources become relevant.

3.2 Previous LEIR electron cooling studies

When commissioned in 2005, the LEIR electron cooling system was the first of a new generation of state-of-the-art coolers for fast phase space cooling of ion beams in storage rings, incorporating recent technologies such as adiabatic expansion, electrostatic bend and variable density electron beam [31]. The design was purposed for stacking Pb^{54+} ion injections from Linac3 for the LHC ion beams, although it was also tested with O^{4+}. Before the installation of the new electron cooling system, LEIR had been converted into an ion storage ring in 1996 from the Low Energy Antiproton Ring (LEAR). At that point, LEAR was modified to include

multi-turn injection and accumulation with the help of the previous electron cooling system. The lifetime of stored Pb^{52+}, Pb^{53+}, Pb^{54+} beams had already been investigated in [40] to study the recombination of the ions with cooling electrons. A series of tests in 1999 investigated the electron cooling and lead ion stacking experimentally [34]. The study observed a strong dependence of the cooling time on the dispersion at the electron cooler and intensity-dependent outgassing of equipment under ion impact in the LEIR vacuum chamber.

Additional losses observed in the 1999 studies are believed to originate from recombination, which is the formation of quasi-recombined weakly bound electron-ion pairs inside the cooling zone, which then break up upon exit from the electron cooler [35]. This effect can have a strong impact on the ion beam intensity reach. Anomalously fast recombination rates for the charge state Pb^{53+} were measured, and confirmed by several additional tests. A similar anomaly in recombination rate had been found for Au^{50+} — isoelectronic with Pb^{53+} — at the TSR-Heidelberg [41]. As stated in [34], the recombination problem can be circumvented by the selection of a suitable charge state, avoiding similar electronic configurations to Pb^{53+} at the ionized level $3d^{10}$. Comparing considered charge states in Table 2.1 with the NIST Atomic Spectra Database of Ionization Energies Data [42], none of the considered charge states in this study appear unsuitable with electron cooler due to high recombination rates. It is hence expected that recombination will not be a problem in this context.

3.3 Numerical electron cooling simulation studies

Numerical simulations are needed to estimate cooling rates while properly incorporating effects such as electron plasma, thermal effects, and magnetic field influences. Available simulation codes for these electron cooling models include VORPAL [43], RF-Track [44], BETACOOL [45], and JSPEC [46]. A numerical study compared VORPAL with the Parkhomchuk and Debrenev-Skrinsky-Meshkov model to investigate a proposed RHIC cooler [47]. An extensive comparison and parametric scan study [48] of RF-Track, BETACOOL and JSPEC have shown that the underlying physics from previous experiments at LEIR was captured in these simulation codes. More recently, the Parkhomchuk model was implemented in `xsuite` [49] and benchmarked against BETACOOL [50], thus validating its use for the LEIR electron cooler.

In the simulation model set-up of this study, ion beam parameters are propagated in a linear LEIR lattice representation, where drag force momentum kicks — calculated with the Parkhomchuk drag force of Eq. (3.4) — are applied every turn. This `xsuite` simulation set-up is based on [50], and the study scenario input was developed jointly with P. Kruyt. Heating effects like intra-beam scattering and space charge are not included, as this would require a more complex non-linear set-up. However, these effects are assumed not to interfere with cooling trends during the simulated beam time of 1.6 s in the LEIR context, especially as the beam at this stage is coasting and not yet captured. The emittance evolution is calculated numerically, and the cooling time τ_{cool} is extracted from the exponential fitting parameter. The assumed LEIR electron cooling parameters — for coasting Pb^{54+} beams at LEIR injection

Parameter	Value
Electron current (I_e)	0.6 A
Cooler length (L)	2.5 m
Electron beam radius (r_e)	25×10^{-3} m
Transverse Temperature ($T_\perp$)	10×10^{-3} eV
Longitudinal Temperature ($T_\parallel$)	1×10^{-3} eV
Magnetic field strength B	0.075 T
Magnetic field imperfection $B_\perp / B_\parallel$	10^{-3}
Geometric emittance $\varepsilon_{x,y}$	14 μm
Momentum spread (uniform)	$\pm 2 \times 10^{-3}$ dp/p

Table 3.1: LEIR Pb beam and electron cooler parameters [51].

— are shown in Table 3.1.

Figure 3.1 shows the simulated normalized horizontal emittance $\varepsilon_x^n = \beta\gamma\varepsilon_x$ (where ε_x is the geometric emittance) as a function of time. Assuming round beams and similar $\beta_{x,y}$ function values at the electron cooler, this trend is the same in the vertical plane as the drag force in Eq. (3.4) acts transversally. For each ion species and assumed LEIR charge state in Table 2.1, the cooling time τ_{cool} is computed from an exponential fit, also including the relative cooling time with respect to Pb^{54+}. A clearly decreasing trend of τ_{cool} for heavier ions with higher charge states emerges.

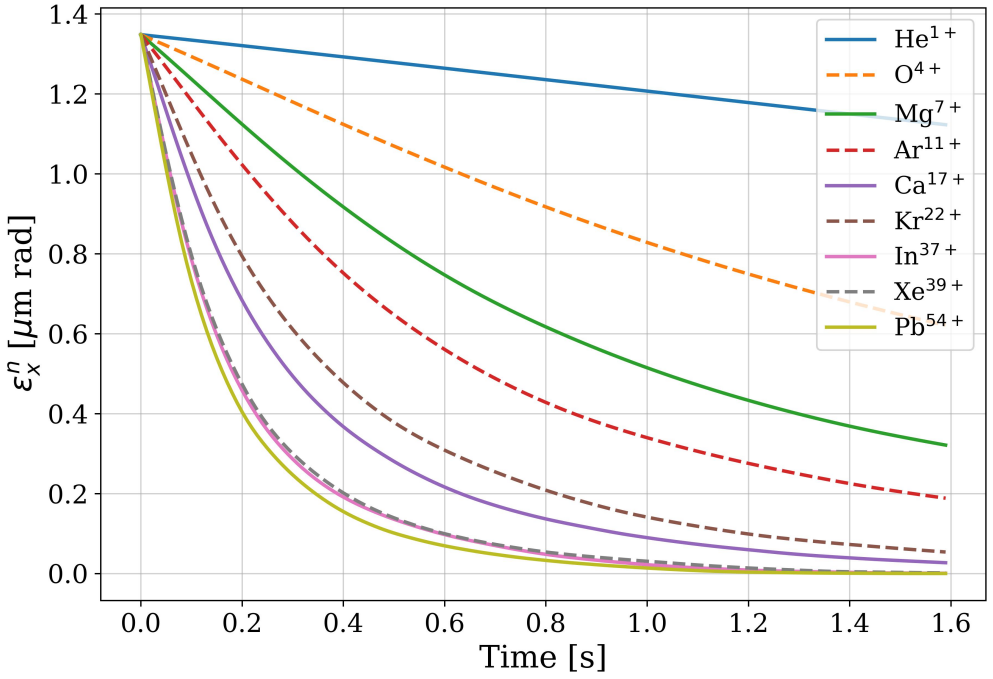


Figure 3.1: Horizontal emittance ε_x^n evolution with LEIR for various ion species with cooling.

Ion	Z	A	charge in LEIR-PS	Cooling time τ_{cool} [s]	Relative cooling time	No. LEIR injections
He	2	4	1	8.69	48.8	1
O	8	16	4	2.01	11.3	1
Mg	12	24	7	1.05	5.9	1
Ar	18	40	11	0.73	4.1	1
Ca	20	40	17	0.33	1.9	4
Kr	36	86	22	0.42	2.4	3
In	49	115	37	0.20	1.1	7
Xe	54	129	39	0.21	1.2	6
Pb	82	208	54	0.18	1.0	8

Table 3.2: Estimated cooling performance in LEIR for future ion species. The cooling times are given as absolute and relative to Pb. The last column indicates the possible number of Linac3 injections into LEIR, considering cooling performance and available cooling time.

With the assumption that the LEIR electron cooler is already at its capacity limit with Pb^{54+}, the number of allowed Linac3 injections is estimated as the floor function of the relative cooling time multiplied by eight injections (the maximum observed numbers). The four lightest ion species He^{2+}, O^{4+}, Mg^{7+} and Ar^{11+} are limited to one Linac3 injection, Ca^{17+} to four, Kr^{22+} to three, In^{37+} to seven and Xe^{39+} to six. At the time of writing, no major LEIR electron cooler upgrade is foreseen, so these estimates should provide approximate upper bounds for the number of allowed injections.

Other ion charge states and isotopes exist and will have different cooling times. It is worth noting how the cooling force in Eq. 3.4 scales for a given electron cooler configuration. The cooling time is defined as $\tau_{\text{cool}} = p_i/F = (m_i V_i)/F$, where p_i is the ion momentum. Since $F \propto Z^2$ and the ion momentum $p_i \propto m_i \propto A$ (for constant velocity), one obtains $\tau_{\text{cool}} \propto A/q^2$ ($q = Z$ for fully stripped ions). In general, the cooling time τ_{cool} of a charge state q and mass number A as compared to Pb is calculated as

$$\tau_{\text{cool}} = \tau_{\text{cool, Pb}} \times \left(\frac{q_{\text{Pb}}}{q}\right)^2 \frac{A}{A_{\text{Pb}}}. \tag{3.6}$$

The simulated relative cooling times from Table 3.2 are compared to Eq. (3.6) (normalized against $^{208}Pb^{54+}$), plotted in Fig. 3.2. Overall, there is good agreement between the simulated cooling times (whose inverse cooling rate $1/\tau_{\text{cool}}$ is shown in the plot) and the cooling scaling law from Eq. (3.6), which will be utilized to estimate the electron cooling performance of different charge states and isotopes in Chapter 6.

Although further experimental studies are needed to validate these estimates, cooling has been tested in LEIR for some lighter ion species. Short O^{4+} beam tests have taken place during LEIR commissioning in 2005 [31, 52], and more recently during the single-bunch O^{4+} pilot beam commissioning during June and July 2025 [13]. Although the 2025 data has not yet

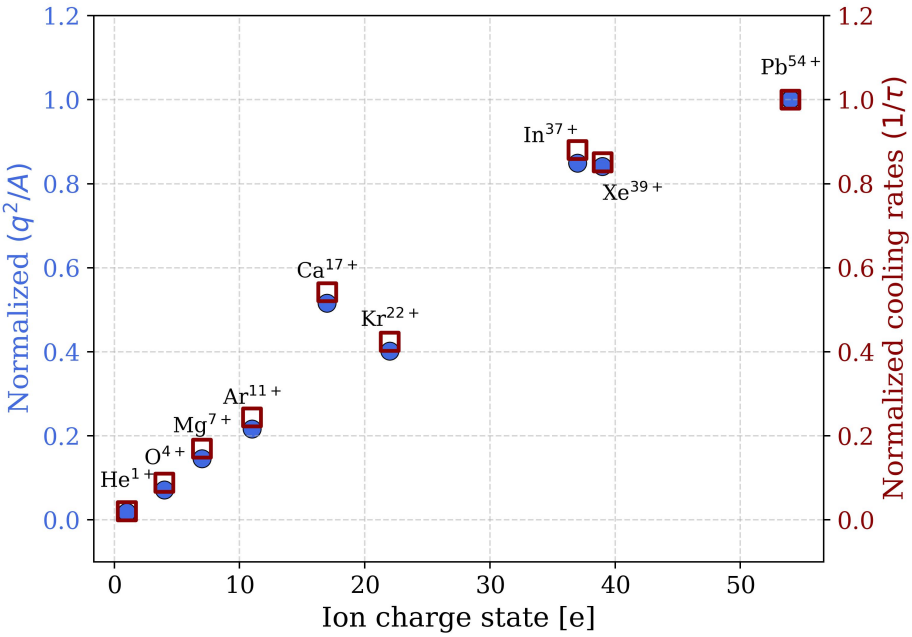


Figure 3.2: Normalized simulated cooling rates $1/\tau_{\text{cool}}$ (red squares) versus the scaling law (in blue) from Eq. (3.6), normalized to $^{208}Pb^{54+}$.

been analyzed in full detail at the time of writing, a single Linac3 injection into LEIR was achieved operationally due to long cooling times, as predicted. Additionally, the short 2024 Mg^{7+} test demonstrated difficulties in going beyond lower intensities and short oven lifetimes, with measured Mg^{7+} currents only reached about 50% of corresponding Pb^{54+} currents [53]. Considerable effort was required to stabilize LEIR electron cooler settings for the single-injection EARLY Mg^{7+} beam that was tested, and insufficient cooling capacity for the multi-injection NOMINAL beam caused excessive beam losses. Although Mg beam commissioning time was limited, one has strong reasons to believe that a single allowed injection for Mg^{7+} is reasonable. Prolonged LEIR cycle lengths could circumvent the problem of longer cooling times, but would lead to increased LHC filling time and more beam degradation.

3.4 Conclusions

The electron cooling performance in LEIR will play a decisive role for the intensity limitations of future ion species in the CERN accelerator complex. This study reviewed the concept of electron cooling, highlighted recent simulation efforts to implement a numerical Parkhomchuk model to estimate cooling times in LEIR, and compared these simulation results with a scaling formula derived within this work, which shows good agreement. In the present LEIR cooler configuration, the longer cooling times of lighter ion species compared to $^{208}Pb^{54+}$ will impose a considerable limit on the number of Linac3 injections, in some cases to a single injection, such as for He, O, Mg, and Ar.

4 Studies of beam interactions with residual gas in the PS

In storage rings, residual gas molecules in the beam pipe can lead to interactions with the particle beam, resulting in losses and emittance growth. In general, these processes can be divided into three main categories:

1. Atomic interactions that alter the beam charge state (driving losses)
2. Inelastic nuclear collisions (driving losses)
3. Elastic nuclear Coulomb scattering interactions (driving emittance growth)

This chapter, largely based on Ref. [54], mainly addresses the questions:

- *To which extent does residual gas currently degrade lead ion beams at CERN?*
- *How will these processes impact future ion species in the CERN accelerator complex?*

4.1 Lifetime studies of atomic charge-changing interactions

This section describes studies of atomic beam-gas interactions carried out in the PS, where these effects are particularly important for ions and instruments to perform such experiments were available. This thesis work contributed to the design and experimental set-up of the neutral gas injection experiment (in collaboration with the PS vacuum team), numerical electron loss and capture model implementation, ion beam lifetime measurements and cross section estimates. First, a theoretical overview of atomic beam-gas interactions is given.

4.1.1 Theoretical description of atomic beam-gas interactions

Atomic interactions of charged ion beams that penetrate targets — gaseous, liquid, and solid — are important for the evolution of the ion charge state. These reactions typically have

much higher cross section than nuclear reactions [55]. Accurate knowledge of these charge-changing atomic processes is fundamental to synchrotrons and beam transfer structures, where charged particles interact with residual gas molecules in the beam pipe [56]. Ion beam losses can occur if the charge state changes, as this results in a different magnetic rigidity, which is typically outside of the acceptance of the accelerator optics, causing the particles to be lost on the vacuum chambers. This effect can potentially cause unwanted detrimental effects, such as increased radiation levels, destruction of sensitive instruments, and significant degradation of the vacuum conditions due to ion-impact-induced desorption [57]. Atomic charge-changing processes are also important for injected beam attenuation functions in plasma devices [58], heavy-ion fusion [59], and in cancer tumor therapy [60]. In addition, the physics understanding of these processes is also essential for the optimization of stripper targets to maximize yields of given charge states [61, 62].

Atomic beam-gas interactions have not been explored consistently in the CERN ion injectors, except for a few studies. Beam-gas interactions were mentioned as a major loss source from the SPS $^{129}Xe^{39+}$ pilot run [63], and the requirements on the LEIR vacuum system for achieving the specified beam lifetime due to these processes were calculated in 2005 [64]. Other accelerator facilities have explored this topic to some degree, such as heavy ion beam lifetimes of the GSI experimental storage ring [57], and the future High Energy Storage Ring (HESR) at FAIR [65]. Two major review studies of such processes – in particular ion collisions with neutral target atoms — are given by [55] and [56].

The two dominant atomic charge-changing effects attributed to beam-gas-induced losses in the CERN ion injector chain are

1. Electron capture (EC) by the projectile:

$$X^{q+} + A \quad \rightarrow \quad X^{(q-k)+} + A^{k+}, \quad k \geq 1 \tag{4.1}$$

2. Electron loss (EL) by the projectile (also denoted ionization or stripping):

$$X^{q+} + A \quad \rightarrow \quad X^{(q+m)+} + \Sigma A + me^{-}, \quad m \geq 1 \tag{4.2}$$

where X^{q+} is the incident projectile with charge state q and A being the target atom. ΣA is the outgoing target, either to be excited or ionized. Electron loss and capture can unfold in several steps. In this study, the focus lies on the total cross sections. In general, EC cross sections dominate at lower energies and remain practically constant until a threshold value, after which a decrease starts at higher energies (because of the velocity mismatch between the projectile and target orbital electrons), where EL instead becomes the main charge-changing process [55, 66]. Systematic heavy-ion cross section measurements of single- and multiple-electron capture and loss are limited in number, often with large reported uncertainties [56].

Electron capture

Many theoretical models have been developed to calculate EC cross sections, including the Classical-Trajectory Monte Carlo (CTMC) method [67], the eikonal approximation [68], the Coulomb Distorted Wave (CDW) approach and the normalized Brinkman-Kramers (NBK) approximation [69]. Such formalisms often only address non-radiative electron capture (NRC), as it often dominates compared to radiative one-electron capture (REC), which becomes important at relativistic collision energies of $E > 200$ MeV/u [55], a process that can also be described as a time-reversed photoionization process occurring in energetic ion-atom collisions [56]. At relativistic energies, the total EC cross section is obtained by the sum of the NRC and REC cross sections

$$\sigma_{\text{EC, tot}} = \sigma_{\text{NRC}} + \sigma_{\text{REC}}. \tag{4.3}$$

REC is predominantly important for few-electron heavy ions at high collision energies (many GeV/u), studied extensively both experimentally and theoretically by [70]. Overall, one of the most versatile tools is the `CAPTURE` code [69], which has been extensively validated for heavy-ion collisions with individual target atoms, across a large energy range. Experimental data for EC cross sections are very scarce, originating mainly from the GSI accelerator facility [71], the Super-HILAC machine at Lawrence Berkeley National Laboratory [72], and the Texas A&M Cyclotron [73].

At high energies below the relativistic case, EC cross sections demonstrate the following asymptotic behavior

$$\sigma_{\text{NRC}} \sim \frac{q^5 I_T^{5/2}}{E^k}, \quad 1 \le k \le 5.5, \quad v^2 >> I_T, \tag{4.4}$$

$$\sigma_{\text{REC}} \sim \frac{q^5 N_T}{E^k}, \quad 1 \le k \le 2, \quad v^2 >> I_T, \tag{4.5}$$

where I_T is the binding energy of the target atom, E is the collision energy, v is the projectile velocity and N_T is the target atom electron number, with index k depending on the collision energy and the electronic shell structure of the particles [55]. The EC cross sections rapidly decrease at increasing collision energies from the E^{-k} dependence, due to an orbital electron velocity mismatch between projectile and target.

Electron capture can also be modeled semi-empirically with the Schlachter formula [74], which applies over a broad range of high-energy highly charged projectiles in gas targets, utilizing generalized reduced coordinates $\tilde{\sigma}$ and $\tilde{E}$, for a target proton number Z_T, and charge state q

$$\tilde{\sigma} = \frac{1.1 \times 10^{-8}}{\tilde{E}^{4.8}} \left[1 - \exp(-0.037 \tilde{E}^{2.2})\right] \times \left[1 - \exp(-2.44 \times 10^{-5} \tilde{E}^{2.6})\right], \tag{4.6}$$

where

$$\tilde{E} = \frac{E}{Z_T^{1.25} q^{0.7}}. \tag{4.7}$$

The EC cross section in cm^2/atom is then computed from the Schlachter formula

$$\sigma_{\mathrm{Schl}} = \tilde{\sigma}\frac{q^{0.5}}{Z_T^{1.8}}, \tag{4.8}$$

for $q \geq 3$ and $\tilde{E} \geq 10$ keV/u. Z_T is the target nuclear charge, and E the projectile energy in keV/u . In the low- and high-energy limits, Eq. (4.8) asymptotically follows

$$\sigma_{\mathrm{Schl}}(E \to 0) \approx 10^{-14}\ [\mathrm{cm}^2/\mathrm{atom}]\ \times \frac{q^{0.5}}{Z_T^{1.8}} \tag{4.9}$$

$$\sigma_{\mathrm{Schl}}(E \to \infty) \approx 1.1 \times 10^{-8}\ [\mathrm{cm}^2/\mathrm{atom}]\ \times q^{3.86} Z_T^{4.2} \tag{4.10}$$

At reduced energies $\tilde{E} > 1000$, the EC cross section is found to be

$$\sigma_{\mathrm{Schl}} = 1.1 \times 10^{-8}\ [\mathrm{cm}^2] \times \frac{q^{3.9} Z_T^{4.2}}{E^{4.8}}. \tag{4.11}$$

Reference [56] suggests that existing theories normally describe experimental σ_{EC} data by a factor 2 or 3, but this discrepancy go up to an order of magnitude in same cases between theory and experiment. The Schlachter formula in Eq. (4.8), the CDW approach, and the CAPTURE code have been demonstrated to agree well, falling within the aforementioned 2-3 factor of the experimental data, in particular above 1-3 MeV/u [75]. In the CERN ion injector chain, the Linac3 extraction energy of 4.2 MeV/u marks the lower energy threshold where these effects are studied.

The Schlachter formula in Eq. (4.8) only considers single-electron capture processes. Multi-electron processes demand more advanced simulation codes, for example `CAPTURE`, `DEPOSIT` and `RICODE-M`, but are mostly important up to only a few MeV/u and are in this context less relevant than single-electron capture, but are worth investigating in future studies for LEIR.

Electron loss

The relativistic Born approximation constitutes the theoretical foundation for ionizing electron loss models, which also consider the magnetic interactions between the colliding projectiles with arbitrary quantum states of projectile electrons and arbitrary targets [76]. Many simulation codes exist for this purpose: `LOSS` for non-relativistic energy ranges [77], and the `LOSS-R` for relativistic energies [78], and `RICODE` to compute cross sections of single-electron loss in ion-atom collisions [79]. `RICODE` considers how colliding particles interact relativistically, but uses radial wave functions that are non-relativistic, based on the assumption that the outer-shell electron ionization — the main contribution to the cross section — can be handled non-relativistically for heavy projectiles with many electrons [56]. To correct for this relativistic factor, the successor `RICODE-M` calculates the relativistic radial functions by solving a) the Dirac-Fock radial equations or b) the Schrödinger equations from binding energy values [79].

Semi-empirical EL cross sections formulae provide a practical alternative to more advanced codes. Starting from the Born approximation and numerical RICODE results for heavy many-electron projectiles, Shevelko [56] postulated a method to calculate EL cross sections over a large energy range

$$\begin{aligned}\sigma_{\text{Shevelko}} =& 0.88\times10^{-16}\ [\text{cm}^2/\text{atom}](Z_T+1)^2 \\ &\times\frac{u}{u^2+3.5}\left(\frac{\text{Ry}}{I_p}\right)^{1+0.01q}\left(4+\frac{1.31}{n_0}\ln(4u+1)\right),\end{aligned} \tag{4.12}$$

with the scaled ion projectile energy u being

$$u=\frac{v^2}{I_p/\text{Ry}}=\frac{(\beta c)^2}{I_p/\text{Ry}}, \tag{4.13}$$

and v the projectile velocity, β is the projectile relativistic beta factor, q is the charge. The projectile ionization potential I_p is expressed in Ry units, 1 Ry = 13.606 eV. The principal quantum number n_0 represents the number of outermost populated projectile electron shells. n_0 and I_p are tabulated in the NIST database [42]. σ_{Shevelko} peaks at $u_{\text{max}}\approx 2$, before it plateaus to a rather constant value. The reported accuracy of Eq. (4.12) compared to RICODE simulations is stated to be within a factor of two for $u>2$. However, the model is not based on the relativistic corrections of RICODE-M and is less reliable at higher energies.

In an attempt to include the Born scaling, screening contributions, anti-screening contributions, and relativistic effects, DuBois [80] proposed an EL cross section target-scaling dependence law for heavy-ion projectiles collisions with any target atom to be

$$\sigma_{\text{Dubois}}=\sigma_H\left[N_{T_{\text{eff}}}+\left(Z_{T_{\text{eff}}}\cdot\exp\left(\frac{-Z_{T_{\text{eff}}}}{v}\right)\right)^2\right], \tag{4.14}$$

with σ_H being the atomic hydrogen stripping cross section, v the impact velocity expressed in atomic units, $N_{T_{\text{eff}}}$ and $Z_{T_{\text{eff}}}$ are

$$Z_{T_{\text{eff}}}=Z_T\left[1-\sqrt{1-\frac{N_{Teff}}{Z_T}}\right], \tag{4.15}$$

$$N_{T_{\text{eff}}}=\langle n\rangle+A(Z_T-\langle n\rangle)\left(-1+\frac{1}{\sqrt{1-\beta^2}}\right). \tag{4.16}$$

As perceived by the projectile electron, these quantities represent the effective charges through the channels of screening and anti-screening, respectively. $\langle n\rangle$ is the average number of active target electrons in the anti-screening channel, from Eq. (19) in [80]. To provide the best fit to the experimental data, the free parameter A was in this study found to be ≈ 10. In most cases, σ_{Dubois} in Eq. (4.14) agrees with experimental loss cross sections for both atomic and molecular targets within the projectile energies E_k spanning up to the tens of MeV/u range, but less at higher projectile energies.

Both semi-empirical formulae of Shevelko and Dubois provide reasonable approximations for EL cross section, but only up to limited energy ranges without relativistic corrections. For the ion projectile energies of the CERN ion injector chain, another version is required. In 2016, Weber [81] proposed a new semi-empirical formula to calculate the total electron loss cross section. This approach combines the energy dependence of Shevelko's model and the target-Z dependence scaling formula of DuBois. In this combined formula, more than one hundred experimental data points (with minimum three different target types, with energies up to 1 GeV/u) from over four decades of research provide the bases for ten fitting parameters c_i, $i \in [0,1\ldots9]$, displayed with two decimals in Table 4.1. In this formula, the single or multiple EL cross section σ_{EL} is

$$\sigma_{\mathrm{EL}} = \tilde{\sigma}_{\mathrm{Shevelko}} \times \tilde{\sigma}_{\mathrm{DuBois}}, \tag{4.17}$$

where

$$\begin{aligned}\tilde{\sigma}_{\mathrm{Shevelko}} = &\frac{c_5(10^{-16})\,u}{u^2+c_6}\left(\frac{\mathrm{Ry}}{I_p}\right)^{c_7+[1-\exp(-c_9u^2)]\frac{q+c_2}{Z_p}} \\ &\times\left(1+\frac{c_8}{n_0}\log\left[(u+1)\gamma_r\right]\right),\end{aligned} \tag{4.18}$$

and

$$\tilde{\sigma}_{\mathrm{DuBois}} = F_1 + \left(F_2 e^{F_3}\right)^2, \tag{4.19}$$

with the relativistic Lorentz factor

$$\gamma_r = \frac{1}{\sqrt{1-\beta^2}}, \tag{4.20}$$

and u

$$u = \frac{(\beta/\alpha)^2}{I_p/\mathrm{Ry}}. \tag{4.21}$$

The parameters F_1, F_2 and F_3 are

$$F_1 = \min\{|N_{\mathrm{eff}} + c_0(Z_T - N_{\mathrm{eff}})(\gamma-1)|, Z_T\}, \tag{4.22}$$

$$F_2 = Z_T(1-\sqrt{1-F_1/Z_T}), \tag{4.23}$$

$$F_3 = \frac{-(F_2^{c_1})}{\left(\sqrt{2E_{\mathrm{kin}}/AU}+\sqrt{2I_p/m_e}\right)/\alpha}, \tag{4.24}$$

where

$$N_{\mathrm{eff}} = \min\{10^{c_3\log_{10}Z_T + c_4(\log_{10}Z_T)^2}, Z_T\}, \tag{4.25}$$

Constant	c_0	c_1	c_2	c_3	c_4	c_5	c_6	c_7	c_8	c_9
Value	10.88	0.95	2.5	1.11	-0.18	2.65	1.36	0.81	1.01	6.14

Table 4.1: Fitted parameters c_i for Eq. (4.17) [81].

and $\alpha = 7.3 \times 10^{-3}$, $AU = 931$ MeV, Ry = 13.606 eV, $m_e = 510.998$ keV. Unlike previous models, the experimental data set includes many Z_T values at different projectile energies, including highly relativistic cases: Au^{52+} at 100 MeV/u [82], Fe^{4+} at 20 MeV/u [83], Xe^{18+} at 6 MeV/u [84], Xe^{45+} at 140 MeV/u [85] and U^{83+} at 955 MeV/u [86]. Figure 4.1 illustrates the semi-empirical Weber formula of Eq. (4.17) compared to the experimental values.

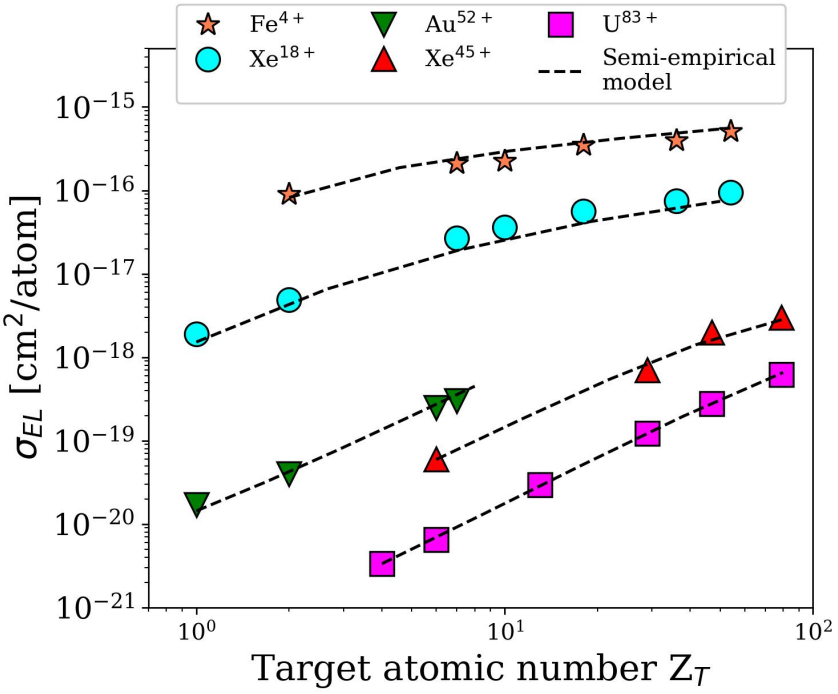


Figure 4.1: Semi-empirical EL model from [81], based on models from Shevelko [56] and DuBois [80]. The colored points represent the experimental data (): Au^{52+} at 100 MeV/u [82], Fe^{4+} at 0.36 MeV/u, Xe^{18+} at 6 MeV/u [84], Xe^{45+} at 140 MeV/u [85] and U^{83+} at 955 MeV/u [86].

Ion beam lifetime estimates

Two combined semi-empirical formulae were numerically implemented in this thesis work: the Schlachter EC formula in Eq. (4.8), and the Weber EL model from Eq. (4.17). These formalisms were synthesized in the open-access Python package `beam_gas_collisions` [87], a practical way to estimate beam lifetimes. The code computes 1) electron capture and electron loss cross sections, 2) projectile energies, and 3) molecular gas densities from estimated gas fractions, from which the estimated beam lifetime is calculated. For accelerators with known residual gas composition, vacuum conditions and projectiles, the software program calculates EC and EL cross sections in the projectile energy range from 0.36 to 955 MeV/u.

The EC and EL model predictions from `beam_gas_collisions` are compared with additional experimental data of U^{28+} on targets of H_2, N_2 and Ar for various projectile energies in Fig. 4.2. In general, measured and predicted EL cross sections agree, as shown in [56]. Following the

positive Z_T scaling, cross sections are higher for Ar targets than on N_2 and H_2 targets. The energies at which EC and EL cross sections matter are also illustrated: EC cross sections dominate at lower energies before rapidly decaying, whereas EL cross sections peak before a slowly decreasing plateau with higher projectile energy. As mentioned already in [75], the Schlachter formula overestimates EC cross sections for higher projectile energies for higher Z_T (Ar targets), a known issue. Nonetheless, in this energy and Z_T regime, EL cross sections dominate by one or two orders of magnitude and this EC discrepancy has a negligible impact.

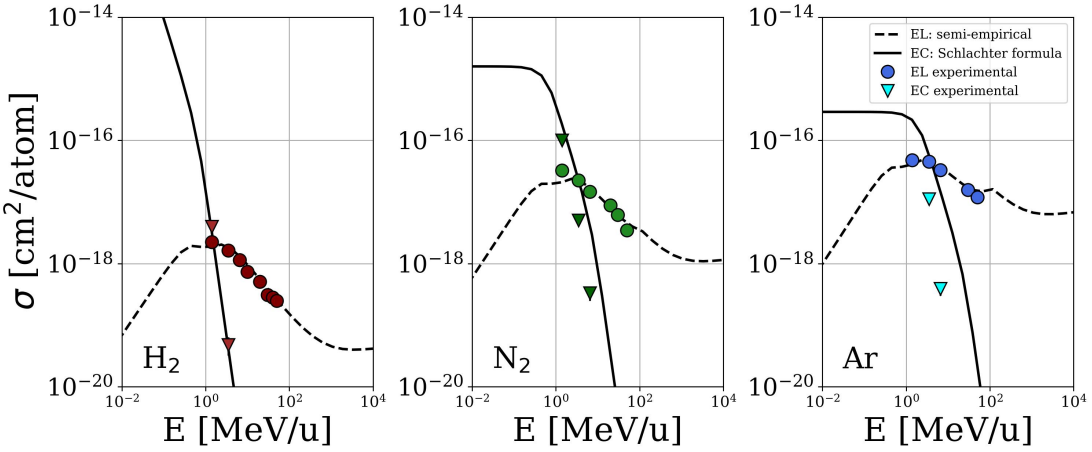


Figure 4.2: EC and EL cross sections of U^{28+} projectiles with H_2 (left), N_2 (middle) and Ar (right) targets over ion energy, compared to semi-empirical prediction models. The experimental EL data points are discussed in further detail in [57]: H_2 [57, 88, 89], N_2 [57, 88, 89, 90] and Ar [57, 71, 89]. EC experimental data points: H_2 [88, 89], N_2 [88, 89] and Ar [89].

The `beam_gas_collisions` program is also capable of computing beam lifetimes. Shevelko mentioned in [56] that the EC formula from Schlachter in Eq. (4.8) together with computed EL cross sections can be utilized to compute beam lifetimes in accelerators [56]. To illustrate the bond between beam intensity and lifetime, the beam intensity (typically measured with a Beam Current Transformer BCT) I over time t can be expressed as

$$I(t) = I(t_0) \cdot \exp\left(-\frac{t}{\tau}\right), \tag{4.26}$$

in which τ from interactions with atomic residual gas is

$$\tau = \frac{1}{\sigma\, n\, \beta\, c}. \tag{4.27}$$

Here, $\sigma = \sigma_{EC} + \sigma_{EL}$ represents the total atomic cross section that changes the charge state, β the fraction of the speed of light at which the projectile travels, c the speed of light and n is the beam pipe molecular density. For example, studies have used Eq. (4.27) to calculate the beam lifetimes of heavy ions in the FAIR facility [65]. It has also been used to study the LEIR dynamic vacuum requirements [64], where the semi-empirical Franzke formula [88] was used, which was extrapolated from single projectile energy results at 1.4 MeV/u. This numerical

beam lifetime prediction framework may be useful to investigate these beam interactions with residual gas in the CERN ion injectors, but also for other accelerators with known vacuum conditions.

A few approximations on how `beam_gas_collisions` treats residual molecules at ambient temperatures and low pressures are worth mentioning. For a mixture of target atoms or molecules, the lifetimes from Eq. (4.27) are summed inversely [64]

$$\frac{1}{\tau_{\text{tot}}} = \sum_{i \in \Omega} \frac{1}{\tau_i}, \tag{4.28}$$

where Ω represents all relevant residual gases, e.g., $\Omega = \{H_2, \text{He}, ...\}$. For every target particle inside the gas mix, the molecular density n is estimated through the ideal gas law

$$n = \frac{P}{kT}, \tag{4.29}$$

where P represents the pressure, k the Boltzmann constant and T the temperature in Kelvin [91]. Dalton's law [92] states that the partial pressure sum of component gases (for individual non-reacting gases) constitutes the total pressure exerted by the gas mixture

$$P_{\text{tot}} = \sum_{i=1}^{n} P_i = P_{\text{tot}} \sum_{i=1}^{n} \frac{n_i}{n_{\text{tot}}}, \tag{4.30}$$

where n_i/n_{tot} represents the molar fraction, which is the ratio of the single gas and total constituent gases. To treat molecules, the additivity cross section rule is used

$$\sigma_{\text{mol}} = \sum_i a_i \sigma(Z_i), \tag{4.31}$$

with a_i being the number of atoms in a given molecule which has atomic number Z_i. The validity of Eq. (4.31) has been confirmed through a linear trend between the target atomic number of noble-gas data to calculate $\sigma(Z_i)$ and the total loss cross section. Typically, this additivity rule is considered reliable for heavy-ion EL for various charge states around the MeV kinetic energy range [93].

4.1.2 Experimental set-up and PS pressure profile reconstruction

A series of gas injection experiments — described in detail in Ref. [54] — were conducted in the PS to validate predicted cross sections $\sigma_{\text{EC, EL}}$. No dedicated gas target for EC and EL cross section measurements exists at CERN. However, the Beam Gas Ionization (BGI) Profile Monitor instrument [94, 95] installed in the PS accelerator features an external neutral gas injection system, connected through a valve to the PS beamline. It typically uses argon (Ar). The injection system includes a Penning gauge and a gas bottle, where a valve connects a turbomolecular pump to the remaining instrumentation. Various programmable “Set Points" (SP) control the injected neutral gas flow into the beam pipe.

Together with F. Ukena, J. Somoza, J. Olsen and R. Alemany Fernández, the gas injection system of the BGI was exceptionally set up in a neutral gas injection experiment, thus generating a controlled pressure bump to act as an effective in-ring gas target. A dedicated Pb ion cycle was prepared in the PS, with the option to use either the EARLY (low-intensity) beam or the NOMINAL (high-intensity) ion beams from LEIR. Projectiles were studied under the influence of the injected target gas in three experiments: A) Pb^{54+} on Ar (Oct 2023), B) Mg^{7+} on Ar (May 2024), and C) Pb^{54+} on He (Sep 2024). In this period, the two available target gases were Ar and He. The main idea of the experiment is to use beam intensity curves to fit the beam lifetime parameter τ from Eq. (4.27) for various Set Points of injected neutral gas quantities. These fitted lifetimes from measurements are then compared to lifetime predictions from the semi-empirical EC and EL interactions in `beam_gas_collisions`. The projectile, injected neutral gas type and energy are shown in Table 4.2.

Projectile in the PS	Kinetic energy [MeV/u]	Target gas
A) Pb^{54+}	72.2	Ar
B) Mg^{7+}	90.2	Ar
C) Pb^{54+}	72.2	He

Table 4.2: Projectile types, beam energy, and the injected target gas for the PS experiments.

The largest source of uncertainty in Eq. (4.27) comes from the average molecular density n, as the PS pressure profile to calculate the average ring pressure is not precisely known. A pressure profile reconstruction effort was undertaken by F. Ukena and J. Somoza (from the PS vacuum team) in two main steps: modelling based on measurements and then usage of this model to simulate the pressure around the BGI instrumentations during the gas injection experiments. The modeling effort is described in detail in Ref. [54], resulting in a 3D geometry representation of 10% of the total PS ring, centered around the BGI instrument location. This represented a key step to estimate the average PS pressure profiles for various Set Points of injected target gas. A pressure profile example prepared by F. Ukena for one of the Set Points is

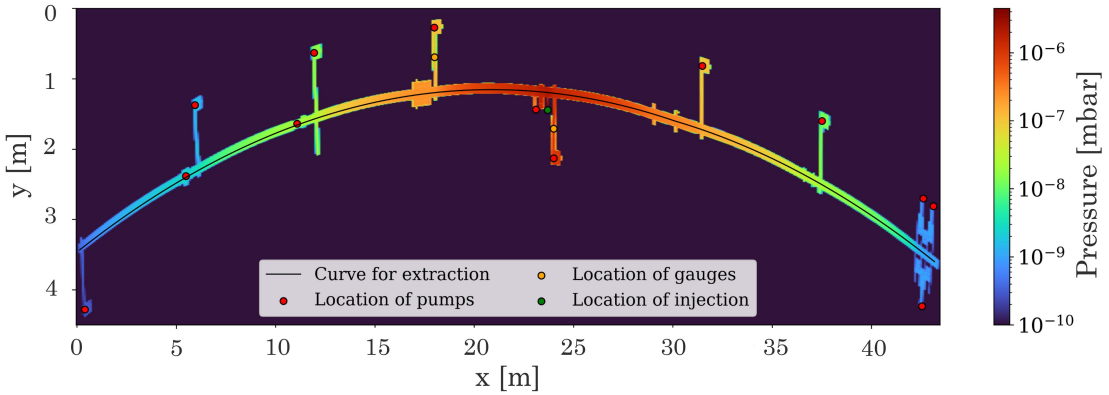


Figure 4.3: 3D image of the Molflow+ model for the PS section around the BGI, with the simulated pressure distribution of Ar for SP 160 (N_2 equivalent). Markings are set at locations of gas injection, gauges, and pumps. Image credit: F. Ukena

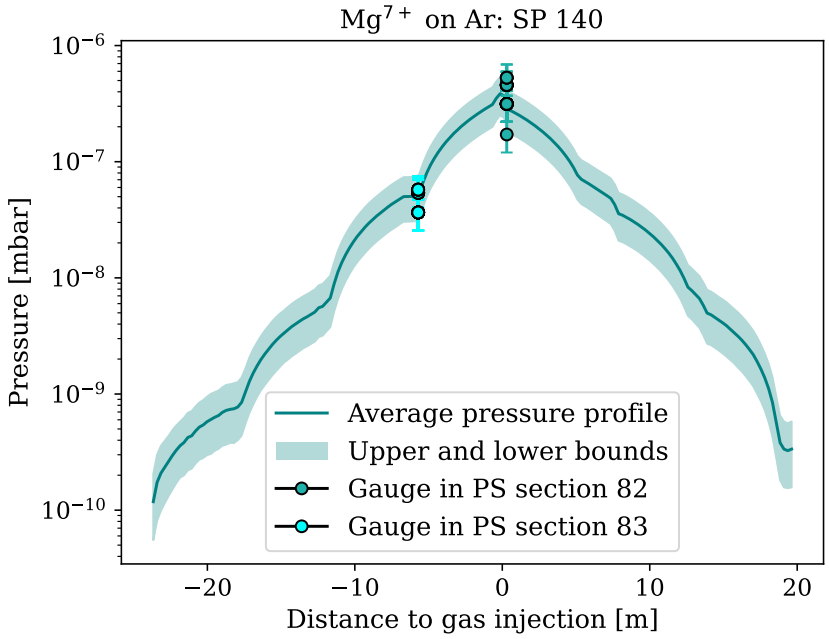


Figure 4.4: PS pressure profile example, centered around the BGI injection system, simulated with Molflow+ for one Set Point (SP) for the Mg^{7+} beam test (with Ar target gas). Two additional pressure gauge measurements near the BGI location are also shown. Image credit: F. Ukena.

illustrated in Fig. 4.3, where the 3D model was employed for gas propagation simulations in the PS with the MolFlow+ program [96, 97], a vacuum simulation Monte Carlo code.

For each case, the pressure profile uncertainty was estimated from combining gauge accuracies and calculated gas flows of various plausible pumping speeds, yielding lower and upper pressure profile uncertainty boundaries. Figure 4.4 shows an example compared to two Penning gauge measurements in the PS.

Another step in the pressure profile reconstruction is to disentangle losses from the in-ring target (pressure bump) from the residual gas baseline pressure or other unknown sources (e.g. machine outgassing). For the higher Set Points, the injected neutral gas is assumed to dominate the pressure. At lower pressures, dynamic vacuum effects and unknown static base pressure values most likely interfere with the injected gas target. To compensate for this effect, the beam lifetime is first measured without any neutral gas injection, allowing to calculate the decay constant from such unknown loss sources and the static base pressure. If from Eq. (4.28) one assumes that loss rates (which are the inverse of lifetimes) are additive, the beam lifetime τ_{bump} from the controlled in-ring target is

$$\frac{1}{\tau_{\text{measured}}} = \frac{1}{\tau_{\text{residual}}} + \frac{1}{\tau_{\text{bump}}} \tag{4.32}$$

$$\Rightarrow \tau_{\text{bump}} = \left(\frac{1}{\tau_{\text{measured}}} - \frac{1}{\tau_{\text{residual}}} \right)^{-1}. \tag{4.33}$$

In addition, a BCT baseline error was observed without any beam present in the machine, and this was compensated for in order to achieve the most accurate measurements possible. Beam lifetimes are measured with bunched beam (radio-frequency RF cavity “ON") and coasting beam (RF cavity “OFF"). In the former case, with a denser longitudinal beam profile, one expects space charge and intra-beam scattering effects to possibly contribute to losses. On the other hand, a longitudinally less dense coasting beam allows the decoupling of losses from such effects. Future studies should address other vacuum effects such as PS vacuum chamber wall outgassing in further detail.

4.1.3 Pb^{54+} lifetime experiment with injected Ar gas

In experiment named (A), the Pb^{54+} beam lifetime was measured for varying pressures of the injected Ar gas. The BCT intensity evolution of the Pb^{54+} beam over the cycle (at injection energy) is shown in Fig. 4.5 for various Set Points. Permutations of beam types were varied: low-intensity beam (EARLY), high-intensity beam (NOMINAL), bunched beam (RF ON) and coasting beam (RF OFF). In Fig. 4.5, the lifetimes decrease with more injected neutral target gas, seemingly independent of the beam type.

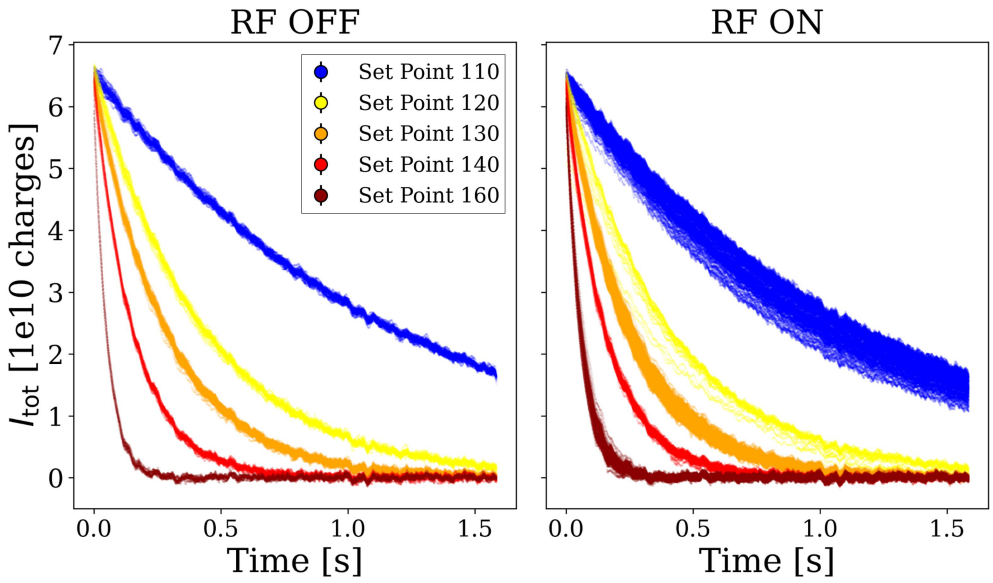


Figure 4.5: Evolution of the intensity profiles for the NOMINAL Pb^{54+} beam for various cases. Blue curves indicate lower Set Points with less gas injected, gradually going to yellow and then darker red for higher Set Points with more abundant gas injections. The large lifetime variation for the lowest Set Point (in blue) where the RF is ON originates from a particularly variable local pressure variation at that exact time stamp, before the pumping speed saturation.

In parallel to the lifetime measurements, the pressure gauge VGP82 value is monitored, as it is located in the vicinity of the BGI device. Figure 4.6 illustrates the beam lifetime for various pressure gauge readouts during the experiment. The lifetime trend with higher pressure gauge readout seems to follow a uniform power law, apart from a small discontinuity at 10^{-7}

mbar, which is most likely due to a Penning gauge voltage switching. This lifetime trend occurs irrespective of the beam type and appears similar for high-intensity beams (circles) and low-intensity beams (triangles).

Also, Fig. 4.6 clearly shows that the target pressure will somewhat fluctuate for the same Set Point due to variations in pumping and saturation speeds. To compensate for this effect, the relative VGP82 fluctuation within each Set Point is used to adjust the pressure profile bounds (lower and upper) in Fig. 4.4 to improve the average target pressure calculation accuracy.

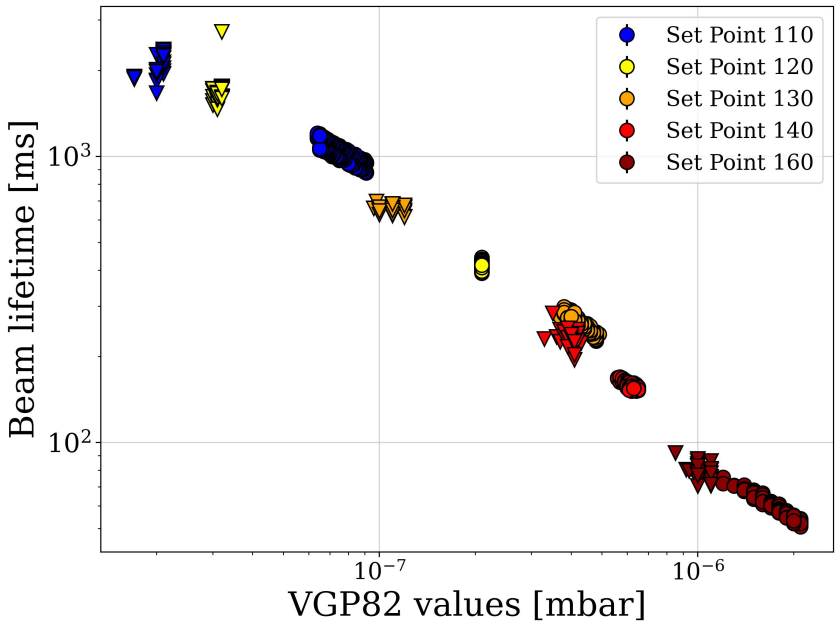


Figure 4.6: Measured Pb^{54+} beam lifetime for various readouts of the pressure gauge device VGP82. High-intensity (NOMINAL) beams are marked as circles, low-intensity beams (EARLY) are marked with triangles.

Figure 4.7 shows the model-measurement comparison for Pb^{54+} on Ar: experimental beam lifetimes τ from Eq. (4.26) versus the predicted value from `beam_gas_collisions` (assuming that the neutral gas target dominates). Note that the target gas composition carries uncertainties below 10^{-9} mbar due to varying outgassing between experiments, and unknown total flows for these Set Points. One observes a decreasing lifetime for higher target pressures, seemingly uncorrelated to beam intensity and longitudinal beam shape (coasting or bunched beam). The predicted semi-empirical lifetime values converge towards the measurements for higher target pressures, as beam-gas interactions begin to dominate among the beam loss mechanisms. Alternatively, these underlying semi-empirical models are not as reliable for lower target pressure values. The underlying factor 2 model uncertainty (at least) for electron capture and electron loss stated by Shevelko [56] are illustrated in the band shaded in gray.

The target pressure error bars indicate the uncertainty bounds from the reconstructed pressure profiles discussed in Sec. 4.1.2, although the uncertainty may be even larger. The lifetime error

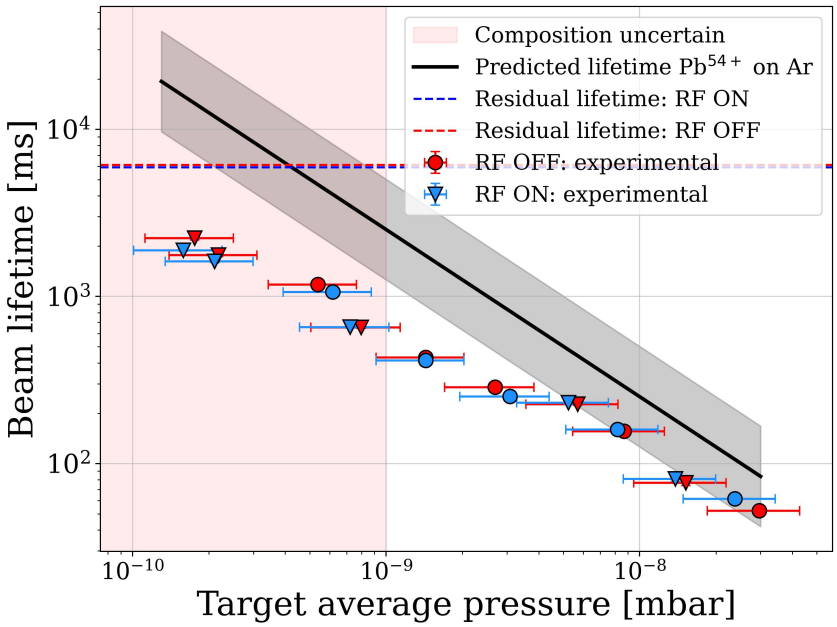


Figure 4.7: Measured beam lifetimes of Pb^{54+} over average target pressure of injected Ar gas, with the prediction from the semi-empirical model in black (with model uncertainty band shaded in gray). Circles indicate NOMINAL beams, triangles indicate EARLY beams. Coasting beams (RF OFF) are colored in red, bunched beam (RF ON) are marked in blue. Residual lifetime indicates the measured beam lifetime without any injected gas. Uncertain gas composition below 10^{-9} mbar is marked in red.

bars combine random variation of measurements in a given Set Point and the fitting error from the lifetime parameter. Typically, these lifetime uncertainties are very small compared to the error on the pressure.

4.1.4 Mg^{7+} lifetime experiment with injected Ar gas

In May 2024, a PS beam lifetime experiment named (B) took place with a Mg^{7+} test beam with a kinetic energy of 90.2 MeV/u, using argon as neutral target gas. For the very first time, the source and Linac3 produced this type of beam, which makes it hard to compare directly with the Pb^{54+} beams used in routine operations. Nonetheless, the available EARLY Mg beams were used in lifetime experiments, in a similar set-up as the Pb^{54+} beams. High BCT noise levels compared to the low beam intensity allowed lifetime trends to be observed only for the three highest target pressures, as shown in Fig. 4.8. The lifetime trend is similar to experiment (A), which decreases for higher target pressures. However, the Mg^{7+} measurements first fall above predicted lifetime before converging to within the prediction uncertainty limits.

Worth noting in this experiment is that the combination of a outer projectile electron that is loosely bound, higher Z_T (which here means heavier than N), and relativistic projectile energies are not represented in Fig. 4.1. As a consequence, this experimental regime may

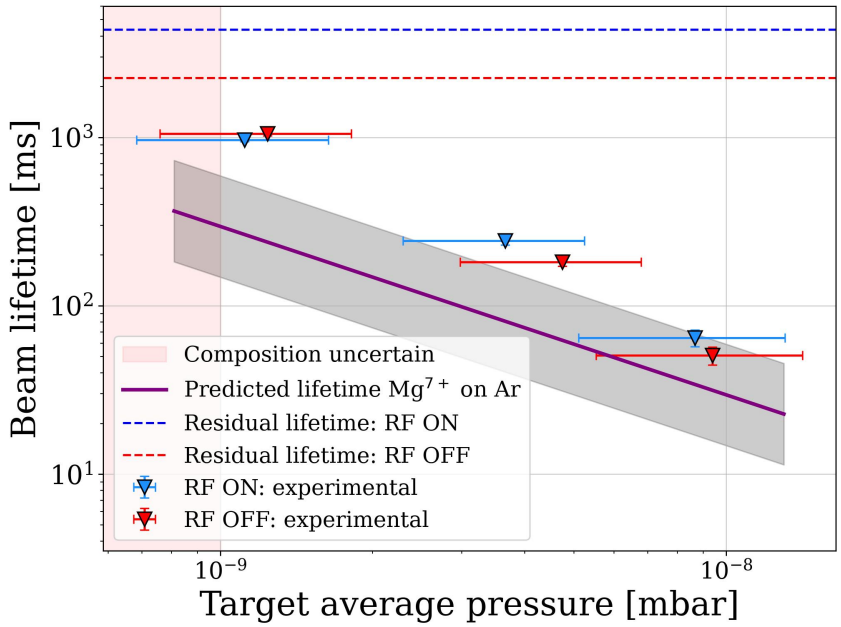


Figure 4.8: Measured Mg^{7+} beam lifetimes over various target pressures from the injected Ar gas, with residual lifetimes marked.

lack a reference point in the empirical parameter optimization for Table 4.1 in [81]. Although EL dominates at this energy, the predicted EC cross sections could be overestimated for high Z targets such as Ar. Despite these caveats, for the highest target pressure, the lifetime measurements still fall within the uncertainty band.

4.1.5 Pb^{54+} lifetime experiment with injected He gas

The third experiment with beam lifetimes, named (C), was performed in September 2024 with Pb^{54+} beams at the kinetic energy of 72.2 MeV/u, this time using neutral He as injected target gas. The measured beam lifetimes over target pressure are shown in Fig. 4.9. At the second-highest Set Point, the predicted Pb^{54+} lifetime on He is approximately 1.9 times above the measurement. Note that cross sections (EC and EL) for Pb^{54+} on He (low Z_T target) are reduced by many orders of magnitude compared to the Ar target in experiment (A) and (B). More injected He gas is needed than Ar to notice its effect on beam lifetimes.

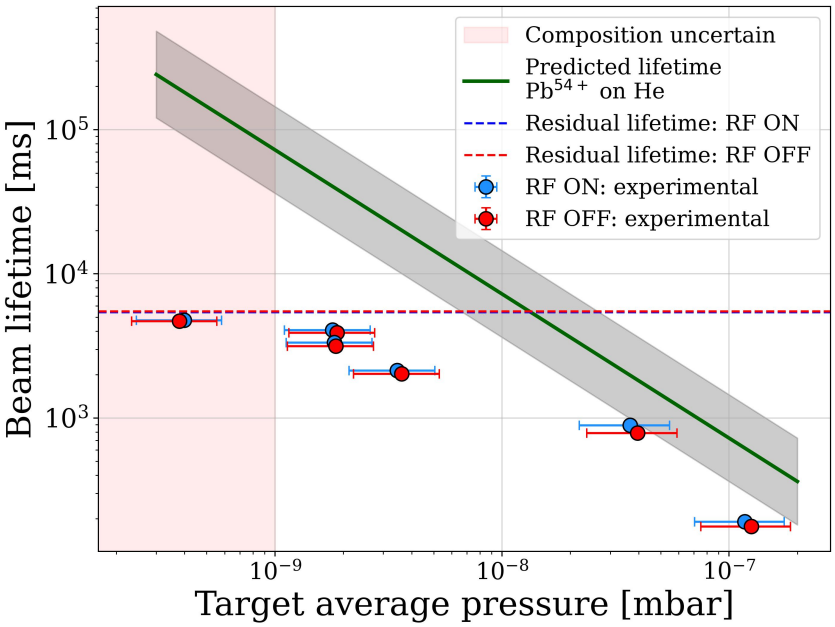


Figure 4.9: Measured Pb^{54+} beam lifetimes for various target pressures from the injected He gas, also showing the residual lifetimes when no gas was injected.

4.1.6 Experimental cross sections from beam lifetime measurements

In the subsequent step, the experimental cross sections σ_{exp} are computed from the measured lifetimes and compared with model predictions $\sigma_{\text{pred.}}$ from `beam_gas_collisions`, where beam-gas interactions are assumed to dominate the losses for higher target pressures. These lifetime measurements and calculated target pressures are used inversely in Eq. (4.27), subtracting the residual lifetime from Eq. (4.33). Only measured lifetimes with average target pressures exceeding 10^{-9} mbar are included, a point below which the target gas composition is too uncertain. To estimate the error on the experimental cross section, errors from lifetime and pressure measurements (assuming they are independent from each other) are combined through the generalized formula for the error propagation from [98]:

$$\sigma_{\hat{R}} = \sqrt{\left(\frac{\partial R}{\partial X}\right)^2 \sigma_X^2 + \left(\frac{\partial R}{\partial Y}\right)^2 \sigma_Y^2} \tag{4.34}$$

where $\sigma_{\hat{R}}$ is the uncertainty in the cross section R, X and Y represent the lifetime and pressure measurements respectively, and σ_X, σ_Y are their respective uncertainties. Figure 4.10 shows the results for the experimental cross sections.

Table 4.3 shows the final results of the experimental cross section studies with gas injection: type of projectile, kinetic energy E_k, type of target gas, residual lifetime from Eq. (4.33). These values are used as input to calculate the predicted cross section $\sigma_{\text{pred.}}$ and the experimental cross section $\sigma_{\text{exp.}}$. Overall, $\sigma_{\text{exp.}}$ converges towards $\sigma_{\text{pred.}}$ at higher target pressures. In this regime, beam-gas interactions dominate compared to other loss sources, a trend also seen

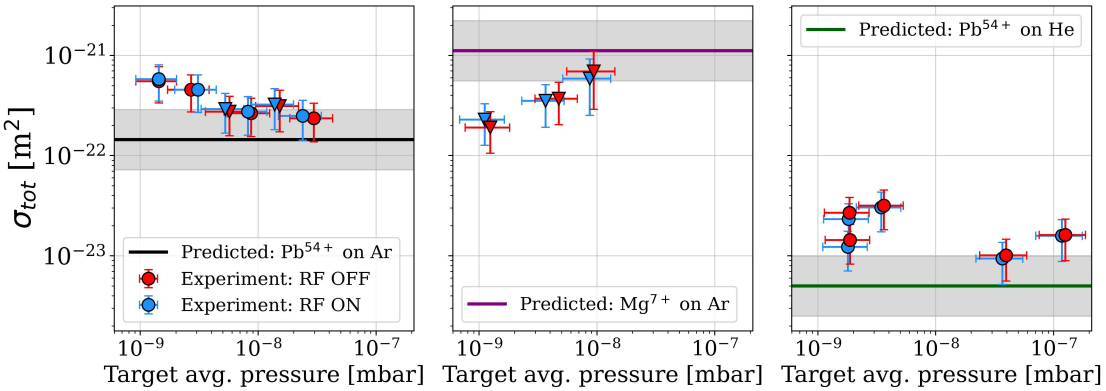


Figure 4.10: Measured and predicted total charge-changing cross sections for the experiments.

in Fig. 4.7, 4.8 and 4.9. Propagating these lifetime trends to experimental cross sections, the predicted Pb^{54+} cross sections are lower than the measurements, as opposed to the prediction for Mg^{7+} on Ar, which falls above.

Experiment	A	B	C
Date	10/2023	05/2024	09/2024
Projectile	Pb^{54+}	Mg^{7+}	Pb^{54+}
E_k [MeV/u]	72.2	90.2	72.2
Target	Ar	Ar	He
RF ON: τ_{res} [s]	5.9 ± 0.2	4.4 ± 1.1	5.4 ± 0.1
RF OFF: τ_{res} [s]	6.1 ± 0.1	2.3 ± 0.7	5.5 ± 0.1
$\sigma_{\text{pred.}}$ [10^{-22} m^2]	1.4 ± 0.7	11 ± 6	0.05 ± 0.03
$\sigma_{\text{exp.}}$ [10^{-22} m^2]	3.6 ± 1.5	4.0 ± 2.1	0.19 ± 0.08

Table 4.3: Experimental results from the three experiments, with semi-empirical predictions.

Whether the beam is bunched or coasting (RF ON versus OFF, respectively) does not have any measurable impact on the experimental cross section or beam lifetimes, confirming that the longitudinal profile does not matter for higher quantities of injected target gas, when losses are dominated by beam interactions with residual gas. For the highest target pressures, $\sigma_{\text{exp.}}$ falls into the gray semi-empirical prediction uncertainty band, within the typical factor 2-3 stated in Ref. [56].

4.1.7 Beam lifetime estimates for future ion species at CERN

To which extent will atomic charge-changing interactions with residual gas molecules affect future ion species? Table 4.4 presents, for energies and projectiles considered for LEIR and the PS, the calculated σ_{EC} from Eq. (4.8) and σ_{EL} from Eq. (4.17) with `beam_gas_collisions`. For the fully stripped ions in the SPS, only electron capture is possible with negligible cross sections. Therefore the SPS cases are not considered in Table 4.4.

		EC cross section [m^2]					EL cross section [m^2]				
Ion	E_k	H_2	H_2O	CH_4	CO	CO_2	H_2	H_2O	CH_4	CO	CO_2
He^{1+}	4.2	3.3E-29	1.0E-25	3.0E-26	1.3E-25	2.3E-25	3.3E-22	2.3E-21	2.2E-21	3.6E-21	5.6E-21
He^{2+}	4.2	2.7E-28	8.1E-25	2.4E-25	1.1E-24	1.9E-24	-	-	-	-	-
O^{4+}	4.2	2.0E-27	5.8E-24	1.7E-24	7.6E-24	1.3E-23	4.0E-22	2.9E-21	2.8E-21	4.5E-21	7.0E-21
O^{5+}	4.2	4.8E-27	1.4E-23	4.1E-24	1.8E-23	3.1E-23	4.1E-22	3.0E-21	2.9E-21	4.6E-21	7.2E-21
O^{8+}	4.2	2.7E-26	6.9E-23	2.5E-23	9.4E-23	1.6E-22	-	-	-	-	-
Mg^{6+}	4.2	9.7E-27	2.6E-23	8.4E-24	3.5E-23	6.1E-23	3.1E-22	2.3E-21	2.2E-21	3.5E-21	5.5E-21
Mg^{7+}	4.2	1.8E-26	4.5E-23	1.5E-23	6.0E-23	1.0E-22	2.1E-22	1.6E-21	1.5E-21	2.4E-21	3.8E-21
Ar^{11+}	4.2	9.3E-26	1.8E-22	7.9E-23	2.6E-22	4.3E-22	1.2E-22	9.0E-22	8.4E-22	1.4E-21	2.2E-21
Ca^{17+}	4.2	5.0E-25	5.4E-22	3.1E-22	8.5E-22	1.4E-21	2.9E-23	2.3E-22	2.2E-22	3.6E-22	5.7E-22
Kr^{22+}	4.2	1.4E-24	9.9E-22	6.3E-22	1.6E-21	2.6E-21	8.2E-23	6.6E-22	6.1E-22	1.0E-21	1.6E-21
In^{37+}	4.2	1.0E-23	3.1E-21	2.2E-21	5.3E-21	8.4E-21	1.1E-23	9.5E-23	8.8E-23	1.5E-22	2.3E-22
Xe^{39+}	4.2	1.2E-23	3.5E-21	2.5E-21	5.9E-21	9.4E-21	1.2E-23	1.0E-22	9.2E-23	1.6E-22	2.5E-22
Pb^{54+}	4.2	4.3E-23	6.9E-21	5.1E-21	1.2E-20	1.9E-20	1.6E-23	1.4E-22	1.3E-22	2.2E-22	3.5E-22
He^{1+}	67	5.6E-35	1.7E-31	5.2E-32	2.2E-31	4.0E-31	3.7E-23	4.6E-22	3.6E-22	7.1E-22	1.1E-21
He^{2+}	245.4	9.0E-37	2.8E-33	8.4E-34	3.6E-33	6.4E-33	-	-	-	-	-
O^{4+}	67.1	3.3E-33	1.0E-29	3.1E-30	1.3E-29	2.4E-29	4.4E-23	5.6E-22	4.3E-22	8.5E-22	1.4E-21
O^{5+}	102.9	1.0E-33	3.2E-30	9.5E-31	4.1E-30	7.3E-30	3.7E-23	5.9E-22	4.1E-22	9.0E-22	1.5E-21
O^{8+}	245.6	9.8E-35	3.0E-31	9.1E-32	4.0E-31	7.0E-31	-	-	-	-	-
Mg^{6+}	67.1	1.6E-32	5.0E-29	1.5E-29	6.5E-29	1.2E-28	3.6E-23	4.5E-22	3.5E-22	6.9E-22	1.1E-21
Mg^{7+}	90.2	7.1E-33	2.2E-29	6.6E-30	2.9E-29	5.1E-29	2.0E-23	3.2E-22	2.3E-22	4.9E-22	7.9E-22
Ar^{11+}	80.7	7.1E-32	2.2E-28	6.6E-29	2.9E-28	5.1E-28	1.4E-23	1.9E-22	1.4E-22	3.0E-22	4.8E-22
Ca^{17+}	183	7.6E-33	2.4E-29	7.1E-30	3.1E-29	5.4E-29	3.1E-24	5.3E-23	3.6E-23	7.9E-23	1.3E-22
Kr^{22+}	70.2	2.1E-30	5.7E-27	1.7E-27	7.4E-27	1.3E-26	1.1E-23	1.5E-22	1.1E-22	2.2E-22	3.6E-22
In^{37+}	108.8	1.9E-30	5.2E-27	1.5E-27	6.7E-27	1.2E-26	2.3E-24	3.8E-23	2.7E-23	5.8E-23	9.4E-23
Xe^{39+}	96.7	4.2E-30	1.1E-26	3.3E-27	1.4E-26	2.6E-26	2.9E-24	4.7E-23	3.3E-23	7.1E-23	1.2E-22
Pb^{54+}	72.1	6.0E-29	1.6E-25	4.8E-26	2.1E-25	3.7E-25	3.4E-24	4.6E-23	3.5E-23	7.0E-23	1.1E-22

Table 4.4: Calculated σ_{EC} and σ_{EL} on target gases H_2, H_2O, CH_4, CO and CO_2 for ion projectiles with kinetic energies (in MeV/u) for two machines at injection: LEIR (top half), and PS (bottom half). Here, $T = 293$ K.

Figure 4.11 shows the two study cases Pb^{54+} and O^{4+} on the common gas target types H_2, H_2O, CH_4, CO and CO_2 . Relatively speaking, EC is more important for Pb^{54+} and EL for O^{4+} in LEIR. The EL cross section for O^{4+} is much higher than Pb^{54+} in both LEIR and the PS.

What about expected beam lifetimes for future ion species? When beam-gas interactions dominate the beam losses, the three PS gas injection experiments in Section 4.1.3-4.1.5 show

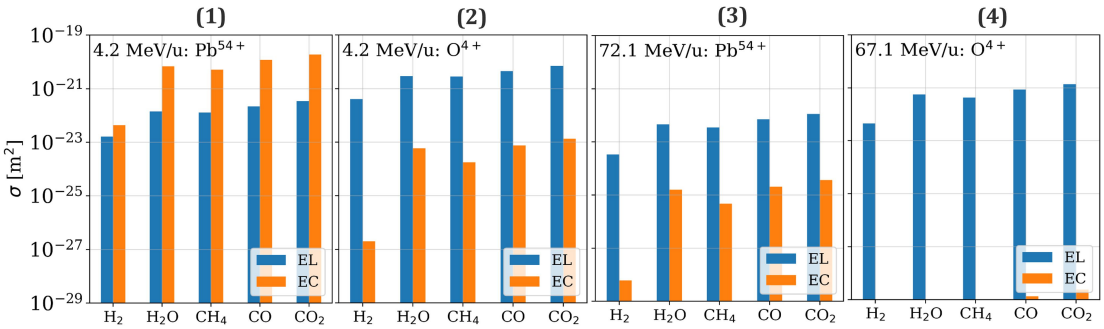


Figure 4.11: Calculated $\sigma_{EC,\,EL}$ on H_2, H_2O, CH_4, CO and CO_2 gas targets for: 1) Pb^{54+} with 4.2 MeV/u, 2) O^{4+} with 4.2 MeV/u, 3) Pb^{54+} with 72.1 MeV/u and 4) O^{4+} with 67.1 MeV/u.

that lifetime predictions from the `beam_gas_collisions` program falls within the typical factor 2-3. Although other unknown loss sources may affect future ion species, these lifetime predictions provide upper beam lifetime limitations for known vacuum conditions within the reported error factor. The prediction model is used to calculate atomic charge-changing lifetime limitations for proposed future ion species in LEIR, PS and SPS. There is a high uncertainty in the actual rest gas composition in the CERN accelerator complex and therefore some assumptions on the *static* vacuum conditions have to be made, as summarized in Table 4.5. Dynamic vacuum conditions and outgassing — that typically affect ion beam lifetimes — are not accounted for, but this approach gives a first-order estimate.

	LEIR	PS	SPS
$\bar{P}$ [mbar]	10^{-11}	1.2×10^{-9}	10^{-8}
H_2 fraction	0.83	0.9	0.905
H_2O fraction	0.02	0.1	0.035
CO fraction	0.04	0	0.025
CH_4 fraction	0.05	0	0.025
CO_2 fraction	0.06	0	0.01
Cycle time [s]	3.6	1.2	≃60

Table 4.5: Assumed average pressure values $\bar{P}$ and rest gas composition (fraction of total particle density) and nominal Pb cycle time duration used in operation. The SPS vacuum conditions are taken from [63]. The LEIR and PS base pressures represent typical gauge measurements from November 2024. The rest gas composition is assumed to be dominated by H_2, but other gas fractions are very approximate.

The predicted lifetimes τ_{tot} at injection energy due to beam-gas interactions for future ion species in LEIR, the PS, and the SPS are shown in Fig. 4.12. Some ion species come in several possible charge states. For example, oxygen can either be stripped directly after the source to O^{8+}, or stripped from either O^{4+} or O^{5+} to O^{8+} after the PS. Lifetimes are much longer in the SPS compared to LEIR and the PS, as electron capture (the only possibility for fully stripped ions) is negligible at these energies. In particular, the PS is the main bottleneck for some partially stripped lighter ions with relatively short lifetimes at injection energy: 4.0 s for He^{1+}, 3.3 s for O^{4+}, 2.9 s for O^{5+}, 4.1 s for Mg^{6+} and 5.5 s for Mg^{7+}.

In the typical operational PS cycle, the beam is immediately ramped from injection energy to an intermediate bunch splitting energy plateau, before the energy ramp to extraction energy. The two main candidate species with seemingly short PS lifetimes are O^{4+} and Mg^{7+}. Calculating the beam lifetime at PS extraction energy, one finds 4.6 s for O^{4+}, and 7.7 s for Mg^{7+}. These lifetimes are longer than at injection energy, but will still affect beam transmission. Figure 4.13 shows a first experimental validation with single-bunch O^{4+} pilot beams in the PS, where an average lifetime of $\tau = 4.4$ s was found along the entire cycle (i.e. including the energy ramp), which falls into this predicted oxygen lifetime interval of 3.3-4.6 s when considering the energy ramp. In general, no major transmission issues from electron loss or capture are expected, except a few charge states of lighter ions.

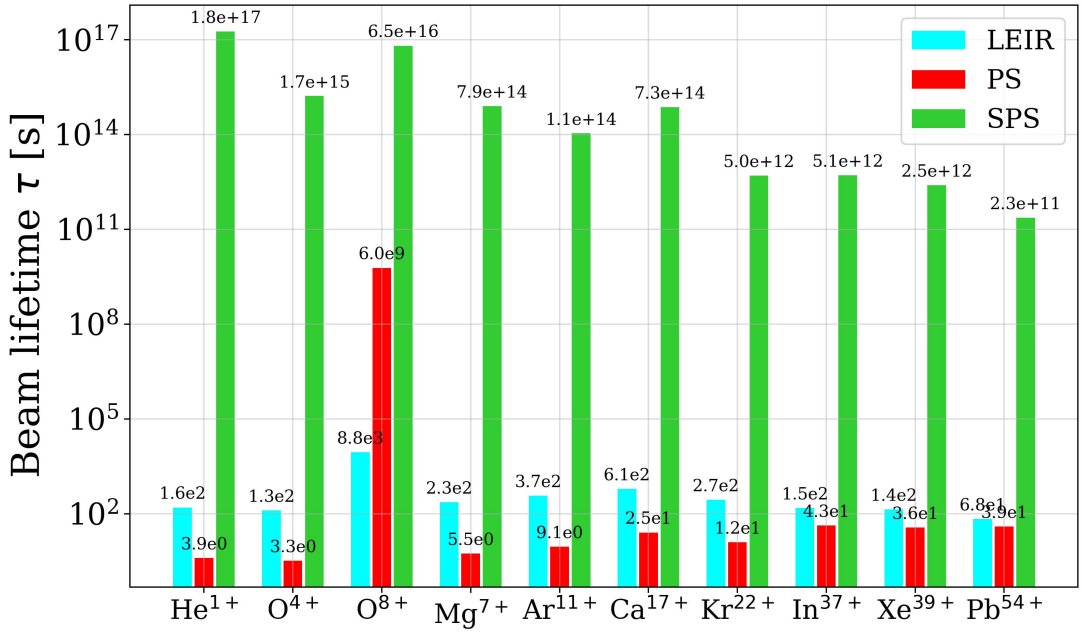


Figure 4.12: Predicted ion beam lifetime at injection due to beam-gas charge-changing interaction with the static base pressure in LEIR, PS, and SPS for some considered future ion species at CERN. Other background losses may be present and further reduce the lifetime.

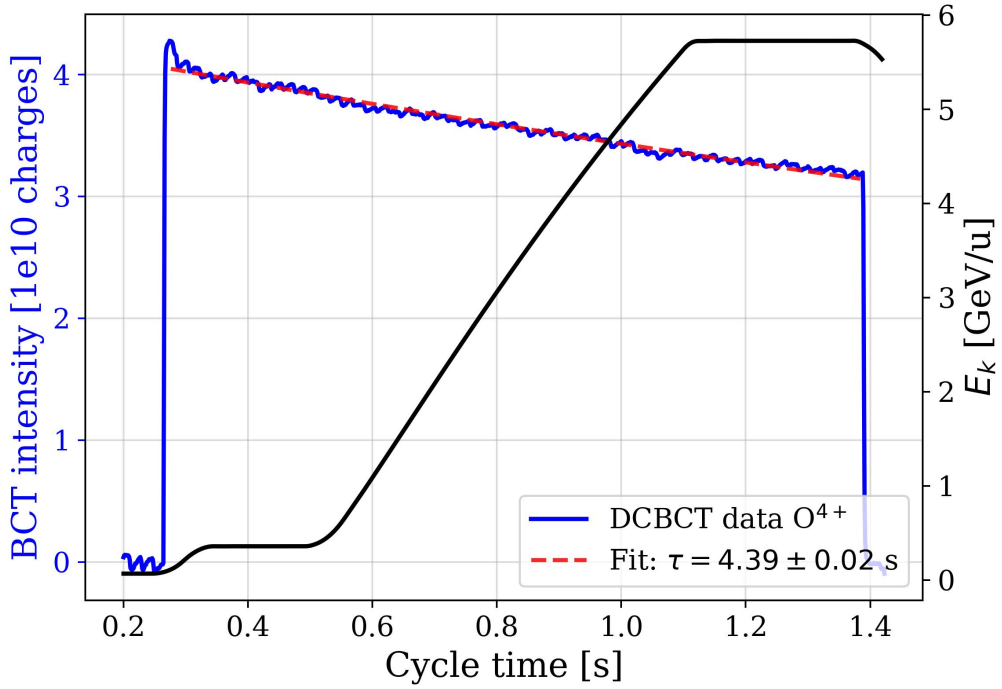


Figure 4.13: Measured DCBCT intensity with single-bunch O^{4+} pilot beams in the PS, June 2025, with fitted lifetime τ. The kinetic energy per nucleon is also shown.

4.2 Beam degradation from inelastic and elastic collisions

Beyond charge-changing atomic interactions with the residual gas, other beam-gas interaction processes include inelastic nuclear collisions (mainly resulting in losses) and elastic nuclear Coulomb scattering processes (mainly resulting in emittance growth). In the context of the CERN ion injector chain, these processes are typically less important than EC and EL. Nuclear collisions and multiple scattering have previously been discarded as negligible for proton beam lifetimes in HERA [99] and in RHIC [100]. Previous SPS proton studies at $p = 120$ GeV/c measured normalized emittance growth rates of about 0.8 mm mrad per hour independent of beam intensity, tunes, and transverse plane, pointing to residual gas scattering as a possible explanation [101, 102].

Multiple scattering cross sections for heavier ions are typically smaller compared to protons [66], scaling with Z_p^2/A_p^2 for a given energy and projectile p. Nonetheless, ion beam lifetime estimates from these collision processes between the projectile ions and nuclei of gas atoms will be treated here quantitatively for the sake of completeness.

4.2.1 Inelastic nuclear collisions

In the geometric picture, the nuclear reaction cross section between a projectile P and a target T is expected to be proportional to the area πR_N^2 "seen" by the projectile, where R_N is the combined nuclear radius. In the context of cosmic radiation, Bradt and Peters [103] proposed in 1950 the first empirical formula for the total inelastic nuclear collision cross section

$$\sigma_N = \pi r_0^2 \left(A_P^{1/3} + A_T^{1/3} - b_0 \right)^2, \tag{4.35}$$

where A is the mass number, b_0 is the overlap parameter and r_0 is the geometrical nuclear radius proportionality constant. For all targets other than hydrogen, the values $r_0 = 1.35$ fm and $b_0 = 0.83$ have been determined experimentally [104]. For hydrogen targets, an effective $A_{t,\mathrm{eff}} = 0.089$ was found. Bradt-Peters formula is assumed to accurately describe high-energy reactions > 1.5 GeV/u. Although all parameters are assumed to be energy-independent, Coulomb shielding and nuclear resonances may decrease the cross sections at very low energies by a few percent [105]. As a rough approximation for molecular targets, mass numbers of constituent atoms are added, neglecting molecular structure and shadowing, which may lower cross sections by a few percent.

For each ion projectile, these cross sections from Eq. (4.35) can be used to estimate lifetimes τ_N from Eq. (4.27). Figure 4.14 shows the total beam lifetimes τ_N due to nuclear collisions (on all relevant target gases in each machine) computed with `beam_gas_collisions`. Unlike atomic charge-changing interactions, different charge states for a given ion species do not matter. Rather, the vacuum conditions and combined mass number (target and projectile nuclei) mainly affect lifetimes. Unlike EC and EL processes, nuclear collision lifetimes in LEIR and the PS are much longer than in the SPS due to better vacuum conditions. Nonetheless, the

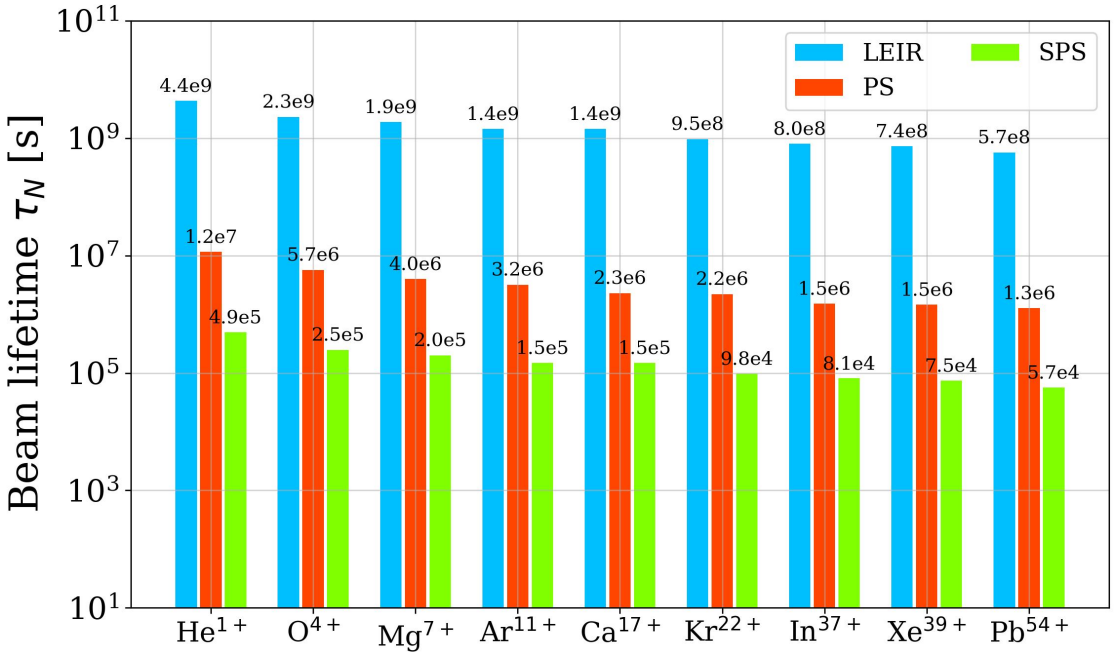


Figure 4.14: Predicted beam lifetimes τ_N due to nuclear collisions with the residual molecules at the static base pressure in LEIR, the PS and the SPS.

shortest computed lifetime is $^{208}Pb^{54+}$ in the SPS — about 5.7×10^4 s $\approx$ 16 hours — which is negligible compared to the longest operational Pb cycle of about 60 s. Regarding cross sections, $^{208}Pb^{54+}$ and CH_4 targets are considered as the extreme case and calculating the total nuclear interaction cross section for this molecule from Eq. (4.35) gives

$$\sigma_{\mathrm{Pb,\,CH_4}} \approx 4.3 \times 10^{-28}\ \mathrm{m}^2, \tag{4.36}$$

which is about four orders of magnitude lower than typical EC and EL cross sections for projectiles in LEIR and the PS from Fig. 4.10. Hence, with the current vacuum conditions, inelastic nuclear interactions with residual gas are of small practical importance in the ion injector chain, when compared to other relevant loss sources.

4.2.2 Elastic nuclear Coulomb scattering

Multiple scattering has been treated in several previous studies, including [66, 99, 100]. In the classical treatment by Jackson [106], the momentum transfer to a projectile with speed β, atomic number Z_i and mass number A_i after colliding with a target atom at rest of corresponding A_t and Z_t is determined by

$$\Delta p_\perp = Z_t e \int_{-\infty}^{\infty} E_\perp(t)\,dt, \tag{4.37}$$

where $E_\perp$ is the electric field perpendicular to the projectile trajectory, as seen by the target at rest [66]. For sufficient target particle masses and collision impact parameters with negligible corresponding integrals of the longitudinal components $E_\parallel$, the mean square of the scattering angle θ is fully derived in [66] to be

$$\langle\theta^2\rangle = 4\theta_{\min}^2 \ln\left(\frac{204}{Z_t^{1/3}}\right), \tag{4.38}$$

with $\theta_{\min}$ begin the minimum scattering angle due to screening of target atom electrons. Assuming independent successive scattering processes, Gaussian angular distributions and a relation with the geometric emittance $\varepsilon_{x,y}$, one finds for small time steps Δt

$$\frac{\langle\Delta\varepsilon_{x,y}\rangle}{\Delta t} = \langle\beta_{x,y}\rangle\frac{\langle\theta^2\rangle}{\Delta t}, \tag{4.39}$$

where $\langle\beta_{x,y}\rangle$ is the average beta function along the lattice. From Eq. (4.38) and (4.39), an expression for the average normalized emittance growth is then derived

$$\frac{d\varepsilon_{u,\,\mathrm{rms}}^n}{dt} \approx 2\pi\gamma_r\beta c\langle\beta_u\rangle n\left(\frac{2Z_iZ_tr_u}{A_i\beta^2\gamma_r}\right)^2 \ln\left(\frac{204}{Z_t^{1/3}}\right), \tag{4.40}$$

where n is the molecular gas density, $r_u = 1.546\times10^{-18}$ m is the classical unit mass particle radius, $u\in\{x,y\}$ and γ_r the relativistic Lorentz factor. At a given temperature and residual gas condition, ions scatter less strongly with larger mass and higher energy.

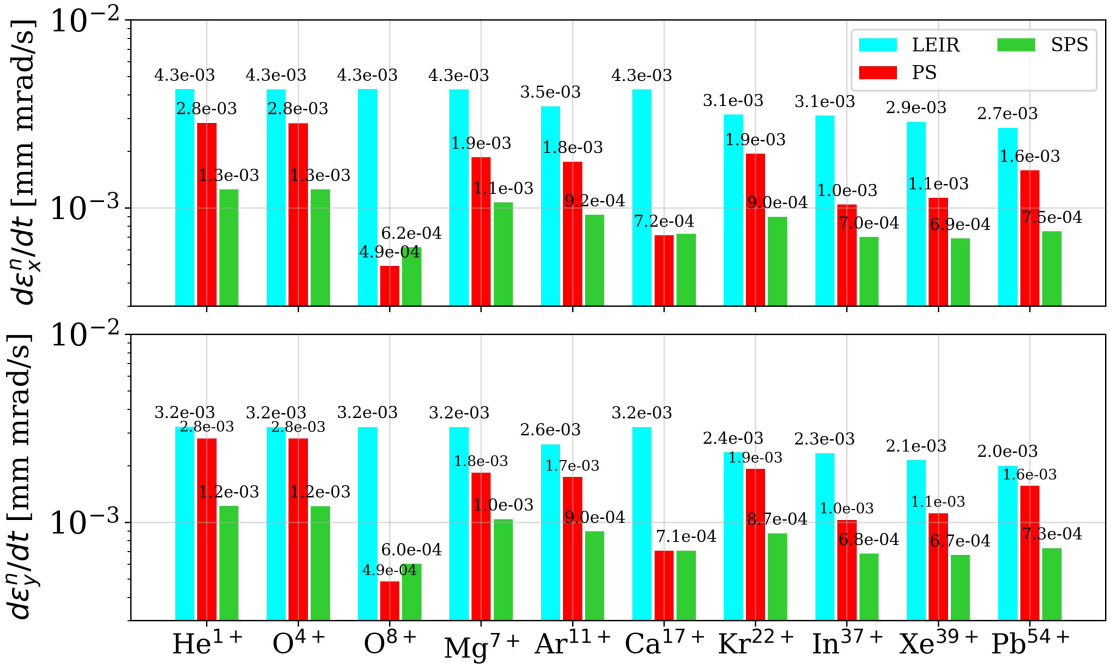


Figure 4.15: Predicted normalized emittance growth rates $d\varepsilon_{x,y}^n/dt$ in mm mrad/s due to residual gas scattering with the baseline pressure in LEIR, the PS, and the SPS.

Figure 4.15 shows the total emittance growth rates due to scattering on residual gas computed with Eq. (4.40) for future ion species in LEIR, the PS and the SPS at injection energy. LEIR accounts for the highest growth rates peaking at $d\varepsilon^n_{x,y}/dt$ = 0.004 mm mrad / s in both transverse planes. In the PS, these growth rates are slightly smaller, around 0.003 mm mrad / s. Yet smaller still are the SPS growth rates peaking at around 0.001 mm mrad / s, where even during the flat bottom (approximately 50 s) of the operational LHC-filling cycle, $\varepsilon^n_{x,y}$, where $\Delta\varepsilon^n_{x,y}$ for $^{208}Pb^{82+}$ beams is less than 0.04 mm mrad over the whole cycle — negligible compared to other emittance growth mechanisms. For the CERN ion injector chain, the impact of elastic scattering on residual gas appears minor compared to other effects.

4.3 Conclusions

The quality of charged ion beams may degrade due to residual gas molecules in the vacuum conditions of the CERN ion injector chain. This chapter analyzed the potential impact of beam-gas interactions, divided into two main categories: 1) atomic charge-changing interactions (electron capture and electron loss) and inelastic nuclear collisions contributing to beam losses, and 2) emittance growth due to elastic Coulomb collisions with residual gas molecules. This thesis work progressed on several fronts to estimate the impact of these effects:

- The Python package `beam_gas_collisions`, a numerical implementation of semi-empirical formulae for EC and EL, was developed to calculate beam lifetimes for given projectiles, target molecules, and vacuum conditions.
- A large 3D geometry modelling effort was carried out by the PS vacuum team to estimate the PS average pressure for each target gas injection experiment, an important model input for the predictions.
- The model predictions were tested in three PS gas injection experiments using the BGI instrument to generate an in-ring gas target. Argon and helium were the available target gases. When beam-gas interactions became the dominant loss mechanisms for large injected target gas quantities, the EC and EL lifetime prediction model agreed with the experiments within the typical model uncertainty of a factor of 2-3 mentioned by previous studies. Experimental cross sections for all concerned EC and EL processed were also computed from the measured beam lifetimes.
- Lifetime predictions for future ion species due to atomic beam-gas interactions in the CERN accelerator complex vary but may set an upper limit for some lighter partially stripped ions, in particular, O^{4+} and Mg^{7+} in the PS.
- Functionalities of `beam_gas_collisions` were extended to compute cross sections of inelastic nuclear collisions and emittance growth rates for elastic nuclear Coulomb scattering. Calculations show that these processes are negligible for future ion species, compared to other processes — in line with previous estimates from Ref. [66, 99].

5 Space charge, tune ripple and IBS effects for ions at the SPS flat bottom

5.1 Introduction: beam degradation mechanisms in the SPS

The main bottleneck of the whole ion injector chain in terms of losses is the SPS flat bottom (FB), where bunches are accumulated at injection energy before being accelerated and then delivered to the LHC, as discussed in Chapter 2. In the SPS, three main beam dynamics effects are suspected to limit the Pb beam intensity and cause emittance growth:

1. Space charge
2. Intra-beam scattering (IBS)
3. Betatron tune modulation from power converter ripples

In this context, the main objectives of this chapter are to:

- Experimentally characterize the tune ripple and its impact in combination with space charge and IBS, leveraging parametric scans in the SPS.
- Develop a realistic SPS Pb FB tracking simulation model with these effects, validated against measurements, and predict the performance of other ion beams such as oxygen.

5.2 Theoretical background

First, it is useful to review the underlying dynamics and interactions that govern particle behavior in accelerators. In addition to the external guiding forces provided by magnets and RF cavities, charged particles within an accelerator interact with the electromagnetic fields generated by other particles within the beam. These self-interactions, known as collective effects, are typically classified into two categories: incoherent and coherent effects.

The first category, *incoherent* effects, impacts particle motion individually across the beam and require specialized devices such as Schottky monitors. The second category, *coherent* effects, affects the beam as a whole — altering its collective statistical moments — and is detectable through standard devices like Beam Position Monitors (BPMs). Notably, tune shifts may arise from both incoherent and coherent effects. For space charge, focus lies on the incoherent contributions in this thesis work. Similarly, intra-beam scattering (IBS) is an incoherent effect. As we shall see, these phenomena play critical roles in the degradation and losses observed for Pb ion beams during the SPS FB segment. In the following sections, each of these two effects will be discussed.

5.2.1 Space charge

One of the most fundamental yet simplest of the collective effects is *space charge* (SC). Electromagnetic forces between charged particles in a high-intensity beam create self-fields, which act as a defocusing lens on the particles in the beam, proportional to the number of charges. An extensive overview of SC concepts is given by Ref. [107], where detailed derivations can be found. The SC effects can be divided into two types: direct and indirect SC. Direct SC represents Coulomb field interactions with other particles considering the beam in free space, whereas indirect SC denotes electromagnetic interactions with induced surface charges / currents in equipment surrounding the beam, such as the vacuum chambers (considered as perfectly conducting in the frame of indirect SC) and magnet poles. In this work, focus is mainly on direct SC, which particularly concerns high-brightness beams of high charge at lower energies. These forces are gradually compensated by the attractive magnetic force of co-moving particles and effectively disappear in the ultra-relativistic limit.

The Hamiltonian of a charged particle in an accelerator can typically be decomposed in one linear part (which describe the dipolar and quadrupolar magnetic fields), and into a non-linear part that contains a potential describing non-linear fields, for example the space charge potential describing direct space charge effects for a stationary beam. Consider a beam of linear particle density N of individual charge e, with a two-dimensional transverse Gaussian distribution

$$\rho(x,y) = \frac{Ne}{2\pi\sigma_x\sigma_y} e^{-\frac{x^2}{2\sigma_x^2}-\frac{y^2}{2\sigma_y^2}}. \tag{5.1}$$

The transverse beam radii $\sigma_{x,y}$ for a horizontally bending accelerator are

$$\sigma_x(s) = \sqrt{\beta_x(s)\varepsilon_x + D_x^2(s)(\Delta p/p)^2}, \tag{5.2}$$

$$\sigma_y(s) = \sqrt{\beta_y(s)\varepsilon_y}, \tag{5.3}$$

with $\varepsilon_{x,y}$ being the geometric emittance, and D_x the horizontal dispersion function. The two-dimensional SC potential [108, 109] that satisfies the Poisson equation for a transversely

Gaussian beam is defined as

$$V_{sc}(x,y) = -\frac{K_{sc}}{2}\int_0^\infty \frac{1-\exp\left[-\frac{x^2}{2\sigma_x^2+t}-\frac{y^2}{2\sigma_y^2+t}\right]}{\sqrt{(2\sigma_x^2+t)(2\sigma_y^2+t)}}dt, \tag{5.4}$$

where the SC perveance K_{sc} is

$$K_{sc} = \frac{2r_0\lambda}{\beta^2\gamma^3} \tag{5.5}$$

and $r_0 = (qe)^2/4\pi\epsilon_0 mc^2$ is the classical particle radius, λ is the particle line density, ϵ_0 is the vacuum permittivity, β and γ are the relativistic factors, and q is charge state. For a longitudinally Gaussian beam, the maximum particle line density is

$$\hat{\lambda} = \frac{N_b}{\sqrt{2\pi}\sigma_z} \tag{5.6}$$

where N_b is the number of ions per bunch (intensity) and σ_z is the longitudinal beam size (bunch length). The SC potential in Eq. (5.4) can be expanded in a Taylor series under paraxial approximation to investigate the systematic SC resonances [20, 110] to evaluate the integral analytically. The potential contains an infinite number of even-order terms in the transverse plane. Up to fourth order, it is given by

$$\begin{aligned} V_{sc}(x,y) = -\frac{K_{sc}}{2}\Bigg[&\left(\frac{x^2}{\sigma_x(\sigma_x+\sigma_y)}+\frac{y^2}{\sigma_y(\sigma_x+\sigma_y)}\right)- \\ &\frac{(2\sigma_x+\sigma_y)x^4}{12\sigma_x^3(\sigma_x+\sigma_y)^2}+\frac{(2\sigma_x+\sigma_y)y^4}{12\sigma_y^3(\sigma_x+\sigma_y)^2}+\frac{x^2y^2}{2\sigma_x\sigma_y(\sigma_x+\sigma_y)^2}\Bigg]. \end{aligned} \tag{5.7}$$

This direct SC force leads to a defocusing effect in both planes and decreases the particle tune Q. The first term inside the square bracket represents the linear force, which results in the linear SC tune shift $\Delta Q_{x,y}$. The second term drives the 2nd-order resonance and causes non-linear detuning with amplitude [20]. The linear SC tune shift is

$$\Delta Q_{x,y} = -\frac{K_{sc}}{4\pi}\oint \frac{\beta_{x,y}(s)}{\sigma_{x,y}(s)(\sigma_x(s)+\sigma_y(s))}ds. \tag{5.8}$$

$\Delta Q_{x,y}$ represents the maximum tune shift, typically experienced by particles in the beam core. Individual particles at higher transverse amplitudes will be affected less by the SC potential $V_{sc}(x,y)$ and have tune shifts smaller than the maximum. The different tune shifts for the different particles of the beam result in the SC *tune spread*, which can numerically be obtained from turn-by-turn data of particle tracking in the ring lattice under the influence of SC forces. For a given particle type and optics configuration, the linear incoherent SC tune shift $\Delta Q_{x,y}$ is proportional to the brightness $\mathscr{B}$, defined as

$$\mathscr{B} = \frac{N_b}{(\varepsilon_x^n+\varepsilon_y^n)/2}, \tag{5.9}$$

where $\varepsilon^n_{x,y}$ is the normalized emittance and N_b is the bunch intensity. Also, due to the dependence on relativistic factors, $\Delta Q_{x,y}$ decreases with higher beam energies. Hence, high-brightness beams of high charge at lower energies are particularly prone to these SC forces.

There are several methods to calculate the electric field forces of the SC potential in Eq.(5.4). Self-consistent models such as the particle-in-cell (PIC) approach calculate the self-fields of a macro-particle beam distribution, spread out throughout a regular grid, using Poisson solvers [111]. These self-consistent models require many thousands, if not millions, of macroparticles and are computationally expensive, but also often entail artificial emittance growth from numerical noise of PIC solvers [112]. As an alternative, Bassetti and Erskine [109] proposed an integral substitution formula for particle colliders to compute the electric fields $\mathbf{E}_{sc} = -\nabla V_{sc}$ from Eq. (5.4)

$$E_u = \frac{\lambda}{4\pi\epsilon_0} u \int_0^\infty dt \frac{\exp\left(-\frac{x^2}{2\sigma_x^2+t} - \frac{y^2}{2\sigma_y^2+t}\right)}{(\sigma_u^2+t)\sqrt{(\sigma_x^2+t)(\sigma_y^2+t)}} \quad \text{with } u \in \{x, y\}, \tag{5.10}$$

for transversely Gaussian distributions, where the electric fields

$$E_y + iE_x = \frac{\lambda}{2\epsilon_0\sqrt{2\pi(\sigma_x^2-\sigma_y^2)}}\left[w\left(\frac{x+iy}{\sqrt{2(\sigma_x^2-\sigma_y^2)}}\right) - \exp\left(-\frac{x^2}{2\sigma_x^2} - \frac{y^2}{2\sigma_y^2}\right) w\left(\frac{x\frac{\sigma_y}{\sigma_x} + iy\frac{\sigma_x}{\sigma_y}}{\sqrt{2(\sigma_x^2-\sigma_y^2)}}\right)\right], \tag{5.11}$$

for $\sigma_x > \sigma_y$ (otherwise indices are switched $x \leftrightarrow y$), are expressed from the complex-valued Faddeeva (error) function $w(x+iy)$

$$w(z) = e^{-z^2}\left(1 + \frac{2i}{\sqrt{\pi}}\int_0^z dt\, e^{t^2}\right). \tag{5.12}$$

Several algorithmic implementations to numerically compute the Faddeeva function have been reviewed in Ref. [113]. This light-weight alternative model is often denoted as “frozen" SC model. Studies of coherent effects require self-consistent models, whereas for the study of incoherent effects the frozen models are often sufficient as long as the beam distribution remains close to Gaussian (at least transversely). If losses occur and the beam profile changes — but the distribution remains Gaussian — the hybrid *adaptive* frozen space charge model updates the SC force elements after a given interval, according to the new bunch intensity and beam size of the evolving distribution, still with the Bassetti-Erskine formula. This thesis work will mainly use such an adaptive frozen SC model.

5.2.2 Impact of resonances and tune modulation

Although SC by itself does not directly cause beam losses, it can have a destructive impact when combined with machine *resonances* in synchrotrons. This can happen through incoherent interactions where individual particles experience a tune shift induced by SC. In the latter case,

three-dimensional dynamic motion in tune space — stemming from the synchrotron motion and longitudinal dependence of SC coupled with chromatic effects — can cause periodic resonance crossing. Such resonance crossings can lead to beam losses and/or emittance growth, particularly when the resonance is driven by magnet errors in the lattice [114]. The resonance condition for the transverse plane is expressed as

$$m\frac{Q_x}{P} + n\frac{Q_y}{P} = r, \tag{5.13}$$

where $|m| + |n|$ are the resonance order, P the periodicity (i.e. a lattice built of P identical cells) and r defines the harmonic of the resonance [115]. Odd values of n indicate skew resonances (i.e. resonances stemming from skew multipole components), even n indicate normal resonances (i.e. resonances stemming from upright multipole components). Resonances in Eq. (5.13) for which $r \in \mathbb{N}$ are called systematic, where the resonance condition is satisfied in each cell and driving terms add up constructively, from misalignments or magnet errors in the ring. If r is not an integer, the driving terms cancel, and the resonance is called non-systematic and is typically suppressed. Furthermore, under certain circumstances, the non-linear SC potential itself can excite resonances directly if the resonances are of even order and contain harmonics that coincide with the lattice periodicity [114, 116].

Figure 5.1 illustrates the incoherent tune spread due to the SC potential in Eq. (5.4) for nominal SPS Pb ion beam parameters at injection. Resonances up to fourth order are marked. The analytical SC tune spread has been calculated numerically with the Python module PySCRDT [110], developed by F. Asvesta, which calculates resonance driving terms (RDTs) from the SC potential of Gaussian beam distributions. Note the “necktie" shape of the tune spread, where red color represents the beam core — the maximum detuning from Eq. (5.8) compared to the set tune — and yellow represents particles in the tails of the distribution, which experience less detuning (as the charge density is lower).

As a particle in a bunched beam performs synchrotron oscillations, the transverse Coulomb forces due to SC vary proportional to the local line density of the bunch charge distribution at the particle’s longitudinal position. The synchrotron motion in combination with SC thus result in a *incoherent* tune modulation with twice the synchrotron tune Q_s. Consequently, this incoherent tune modulation may periodically satisfy the resonance condition in Eq. (5.13) and cause *trapping* of individual particles on resonance islands, slowly increasing their transverse amplitude. Eventually, particles with too high amplitudes will be lost on the physical machine aperture. Alternatively, if the resonance crossing happens fast enough, a single crossing will result in a kick to the particle action invariant and lead to *scattering*. This phenomenon has been investigated in various studies at GSI and at CERN [112, 117, 118, 119, 120]. Synchro-betatron coupling through chromaticity further complicates the picture, as it leads to an additional tune modulation (at Q_s) [121].

Typically, the beam dynamics of a bunched beam with SC in a ring leads to **two distinct regimes**, depending on how the tune spread from Fig. 5.1 overlaps the resonance: 1) **loss-**

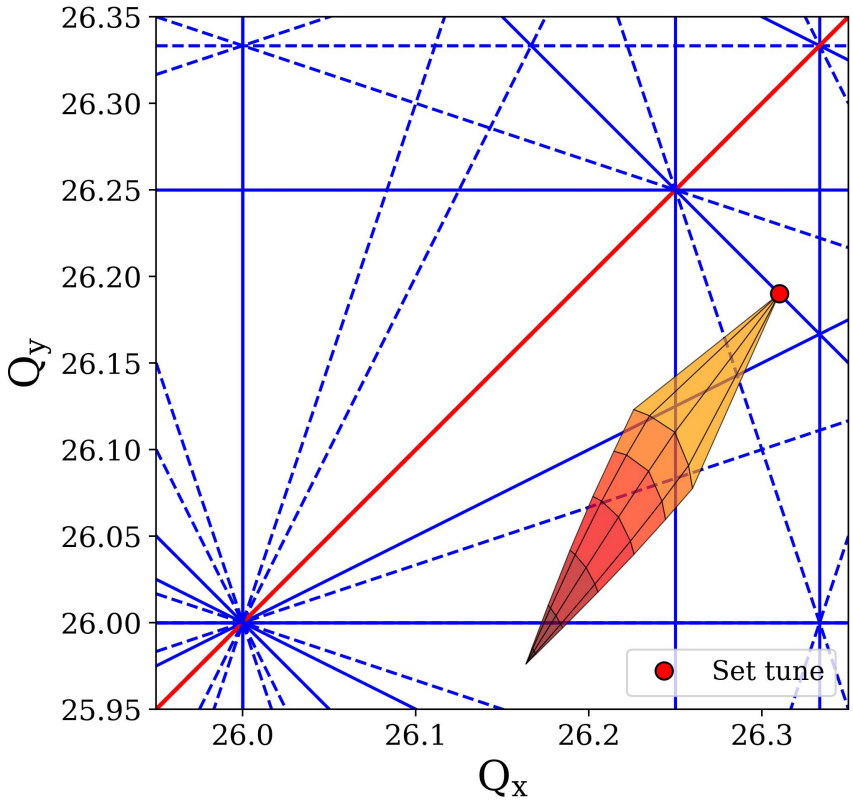


Figure 5.1: Resonance diagram up to fourth order for nominal SPS Pb parameters in Q26 optics, with machine periodicity $P = 6$. Red is systematic, blue is non-systematic. Solid lines indicate normal and dashed lines indicate skew resonances.

dominated or 2) **emittance-growth-dominated** regime [110, 119, 122]. Figure 5.2 illustrates this for the example of the $Q_x = 26.33$ resonance. For set tunes Q_{x_0}, Q_{y_0} just above the resonance, beam losses dominate (red dip) and reductions in both emittances and bunch lengths are observed. In this regime, high-amplitude particles diffuse into a halo when periodically crossing the resonance during the longitudinal motion. On the other hand, when approaching higher machine tunes, more of the particles in the beam core will overlap the resonance, leading to fewer losses but stronger emittance blow-up (of the core distribution).

In addition to space charge and chromaticity, tune modulation can be caused by external sources such as power converter ripples in quadrupole magnets. The effect of such tune modulations has been studied extensively in the past [99, 123, 124, 125, 126] but not in the context of space charge effects. In fact, the beam dynamics of a high brightness bunched beam already affected by SC and IBS is even further complicated by external tune modulations with tune Q_m. In this case, the resonance condition previously discussed in Eq. (5.13) takes the form

$$n_x Q_x + n_y Q_y + n_s Q_s + n_m Q_m = r, \tag{5.14}$$

in which the characteristic *sideband* resonances can result in enhanced chaotic motion and

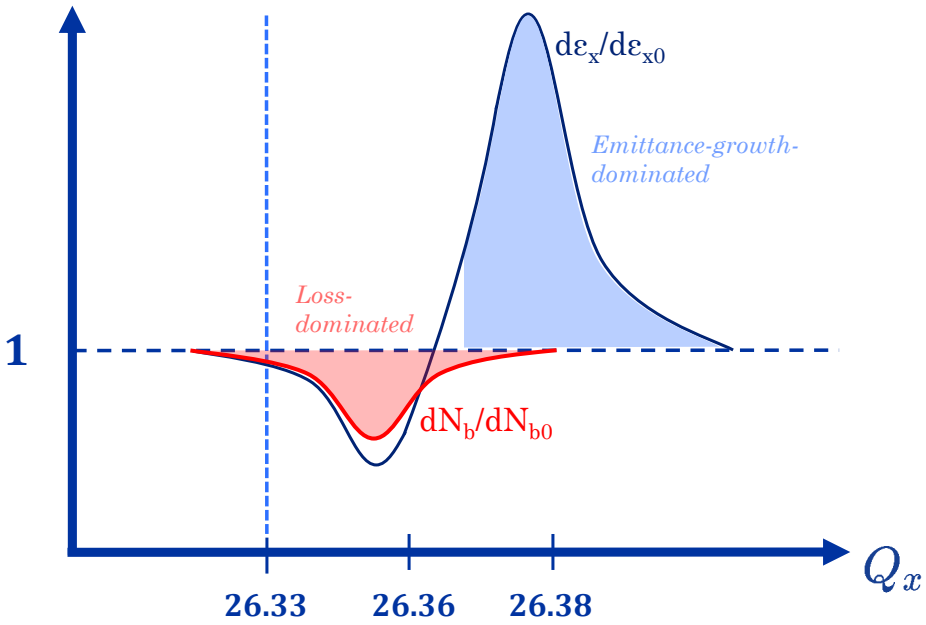


Figure 5.2: Illustration of the loss-dominated (red) versus emittance-dominated (blue) regimes while crossing the example resonance $Q_x = 26.33$ (vertical dashed blue line). Scanning the horizontal working point from left to right, high-amplitude particles will at first cross the resonance, diffuse to higher amplitudes while forming a halo and get lost, causing a characteristic dip on the bunch intensity. For higher set tunes, the tune footprint representing the beam core (dark-red part of footprint in Fig. 5.1 with SC tune ΔQ_x) will overlap the resonance, leading to core ε_x^n blow-up rather than losses.

thus enhanced beam degradation. To understand this complicated dynamics, a simulation model of the SPS has been developed in the scope of this thesis.

5.2.3 Intra-beam scattering

Intra-beam scattering (IBS) denotes the stochastic process of multiple small-angle Coulomb scattering of charged particles in a beam. This beam-degrading effect leads to momentum exchange between the planes and/or emittance growth. IBS is an important effect for highly charged dense ion beams at lower energies, but is also visible in proton beams stored for many hours in high-energy storage rings. Numerous studies have been carried out in the CERN accelerator complex to identify and quantify the impact of IBS, including in the context of LHC ion beams [127], CLIC damping rings [128, 129], non-Gaussian LHC proton beams [130], and the LHC ion injectors [131].

For analogy, the IBS process can be compared with the scattering of gas molecules in an enclosed space, with the important difference being the dispersion caused by the curvature in storage rings. This dispersion causes any sudden change in energy to change the beta-

tron amplitudes and couple longitudinal synchrotron oscillations with transverse betatron oscillations. In this sense, IBS can be regarded as a diffusion process across all three spatial dimensions, unlike the closely related Touschek effect, where a single Coulomb scattering effect leads to energy transfer from the horizontal to longitudinal direction [132].

To obtain the rate of change of the dimensions of the beam, one can study the growth rates $1/\tau$ of the normalized rms phase space Γ

$$\Gamma = \int f d^3x d^3p, \tag{5.15}$$

where f is the canonical phase space distribution function, described by

$$f = \exp(-S), \tag{5.16}$$

with the matrix S being defined, with $i \in \{x, y, z\}$ as

$$S = \frac{1}{2} A_{ij} \frac{p_i}{p} \frac{p_j}{p} + \frac{1}{2} B_{ij} x_i \frac{p_j}{p} + \frac{1}{2} C_{ij} x_i x_j, \tag{5.17}$$

and A_{ij}, B_{ij} and C_{ij} are matrices. x_i is the particle coordinate, p_i the momentum and $p = \beta\gamma Mc$ [133]. The total six-dimensional growth rate can be written as

$$\frac{1}{\tau} = \frac{1}{\Gamma}\frac{d\Gamma}{dt} = \frac{1}{\varepsilon_x}\frac{\varepsilon_x}{dt} + \frac{1}{\varepsilon_y}\frac{\varepsilon_y}{dt} + \frac{1}{\sigma_p^2}\frac{d\sigma_p^2}{dt}. \tag{5.18}$$

All available theories and formalisms describing IBS [133, 134, 135, 136] typically calculate the individual growth rates (sometimes denoted rise times) in the horizontal (x), vertical (y), and momentum plane (p), defined as

$$\frac{1}{\tau_x} = \frac{1}{\varepsilon_x}\frac{d\varepsilon_x}{dt}, \tag{5.19}$$

$$\frac{1}{\tau_y} = \frac{1}{\varepsilon_y}\frac{d\varepsilon_y}{dt}, \tag{5.20}$$

$$\frac{1}{\tau_p} = \frac{1}{\sigma_p}\frac{d\sigma_p}{dt}. \tag{5.21}$$

All the growth rates $1/\tau_i$ depend on large integrals involving beam properties such as charge, bunch energy, optics, and energy spread [137]. The dependence is especially complicated through dispersion coupling across the three planes, which in turn couples both the betatron and synchrotron oscillations. The functional growth rate dependence can typically be expressed as

$$\frac{1}{\tau_i} = A\Big\langle f_i(\text{optics}, \gamma, \varepsilon_x, \varepsilon_y, \sigma_z)\Big\rangle, \tag{5.22}$$

where A is the six-dimensional invariant phase space volume of a bunched beam

$$A = \frac{cN_b r_0^2}{64\pi^2\beta^3\gamma^4\varepsilon_x\varepsilon_y\sigma_p\sigma_z}, \tag{5.23}$$

with c being the speed of light and σ_z is the RMS bunch length. The $1/\gamma^4$ dependence leads to a *strong diminishing effect with higher energies*. For coasting beams, the substitution $\sigma_z = C_0/2\sqrt{\pi}$ is typically made for a machine circumference C_0.

The transition energy plays an important role in the IBS behavior. The machine curvature causes so-called “negative mass behavior" of the particle, meaning that a particle above transition energy with larger momentum has a smaller angular velocity than a particle with smaller momentum [134]. In this way, a particle takes more time to go around the machine when accelerated and behaves like a particle with negative mass, such that an equilibrium of particles above the transition energy cannot exist and emittance will increase in all spatial planes. On the other hand, below transition energy, the emittance can grow in one plane at the expense of another plane; negative and positive growth rates for the three planes can co-exist simultaneously in this regime, and an equilibrium can exist.

The IBS theory was first presented in the context of accelerators by Piwinski [134], and eventually extended by Martini [138] to allow for the variation of lattice parameters. Bjorken and Mtingwa (BM) used different techniques to include the most general situation encountered in a strong-focusing lattice [133]. Furthermore, Bane et al. further developed the Piwiniski method to include the strong focusing effect, and proposed several high-energy approximations [139]. Nagaitsev presented a study in 2005 for faster numerical evaluation of the BM elliptic integrals by reducing the number of computed integrals from three to two [135]. Zenkevich presented a kinetic IBS analysis through the Fokker-Planck equation, picturing IBS processes in storage rings as a “collective map" using the Langevin equation and including the IBS process in turn-by-turn macroparticle tracking [136]. Here, some of the most important formalisms are briefly reviewed for context and to motivate the choices made for this thesis work.

Standard and modified Piwinski formalism

The standard Piwinski method assumes Gaussian particle distributions and Coulomb collisions of particles following the classical Rutherford cross section [134]. This formalism includes phase space couplings of various degrees of freedom. The emittance growth rates are

given by

$$\frac{1}{\tau_x} = A\left\langle f\left(\frac{1}{a},\frac{b}{a},\frac{c}{a}\right) + \frac{D_x^2\sigma_p^2}{\sigma_x^2} f(a,b,c)\right\rangle, \tag{5.24}$$

$$\frac{1}{\tau_y} = A\left\langle f\left(\frac{1}{b},\frac{a}{b},\frac{c}{b}\right) + \frac{D_y^2\sigma_p^2}{\sigma_y^2} f(a,b,c)\right\rangle, \tag{5.25}$$

$$\frac{1}{\tau_p} = A\left\langle \frac{\sigma_h^2}{\sigma_p^2} f(a,b,c)\right\rangle, \tag{5.26}$$

where the brackets denote the average over the full machine circumference, using

$$\frac{1}{\sigma_h^2} = \frac{1}{\sigma_p^2} + \frac{D_x^2}{\sigma_{x\beta}^2} + \frac{D_y^2}{\sigma_{y\beta}^2}, \qquad \sigma_{x,y}^2 = \sigma_{x\beta,y\beta}^2 + D_{x,y}^2\sigma_p^2. \tag{5.27}$$

In the Piwinski formalism, the function f is defined as

$$f(a,b,c) = 8\pi\int_0^1 \left(2\ln\left(\frac{c}{2}\left(\frac{1}{\sqrt{P}}+\frac{1}{\sqrt{Q}}\right)\right) - 0.577...\right)\frac{1-3x^2}{\sqrt{PQ}}\,dx, \tag{5.28}$$

with

$$P = a^2 + (1-a^2)x^2, \qquad Q = b^2 + (1-b^2)x^2, \tag{5.29}$$

and

$$a = \frac{\sigma_p}{\gamma\sigma_{x_{\beta'}}}, \qquad b = \frac{\sigma_p}{\gamma\sigma_{y_{\beta'}}}, \qquad c = \sigma_p\beta\sqrt{\frac{2d}{r_0}}, \tag{5.30}$$

where d is the impact parameter. The function f has the interesting properties

$$f(a,b,c) = f(b,a,c), \tag{5.31}$$

$$f(a,b,c) + \frac{1}{a^2}f\left(\frac{1}{a},\frac{b}{a},\frac{c}{a}\right) + \frac{1}{b^2}f\left(\frac{1}{b},\frac{a}{b},\frac{c}{b}\right) = 0, \tag{5.32}$$

$$f(1,1,c) = 0, \tag{5.33}$$

Together with the property

$$\sigma_p = \sqrt{\frac{1}{\gamma^2} - \frac{D_x^2}{\beta_x^2} - \frac{D_y^2}{\beta_y^2}} = \sigma_{x_{\beta'}}^2 = \sigma_{y_{\beta'}}, \tag{5.34}$$

an equilibrium can be reached, but only below the transition energy. Above transition, emittances in all three planes will grow simultaneously.

Bjorken-Mtingwa (BM) formalism

With the original relativistic “Golden Rule" for the transition rate due to two-body scattering, Bjorken et al. underlines that kinetic energy is conserved in the Coulomb scattering process according to Eq. (2.3) in [133]. However, in a strong-focusing lattice, kinetic and potential energy are exchanged, and the Golden Rule does not lead to the same invariant of motion. Instead, the transverse emittance growth rate and the relative energy spread are found to be

$$\frac{1}{\tau_i} = 4\pi A \ln\left(\frac{r_{\max}}{r_{\min}}\right)\left\langle \int_0^\infty \frac{d\lambda \lambda^{\frac{1}{2}}}{\det(L+\lambda I)^{\frac{1}{2}}} \left\{ \mathrm{Tr}L^{(i)}\mathrm{Tr}\left(\frac{1}{(L+\lambda I)}\right) - 3\mathrm{Tr}L^{(i)}\left(\frac{1}{(L+\lambda I)}\right)\right\}\right\rangle, \tag{5.35}$$

where $r_{\max}$ and $r_{\min}$ are the maximum and minimum impact parameters of the collision of two particles in the bunch. The auxiliary matrices L can be defined as

$$L = L^{(p)} + L^{(x)} + L^{(y)} \tag{5.36}$$

with

$$L^{(p)} = \frac{\gamma^2}{\sigma_p^2}\begin{pmatrix} 0 & 0 & 0 \\ 0 & 1 & 0 \\ 0 & 0 & 0 \end{pmatrix}, \tag{5.37}$$

$$L^{(x)} = \frac{\beta_x}{\varepsilon_x}\begin{pmatrix} 1 & -\gamma\Phi_x & 0 \\ -\gamma\Phi_x & \gamma^2\mathscr{H}_x/\beta_x t & 0 \\ 0 & 0 & 0 \end{pmatrix}, \tag{5.38}$$

$$L^{(y)} = \frac{\beta_y}{\varepsilon_y}\begin{pmatrix} 0 & 0 & 0 \\ 0 & \gamma^2\mathscr{H}_x/\beta_x t & -\gamma\Phi_y \\ 1 & -\gamma\Phi_y & 0 \end{pmatrix}, \tag{5.39}$$

where the lattice function is

$$\Phi_{x,y} = D'_{x,y} - \frac{\beta'_{x,y}D_{x,y}}{2\beta_{x,y}}, \tag{5.40}$$

and

$$\mathscr{H}_{x,y} = \frac{1}{\beta_{x,y}}\left[D_{x,y}^2 + \left(\beta_{x,y}D'_{x,y} - \frac{1}{2}\beta_{x,y}D_{x,y}\right)^2\right]. \tag{5.41}$$

There is a simpler expression for the total growth rate $1/\tau$, considering the eigenvalues $\lambda_1 \geq \lambda_2 \geq \lambda_3$ of the matrix L

$$\frac{1}{\tau} = 4\pi A \ln\left(\frac{r_{\max}}{r_{\min}}\right)\left\langle (\lambda_1-\lambda_2)^2 \int_0^\infty \frac{d\lambda\lambda^{\frac{1}{2}}}{(\lambda_1+\lambda)^{3/2}(\lambda_2+\lambda)^{3/2}(\lambda_3+\lambda)^{1/2}} + \text{ two cyclic permutations}\right\rangle \tag{5.42}$$

In a strong-focusing lattice, the eigenvalues λ_i can mostly not be equal, and emittance will grow [133]. However, the integral expression H that is averaged around the lattice can, in some cases when $\lambda_1 > \lambda_2 \approx \lambda_3$, be analytically evaluated

$$\begin{aligned} H &= \left[(\lambda_1 - \lambda_2)^2 \int_0^\infty \frac{d\lambda \lambda^{\frac{1}{2}}}{(\lambda_1+\lambda)^{3/2}(\lambda_2+\lambda)^{3/2}(\lambda_3+\lambda)^{1/2}} \right. \\ &\quad \left. + \text{ two cyclic permutations} \right] \\ &= \left[\frac{2(\lambda_1+2\lambda_2)}{\sqrt{\lambda_2(\lambda_1-\lambda_2)}} \arcsin\sqrt{\frac{\lambda_1-\lambda_2}{\lambda_1}} - 6 \right], \end{aligned} \tag{5.43}$$

When $\lambda_1 > \lambda_2 > \lambda_3$, integrals in H can be expressed in terms of three elliptic integrals of the first and second kind, which, after lengthy manipulations, can be evaluated analytically from tables containing elliptic integrals. Over time, efforts have been made to incorporate non-relativistic factors and dispersion effects in the L matrices in Eq. (5.36) [140, 141].

Nagaitsev formalism

The Bjorken-Mtingwa integral H in Eq. (5.43) is useful for strong-focusing lattices, but can be lengthy to evaluate. In 2005, Nagaitsev showed that IBS growth rates can be represented as closed-form expressions with the help of symmetric elliptic integrals, which can be efficiently computed with a recursive method using the so-called duplication theorem [135]. As presented in the Bjorken-Mtingwa formalism, some IBS rates can be expressed with the following combination Ψ of elliptic integrals

$$\Psi(x,y,z) = -2xR_D(y,z,x) + yR_D(z,x,y) + zR_D(x,y,z), \tag{5.44}$$

where $R_D(x,y,z)$ is a symmetric elliptic integral of the second kind

$$R_D(x,y,z) = \frac{3}{2}\int_0^\infty \frac{dt}{\sqrt{(t+x)(t+y)(t+z)^3}}, \tag{5.45}$$

which contains many useful properties. The six-dimensional growth rate from Equation (3.6) in the Bjorken-Mtingwa paper [133] can be expressed as

$$\begin{aligned} \frac{1}{\tau} &= \frac{1}{\Gamma}\frac{d\Gamma}{dt} \\ &= \frac{2\pi^2 N c r_0^2 m \ln(r_{\max}/r_{\min})}{3\gamma\Gamma} \int_0^{C_0} \frac{ds}{C_0\sqrt{\lambda_1\lambda_2\lambda_3}} \left[\lambda_1 \Psi\left(\frac{1}{\lambda_1}, \frac{1}{\lambda_2}, \frac{1}{\lambda_3}\right) \right. \\ &\quad \left. + \text{ two cyclic permutations} \right], \end{aligned} \tag{5.46}$$

where $\lambda_{1,2,3}$ are the eigenvalues of the matrix A in Equation (5.17). The IBS growth rates for a few simplifying cases can then be numerically calculated, including for uncoupled betatron

oscillations, smooth beam approximations, round beam approximations, and for coasting beams. By reducing the number of integrals from three to two, the calculation speed can be significantly enhanced compared to the standard BM formalism.

Kinetic theory

An alternative approach to describe IBS is the kinetic theory, based on the solution of the Fokker–Planck equation (FPE) expressed in invariant space as proposed by Zenkevich in 2006 [136]. The main idea of this approach assumes that most of the IBS interactions take place in the beam “core", which can often be modeled as a Gaussian. Friction and diffusion rates are functions of particle momentum, Twiss parameters, and RMS values of beam invariants. Following the Bjorken scheme, calculating the friction and diffusion coefficients can be reduced to one-dimensional integrals depending on the Twiss parameters. A map in momentum space, bridging the changes in longitudinal and horizontal momenta, can be constructed with the Langevin equation

$$P_i(t+\Delta t) = P_i(t) - K_i P_i(t)\Delta t + \sqrt{\Delta t}\sum_{j=1}^{3} C_{i,j}\zeta_j, \tag{5.47}$$

where K_i are the friction coefficients, ζ_i are random numbers, and $C_{i,j}$ are the integrals accounting for correlations between coupled horizontal and longitudinal degrees of freedom, related to the diffusion coefficients $D_{i,j}$. For every turn, all particles receive a momentum kick that depends on the parameters and longitudinal position of the beam. The friction coefficient K_i and the diffusion coefficient $D_{i,j}$ are defined according to Eq. (20) and (21) from [136]:

$$K_i = \frac{A}{\langle P_i^2\rangle}\int_0^\infty d\lambda \frac{\sqrt{\lambda}}{\sqrt{\det\lambda}}\Lambda_{ii}^{-1}, \tag{5.48}$$

$$D_{ij} = A\int_0^\infty d\lambda \frac{\sqrt{\lambda}}{\sqrt{\det\lambda}}(\delta_{ij}\mathrm{Tr}(\Lambda^{-1}) - \Lambda_{ij}^{-1}). \tag{5.49}$$

The diffusion kernels from [133] can be used to find an expression for the integrals I_{ij} contained in Eq. (5.35) to find the IBS growth rate

$$I_{ij} = A\int_0^\infty d\lambda \frac{\sqrt{\lambda}}{\sqrt{\det\lambda}}(\delta_{ij}\mathrm{Tr}(\Lambda^{-1}) - 3\Lambda_{ij}^{-1}) = D_{ij} - \delta_{ij}2\langle P_i^2\rangle K_i. \tag{5.50}$$

Using the above expression to simplify the Bjorken-Mtingwa growth rate expressions in

Eq. (5.35), the growth rates become

$$\frac{1}{\tau_x} = \left\langle \frac{\beta_x}{\varepsilon_x} I_{xx} - 2\gamma \frac{\beta_x \Phi_x}{\varepsilon_x} I_{xz} + \gamma^2 \frac{H_x}{\varepsilon_x} I_{zz} \right\rangle, \tag{5.51}$$

$$\frac{1}{\tau_y} = \left\langle \frac{\beta_y}{\varepsilon_y} I_{yy} - 2\gamma \frac{\beta_y \Phi_y}{\varepsilon_y} I_{yz} + \gamma^2 \frac{H_y}{\varepsilon_y} I_{zz} \right\rangle, \tag{5.52}$$

$$\frac{1}{\tau_z} = \left\langle \frac{\gamma^2}{\delta_p^2} I_{zz} \right\rangle. \tag{5.53}$$

With the substitutions

$$G_i = \frac{\beta_i}{\varepsilon_i} D_{ii} - 2\gamma \frac{\beta_i \Phi_i}{\varepsilon_i} D_{iz} + \gamma^2 \frac{H_i}{\varepsilon_i} D_{zz}, \tag{5.54}$$

$$F_i = 2K_i + 2\gamma^2 \frac{H_i}{\varepsilon_i} \sigma_p^2 K_z, \tag{5.55}$$

that in the longitudinal plane becomes

$$G_i = \frac{\gamma^2}{\sigma_\delta^2} D_{zz}, \tag{5.56}$$

$$F_i = 2\gamma^2 K_z, \tag{5.57}$$

the growth rates for $i = x, y, z$ can be expressed as

$$\frac{1}{\tau_i} = G_i - F_i, \tag{5.58}$$

and the Langevin kick from Equation (5.47) has the following form

$$P_i(t + \Delta t) = P_i(t) - F_i P_i(t) \rho(z) \Delta t + \sqrt{2 G_i \Delta t \rho(z)} \zeta_i, \tag{5.59}$$

where $\rho(z) = 2\sigma_z \sqrt{\pi} \lambda(z)$, $\lambda(z)$ is the normalized longitudinal line density at position z within the bunch, and ζ_i is a random number in terms of standard deviations [131].

Kinetic theory with Nagaitsev formalism

Similarly, the growth rates for the kinetic formalism can be expressed with the reduced elliptic integrals from the Nagaitsev formalism [135], described above, for faster numerical evaluation. Only considering horizontal dispersion D_x — as the vertical dispersion is, relatively speaking, much smaller in a circular accelerator — in the horizontal plane, one finds new expressions for F_i and G_i. In the horizontal plane, we have

$$G_x = \left[D_{xx} + \left(\frac{D_x^2}{\beta_x} + \Phi^2 \right) D_{zz} + D_{xz} \right], \tag{5.60}$$

$$F_x = \left[K_x + \left(\frac{D_x^2}{\beta_x} + \Phi^2 \right) K_z \right], \tag{5.61}$$

whereas in the vertical and longitudinal plane with $j = y, z$ these coefficients simply reduce to

$$G_j = D_{jj}, \tag{5.62}$$

$$F_j = K_j, \tag{5.63}$$

and the total growth rate then becomes for the horizontal and vertical case $i = x, y$

$$\frac{1}{\tau_i} = \frac{\beta_i}{\varepsilon_i} A\Big[G_i - F_i\Big], \tag{5.64}$$

and in the longitudinal case

$$\frac{1}{\tau_z} = \frac{\gamma^2}{\sigma_\delta^2} A\Big[G_{zz} - F_z\Big], \tag{5.65}$$

where the matrix A originates from Equation (5.17). The diffusion coefficient D_{ij} and friction coefficient K_i can be expressed with elliptic integrals R_D from Equation (5.45), for instance

$$D_{xx} = \frac{1}{2}[2R_1 + R_2(1-f) + R_3(1+f)], \tag{5.66}$$

$$K_x = [R_2(1+f) + R_3(1-f)], \tag{5.67}$$

where

$$R_1 = \frac{1}{\lambda_1} R_D\left(\frac{1}{\lambda_2}, \frac{1}{\lambda_3}, \frac{1}{,}\lambda_1\right), \tag{5.68}$$

and λ_i are the eigenvalues of the L matrix defined in Equation (5.36). R_2 and R_3 are found in expressions similar to Equation (5.68) but with cyclic permutations. $f = f(\text{optics})$ represents the dependency on the optics functions of the lattice. With respect to the kinetic theory using the Bjorken-Mtingwa expressions, the Nagaitsev formalism allows for better integral convergence and usage for a wider range of accelerators, also above transition. As the elliptic integrals to be evaluated numerically are only two rather than three, as in the case of Bjorken-Mtingwa, the numerical integration is between 20-80 times faster, which allows for quicker multi-turn tracking. The longitudinal line density, as well as bunched and coasting beam shapes, are accounted for.

An extensive numerical implementation and benchmarking study of this hybrid Nagaitsev-kinetic formalism was recently undertaken by M. Zampetakis [131]. *This hybrid kinetic approach with the faster integral evaluation of Nagaitsev should not be confused with the purely analytical Nagaitsev formalism, which solely computes growth rates.* At the time of writing, this method provides the highest numerical efficiency with flexibility to be used both below and above transition, which not all formalisms can do. The main advantage of the kinetic theory is the ability to numerically compute kicks, which, unlike analytical growth rates, can be combined with other effects in macro-particle tracking simulations. For this reason, this thesis work will mainly use the hybrid Nagaitsev-kinetic formalism with the Langevin equation from Eq. (5.59).

5.2.4 Small note on statistical moments, beam distributions and q-Gaussians

Although many SC and IBS formalisms assume transversely Gaussian beam profiles, a more generic mathematical description is required in case of enhanced tail population and particle redistribution due to these effects. In particular, the *longitudinal* SPS Pb beam profiles are typically not Gaussian. Here, a short digression on how distributions and their quantitative comparisons are handled in this thesis work is provided. First, the Gaussian probability density function [142] is defined as

$$f(u) = \frac{1}{\sqrt{2\pi\sigma^2}} e^{-\frac{(x-\mu)^2}{2\sigma^2}}, \tag{5.69}$$

where μ is the expectation value and σ^2 its variance. *Statistical moment* is useful to compare various distributions. The zero-order moment gives the normalization of a six-dimensional beam distribution $f(x, y, z, x', y', \delta, s)$ in any of its planes

$$1 = \int f(u; s) d^6 u, \tag{5.70}$$

where $u \in \{x, y, z, x', y', \delta\}$ is any of the six-dimensional phase space coordinates. The first-order (dipole) moment is equivalent to the expectation value concerning f, also denoted the centroid $\langle u \rangle$

$$\langle u \rangle(s) = \int u f(u; s) du, \tag{5.71}$$

which for a Gaussian distribution is simply μ. Any higher n^{th}-order statistical moment in relation to any value c, for example around the centroid such that $c = \langle u \rangle$, is expressed as

$$u_s = \int (u - c)^n f(u; s) du. \tag{5.72}$$

The variance $\sigma^2 := u_2$ is identified as the second central moment, whose positive square root σ is the standard deviation around the mean. Another important quantity is the so-called Root Mean Square (RMS), or the quadratic mean, which is important to uniformly compare shapes and moments of different distribution types. The RMS second moment (for instance, the beam distribution length or width) bunch length σ_{RMS} of a continuous probability density function $f(u)$ in the interval $[a, b]$ and centered around the origin is defined as

$$\sigma_{\text{RMS}} = \sqrt{\frac{1}{b-a} \int_a^b u^2 f(u) dx}, \tag{5.73}$$

which for a Gaussian distribution with $\mu = \langle u \rangle = 0$ is simply the square root of the variance $\sqrt{\sigma^2} = \sigma$. For other distributions, this quantity may have to be evaluated numerically.

One of the most robust non-Gaussian beam profile descriptions that quantitatively accounts for core and tail populations is the q-Gaussian function, described in detail in Refs. [129, 143]. The q-Gaussian has a higher flexibility than binomial, Gaussian, and double-Gaussian

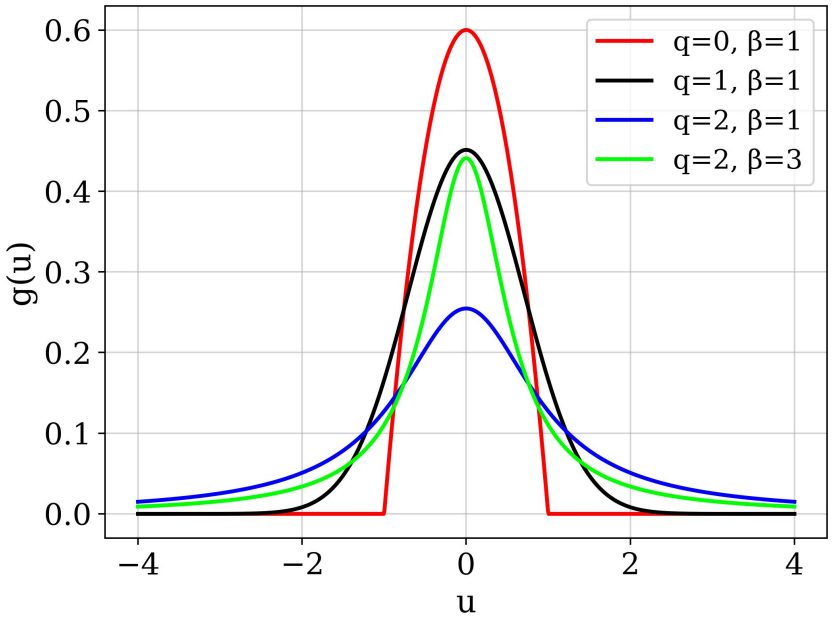


Figure 5.3: q-Gaussian distribution function g for various q and β_q values.

functions to describe particle population. Its probability density function $g(u)$ is defined as

$$g(u) = \frac{\sqrt{\beta_q}}{C_q} e_q^{-\beta_q u^2}, \tag{5.74}$$

where C_q is a normalizing constant

$$C_q = \begin{cases} \frac{2\sqrt{\pi}}{(3-q)\sqrt{1-q}} \frac{\Gamma\left(\frac{1}{1-q}\right)}{\Gamma\left(\frac{3-q}{2(1-q)}\right)} & \text{, for } -\infty < q < 1 \\ \sqrt{\pi} & \text{, for } q = 1 \\ \frac{\sqrt{\pi}}{\sqrt{q-1}} \frac{\Gamma\left(\frac{3-q}{2(q-1)}\right)}{\Gamma\left(\frac{1}{q-1}\right)} & \text{, for } 1 < q < 3 \end{cases} \tag{5.75}$$

and the q-exponential e_q is described by

$$e_q(x) = \begin{cases} \exp(x) & \text{, if } q = 1 \\ (1 + (1-q)x)^{\frac{1}{1-q}} & \text{, if } q \neq 1 \text{ and } (1 + (1-q)x) > 0 \\ 0 & \text{, if } q \neq 1 \text{ and } (1 + (1-q)x) \leq 0 \end{cases} \tag{5.76}$$

where β_q is a positive number, Γ the gamma function and q describes the tail weight as compared to the core. $q < 1$ indicates a distribution with “light" tails and $q > 1$ heavy tails. If $q \to 1$, $e_q(x) \to \exp(x)$ approaches the Gaussian description in Eq. (5.69). The q-Gaussian function for various parameter values is illustrated in Fig. 5.3. Starting from Eq. (5.73), the

σ_{RMS} of the q-Gaussian function $g(u)$ in Eq. (5.74) is

$$\sigma_{\mathrm{RMS}} = \begin{cases} \sqrt{\frac{1}{\beta_q(5-3q)}}, & \text{for } q < 5/3 \\ \infty, & \text{for } 5/3 \leq q < 2 \\ \text{undefined}, & \text{for } 2 \leq q < 3. \end{cases} \tag{5.77}$$

The q-Gaussian distribution function and its moments will be important for this thesis work to quantify the beam and tail distributions of non-Gaussian profiles.

5.3 Characterization of the SPS tune ripple

Historically, tune modulations at $n \times 50$ Hz (n being the harmonic) frequencies have been observed in the SPS. They are caused by power converter ripple on the main quadrupole circuits, and have been identified as important ingredient for beam loss mechanisms of high brightness proton bunches [119]. In the SPS, the main focusing (QF) and defocusing (QD) quadrupoles — 108 of each type — are powered in two large circuits with the currents I_{QD} , I_{QF}, respectively. These chains of magnets behave similar to a transmission line [144]. A detailed SPS power supply ripple study was carried out in 1994, which mapped measured transmission line characteristics of single magnets and magnet chains into simplified circuit models [145]. If a voltage spectrum is applied at the power converters, there is a frequency response due to a **low-pass filtering** effect, which attenuates the current at higher frequencies as compared to the one measured using DC current transformers (DCCTs) at the power converter output. In this 1994 circuit model, the damping effects of eddy currents induced in the vacuum chambers were electrically represented as a damping resistor. This modelling was first done for the SPS main dipoles and then for the SPS quadrupoles. However, no beam shielding measurements were done for the latter, so the model parameters cannot be used directly here. The resulting power and quadrupolar circuit model from this study are shown in Fig. 5.4: a symmetric Pi section filter with additional damping elements. Shielding by the beam pipe has also been considered in previous studies, for example in HERA [99], where, however, virtually no shielding effect was found on tune ripples for warm sections of the stainless steel beam pipe.

The characteristic 50 Hz components are believed to originate from the electrical grid (the higher harmonics, in particular the 600 Hz component, are due to the rectification in the power converters) and affect notably the spill quality of slow extracted beams for the CERN North Experimental Area (NA) [146]. For this reason, a noise compensation system was developed for actively injecting a voltage modulation in the main SPS quadrupole circuits (QF and QD) at 50 Hz, 100 Hz, and 150 Hz at adjustable phase and amplitude [146].

The impact of this power converter noise compensation scheme on reducing the beam quality degradation of the ion beams on the SPS FB has been tested for the first time in October 2024. An example of the beam intensity along the SPS cycle with the compensation scheme is shown

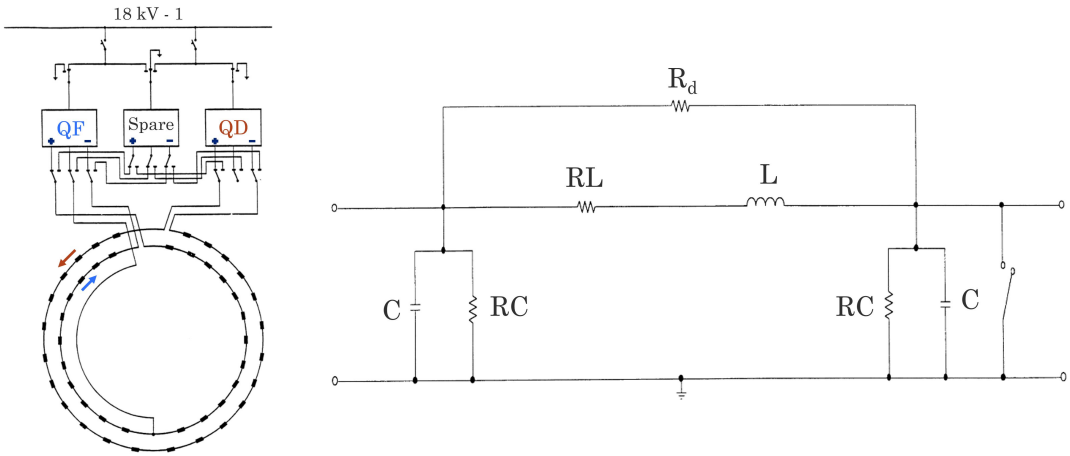


Figure 5.4: Powering (left) and circuit model (right) of SPS quadrupole magnet chains. The QD string with 108 units is powered with one power supply, and the QF chain is nowadays also operated in one large circuit of 108 quadrupoles. The circuit model is similar to a symmetric Pi-section filter with additional damping elements. Circuit elements include capacitors (C), two resistors (RC) in parallel with the capacitor, an inductor (L), and a resistor (RL) in series with the inductor. The switch corresponds to measurements with open or closed loop. The shielding effect on the beam pipe (stainless steel) is electrically modeled as a small damping resistor R_d. Graphics adapted from Ref. [145].

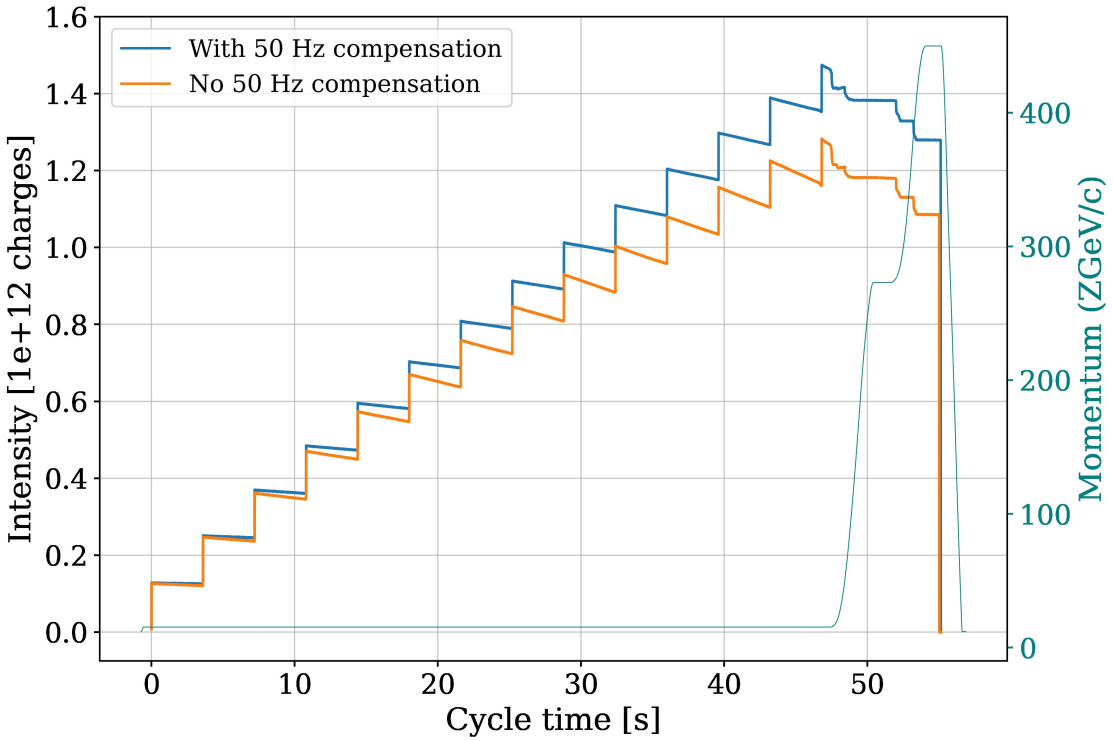


Figure 5.5: Impact of 50 Hz noise compensation on the operational SPS Q26 Pb cycle.

in Fig. 5.5, *improving the total Pb ion beam transmission by up to 20%.* Clearly, minimizing the $n \times 50$ Hz tune modulation components is an important contribution for improving the SPS Pb ion beam performance, contributing to record-high SPS Pb flat bottom intensity transmissions in November 2024. In what follows, the focus is put on measuring and quantifying the tune ripple in the SPS, as this is essential for the development of an SPS simulation model.

First, a series of DCCT measurements were conducted during the SPS Pb ion beam commissioning in October and November 2024 in order to analyze the spectral content of the power converter currents. In this analysis, mormalizing the FFT (i.e. dividing by the number of sampling points) allows a comparison between spectra of different sampling points, if necessary. Figure 5.6 shows an example of the measured QD and QF main circuit currents

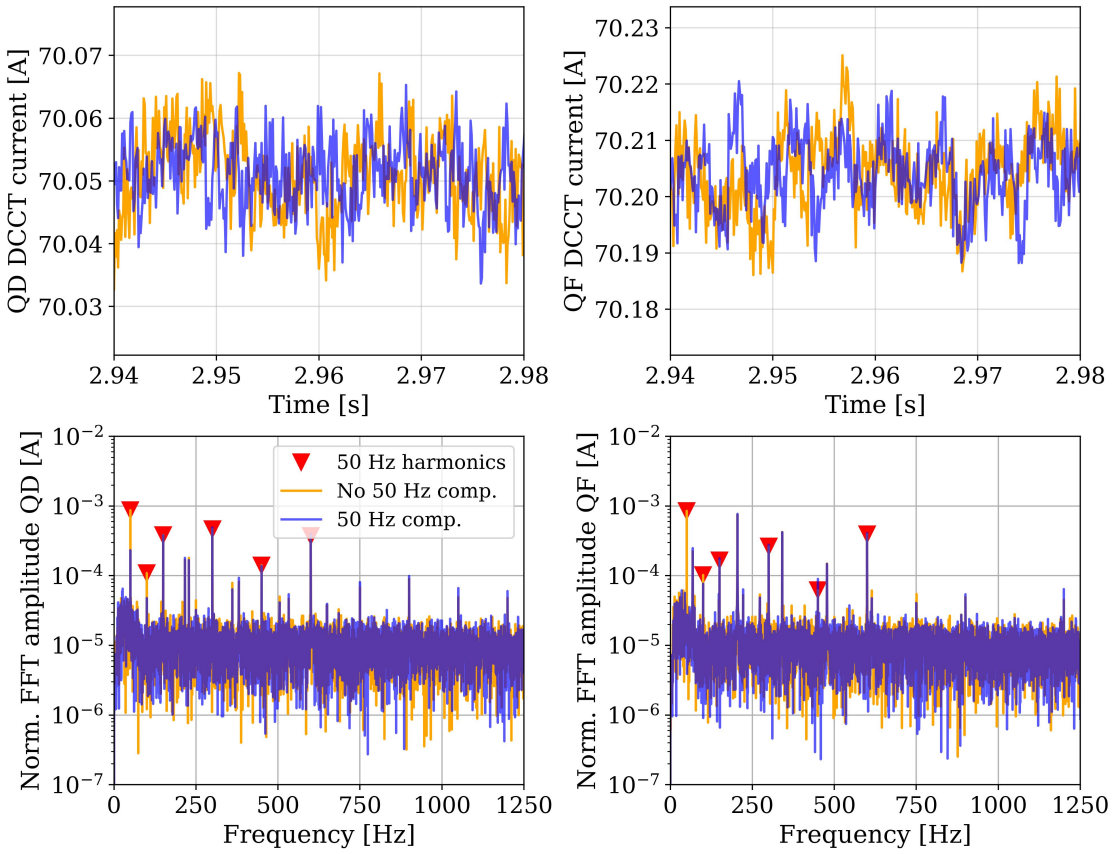


Figure 5.6: Top row: example of measured QD and QF main circuit currents (excerpt of 0.04 s) with the 10 kHz DCCT device from Nov 25$^{\text{th}}$ 2024: no noise compensation (orange), and with 50 Hz compensation (blue). In the QF case (top right), note the dominant 50 Hz oscillations (two periods in this time window) in the orange uncompensated curve, whereas the blue 50 Hz-compensated curve is dominated by smaller faster oscillations. Bottom row: respective normalized FFT spectra, where relevant 50 Hz n harmonics are indicated by red markers. Note, in this particular case, how the 50 Hz noise amplitude is completely compensated in the QF case (bottom right, leftmost peak), and significantly reduced also in the QD case where full compensation was not yet achieved (bottom left).

with the 10 kHz DCCT device, without any compensation (orange) and with successful 50 Hz compensation (blue), which in this case was particularly effective for the QF current.

The SPS flat bottom transmission improvement (by up to 20%) in Fig. 5.5 was achieved by compensating the normalized FFT amplitude at 50 Hz in both QD and QF circuits to below 5×10^{-4} A each, corresponding in spectrum to sinosoidal oscillation amplitude of 1 mA. Other 50 Hz harmonics up to 600 Hz, intrinsic to the 12 pulse thyristor rectifier power converter, are present in the spectra irrespective of the compensation of the 50 Hz noise component. In addition to 50 Hz, the most important noise frequencies were typically found to be 600, 150, and 300 Hz.

To understand this phenomenon in detail and *how the power converter ripples are actually translated to tune modulation* — also considering the aforementioned low-pass filtering effect of the transmission line characteristics and of the vacuum chambers — additional data from a 2018 SPS proton study is used. Back then, measurements of the SPS tune ripple were performed in a dedicated set-up [147]. After attempting to correct machine non-linearities as much as possible (linear chromaticity and amplitude detuning), a single kick induced betatronic oscillations that lasted for more than 70 000 turns, corresponding to about 1.5 s of measurement time. Figure 5.7 shows an example of turn-by-turn (TBT) beam oscillations measured with the dedicated high sensitivity pick-up as measured during this 2018 campaign.

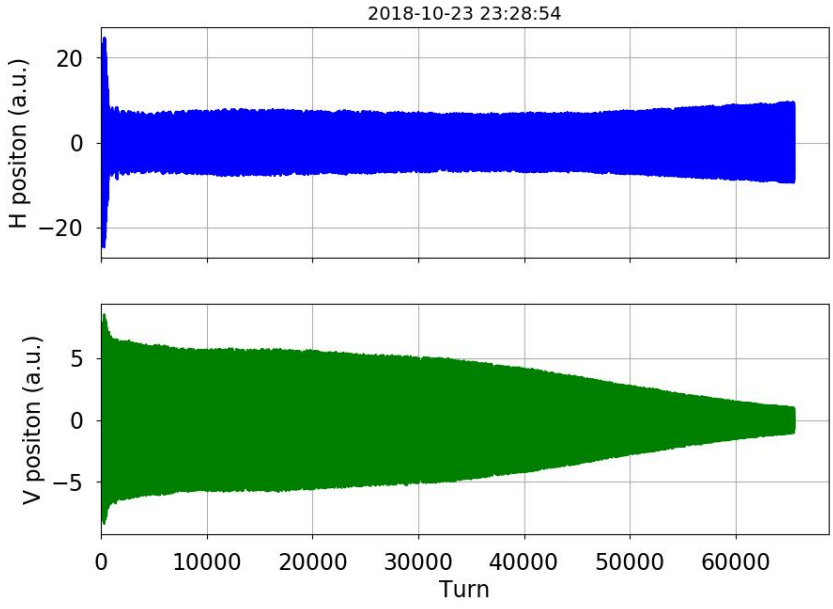


Figure 5.7: Example turn-by-turn data of kicked SPS proton beam in the horizontal (blue) and vertical (green) plane after a single kick from the 2018 measurements. Image credit: [147].

Figure 5.8 (at the top) shows the resulting tune evolution as obtained using a 40-turn sliding window of the TBT oscillations. The spectral components (i.e. the tunes) were determined with the Python module PyNAFF [110], which employs the Numerial Analysis of Fundamental Frequencies (NAFF) algorithm [148]. At the time, the window size of 40 turns was determined

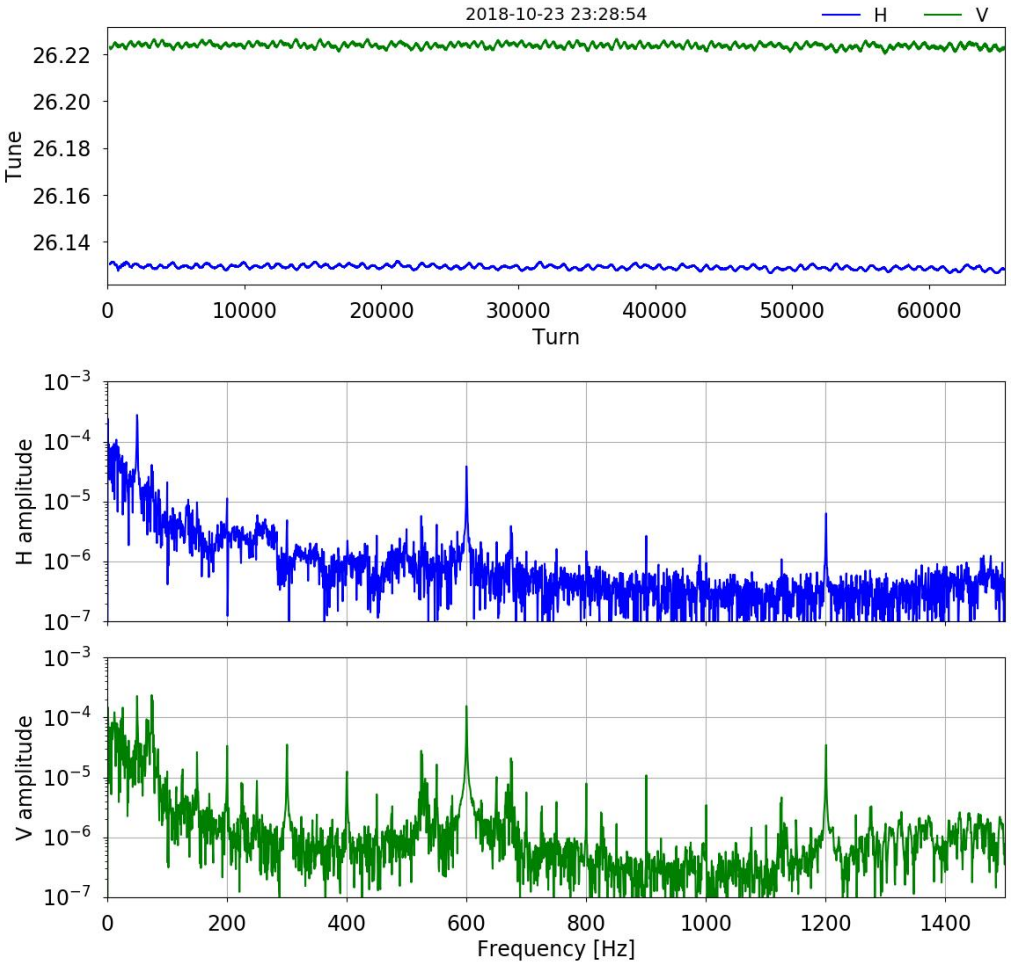


Figure 5.8: Transverse tune evolution (top) from a 40-turn sliding window of the 2018 beam oscillation measurements in Fig. 5.7. The two bottom plots show the normalized FFT of the tune evolution, with the 50 and 600 Hz peaks visible. Image credit: [147].

as a compromise between time resolution and tune precision, also to include higher frequency components in the analysis. A subsequent FFT analysis of the turn-by-turn tune evolution as displayed in Fig. 5.8 (bottom plots) shows the tune modulations present in the beam motion. Before the FFT analysis, the signal mean is subtracted such that DC component is suppressed. The 50 Hz but also the 600 Hz components stand out, but even the 1200 Hz (second harmonic of the 600 Hz induced by the 12 pulse rectifier) can be clearly measured. The background “noise floor" attenuates with higher frequencies.

To quantify potential systematic effects of the analysis technique, a simulation study is undertaken to emulate the 2018 measurements. The primary goal was to verify that the 40-turn sliding window used for tune analysis does not significantly attenuate the measured amplitude of high-frequency ripple components. In the simulations, a single Pb particle is kicked in an SPS tracking simulation model for 70 000 turns, with externally excited ripple frequencies.

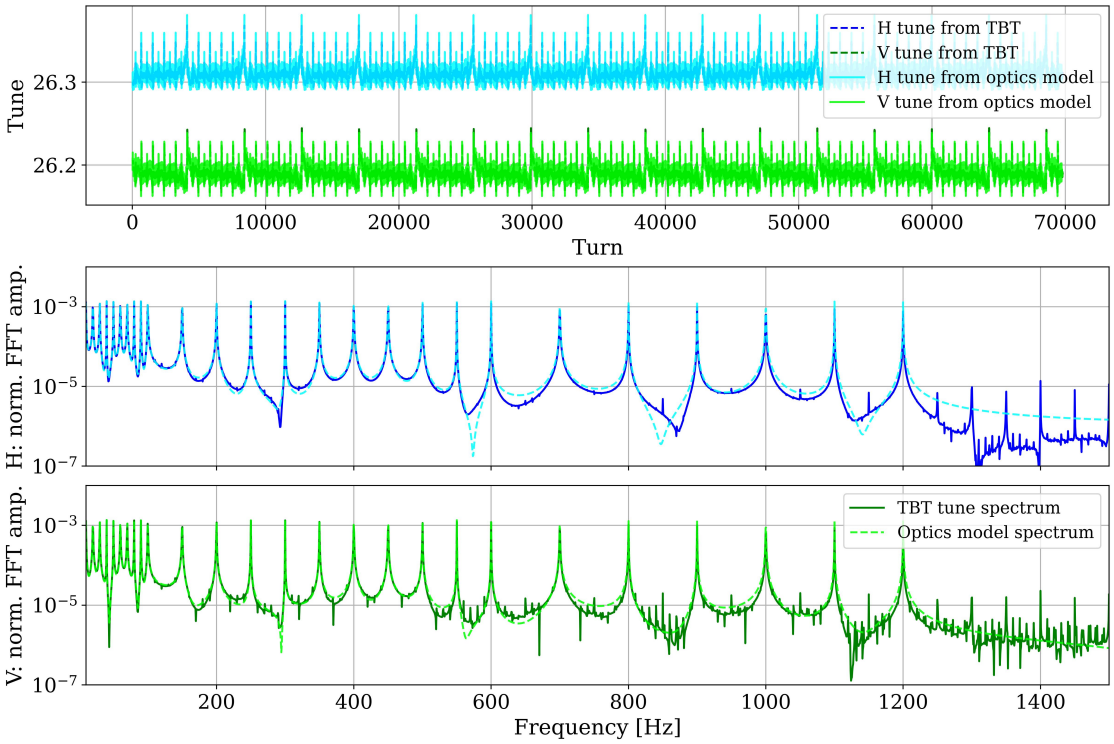


Figure 5.9: Tune evolution (with 40-turn sliding analysis window) from a simulated kicked Pb particle over 70k turns (TBT motion), compared to the expected tune from the optics model (top). The bottom plots show the normalized FFT spectra of these signals.

This ripple signal is directly applied to the normalized quadrupolar gradients $k_{\mathrm{QD,\,QD}}$ of the SPS main quadrupoles. The synthesized signal is composed of frequencies ranging from 10 to 1200 Hz, the area of interest.

The tune evolution is then computed from the simulated turn-by-turn motion using the same 40-turn sliding NAFF algorithm as in the measurements. This beam-derived tune is compared to the theoretical tune, which is calculated directly from the known quadrupole gradient ripple. As shown in Fig. 5.9, the normalized FFTs of both tune signals show excellent spectral agreement. This confirms that while the 40-turn window inherently acts as a low-pass filter, its frequency response of this window size choice is sufficiently flat across the region of interest. The amplitude of ripple components up to 1200 Hz is accurately reproduced, thus validating the analysis technique. As will be shown in Section 5.5.4, ripple frequencies beyond this range have a negligible impact on beam degradation.

From the same intervals on Nov 9$^{\mathrm{th}}$ 2018, a systematic comparative spectral analysis is performed in this thesis work between a) the TBT measurements of the kicked beam motion, and b) current measurements (at the input of the quadrupole circuits) using a 50 kHz DCCT. One example is shown in Fig. 5.10. The current measurements are used to calculate normalized quadrupolar strengths, using magnet transfer functions that translate current to magnetic

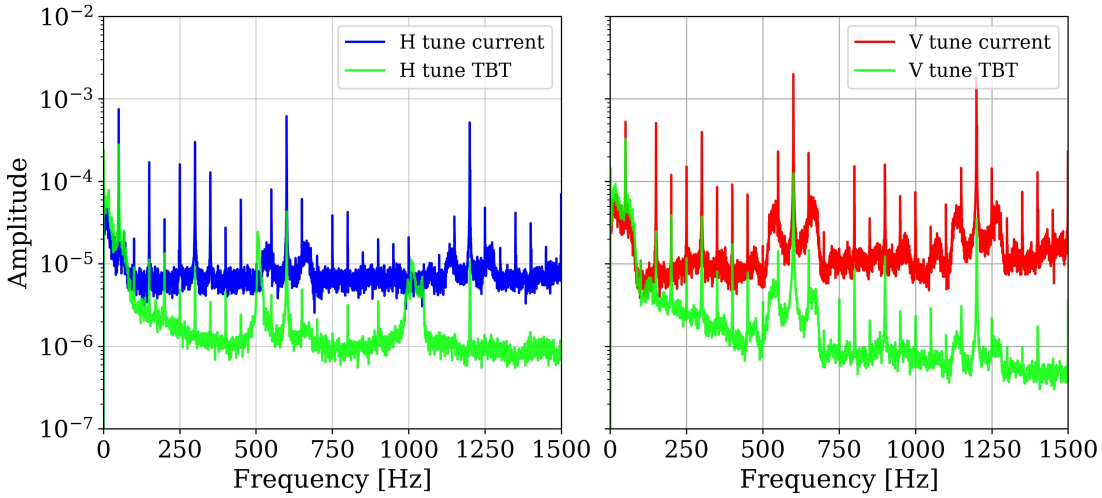


Figure 5.10: FFTs (normalized by the number of sampling points, in tune amplitude) of tune evolution from a) main quadrupolar circuit currents using the optics model and b) TBT beam data. Both data sets were taken on Nov 9th 2018, with SPS Q26 protons. In the green TBT data, notice the synchrotron motion peaks visible at around 500 and 1000 Hz.

field. With known beam momentum, the tunes can be calculated from these normalized quadrupolar strengths and the SPS optics model [149]. Note that in Fig. 5.10, a “noise floor" is observed in the current spectrum, starting from about 100 Hz, which is particularly visible in the horizontal plane (blue line). On the other hand, at this point, the TBT spectrum attenuates further to a lower amplitude level.

This spectral ratio in frequency space (TBT oscillations versus measured current) is an important ingredient to construct a transfer function to translate power converter ripples to actual tune modulations as seen by the beam. To *semi-empirically* capture the underlying physics of the transmission line behavior, similar circuit analogies as in Ref. [145] are used to create a fitting model of the low-pass filter. In circuit theory, the transfer function $H(f)$ is often used (in frequency space) to characterize the frequency response of a given circuit [150]. Four simple circuit options have been tested here:

- **LC section**: one capacitor and one inductor

$$H(f) = \frac{A}{1+\left(\frac{f}{f_c}\right)^B} \tag{5.78}$$

- **C section**: one capacitor

$$H(f) = \frac{A\left(\frac{f}{f_c}\right)}{1+\left(\frac{f}{f_c}\right)^B} \tag{5.79}$$

- **Combined LC and C**: sum of C and LC sections

$$H(f) = H_{LC}(f) + H_C(f) = \frac{A_1}{1 + \left(\frac{f}{f_{c1}}\right)^{B_1}} + \frac{A_2\left(\frac{f}{f_{c2}}\right)}{1 + \left(\frac{f}{f_{c2}}\right)^{B_2}} \tag{5.80}$$

- **Pi section**: two capacitors, one inductor (simplified version from Fig. 5.4)

$$H(f) = \frac{A}{1 + \left(\frac{f}{f_c}\right)^{B} + \left(\frac{f}{f_c}\right)^{2B}} \tag{5.81}$$

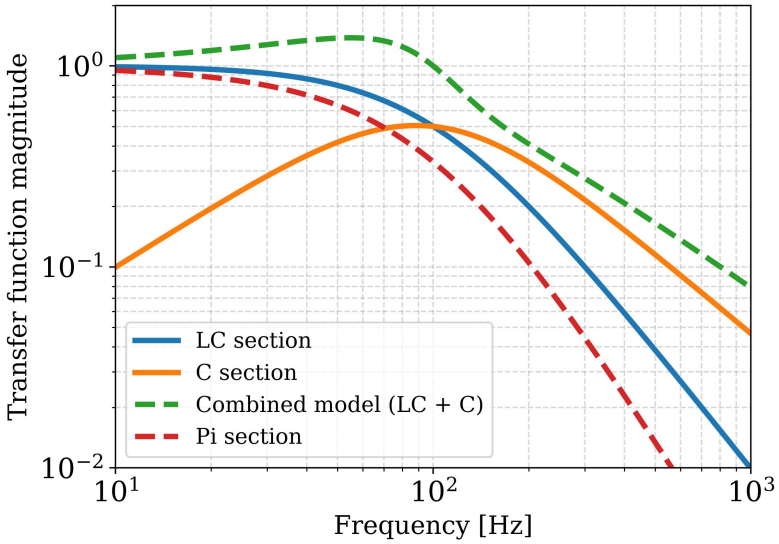


Figure 5.11: Circuit-inspired transfer function models used as the ansatz to fit the empirical transfer function spectral data ratio TBT versus quadrupolar circuit current. In this example, all functions are scaled to one, with cut-off frequency $f_c = 100$ Hz.

with scaling parameter A, cut-off frequency f_c (after which higher frequencies are damped), and power-law roll-off with exponent B. An illustrative comparison of these transfer functions example is shown in Fig. 5.11.These four transfer functions are fitted to the spectral ratio (TBT over circuit current) from Fig. 5.10 using non-linear least squares optimization. A quantitative comparison can be based on the coefficient of determination (goodness of fit) R^2, defined as

$$R^2 = 1 - \frac{\sum_i (y_i - H_i)^2}{\sum_i (y_i - \bar{y})^2}, \tag{5.82}$$

of data points y_i with mean $\bar{y}$. Using the R^2 parameter, the **combined LC + C section** demonstrates a superior fit to the measured data compared to the other models, as illustrated in Fig. 5.12. This particular transfer function model is subsequently implemented in the SPS simulation to accurately adjust the amplitude of the 50 Hz ripple harmonics measured in the DCCT currents. While models with more parameters carry an inherent risk of overfitting

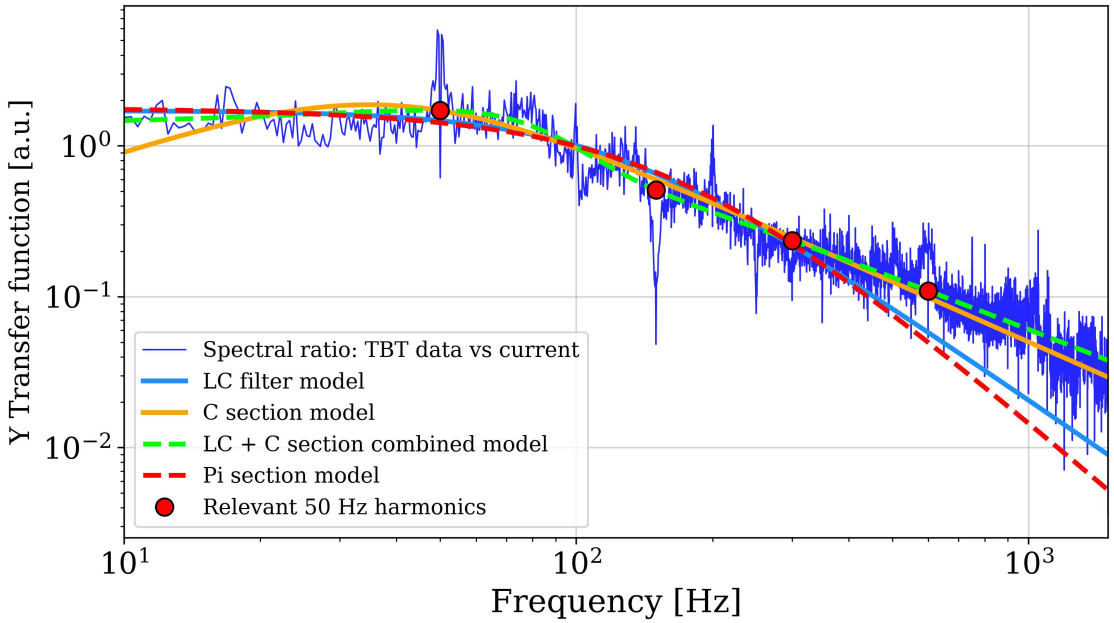


Figure 5.12: Semi-empirical transfer functions $H(f)$ fitted to the spectral ratio TBT versus spectral current from Fig. 5.10, here in the vertical plane which appears less affected by the "noise floor". Goodness of fit R^2 values are: a) 0.79 for the LC model, b) 0.76 for the C model, c) 0.83 for the combined LC + C model, and d) 0.78 for the Pi model. With the LC + C model fit, f_c = 88 Hz. Values of the combined LC + C section model are at relevant harmonics above f_c: 0.51 at 150 Hz, 0.24 at 300 Hz, 0.11 at 600 Hz.

for broad predictive tasks (where adjusted R^2 would typically be preferred), the primary goal for this analysis is a precise description of the observed transfer function within this specific dataset, particularly at key frequencies of interest (e.g., 50, 150, 300, 600 Hz). For this descriptive purpose, the R^2 measure directly reflects the model's fidelity to the observed data and fulfills the practical requirements. Once again, for the quadrupolar mode, the 1994 study did not measure the shielding of the field due to the vacuum chamber, a reason for why this model was not used directly here.

This model entails some limitations. If there is a limit on the noise floor in either of the two measurements, the inferred transfer function will be affected. Also, these TBT and current measurements are not synchronized to the turn level, which complicates the picture and makes detailed incorporation of phase shifts (in addition to amplitude comparisons) difficult. The Pi section model, which resembles closest to the circuit model of the 1994 study, may be the more accurate, despite a lower R^2 value for this dataset. A more refined analysis is beyond the scope of this thesis, but this semi-empirical LC + C model represents a pragmatic approach to find the low-pass filtering effect on the ripple amplitude for the simulation studies.

To summarize: previous studies have shown that tune modulations from power converter ripples in the SPS main quadrupoles lead to beam losses, confirmed by the effects of testing a noise compensation scheme in 2024 for Pb ion beams. A 1994 SPS power supply ripple

study [145] observed transmission line characteristics of the quadrupolar magnet series, leading to a low-pass filtering effect of ripple frequencies. Measurements of current and turn-by-turn oscillation from a 2018 campaign [147] allowed us to quantify the high-frequency ripple attenuation in the magnet circuits through an empirical transfer function. Of all tested fitting functions inspired from circuit theory, the LC + C transfer function model proved to semi-empirically best describe this low-pass filtering effect (for this particular dataset) with the R^2 benchmark. This function is used to *predict the effective tune ripple* (as seen by the beam) by *amplitude-adjusting* measured 50 Hz harmonics (above the cut-off frequency) from measured circuit currents.

5.4 Development of a predictive SPS ion tracking model

5.4.1 Rationale and simulation framework

Detailed studies of SC, IBS, and tune ripple effects (discussed in Section 5.1) and their interplay with magnet imperfections require numerical multi-particle tracking simulations. In this thesis work, an SPS ion FB tracking simulation model has been developed to study these effects in the framework of the open-source Python package `fma_ions` [151, 152], leveraging `xsuite` [49] functionalities. The latter represents a unification effort of various beam dynamics simulation tools developed at CERN over several decades, allowing for symplectic particle dynamics modeling. The ecosystem contains sub-packages such as `xtrack` (tracking engine), `xfields` (collective effects), and `xpart` (particle object generation) — both on CPU and GPU computing platforms. Recently, `xsuite` has matured significantly to cover many lattice models and beam dynamics effects. This thesis work systematically tested and validated ion beam effects in the SPS with `xsuite` tools, also making several contributions to functionalities and modules of these sub-packages. In this section, the following aspects in the SPS ion tracking model development are discussed: lattice description, mechanical aperture, magnet errors, SC, IBS, and tune ripple.

5.4.2 SPS machine model

Lattice description

Here, the specific lattice model is briefly described and the Q26 optics used for SPS Pb ion operations. Table 5.1 summarizes the key ring parameters for Pb ions. From the CERN official optics repository [149], the MAD-X [153] lattice description file `SPS_LS2_2020-05-26.seq` — the latest version with complete associated aperture file at the time of writing — is imported into `xsuite` to define the beamline elements and calculate the transfer maps used for particle tracking. Figure 5.13 shows the layout of the optics functions $\beta_{x,y}$ and $D_{x,y}$ along one sixth of the SPS lattice, with six-fold periodicity. The Q26 ion optics features maximum beta function values $\beta_x \approx 107.5$ m and $\beta_y \approx 108.2$ m.

Table 5.1: The SPS ion parameters for Pb ions at injection energy, as used in simulations. Tunes and chromaticities correspond to values measured during experimental studies.

SPS lattice parameters for Q26 ion optics (2024)	
Circumference [km]	6.911
$^{208}Pb^{82+}$ rest mass [GeV/c^2]	193.7
E_k per nucleon at inj. [GeV/u]	5.9
Relativistic gamma γ	7.31
Momentum compaction factor	0.0016
Harmonic number h	4653
RF voltage V_{RF} [MV]	3.0
Betatron tunes $Q_{x,y}$	26.31, 26.19
Linear chromaticities $Q'_{x,y}$	−0.4, −0.4

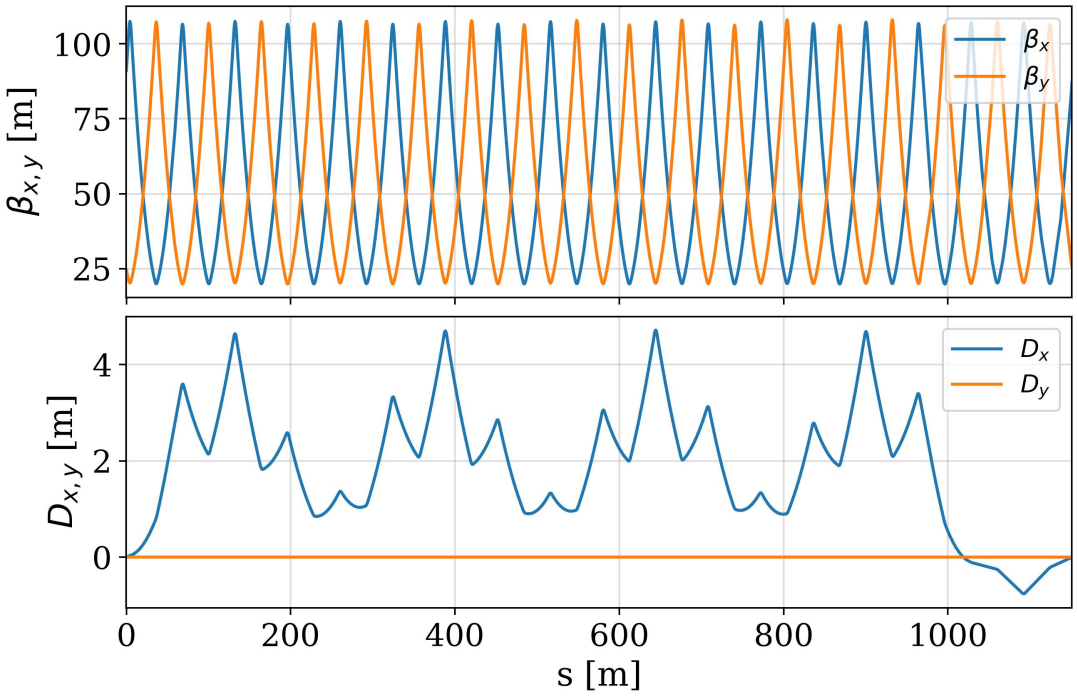


Figure 5.13: Optics functions for Q26 ion optics along one sixth of the SPS lattice (with sixfold periodicity), here starting from a point of minimal horizontal dispersion D_x.

Mechanical aperture

Beam losses occur on the mechanical aperture, including elements such as the vacuum chamber, collimators, and other inner surfaces. The SPS optics repository aperture classes [149] are used to define the physical aperture restrictions of the lattice model.

An important figure of merit is the minimum acceptance A, which is the number of beam size standard deviations available within the space between the beam orbit and the inner wall of

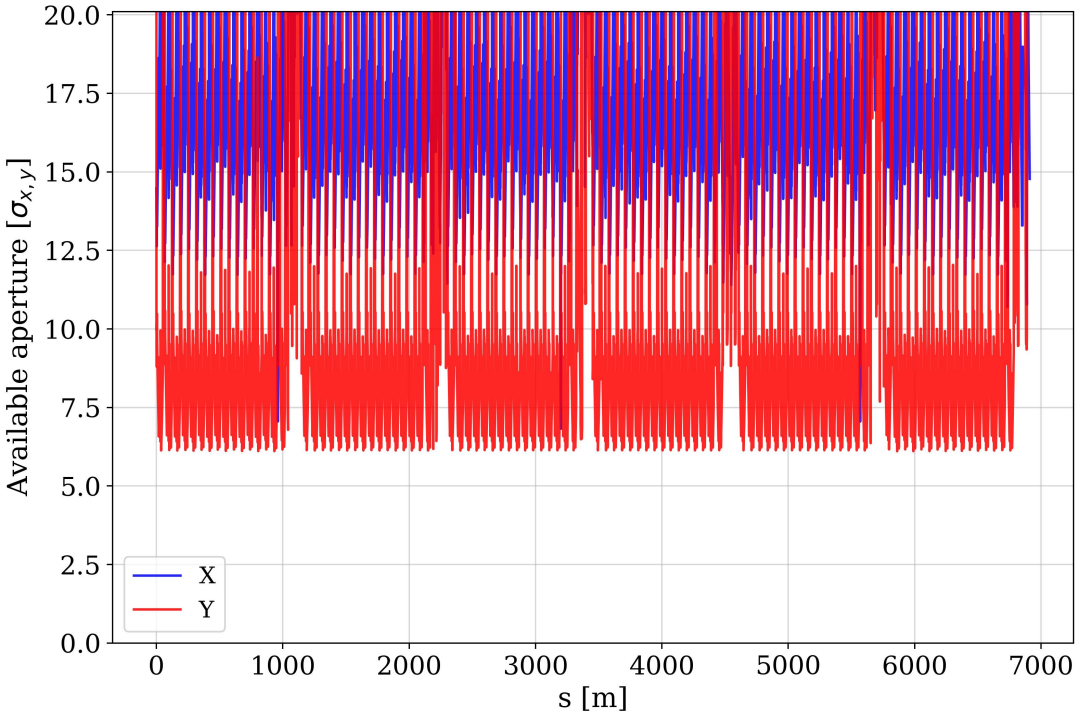


Figure 5.14: Available aperture (acceptance) for LHC type Pb beams in SPS with Q26 optics, with $\varepsilon^n_{x,y} = (2.3, 1.3)$ mm mrad and $\Delta p/p = 10^{-3}$ at the injection energy.

the chamber, defined as

$$A_{x,\,\mathrm{min}} = \min\left(\frac{\mathrm{aper}_x(s) - |x(s)|}{\sigma_x(s)}\right), \tag{5.83}$$

where beam sizes $\sigma_{x,y}$ are defined in Eq. (5.2), $x(s)$ is the horizontal position from the reference trajectory and $\mathrm{aper}_x(s)$ is the horizontal mechanical aperture of the machine (circular radius), with y replacing x for the vertical case. Figure 5.14 shows the acceptance A (available aperture) across the SPS Pb Q26 lattice with normalized emittances $\varepsilon^n_{x,y}$ as measured during the 2024 Pb run with nominal LHC Pb ion beams, i.e. $\varepsilon^n_{x,y} = (2.3, 1.3)$ mm mrad. The machine aperture restrictions are much tighter in the vertical plane: $A_{y,\,\mathrm{min}} \approx 6.1$ systematically in the middle of the FODO cells in between the MBA and MBB type dipoles, compared to $A_{x,\,\mathrm{min}} \approx 6.8$ in three locations, but mostly $A_x \gtrsim 13.5$.

Closed-orbit distortions and machine elements misalignments will reduce the mechanical aperture, but it is not known to what extent and where in the lattice. To address this phenomenon in the simulations, two “effective" aperture elements are installed at the horizontal wire scanner ($\mathrm{aper}_x = 0.025$ m at `BWSRC.51637`) and vertical wire scanner ($\mathrm{aper}_y = 0.013$ m at `BWSRC.41677`) locations, corresponding to the experimentally observed cut of transverse profiles during the 2024 SPS ion measurements. An illustrative example of these observed cuts is shown in Fig. 5.15.

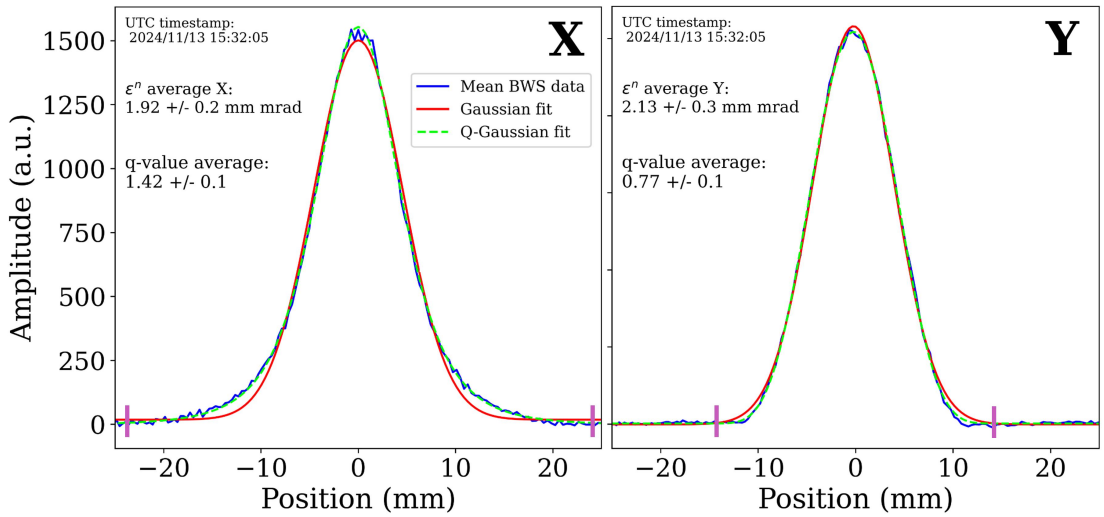


Figure 5.15: Measured average transverse Pb beam profile examples in the SPS at the end of FB (around 48 s). Gaussian and q-Gaussian profile fits are also shown. The transverse cuts from the “effective" aperture elements are shown as purple vertical lines (at their approximate locations), a point below which the beam profiles were observed during measurements.

Optics imperfections

Magnetic field gradient errors can distort the optics functions of the machine lattice and cause unwanted losses. For example, quadrupolar gradient errors can lead to beating of the beta functions (“beta-beating") $\Delta\beta_{x,y}/\beta_{x,y}$, which are variations of the beta function compared to its design values. This effect can potentially cause beam losses due to reduced available aperture. Considering random quadrupole strength errors Δk_i distributed in the lattice, the root-mean-square (RMS) beta-beating is

$$\left(\frac{\Delta\beta_{x,y}}{\beta_{x,y}}\right)_{\mathrm{RMS}} = \frac{1}{2\sqrt{2}|\sin(2\pi Q_{x,y})|}\left(\sum_i \Delta k_i^2 \beta_{x,y}^2\right)^{1/2}. \tag{5.84}$$

Beta-beat measurements in SPS Q26 optics were carried out in November 2024 by P. Zisopoulos [154]. Using 113 horizontal and 114 vertical beam position monitors (BPMs) around the SPS, two methods were tested to study the betatron oscillations of a kicked beam at $Q_{x,y} = (26.29, 26.26)$:

- *Phase method*: the beta-beat can be reconstructed from the measured betatronic phase beating between BPMs. The method that uses the phase advance between three BPMs to determine the beta beating values at these BPMs. If the phase advance is close to 90 degrees (like in the Q26 optics of the SPS), systematic errors are introduced, and the error on the measured beta function approaches large values [155].
- *Amplitude method*: direct oscillation amplitude measurements from the FFT spectra at

each BPM position. This method is however subject to the BPM calibration errors.

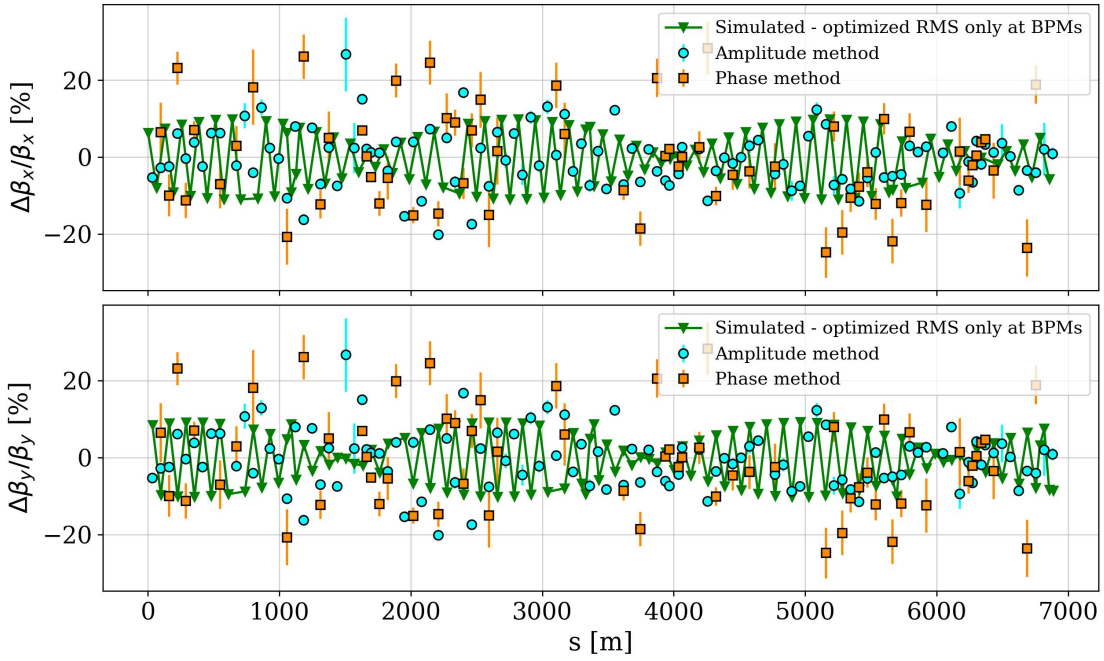


Figure 5.16: Measured SPS Q26 beta-beat, using the amplitude and phase methods (credit: P. Zisopoulos). In the simulations, two quadrupole errors were numerically optimized to generate the same RMS beta-beat as measured at the functional BPM locations. For an integer tune of 26, the beating oscillation tune is $26 \times 2 = 56$.

The resulting measurement from the two methods can be seen in Fig. 5.16. Due to the systematic errors of this method stemming from the 90 degree phase advance, the amplitude method is considered more trustworthy in the case of SPS Q26 optics. The relatively low intensity of the ion beams ($N_b = 2 \times 10^8$ ions per bunch) and using a single bunch beam ensure that no phase spread is introduced in the particles, which would lead to errors in the tune measurements. The computed RMS values $(\Delta\beta_{x,y}/\beta_{x,y})_{\mathrm{RMS}}$ from the measurements of all functional BPMs are 7.5% horizontally and 7% vertically.

The exact distribution of quadrupolar gradient errors around the SPS lattice is unknown. Previous simulation studies had introduced a single quadrupolar error to emulate a 5-10% beta-beating [131, 156], but this approach does not allow controlling the beta-beating in each plane individually. Here, two single quadrupolar errors (one on a QF magnet, one on a QD magnet) are inserted in the machine model and numerically optimized to generate these RMS beta-beat values.

Nonlinear magnet imperfections

Another important component of the SPS simulation model is to establish a nonlinear optics model to reproduce the chromatic properties of the machine. For a given momentum

deviation $\delta = \Delta p/p$, the betatron tune dependence can be written as

$$Q_{x,y}(\delta) = Q_{x,y} + Q'_{x,y}\delta + \frac{1}{2}Q''_{x,y}\delta^2 + \frac{1}{6}Q'''_{x,y}\delta^3 + \frac{1}{24}Q''''_{x,y}\delta^4 + \ldots, \tag{5.85}$$

where $Q'_{x,y}$ corresponds to the linear chromaticity, dominated by quadrupoles (natural chromaticity) and sextupole components in dispersion regions. On the other hand, $Q''_{x,y}$ is dominated by octupoles in regions of dispersion, and so on. The SPS non-linear chromaticity was already studied in a series of measurements between 2000 and 2002 [157, 158], followed by subsequent measurements in 2012 [159]. To model this effect, the established SPS main magnet multipole components are used from individual fits of the corresponding chromaticity measurements from Table 4.4 in Ref. [159].

5.4.3 Space charge implementation

The frozen SC model and its adaptive version were already discussed in Section 5.2. The Bassetti-Erskine formulae in Eq. (5.11) provide the electric field needed to compute the kick applied to the macroparticles, according to their transverse but also to longitudinal position within the bunch. During one synchrotron revolution, the macroparticles pass through the longitudinal distribution twice. *A crucial assumption behind the transverse kick of the Bassetti-Erskine formalism is that the longitudinal macroparticle motion is slow compared to the transverse oscillations*, which is the case for Q20 and Q26 proton optics. This condition is needed for symplecticity, in other words, to preserve the phase space volume. However, this is no longer fully true for SPS Q26 Pb ions with $1/Q_s = 21.25$. This relatively fast synchrotron motion causes the simulated macroparticles to cross the longitudinal distribution once per 10.6 turns. With this fast synchrotron motion, the symplecticity condition is no longer fulfilled, and a longitudinal macroparticle kick is required to preserve the phase space volume.

This thesis work contributed to two main improvements in the `xfields` sub-package for the frozen SC model, starting from the SPS Q26 ion case:

- **Longitudinal frozen SC kicks for symplecticity**: together with G. Iadarola, functionalities and examples were implemented numerically to compute the longitudinal macroparticle kick required to preserve the phase space volume.

- **Longitudinal q-Gaussian line density profiles**: previously, only longitudinally Gaussian beam profiles were available for the SC potential. This thesis work extended this description to include q-Gaussians for Section 5.2.4 as a generalization.

A detailed mathematical description of these implementations is written in “Chapter 6: Space Charge" of the `xsuite` physics manual [49, 160]. Here a short review is provided to clarify the context of the implemented longitudinal kick. In the modulated 2D case (frozen SC potential),

when the beam distribution can be factorized as

$$\rho_0(x,y,\zeta) = q_0\lambda_0(\zeta)\rho_\perp(x,y), \tag{5.86}$$

the electric potential Φ can also be factorized into a transverse and a longitudinal part:

$$\phi(x,y,\zeta) = q_0\lambda(\zeta)\phi_\perp(x,y), \tag{5.87}$$

where $\phi_\perp(x,y)$ is the solution of the following 2D Poisson equation:

$$\frac{\partial^2\phi_\perp}{\partial x^2} + \frac{\partial^2\phi_\perp}{\partial y^2} = -\frac{1}{\epsilon_0}\rho_\perp(x,y) \tag{5.88}$$

The SC kicks per turn are calculated using the transverse potential $\Phi_\perp(x,y)$ and the longitudinal line density $\lambda_0(\zeta)$, starting from the Lorentz force. The kicks on the normalized momenta $(p_x/P_0, p_y/P_0)$ are given by (Eqs. 6.54, 6.55 in the manual):

$$\frac{\Delta p_x}{P_0} = F\cdot\lambda_0(\zeta)\cdot\frac{\partial\Phi_\perp(x,y)}{\partial x} \tag{5.89}$$

$$\frac{\Delta p_y}{P_0} = F\cdot\lambda_0(\zeta)\cdot\frac{\partial\Phi_\perp(x,y)}{\partial y} \tag{5.90}$$

where $P_0 = m_0\beta_0\gamma_0 c$ is the reference momentum, and the factor F is defined as:

$$F = -\frac{qq_0L(1-\beta_0^2)}{m_0\gamma_0\beta_0^2c^2} = -\frac{qq_0L}{m_0c^2\beta_0^2\gamma_0^3} \tag{5.91}$$

q represents the individual particle charge, q_0 and m_0 are the reference particle charge and mass, L is the interaction length, and β_0, γ_0 are the relativistic factors. For non-negligible synchrotron motion, preserving symplecticity requires adding a longitudinal kick $\Delta\delta \approx \Delta P_z/P_0$, which depends on the derivative of the line density $d\lambda_0/d\zeta$ and the potential $\Phi_\perp(x,y)$:

$$\Delta\delta = F\cdot\frac{d\lambda_0(\zeta)}{d\zeta}\cdot\Phi_\perp(x,y) \tag{5.92}$$

The potential $\Phi_\perp(x,y)$ required for Eq. (5.92) is obtained by numerically integrating its gradient components (which determine the transverse field) from the origin:

$$\Phi_\perp(x,y) = \int_{(0,0)}^{(x,y)}\nabla_\perp\Phi_\perp\cdot d\mathbf{l}' = \int_{(0,0)}^{(x,y)}\left(\frac{\partial\Phi_\perp}{\partial x'}dx' + \frac{\partial\Phi_\perp}{\partial y'}dy'\right) \tag{5.93}$$

This complete formulation ensures the SC interaction model correctly preserves phase space volume, preventing artificial emittance growth associated with non-symplectic models under fast synchrotron motion. Figure 5.17 shows an SPS Q26 ion example with a single test particle, with and without applying the new longitudinal kick for symplecticity. Without the longitudinal correction kick, the longitudinal amplitude grows unrealistically over only a few thousand

turns. These improvements will be of benefit for the `xsuite` community in conditions with frozen space charge and fast synchrotron motion.

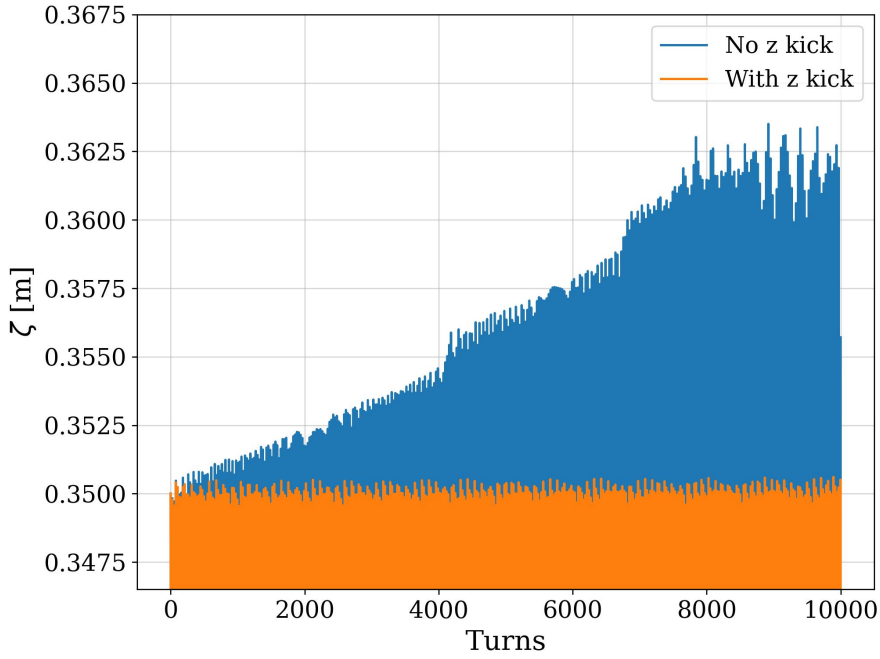


Figure 5.17: SPS Q26 Pb simulation example with frozen SC showing the longitudinal amplitude ζ of a test particle, with and without the implemented longitudinal kick.

For the SPS simulation model set-up, 1080 frozen “adaptive" SC elements are installed around the lattice to provide these kicks in all three planes. The number 1080 was chosen for two reasons: a) this number preserves the symmetry in a sixfold symmetric SPS lattice and is a multiple of the 108 FODO cells, and b) convergent behavior for the SPS Pb ion case was found at this number. These elements are adjusted every 20 turns according to fitted beam size and recorded losses.

5.4.4 IBS model implementation

IBS formalisms were already discussed on a theoretical level in Section 5.2.3. To set up a realistic IBS model in the tracking simulations, this thesis work implemented the following:

- **Kinetic kick element**: for SPS Pb ions below transition energy, the kinetic kick from Eq. (5.59) is used, numerically implemented in `xfields` in 2024 by F. Soubelet and M. Zampetakis [161]. To further enhance computational efficiency, the IBS kick is recalculated only every 2000 turns, based on observed beam profile changes. Also, this thesis work contributed to enabling GPU-compatibility for this IBS kick element, together with F. Soubelet. Various computing platform tests showed that GPU usage accelerated tracking by at least a factor of 7.5 compared to CPUs. Without this added

GPU-compatibility, millions of tracking turns (needed to study e.g. long-term emittance growth) in the SPS ion FB simulation set-up with thousands of macroparticles would not have been feasible.

- **Longitudinal collimation element**: Due to the IBS kicks, particles in the machine may fall out of the longitudinal acceptance of the RF bucket. In simulations, these particles that are kicked out of the RF bucket will drift away from the bunch and artificially inflate the bunch length. A numerical longitudinal collimator element with the RF bucket length is inserted to eliminate macroparticles that fall outside these limits to reproduce the measurement of fast beam current transformers that provide bunch-by-bunch intensities (which can however also measure uncaptured beam).

- **Convergence studies of IBS parameters**: This thesis work performed systematic convergence studies of the kinetic IBS kick formalism in `xsuite` for multiple set-ups, parametrically scanning beam parameters (e.g, emittances, bunch intensities, and macroparticle numbers), both for protons and ions. The full results and details are explained in Ref. [162]. Emittance growth rates from Eq. (5.51) were compared with corresponding analytical growth rates using the Nagaitsev formalism during particle tracking. In general, good agreement between the formalisms was found, also for nominal SPS Q26 ion parameters at injection energy (below transition energy), where Fig. 5.18 shows a test case for beam parameters close to 2024 Pb operations. In general, the sensitivity study showed that the simulated IBS effect converged after the interval 5000-10000 macroparticles. The simulation studies presented in this thesis were performed with 20 000 macroparticles, as there is practically no computational penalty for the GPU-based tracking in `xsuite` compared to using a lower number of macroparticles. In this way, the numerical noise in the simulations is minimized.

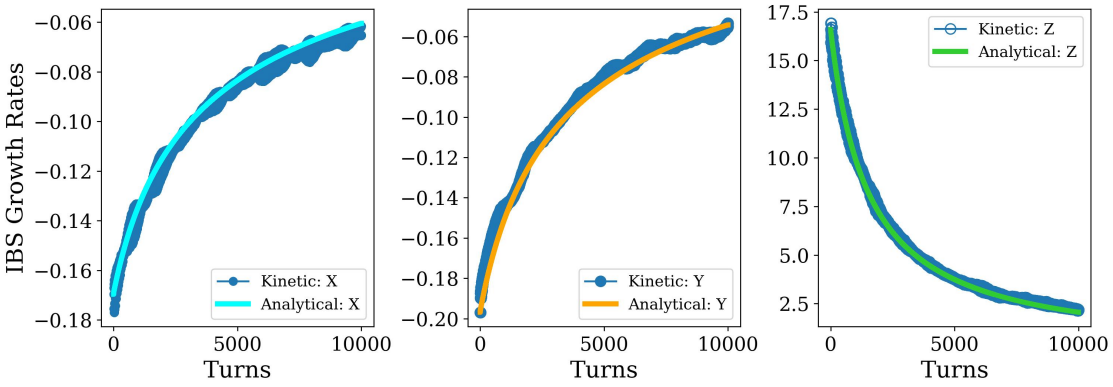


Figure 5.18: SPS Q26 Pb tracking simulation example with a kinetic IBS kick element, with analytical Nagaitsev growth rates periodically computed in parallel from the same beam parameters. In this example, the initial parameters are: $\varepsilon^n_{x,y} = (1.3, 0.9)$ mm mrad, $N_b = 5.7 \times 10^8$ ions per bunch, $\sigma_z = 0.04$ m — shorter than the nominal SPS Pb bunch length to produce faster trends during 10 000 turns.

5.4.5 Tune ripple implementation

The ripple effect was implemented in the SPS ion FB tracking simulation model from the tune modulation theory in Section 5.2 and the experimental tune ripple characterization in Section 5.3. To emulate a realistic power converter tune ripple component, time-dependent signals in the normalized quadrupolar gradient $k_{QD}(t)$ and $k_{QF}(t)$ are added. The correct phase and normalized spectral amplitude for all superimposed frequencies are considered, according to the measured DCCT current ripple. The main measured 50 Hz harmonics ripple components are included in the signal: 50, 150, 300, and 600 Hz. The fitted transfer function $H(f)$ is then applied for amplitude-attenuation of the 150, 300, and 600 Hz components — recall the fitted cut-off value $f_c = 88$ Hz in Fig. 5.12. During the tracking, turn-by-turn, $k_{QD}(t)$ and $k_{QF}(t)$ are then effectively used to modulate the tunes.

5.5 Benchmarking simulations against measurements

This section presents measurements during dedicated parametric scans from the 2024 SPS Pb ion campaign to benchmark simulations from the model development of Section 5.4.

5.5.1 Bunch intensity scan

With stable 50 Hz quadrupole noise compensation, the number of Linac3 injections into LEIR was scanned on Oct 30th 2024 to vary the number of injected ions per SPS bunch. In this way, a quantitative relation between bunch intensity, emittance growth, and losses could be established. Figure 5.19 highlights the SPS Pb bunch intensity evolution. In parallel, transverse

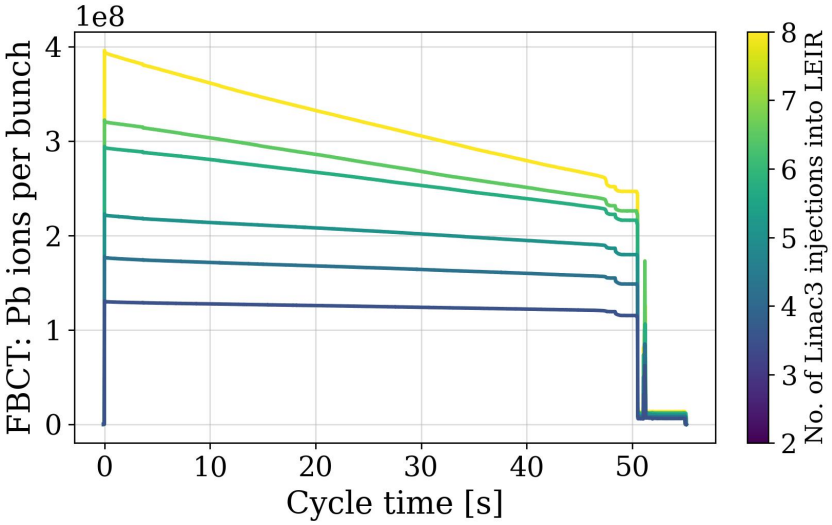


Figure 5.19: Measured fast BCT (FBCT) intensity during a scan of injected SPS Pb bunch intensities, varying the number of LEIR pulses.

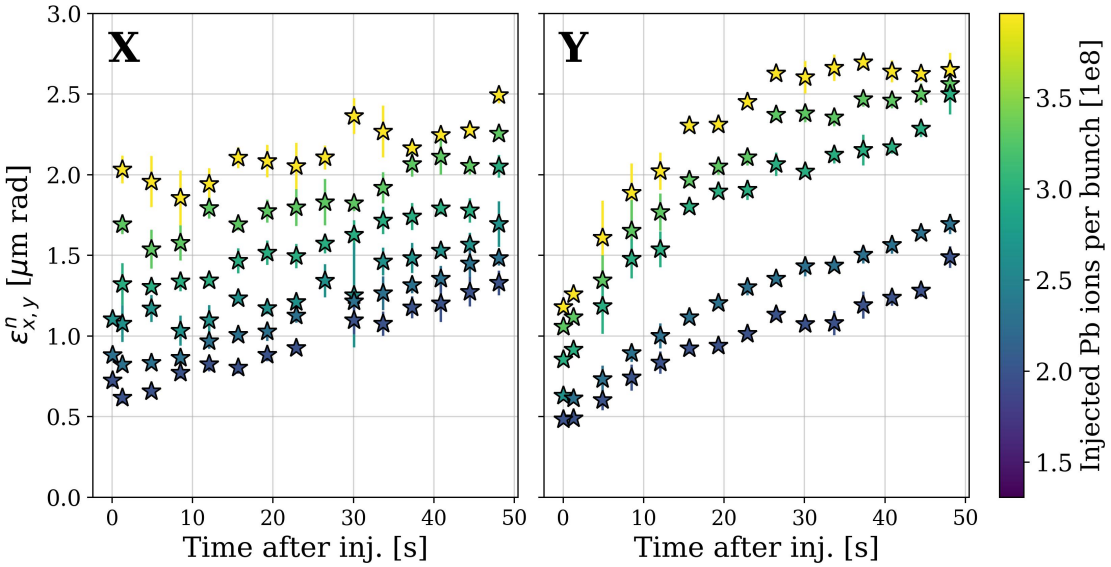


Figure 5.20: Measured normalized emittances $\varepsilon^n_{x,y}$ during the bunch intensity scan in Fig. 5.19.

emittance measurements were conducted, as shown in Fig. 5.20. The corresponding emittance and FB transmission trends are shown in Fig. 5.21. One observes a linear degradation trend in FB transmission as a function of the injected bunch intensity, qualitatively similar to 2016 measurements [163]. However, in 2016, 60% fewer extracted charges were achieved for a

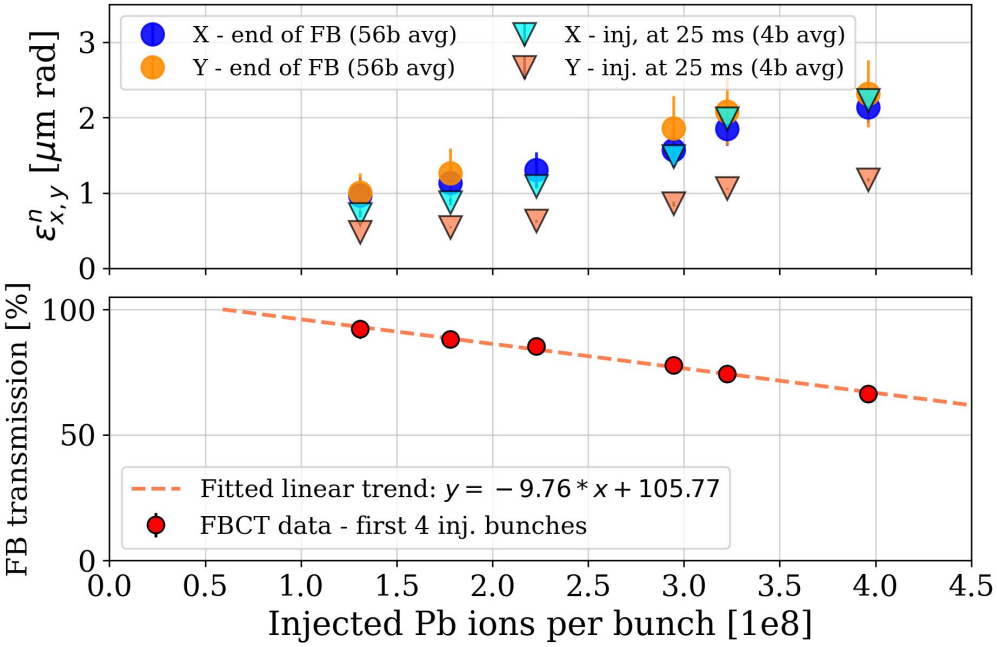


Figure 5.21: Measured FB transmission (of the first bunch 48 s after injection) from Fig. 5.19 , and initial and final emittances from Fig. 5.20, for various injected Pb bunch intensities in the SPS. Note the large ε^n_y blow-up, compared to ε^n_x.

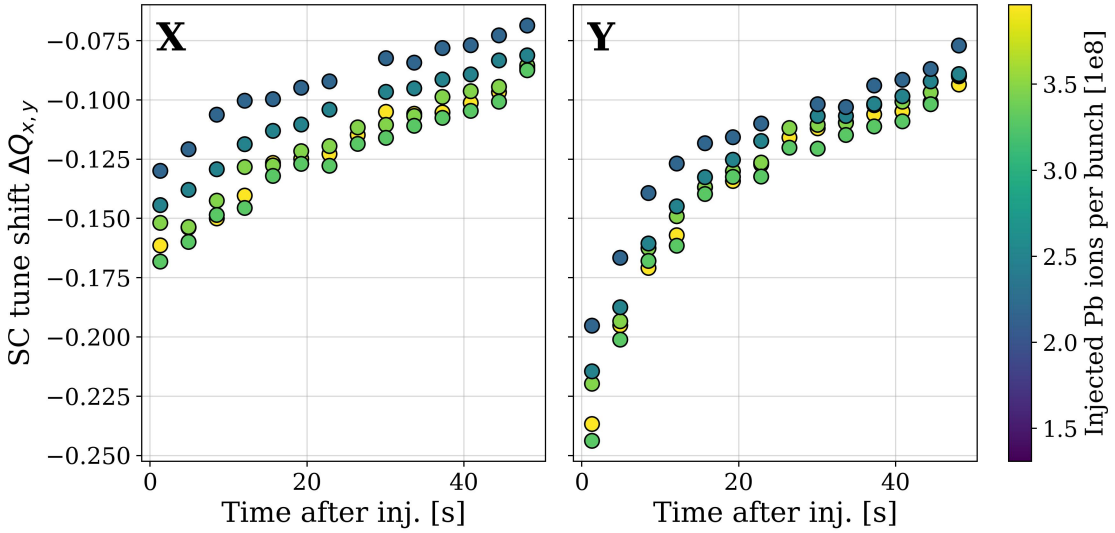


Figure 5.22: Calculated SC tune shift $\Delta Q_{x,y}$ evolution from Eq. (5.8) with input from the bunch intensity scan in Fig. 5.19 and 5.20. In particular, note the convergence in Y.

7-injection scheme over a 21.6-second-long FB (half the present FB length), highlighting the notable ion injector performance improvements achieved since.

The evolution of the SC tune shift $\Delta Q_{x,y}$ from Eq. (5.8) and brightness $\mathscr{B}$ from Eq. (5.9) during the SPS Pb FB are reconstructed in Fig. 5.22 and 5.23, using the bunch intensity from Fig. 5.19 and normalized emittances from Fig. 5.20. Both $\mathscr{B}$ and ΔQ_y (the plane with the highest tune shift) show converging trends, independent of injected bunch intensities.

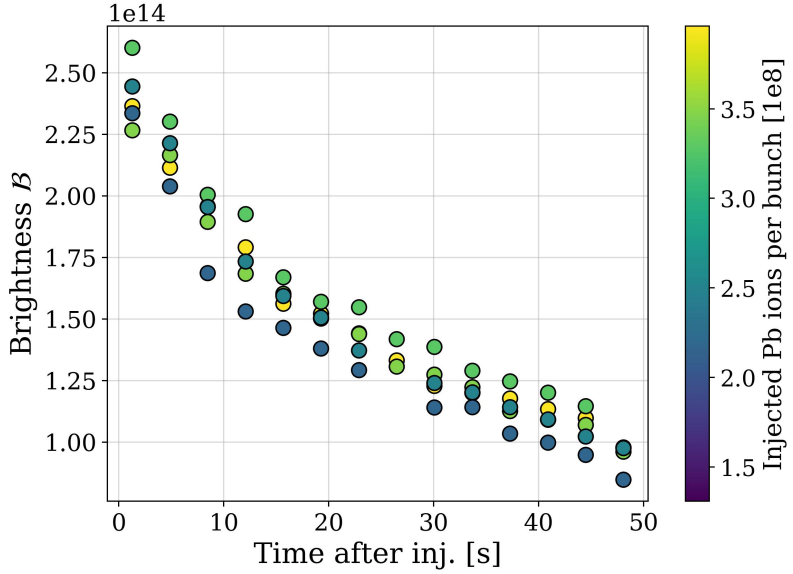


Figure 5.23: Calculated brightness $\mathscr{B}$ trend from Eq. (5.9) with input from Fig. 5.19 and 5.20.

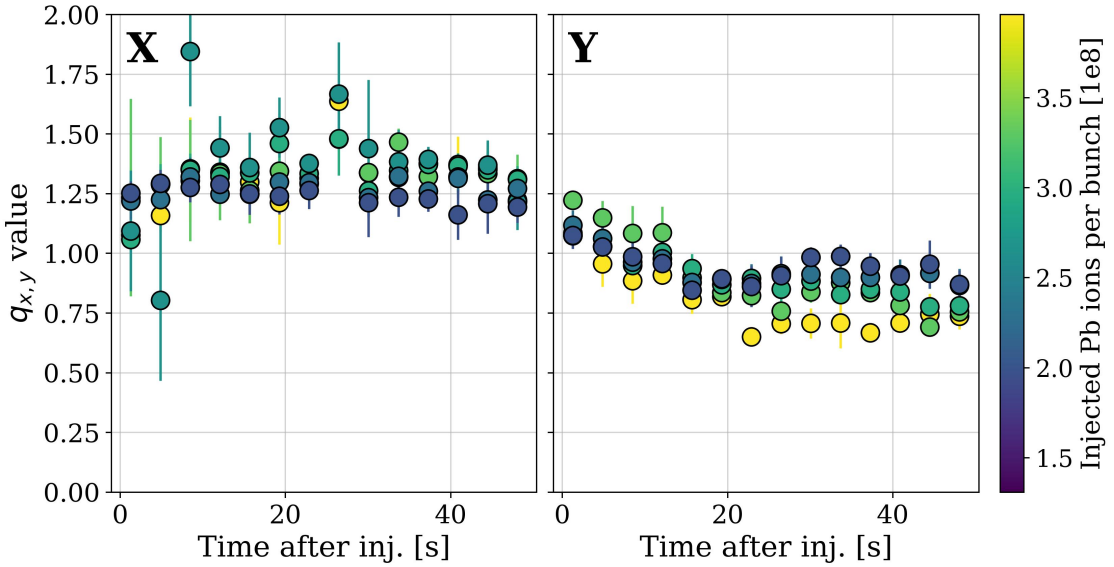


Figure 5.24: Fitted $q_{x,y}$ values from beam profiles during the bunch intensity scan in Fig. 5.19.

What about the evolution of transverse beam tails? Figure 5.24 shows the evolving $q_{x,y}$ value, from Eq. (5.74), during the cycle from Wire Scanner (WS) beam profile fits. For both planes at injection, the transverse beam profiles are relatively Gaussian (close to $q = 1$). During the flat bottom, the tails become *overpopulated* ($q > 1$) for all injected intensities in the horizontal plane. In the vertical plane, the tails become *underpopulated* ($q < 1$) during the cycle, more strongly with higher injected intensity. This may be correlated with the strong core ε_y^n blow-up in Fig. 5.20. Also the longitudinal Pb beam profile was measured with the SPS Wall Current Monitor (WCM), with an example shown in Fig. 5.25. To discard artificial ringing in the measurement caused by the limited bandwidth of the cables on the longitudinal pick-up, the profile is cut on the righthand side.

A SPS simulation campaign was undertaken with the set-up presented in Section 5.4, using the `fma_ions` and `xsuite` numerical toolkits. In each case, simulated starting beam parameters ($\varepsilon_{x,y}^n$, N_b, and σ_z) were adjusted as closely as possible to each corresponding measurement from the bunch intensity scan of Fig. 5.19. The injected profile is modeled as transversely Gaussian, but longitudinally modeled as q-Gaussian with $q = 0.72$, as measurements show in Fig 5.25, with an equivalent longitudinal frozen SC profile.

Three seconds of beam time (about 130 000 turns) were simulated with the gradual addition of various effects, as shown in Fig. 5.26. The results are displayed as normalized beam loss per second (the normalized slope from a linear fit). A few observations can be made. SC and IBS alone cannot explain the measured loss patterns, nor can their superposition with non-linear magnet errors (ME) and beta-beat. The addition of tune ripple to SC and IBS with only ME (pink squares) or only with beta-beat (green squares) increases the loss rates, but not sufficiently to explain the measurements — both ME and beta-beat are required. The $n \times 50$ Hz noise components appear to play a key role in reproducing measured losses. There is no single

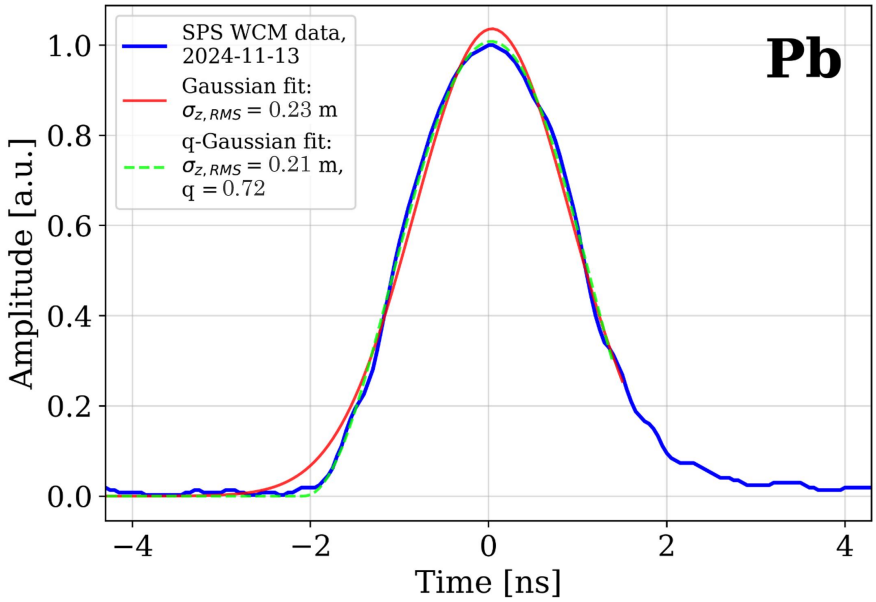


Figure 5.25: Example of measured Wall Current Monitor (WCM) signal of a longitudinal profile shortly after injection for SPS Pb beams, with Gaussian and q-Gaussian fit.

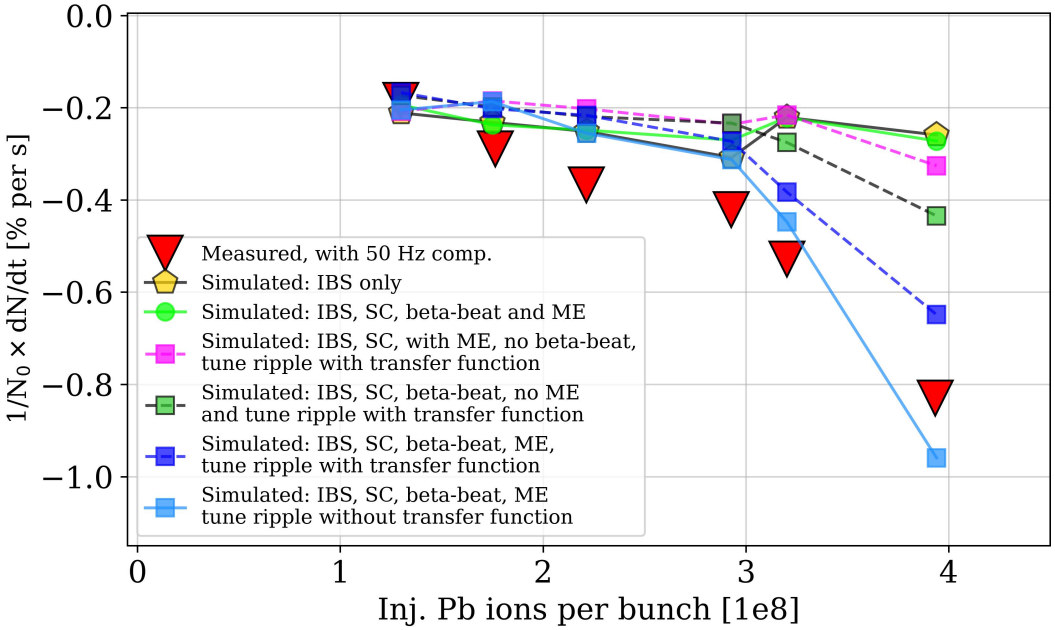


Figure 5.26: Measured and simulated SPS percentual change (effectively normalized beam loss per second) from the fitted linear normalized slope of curves in Fig. 5.19 (the first 3 seconds). The simulated effects are added gradually: IBS, adaptive SC, beta-beat, non-linear magnet errors (ME), tune ripple, and its transfer function $H(f)$.

loss driver that is capable of a full loss explanation, nor can the sum of each effect. Rather, the *interplay* of all these superimposed effects seems necessary to explain the measurements.

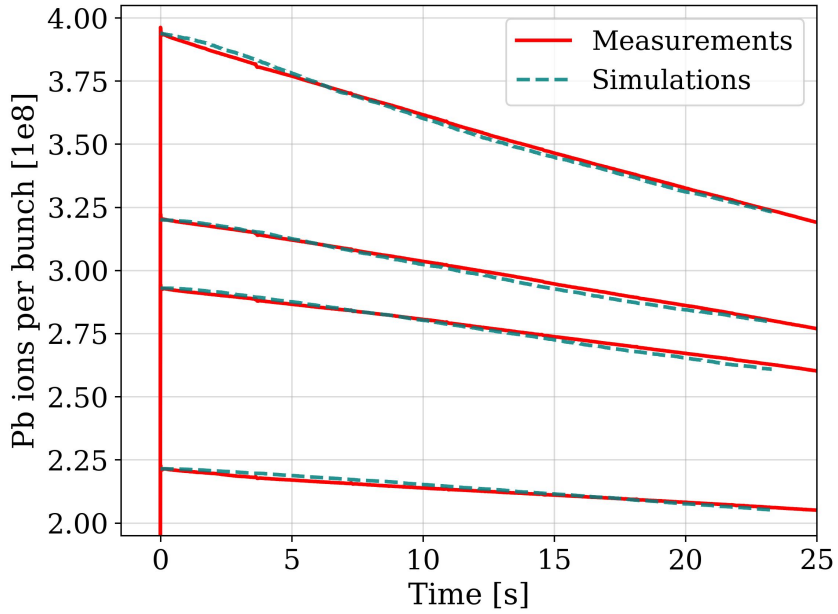


Figure 5.27: Extended 1M-turn simulation of the SPS Pb bunch intensity scan from Fig. 5.19: measurements and simulated “best" model: dark-blue squares from Fig. 5.26 with IBS, adaptive SC, beta-beat, non-linear magnet errors, and transfer function-corrected tune ripple.

Without transfer function $H(f)$ correction of the tune ripple, the simulated loss rate of all effects (light-blue squares) exceeds the measured value for the highest intensity. To confirm its validity, the “best" model at the time of writing (dark-blue squares) — with all effects and transfer function applied to the tune ripple — is simulated for an extended one million turn tracking simulation campaign to compare with the bunch intensity scan measurements. Each such simulation requires about 11 days of GPU cluster runtime. In Fig. 5.27, the simulations *closely follow the measurements* within less than a few percent, explaining a majority of the losses.

5.5.2 50 Hz noise amplitude scan

On Nov 13$^{\text{th}}$ 2024, the 50 Hz noise amplitude impact on SPS Pb beam transmission was experimentally investigated, as shown in Fig. 5.28. Starting from a stable 50 Hz compensation scheme, the 50 Hz noise frequency component was then *intentionally increased* in both the QF and QD main circuits using the capability of adding a voltage modulation at the power converter input. The bunch intensity was measured for various 50 Hz amplitudes (summed QD and QF) in the normalized FFTs.

The corresponding normalized emittance evolution was also measured, as shown in Fig. 5.29. Higher 50 Hz noise amplitudes increase the losses, but not linearly as in the bunch intensity

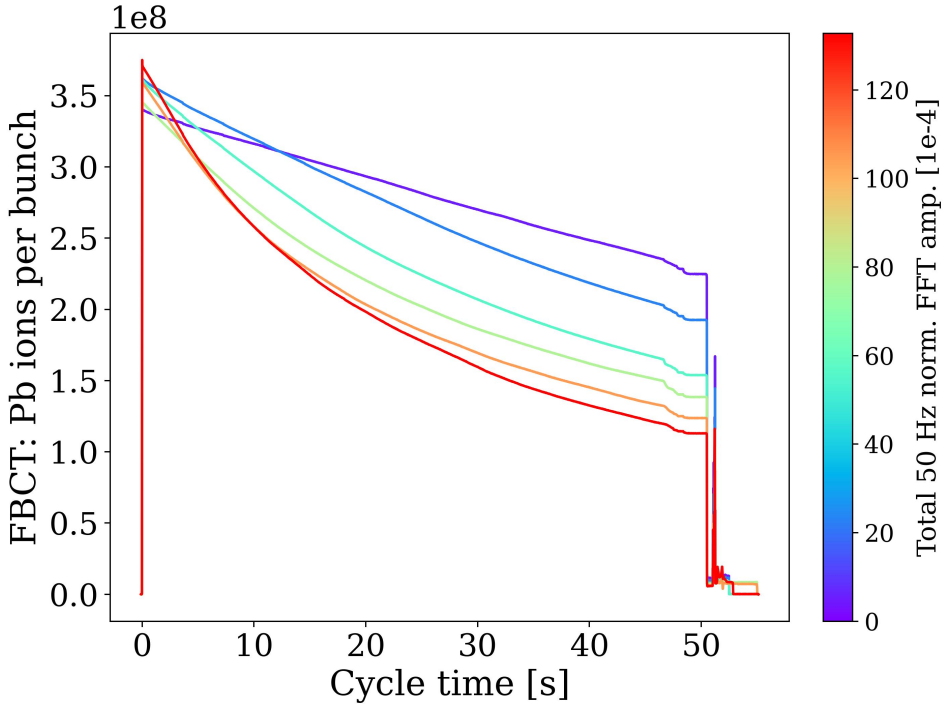


Figure 5.28: Bunch intensity evolution for various intentionally activated 50 Hz noise amplitudes (summed from normalized FFTs of the QD and QF main circuit currents).

scan in Fig. 5.19. Also, ε_y^n appears to blow up faster with higher noise amplitude. The tail evolution as a function of 50 Hz noise level is shown in Fig. 5.30. Similarly to the bunch intensity scan in Fig. 5.24, the evolving $q_{x,y}$ value increases in the horizontal plane (growing

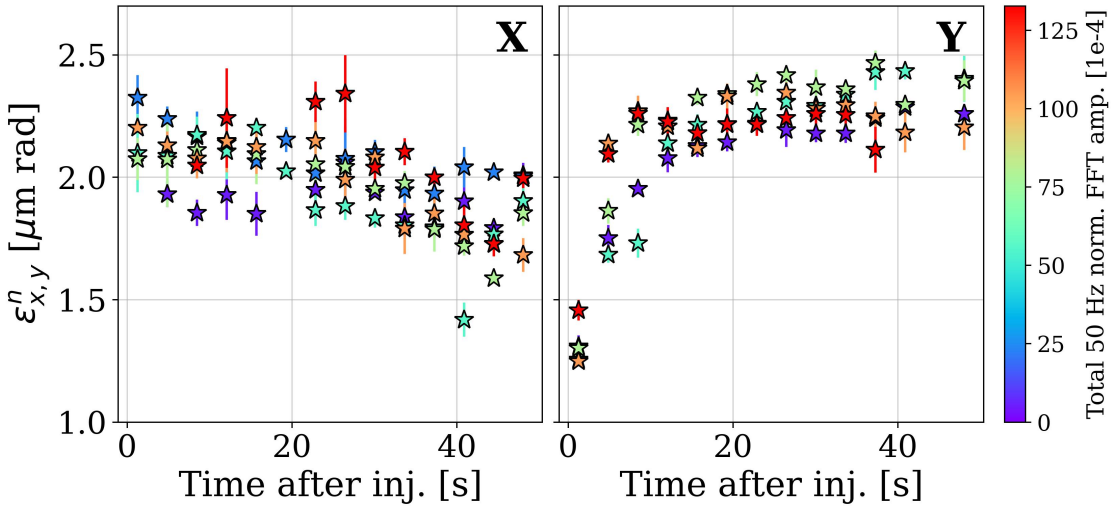


Figure 5.29: Normalized emittance evolution for various intentionally activated 50 Hz noise amplitudes. Note the fast ε_y^n blow-up (right) for the highest noise amplitude (red), before it flattens out. On the other hand, ε_y^n keeps growing for some intermediate noise levels (green).

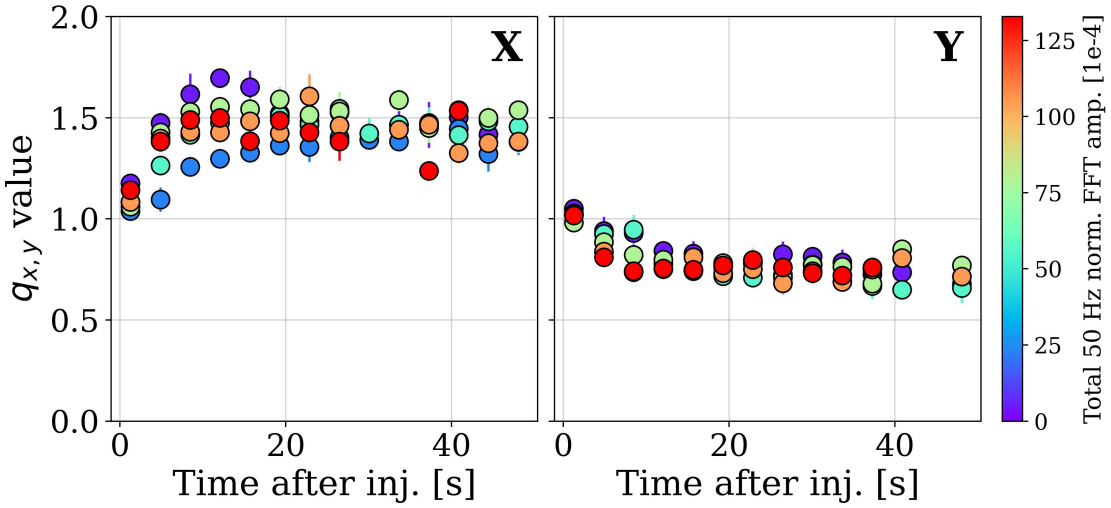


Figure 5.30: Measured $q_{x,y}$ values during the 50 Hz noise level scan in Fig. 5.28.

tails with respect to the core) and decreases in the vertical plane, hinting to the strong core blow-up in the latter. Unlike the bunch intensity scan, there is no clear q_y difference between the injected 50 Hz noise levels.

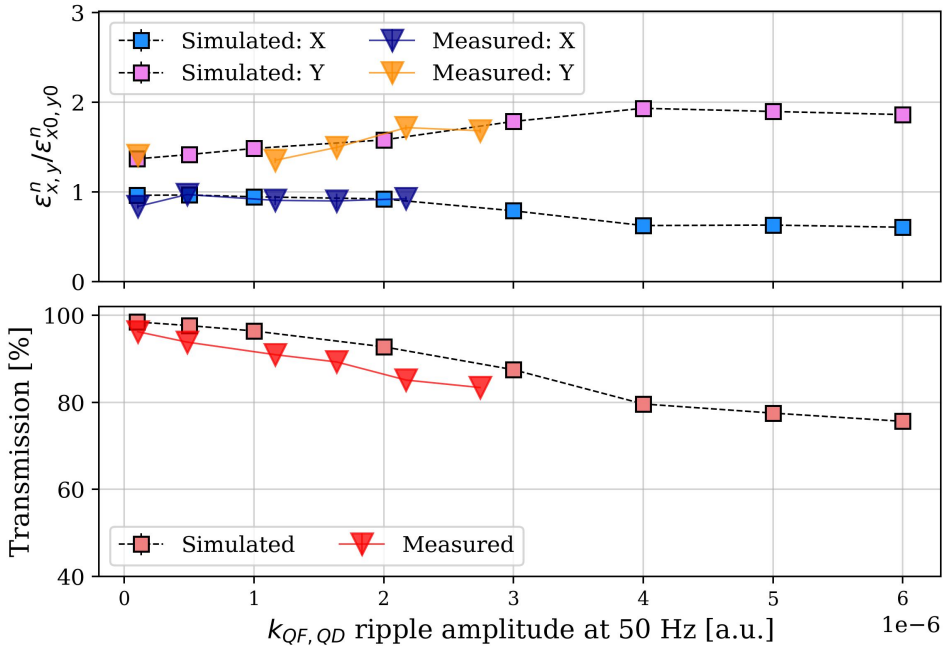


Figure 5.31: Measured and simulated relative normalized emittance growth and transmission after 4.6 s (200k turns in tracking) for various intentionally activated 50 Hz noise amplitudes (summed from QD and QF main circuits).

The 50 Hz noise amplitude scan measurements from Fig. 5.28 are simulated for 200 000 turns (4.6 s in the machine), a point in the cycle where also emittance measurements were made. The

"best" simulation model was used: adaptive SC, beta-beat, magnet errors, IBS, and tune ripple signals based on DCCT measurements, adjusted with the fitted transfer function. Figure 5.31 presents the simulation results compared to measurements. A higher 50 Hz noise amplitude leads to higher losses and larger ε_y^n growth. Although not all measured losses are explained, the simulation results *largely capture the trend* and *account for a majority of the measured losses.*

5.5.3 Transverse tune scans with short cycles

A shorter SPS Pb cycle with a 3-second-long injection plateau was set up on Nov 25$^{\text{th}}$ 2024 — with and without the 50 Hz compensation — to scan transverse tunes: 1) vertical tune Q_y, and 2) horizontal tune Q_x. These measurements were conducted to study the beam behavior during resonance crossings similar to previous space charge studies done in e.g. the PS [112, 120], and in SIS18 [118]. During each scan, the transverse tune in the other fixed plane is kept fixed at the setting with best transmission. The Q_y scan measurements with corresponding simulations are shown in Fig. 5.32.

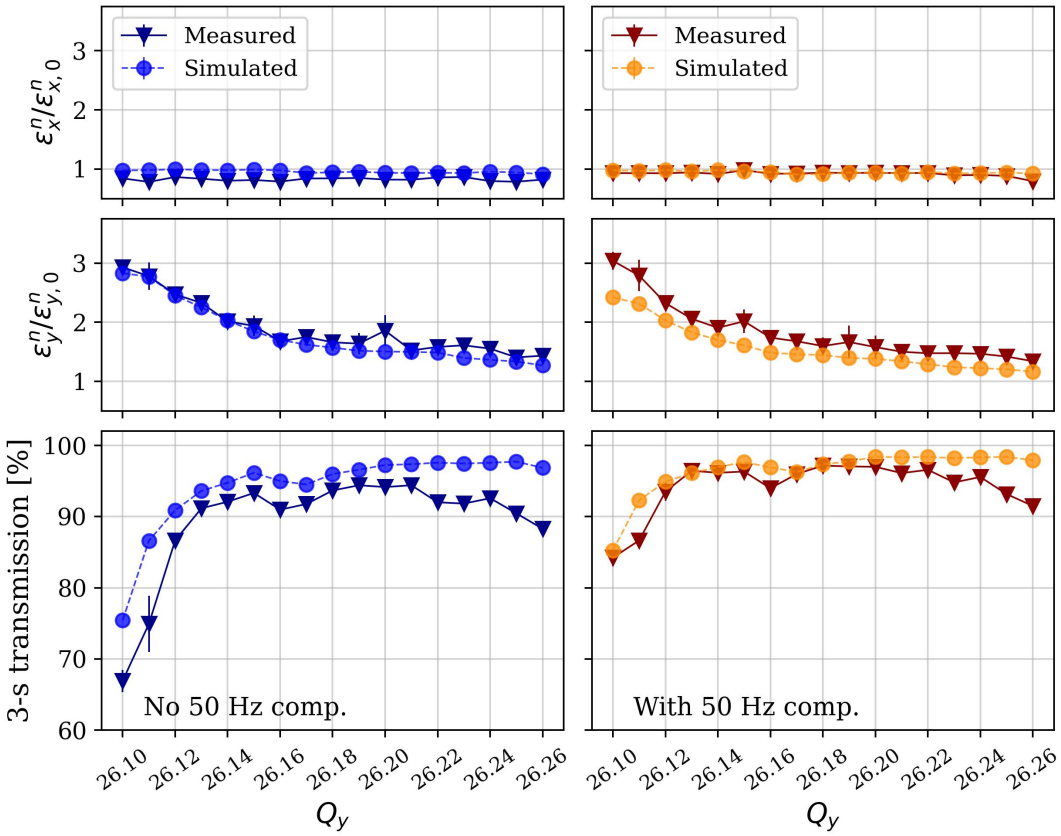


Figure 5.32: Measurements from Q_y scan (130k turns) with corresponding simulations, without 50 Hz compensation (left column) and with 50 Hz compensation (right column), at $Q_x = 26.31$.

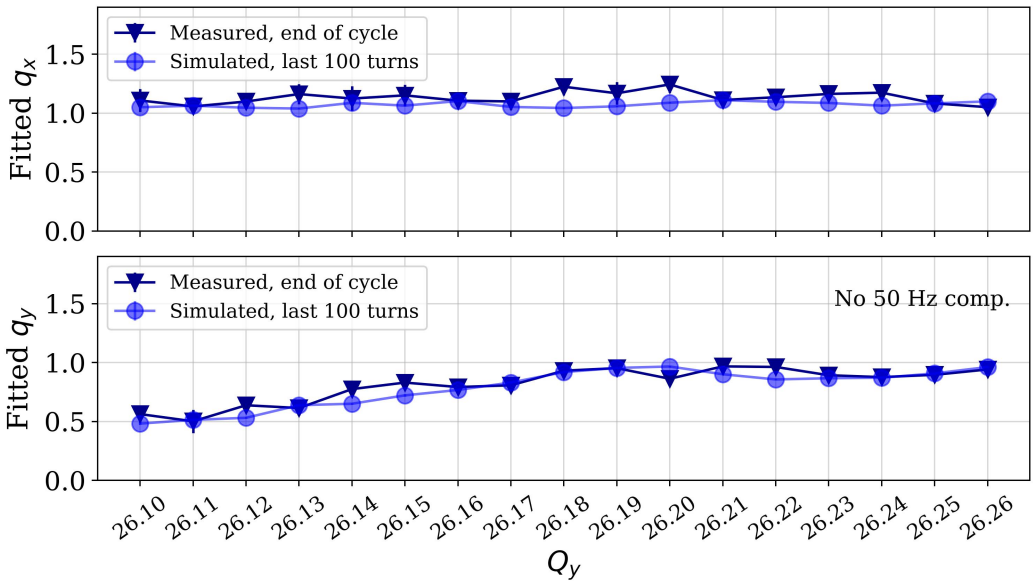


Figure 5.33: Fitted q-values from the Q_y scan *without 50 Hz comp.* from Fig. 5.32.

The simulation model captures the measured trend, explaining most measured losses (3-second transmission) and ε_y^n growth, both with and without the 50 Hz compensation. For $Q_y > 26.24$ values, the $Q_x - 2Q_y$ resonance may play a stronger role in the machine than in the simulations. Figure 5.33 shows the $q_{x,y}$, the final tail population, of fitted beam profiles — measured and simulated — at the horizontal wire scanner location. For lower Q_y, there is

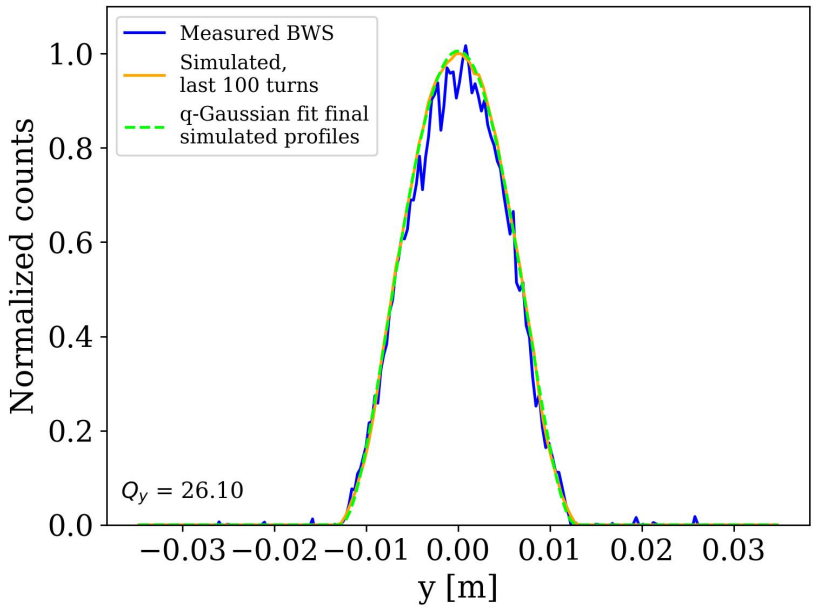


Figure 5.34: Measured and simulated final Y beam profile at `BWSRC.41677` for $Q_{x,y}$ =(26.31, 26.10) in Fig. 5.32, also with q-Gaussian fit, after 130k turns without 50 Hz compensation.

strong core blow-up and a convergence to more parabolic beam profiles (smaller tail populations compared to the core), something the simulations also capture well. For the working point $Q_{x,y}$ =(26.31, 26.10) with the strongest losses, one observes good agreement between measured and simulated beam profile without 50 Hz compensation, as illustrated in Fig. 5.34.

During the Q_x scan, the resonance $Q_x = 26.33$ was excited with an extraction sextupole (LSE) in addition to the natural nonlinear machine errors. The measured and simulated Q_x scan results (with and without the 50 Hz compensation) are shown in Fig. 5.35 and 5.36.

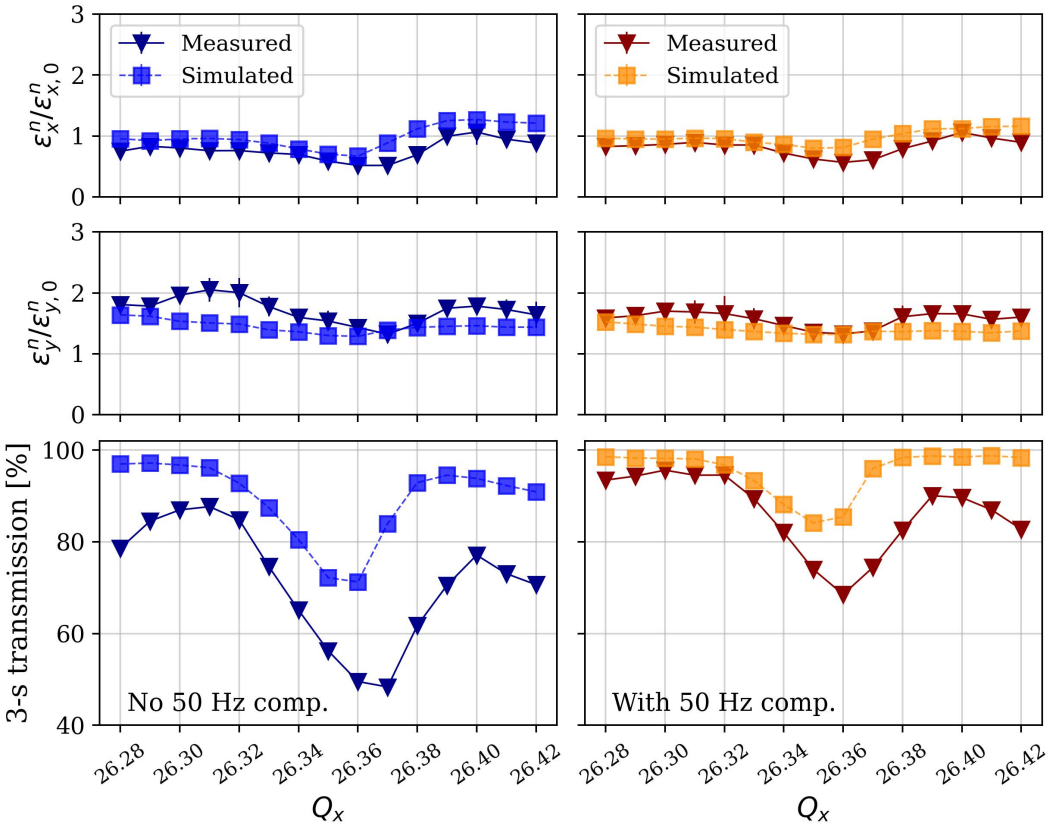


Figure 5.35: Q_x scan with excited LSE sextupole (with current `LSE.12402/I` = −3.0 A): without 50 Hz comp. (left column) and with 50 Hz comp. (right column), at $Q_y = 26.19$.

Although largely captured qualitatively, the simulations do not quantitatively explain the measured loss trend as well as the Q_y scan in Fig. 5.32. For example, at the highest loss point ($Q_x = 26.35, 26.36$), the simulation model explains around half of the measured losses. Note that the *two regimes* (loss followed by ε_x^n growth after $Q_x = 26.36$) discussed in Fig. 5.2 from Section 5.2 appear. Additional resonances not captured by the simulations seem to come into play, observed in the measured ε_y^n growth. For example, the simulations do not explain the measured ε_y^n growth (around $Q_x = 26.31$ and 26.40).

In Fig. 5.37, measured and simulated final beam profiles are compared at two Q_x values from the scan in Fig. 5.35: 1) at the strongest measured loss point $Q_x = 26.37$, and 2) $Q_x = 26.39$,

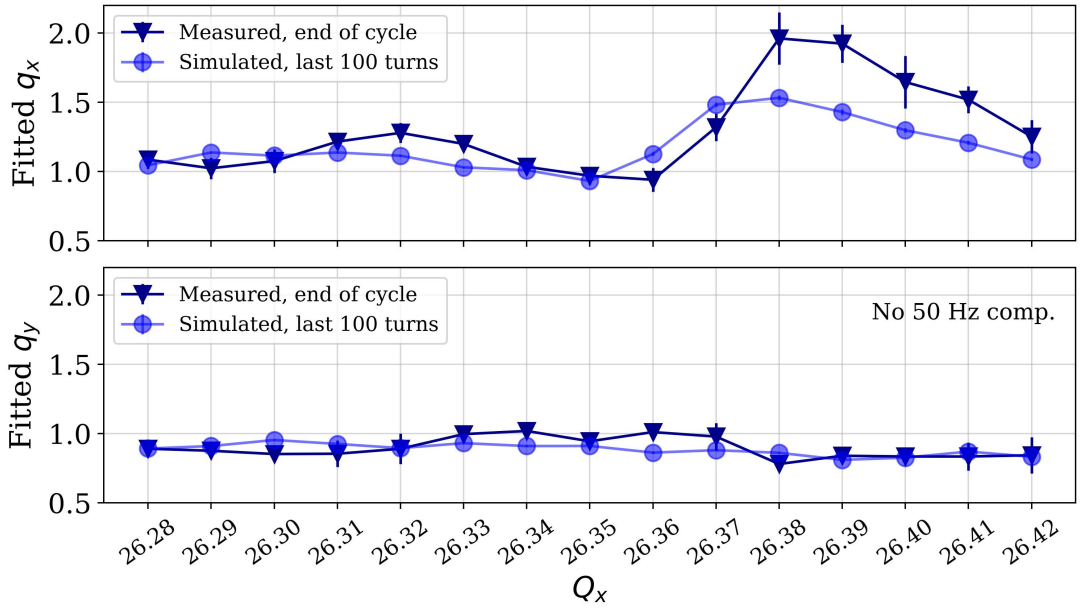


Figure 5.36: Fitted q-values from the Q_x scan *without 50 Hz comp.* from Fig. 5.35.

the tune with one of the strongest tail and core emittance blow-up. At $Q_x = 26.37$, despite a qualitative agreement in beam profile shape, simulations show stronger ε_x^n growth whereas the measurements instead show stronger losses. At $Q_x = 26.39$, the measured and simulated beam profiles agree well in shape, despite stronger measured losses and a marginally larger tail population; the measured profile shows $q_x = 1.9$ and the simulated $q_x = 1.5$ from Fig. 5.36.

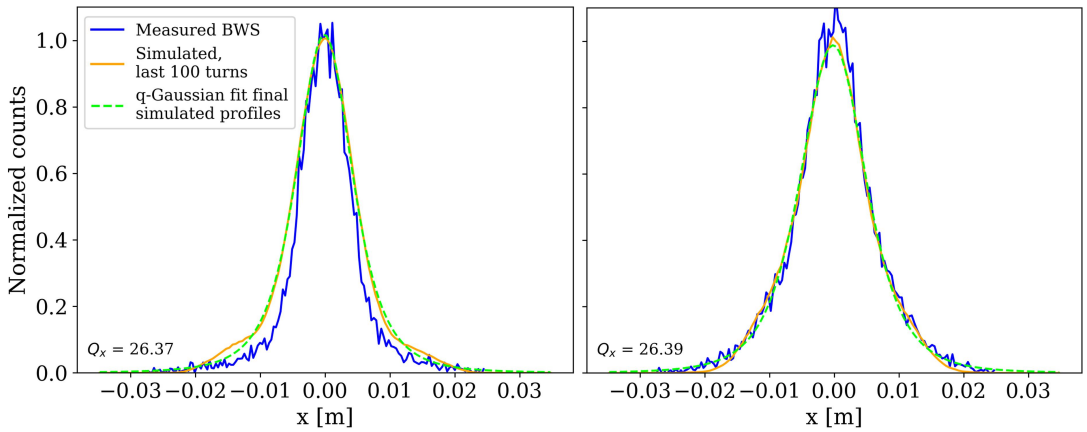


Figure 5.37: Measured and simulated final X beam profiles at `BWSRC.51637` for $Q_x = 26.37$ (strongest loss point) and $Q_x = 26.39$ (one of the strongest tail and core emittance blow-up points) in Fig. 5.35, after 130k turns with excited sextupole and without 50 Hz compensation. q-Gaussian fit is also shown. Here, Q_y =26.19.

For the Q_x scan, this loss-emittance discrepancy between measurements and simulations is qualitatively similar to previous horizontal resonance crossings studies in the SPS [147] and in

SIS18 [118]. In these measurements, the $Q_x - 2Q_y$ resonance may be stronger compared to the simulations, an effect further enhanced with the sextupolar excitation, whose strength both measurements and simulations proved very sensitive to. Additional tune scan measurements are encouraged in adjacent working point regimes — with and without resonance excitations — to map these losses in further detail. Also, future studies should focus on more refined lattice non-linearities and even more sophisticated tune ripple model. Overall, agreement between the simulations and measurements is observed from the $Q_{x,y}$ scan, except in the strongest loss regimes for the Q_x scan with sextupolar excitation.

5.5.4 Ripple frequency scan in simulations

The SPS Pb simulation model set-up is also used to address another question: *for a given amplitude, which ripple frequencies are the most important for SPS Pb beam losses?* Starting from the uncompensated 50 Hz ripple frequency amplitude, the “best" model with *one single ripple frequency per run* was simulated for 70 000 turns to study the beam loss sensitivity to ripple frequency. No ripple (0 Hz) was tested, followed by a range of frequencies from 10 to 3600 Hz, all cases with the same ripple amplitude as the measured uncompensated 50 Hz levels, shown in Fig. 5.38. *Here, the transfer function was not applied such that ripple frequencies could be studied equally.* To provoke faster losses, the strongest loss point $Q_x = 26.36$ with the excited sextupole from Fig. 5.35 was used. It should be noted that the result might change for other working points (due to the location of resonance sidebands in the tune working

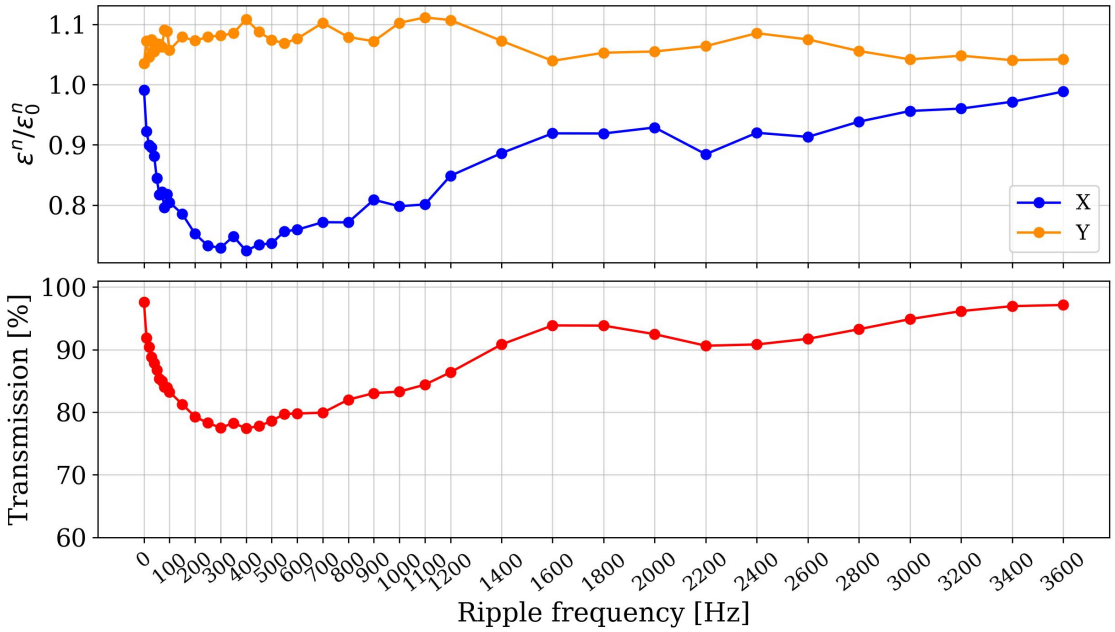


Figure 5.38: Simulated tune ripple frequency scan from 10 to 3600 Hz (with noise amplitude from the measured uncompensated 50 Hz noise level) at $Q_{x,y} = (26.36, 26.19)$, for 70k turns. The LSE sextupolar current was set to `LSE.12402/I` $= -3.0$ A to provoke faster losses.

diagram). However, studies at other working points are beyond the scope of this thesis and should be studied in the future.

Figure 5.38 shows how, for a given amplitude, transmission dips at around 300 Hz, before increasing again. An intermediate, less loss-prone, area around 1600 Hz is found. At 3600 Hz, losses are practically back to the zero-ripple case. Although the 50 Hz ripple component dominates in the current measurements, *other noise frequencies below 1200 Hz should not be underestimated, especially with lattice non-linearities.*

5.6 Oxygen beams in the SPS

5.6.1 Space charge limit and projections for oxygen

How will these space charge and IBS effects impact future ion species, such as oxygen? To first order, beam dynamics limitations from space charge (SC) effects are proportional to the tune shift ΔQ_u, calculated as an integral of the optics functions around the circumference of the ring. Here it is presented in a slightly rewritten form from Eq. (5.8):

$$\Delta Q_u = -\frac{r_0 \hat{\lambda}}{2\pi\gamma(\gamma^2-1)} \oint \frac{\beta_u(s)}{\sigma_u(s)\left(\sigma_x(s)+\sigma_y(s)\right)} \mathrm{d}s, \tag{5.94}$$

where $u \in \{x, y\}$, β_u is the betatron function, and σ_u the geometric beam size. $r_0 = (qe)^2 / (4\pi\epsilon_0 mc^2)$ is the classical particle radius, with q being the charge state, m the ion mass, e the elementary charge and ϵ_0 the vacuum permittivity. $\hat{\lambda}$ is the peak longitudinal line density from Eq. (5.6), N_b the bunch population and σ_z the rms bunch length. From this notion, the **space-charge limit** (SCL) for a given ion species is defined as *the bunch intensity at which space-charge forces become equivalent to those of the highest-intensity Pb beams achieved in 2024 with the corresponding transverse emittances.* This approach allows for easier direct comparison between ion species at equivalent space charge effects, which is particularly useful in LEIR and the SPS, which are believed to be limited by SC.

First, the limiting space-charge tune-shift $\Delta Q_{u,\mathrm{Pb}}$ in LEIR and the SPS is calculated from Eq. (5.94) and the operationally achieved Pb bunch intensity $N_{b,\mathrm{Pb}}$ during 2024, i.e. considering that both LEIR and the SPS were operated at the SCL. Equating this SC tune shift to the Eq. (5.94) for another species, the estimated maximum bunch intensity N_b is

$$N_b = \frac{-2\pi\sqrt{2\pi}\gamma(\gamma^2-1)\sigma_z \Delta Q_{u,\mathrm{Pb}}}{r_0 e \oint \frac{\beta_u(s)}{\sigma_u(s)(\sigma_x(s)+\sigma_y(s))}\mathrm{d}s}. \tag{5.95}$$

Second, to simplify this formula, some approximations are made: a) that the dispersive contribution to σ_u is small compared to the betatronic one, such that $\sigma_u \approx \sqrt{\epsilon_u \beta_u(s)}$, with ε_u being the geometric transverse emittance, and b) that the beams are round ($\varepsilon_x = \varepsilon_y$), and c) that the optics configurations do not change across the ion species, and d) that all ion

species have similar geometric emittances, Eq. (5.95) simplifies into a new expression for the SC-limited bunch intensity of the new ion species compared to Pb

$$N_b \approx N_{b,\mathrm{Pb}} \frac{q_{\mathrm{Pb}}^2 m \gamma(\gamma^2-1)}{q^2 m_{\mathrm{Pb}} \gamma_{\mathrm{Pb}} (\gamma_{\mathrm{Pb}}^2-1)}. \tag{5.96}$$

Does this SCL play a role in observed loss patterns, simulated and measured? First, with the best available SPS ion FB tracking simulation model at the time of writing, the oxygen beam performance is simulated to study these beam-degrading effects. At SPS injection, the relativistic Lorentz factor $\gamma_{\mathrm{Pb}} = 7.31$ and projected for oxygen to be $\gamma_{\mathrm{O}} = 7.08$ — relatively similar energies. Before running any simulations, the theoretical notions from Section 5.2 are revisited to understand how the SC and IBS effects scale for a given optics, normalized emittances and beam energies:

- The **SC tune shift** from Eq. (5.8) scales as $\Delta Q_{x,y} \propto r_0 \propto q^2/m$
- The **IBS growth rates** $1/\tau_i$ from Eq. (5.22) and (5.23) scale as $1/\tau_i \propto A \propto r_0^2 \propto q^4/m^2$

IBS scales much faster with charge compared to SC, and *one should expect a much smaller relative IBS impact on oxygen compared to lead.* To quantitatively test this statement, the "best" SPS FB tracking simulation set-up for Pb beams from the bunch intensity scan in Fig. 5.26 is used: beta-beat, non-linear magnet errors, adaptive SC, and transfer function-corrected tune ripple, with 50 Hz compensation. The oxygen bunch intensities (keeping the normalized $\varepsilon_{x,y}^n$ identical to Pb, unlike the identical geometric emittances considered for the Injector Model later in Chapter 6) are adjusted to achieve *similar SC tune shifts as Pb:* $\Delta Q_{x,y,\,\mathrm{Pb}} \approx -(0.15, 0.25)$. For both O and Pb, simulations with and without IBS are tested.

The results from these simulations are found in Fig. 5.39, plotted over Pb-equivalent bunch intensity using Eq. (5.96) inversely for easier comparison. The dashed red line marks the space charge limit for oxygen at $N_b = 28 \times 10^8$ ions per bunch, where the space charge tune shifts $\Delta Q_{x,y}$ is equivalent to the ones of the highest SPS Pb intensities achieved in 2024.

Without IBS (triangles), the loss rate evolution shape is relatively similar between Pb and O, as expected for similar input $\Delta Q_{x,y}$ values. For the oxygen case, *adding IBS increases the loss rate only marginally* , visible only at the highest intensity. In comparison, adding IBS *shifts the whole Pb loss rate curve down uniformly*, mostly due to losses out of the RF bucket. At the highest injected intensity, adding IBS increases the loss rate threefold for Pb, but only about 40% for oxygen. Relatively speaking, the IBS contribution to the combined effect of magnet errors, space charge and tune ripple appears much larger for Pb than for O beams.

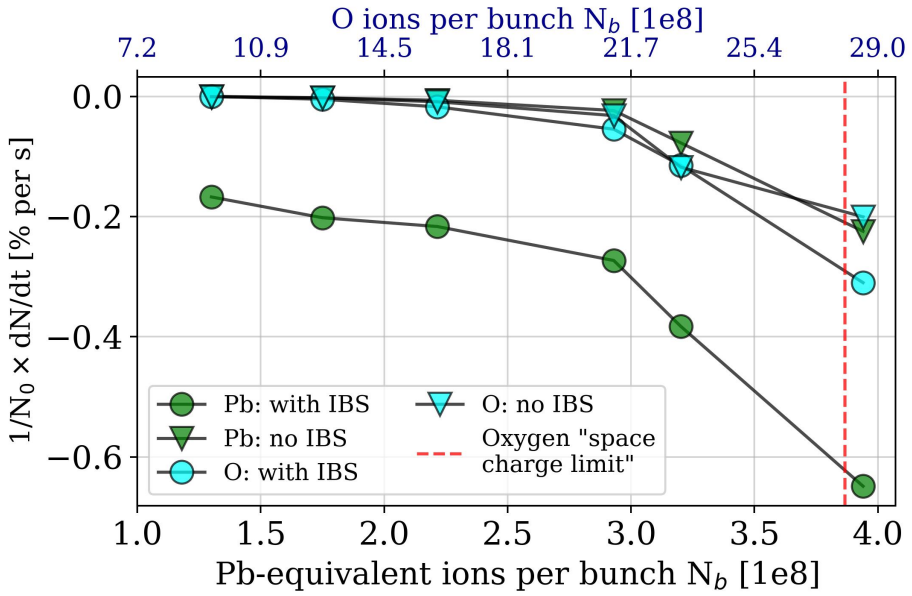


Figure 5.39: Simulated SPS intensity scan comparisons between O and Pb beams, using a set-up similar to Fig. 5.26. In the scan, $\epsilon^n_{x,y}$ and $\Delta Q_{x,y}$ are set identical at injection for Pb and O, by adjusting the O bunch intensity. The plot shows the percentual rate of change $1/N_0 \times dN/dt$ (effectively normalized beam loss per second) from linear fits of the first 130k turns for Pb and O beam, expressed in the Pb-equivalent bunch intensity in ions per bunch for easier comparisons. The O bunch intensities are converted to their Pb-equivalent using Eq. (5.96) inversely: $N_{b,\,\text{Pb-equiv.}} \approx N_{b,\text{O}} \times [q^2_\text{O} m_\text{Pb} \gamma_\text{Pb}(\gamma^2_\text{Pb} - 1)]/[q^2_\text{Pb} m_\text{O} \gamma_\text{O}(\gamma^2_\text{O} - 1)]$. All cases represent the "best" model with magnet errors, beta-beat, adaptive SC, and tune ripple with transfer function (with 50 Hz compensation), but with IBS switched on and off. The space charge limit for O (at $N_b = 28 \times 10^8$ ions per bunch) is also marked, the point at which the maximum space charge tune shift is equivalent to operational SPS Pb beams.

5.6.2 Simulation benchmarking against preliminary oxygen measurements

Measurements from the single-bunch O^{8+} pilot beam commissioning in early July 2025 [13] have allowed preliminary comparisons with the SPS FB tracking simulation model described in Section 5.4, now used for O beams. It should be noted that the production scheme for O used in this test run differs from the one of Pb beams used in routine operations. For example, LEIR captures two bunches in $h = 2$ but transfers only one bunch to the PS, where no bunch splitting occurs. Despite the short two-week time frame allowed to prepare and optimize these beams, such measurements can provide first insights into whether the model scales as expected.

In a parametric scan on July 3$^{\text{rd}}$ 2025, the injected SPS bunch intensity was varied in the most stable configuration possible, with 50 Hz noise compensation. As only one Linac3 injection was possible for O ions (compared to eight for Pb), the LEIR intensity was varied by adjusting the slit just after the source, before the radio-frequency quadrupole (RFQ), to decrease the Linac3 pulse length. A typical Wall Current Monitor measurement from this scan shows the

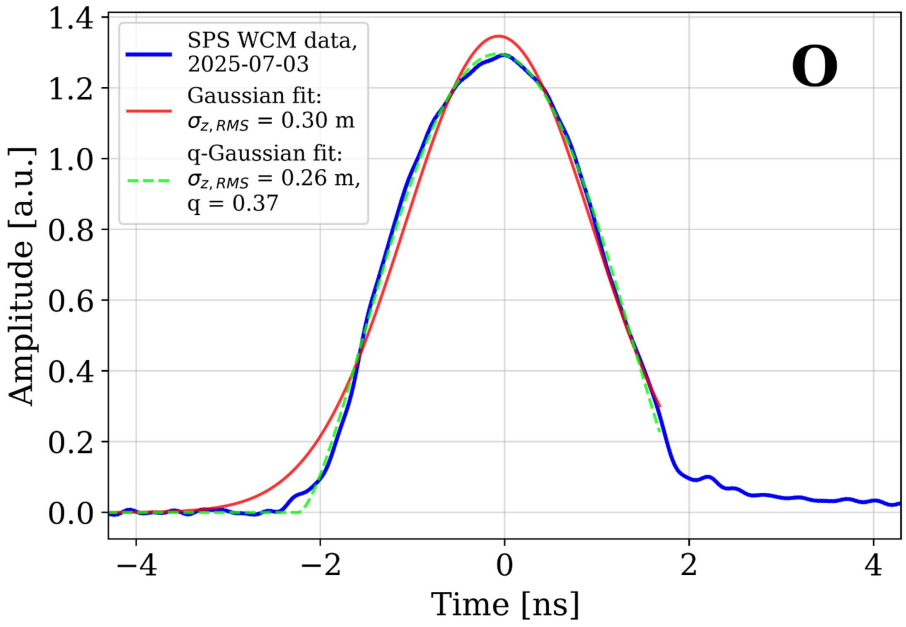


Figure 5.40: Example of measured Wall Current Monitor (WCM) signal of longitudinal profile shortly after injection of O beams in the SPS, with Gaussian and q-Gaussian fit.

longitudinal profile in Fig. 5.40. Figure 5.41 shows the measured FBCT bunch intensity (the first injected bunch) and corresponding simulations, with measured O input parameters. During this scan, the working point was set to $Q_{x,y} = (26.31, 26.25)$, where minimal emittance growth was observed. During this intensity scan, normalized emittances $\varepsilon^n_{x,y}$ and q-values were extracted from wire scanner profiles, as shown in Fig. 5.42. Comparing to the corresponding highest-intensity Pb beam from Fig 5.20 and 5.24, the highest-intensity O beam features:

- **Round beams**: $\varepsilon^n_{x,y} \approx 1.3$ mm mrad in both planes for O beams, unlike Pb beams from late 2024 for which $\varepsilon^n_x \approx 2.1$ mm mrad and $\varepsilon^n_x \approx 1.1$ mm mrad at injection.
- **Higher horizontal tail population**: at injection, O beams are approximately Gaussian ($q = 1$) in the vertical plane but have large horizontal tail populations with $q_O \approx 1.4$. On the other hand, Pb beams can largely be considered transversely Gaussian at injection.
- **Longer bunches**: compared to Pb beams in Fig. 5.25, the O beams are *longer* ($\sigma_{z,\,\mathrm{RMS}} =$ 0.26 m versus 0.21 m) and are *more binomial* (smaller q-values): $q = 0.37$ versus 0.72.

The measured and simulated 10-second O beam transmission during flat bottom from the intensity scan (from Fig. 5.41) are compared in Fig. 5.43. The intensity scan was done at the working point $Q_{x,y} = (26.31, 26.25)$ that was chosen for the LHC pilot run. The simulated O results has systematically 5-6% less losses compared to the measured transmission. It should be noted that at these tunes, the transmission was lower than at the working point with the best transmission, $Q_{x,y} = (26.31, 26.19)$, used for Pb beams. The 10-second SPS Pb beam

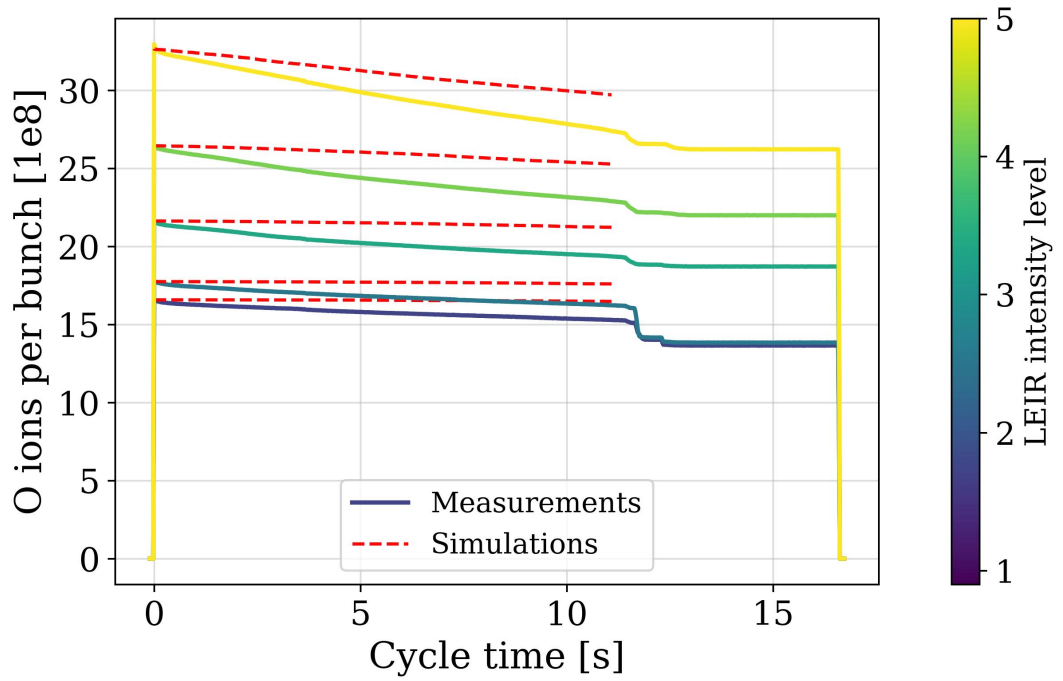


Figure 5.41: FBCT measurements from the SPS O bunch intensity scan from July 3rd 2025, with $Q_{x,y} = (26.31, 26.25)$. Simulations represent the simulated "best" model: with IBS, adaptive SC, beta-beat, non-linear magnet errors, and transfer function-corrected tune ripple.

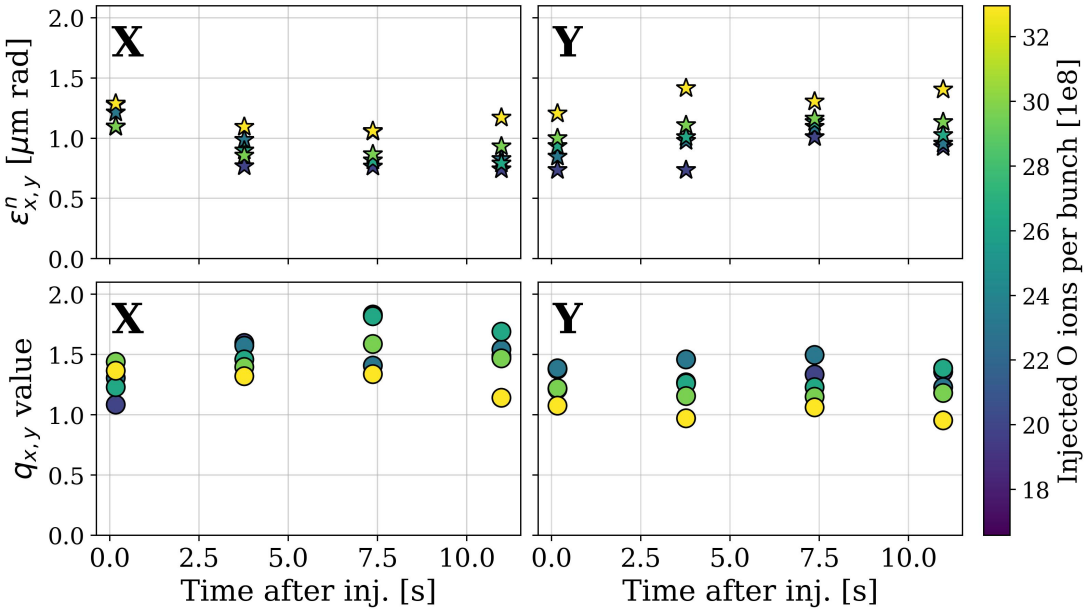


Figure 5.42: Measured normalized emittances $\varepsilon^n_{x,y}$ and fitted q-values from wire scanner profiles during the SPS O bunch intensity scan from Fig 5.41.

transmission for this vertical tune $Q_y = 26.19$ from Fig. 5.41 and one corresponding O beam transmission (simulated and measured) at this tune are shown in Fig. 5.44.

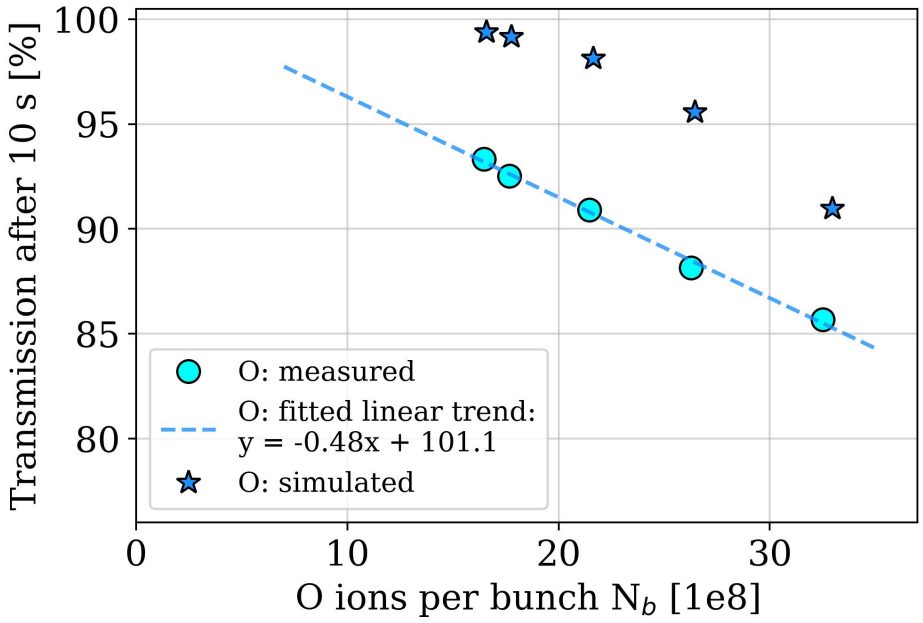


Figure 5.43: 10-second transmission from measured and simulated SPS O intensity scans from Fig. 5.41, for the working point $Q_{x,y} = (26.31, 26.25)$ used by the LHC pilot beams.

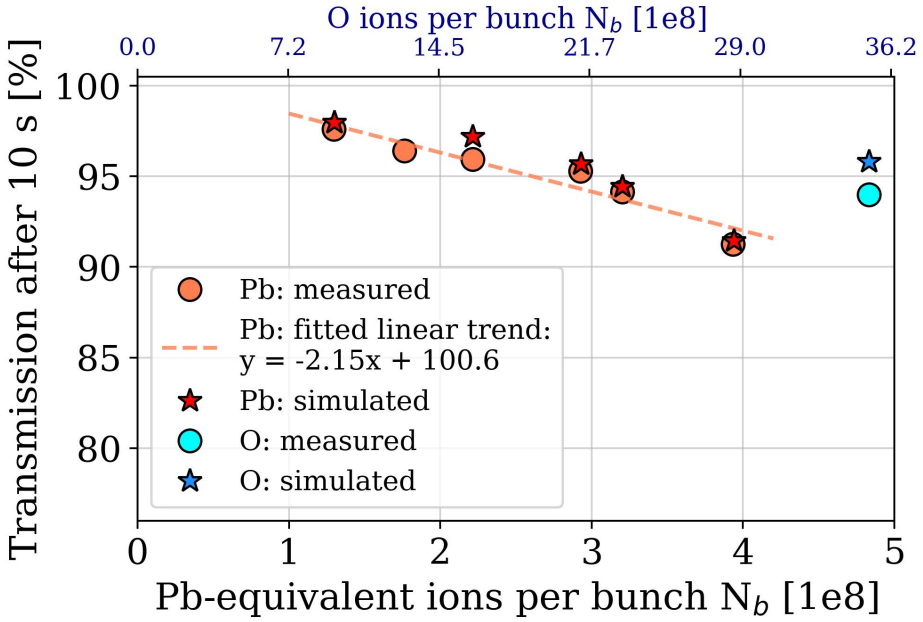


Figure 5.44: 10-second transmission from measured and simulated SPS Pb intensity scans from Fig. 5.19, for the working point $Q_{x,y} = (26.31, 26.19)$ that is optimized for transmission. Measured and simulated 10-s O beam transmission for this working point is also shown, also expressed in its Pb-equivalent bunch intensity, as obtained by inversely applying Eq. (5.96).

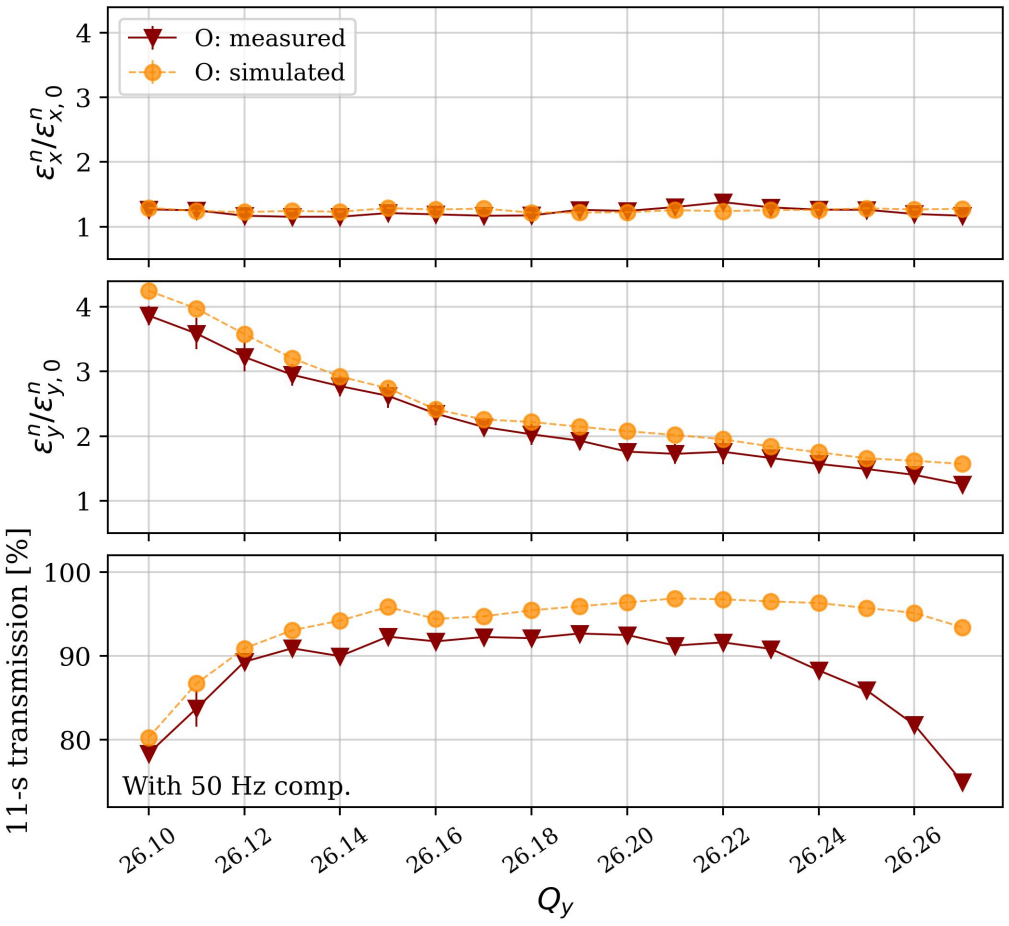


Figure 5.45: Measured FBCT transmission and emittance growth of the first injected O bunch during the Q_y scan (after 11.0 s) with corresponding simulations (476k simulated turns). The 50 Hz compensation was active, and $Q_x = 26.31$.

In addition, from this observed transmission sensitivity to tune, a parametric vertical tune scan was performed for the SPS O beams in the interval $Q_y = [26.10, 26.27]$, as shown in Fig. 5.45. This set-up was similar to the Pb case in Fig. 5.32. The 50 Hz noise compensation was active, but was somewhat less stable than for the Pb case. The normalized FFT amplitude at 50 Hz in both QD and QF circuits was not always possible to be kept below 5×10^{-4}, but sometimes fluctuated to 8×10^{-4}. Despite a stronger vertical emittance growth, the working point $Q_{x,y} = (26.31, 26.19)$ appears better from a transmission point of view — measured 94% compared to 90% for $Q_y = 26.25$ used for the intensity scan — just like for the Pb beams. Note that the model does not reproduce the significant increase of losses for tunes approaching $Q_y = 26.25$. The reason for this could be that the model is missing some resonance excitation caused by magnet imperfections (space charge induced resonances are already included in the model). Future studies with multipolar correctors could aim at compensating such resonances to enable a higher beam brightness with good beam transmission.

Some additional O beam differences from the Pb beam measurements are worth listing for even further refinement of the SPS flat-bottom ion simulation model:

- **Larger longitudinal emittance**: although the simulation model includes the longitudinal WCM profiles from Fig. 5.40, losses out of the RF bucket may not be fully captured by the model as well as for the shorter Pb bunches.
- **Larger tails**: space charge and IBS models used in the simulation models assume transverse Gaussian bean profiles, which for O beams is not true in the horizontal plane.
- **Ripple amplitude**: the SPS quadrupolar circuit currents $I_{\mathrm{QD,\,QF}}$ were typically different for O beams (typically around 50 A) compared to the corresponding currents used for Pb beams (around 70 A). The tune ripple model framework is built on the Pb reference case discussed in Section 5.3, and would require further adjustment to exactly represent the O case with correct tune ripple amplitudes.
- **Effective aperture**: if the O beam orbit was not corrected as well as for Pb beams, the effective aperture model — explained in Section 5.4 to account for misaligned mechanical aperture elements — would likely need some readjustment.

5.7 Achievements in SPS Pb ion operation

Here, some contributions of this thesis work to the operational improvements of Pb ion beams up until (and including) the SPS are briefly highlighted. Optimizations along the whole injector chain culminated in record-breaking bunch intensities in November 2024 and resulted in unprecedented average daily integrated LHC ion luminosity values [164, 165]. Some of the notable ion injector performance improvements (compared to 2023) were highlighted in Ref. [166] and include:

- Changing the Linac3 pulse duration from 200 to 300 μs, effectively increasing the number of injected charges by 50% (with the caveat of faster Linac3 stripper foil aging)
- The outgoing Linac3 Pb current was improved from 30 uA to 32 uA
- LEIR parameter optimization of kicker magnets, bumpers and orbit clean-up
- Increasing the number of LEIR pulses from seven in 2023 to eight in 2024
- Improving the LEIR-PS transmission from 88% in 2023 to above 95% in 2024, thanks to better transfer line steering.
- 50 Hz noise compensation scheme for SPS Pb ions, described in Section 5.1

Once a steady 50 Hz noise compensation on the quadrupole power converters was established, a systematic transverse tune (Q_x, Q_y) optimization campaign was performed for the SPS Pb

FB, as shown in Fig. 5.46. Fast wire scanner measurements of the normalized emittances $\epsilon^n_{x,y}$ were done at injection (25 ms) and at the end of the FB (47375 ms). The bunch-by-bunch intensity was measured with the fast BCT (FBCT). Balancing emittance blow-up and loss minimization, the ideal working point was established as $Q_{x,y} = (26.31, 26.19)$, with SC tune shifts $\Delta Q^{\text{inj}}_{x,y} \approx (-0.15, -0.25)$ as computed from Eq. (5.8). This initial tune optimization done in this thesis work combined with the listed ion injector improvements resulted in more than 130×10^{10} total extracted Pb charges per cycle, **more than 40% higher** than the LHC Injector Upgrade (LIU) ion project objectives [18].

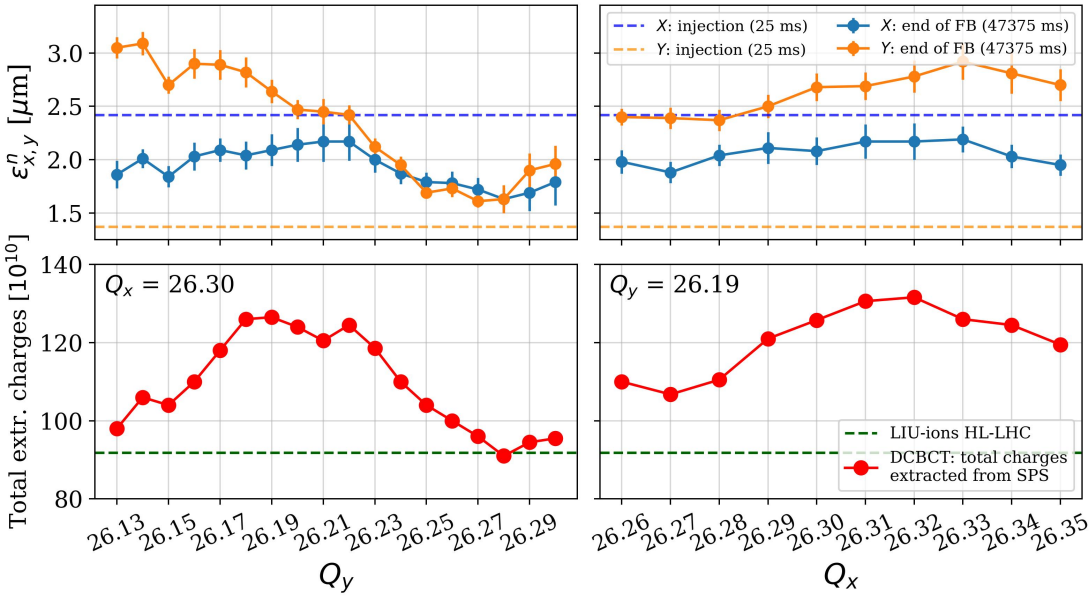


Figure 5.46: Tune scan of Q_y (left) and Q_x (right) for the nominal 14-injection SPS Pb ion cycle.

5.8 Conclusions

This chapter presented SPS ion study results from measurements and simulation benchmarking efforts. The main points and key contributions in this thesis work include:

- The 50 Hz noise compensation scheme and working point optimization — combined with other ion injector chain improvements — allowed extraction of **record-breaking Pb intensities from the SPS**, more than 40% above LIU ion targets.
- The **tune ripple** in the measured SPS main quadrupolar circuits was **spectrally characterized**. Additional current and beam ripple data from 2018 — together with electrical circuit models inspired from a 1994 SPS power converter study — allowed a **semi-empirical transfer function** $H(f)$ to be constructed, allowing 2024 current measurements to be translated to actual beam tune ripple for the simulations.
- An SPS Pb flat-bottom **tracking model** was developed with relevant effects: magnet

errors, beta-beat, adaptive frozen SC, kinetic IBS kicks, and tune ripple with the transfer function $H(f)$. This model was condensed into the open-access Python package `fma_ions`. In parallel, numerical contributions to the `xfields` and `xpart` packages include frozen space charge symplecticity, SC potentials for q-Gaussian longitudinal profiles, IBS kinetic kick validation, and GPU speed-up.

- Measurements from **parametric scans** mapped SPS Pb ion beam behavior over intentional 50 Hz noise amplitude levels, injected bunch intensities, and transverse tunes — results used for benchmarking the SPS Pb FB simulation model. The complete simulation model could **largely capture the trends** and **explain the majority of losses** from the experimental scans. The $n \times 50$ Hz harmonics play a major role, where the total interplay with SC and IBS is required to explain the beam degradation.

- The model was used for **SPS oxygen beam projections**, and confirmed the analytical hypothesis that for similar SC effect levels, the relative IBS impact is much larger for Pb beams than for O. A preliminary oxygen bunch intensity scan demonstrated a linear transmission degradation with higher injected intensity, which however was done at the suboptimal transmission tune working point used by the LHC pilot beams. A subsequent vertical tune scan confirmed that $Q_y = 26.19$ enabled maximal transmission, just like the Pb beams. However, the O beam measurements showed larger loss rates and higher resonance sensitivity than what the simulation model could explain, which calls for further studies. Non-Gaussian transverse and large longitudinal O beam profiles at injection could play a role in this discrepancy, but additional studies need to confirm this cause.

- Future space charge and IBS models — which presently assume Gaussian transverse profiles — should investigate sensitivity to under- or overpopulated tails with $q \neq 1$. Also, more refined lattice non-linearities and particular resonances should be targeted in further detail, where model accuracy plays an important role. Even more detailed tune ripple models with additional harmonics (not only 50, 150, 300 and 600 Hz) should also be tested.

- A future SPS noise compensation scheme should aim for higher reliability and target not only 50 Hz but also the other harmonics — notably 150, 300, and 600 Hz — to further improve ion beam transmission.

6 The Injector Model and future LHC ion luminosity production

This final chapter addresses the main question:

- *Which ion species and beam production schemes maximize the integrated LHC ion nucleon-nucleon luminosity production?*

The results documented in this chapter are also a part of this publication [167].

6.1 Injector Model description

One of the main contributions of this thesis work is the development of the **Injector Model**. The objective is to realistically propagate bunch intensities through the injectors to LHC injection for any ion species, used as input for LHC ion luminosity production simulations. Starting from the nominal Pb beam production in the ion injector chain described in Chapter 2, other production schemes and ion species can also be explored. Chapter 4 showed that beam-gas interactions can limit the transmission of some partially stripped ions in the PS. Chapter 5 showed that a combination of space charge (SC), tune modulations due to power converter ripples, and intra-beam scattering (IBS) effects contribute to the ion beam intensity limitations in the SPS, which to some extent also limit LEIR. This section describes the Injector model structure and how various effects are taken into account.

The Injector Model is accessible through a publicly accessible Python package [168]. The program propagates ion beam parameters through each accelerator across the CERN ion injector chain: Linac3, LEIR, the PS and the SPS. The flowchart of this algorithm is schematically illustrated in Fig. 6.1. For a given ion species, the model propagates the bunch intensity in each machine, computing the maximum achievable injected intensity in each machine. Various factors are considered, including:

- **Future ion species parameters** and their **source/Linac3** performance were already presented in Table 2.1. To fill LEIR, up to 8 possible injections from Linac3 are considered

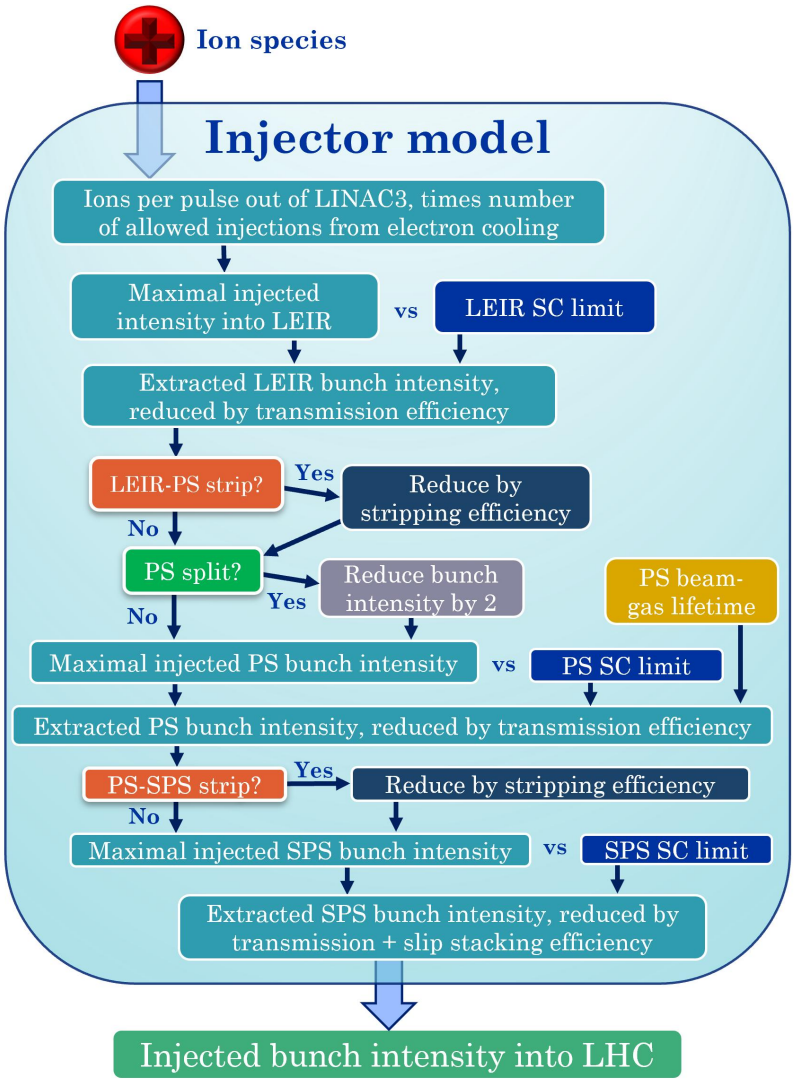


Figure 6.1: Flowchart of the Injector Model.

with a 300 μs pulse length, as achieved for Pb in 2024.

- **Transmission**, injection inefficiencies, magnet field limitations, and other loss sources based on experimental Pb values from 2024, as summarized in Table 6.1.
- The **LEIR electron cooling** performance was already discussed in Chapter 3. This effect limits the number of Linac3 pulses into LEIR for future ion species and new charge states according to Table 3.2.
- **Beam-gas interactions** are expected to limit the PS transmission for some lighter ion species, as discussed in Chapter 4.
- A **space charge limit** in LEIR and the SPS from Eq. (5.96), already discussed in Sec. 5.6.1, sets an additional assumed upper limit to possible propagated bunch intensities to the

next machine, above which excessive losses are expected. Such limitations in the PS have so far not caused any bottlenecks due to the fast energy ramping of the machine after beam injection: the SC tune shift decreases rapidly some tens of milliseconds after injection [169].

- **Bunch splitting** in the PS: either kept as in present Pb operations (halving the bunch intensity), or simply omitted.
- **Stripper foils** (with associated losses) between Linac3 and LEIR, as well as between the PS and the SPS, are also considered. In the baseline scenario, the PS-SPS stripper foil is assumed to be the main loss driver in the PS-SPS transfer line. Also, similar PS-SPS stripping efficiencies are assumed, conservatively using the value listed in Table 6.1 for all ion species, unless stated otherwise.

	Standard scheme
Max no. Linac3 pulses	8
LEIR injection efficiency	50%
N.o. bunches in LEIR	2
LEIR transmission efficiency	76%
LEIR-PS transmission efficiency	93%
PS transmission efficiency	92%
N.o. extracted bunches from PS	4
PS B_{min}	0.0383 T
PS B_{max}	1.26 T
Stripping efficiency PS-SPS	90%
SPS transmission efficiency	72%

Table 6.1: Assumed injector parameters in the baseline scenario, based on operational experience with Pb [170] and LIU ion beam parameters [171].

As a starting point, a beam production scheme similar to the present Pb injector scheme in Chapter 2 is used, which is called “baseline". Possible improvements in the production scheme are discussed in Section 6.2.2. For each ion species, the Injector Model calculates the relativistic gamma factor γ at injection and extraction from each machine, considering the magnetic rigidity from Eq. (2.1) in each accelerator, already discussed in Chapter 2. At extraction of Linac3, a fixed γ is assumed as defined by the linac structure. Also, the proton-equivalent momentum p/q is calculated to verify whether injection does not happen at a too low momentum for the accelerator dipole magnets, in particular for the PS, to handle. The PS dipole magnetic field ramps from a minimum of $B_{\text{min}} = 0.0383$ T to a maximum field of $B_{\text{max}} = 1.26$ T. Identical geometric $\varepsilon_{x,y}$ and σ_z (from Pb operation) are assumed for all ion types to enable the use of the space charge limit from Eq. (5.96). Also, beam losses and degradations are assumed to depend only on the machine properties, for instance non-linearities and beam behavior at different high-order resonances, and not on the particle type.

Experiments other than those at the LHC might also find the Injector Model useful. For

example, lighter ion species have been requested by CERN North Area (NA) fixed-target experiments such as NA61/SHINE [172], where the Injector Model can provide insights into deliverable beam intensities in future studies.

Transmission efficiencies

For the number of ions before capture in LEIR, a constant injection efficiency of 50% and no losses in between injections are assumed. In reality, further limitations from decreasing injection efficiencies along the injection plateau as well as losses during the accumulation process may further limit the total accumulated intensity in LEIR. For example, the effective transmission (including varying injection efficiencies and losses on the injection plateau) for Pb ions is typically about 70%. For O ions, an effective transmission on the injection plateau of more than 90% was measured in the pilot run in 2025. These effects need to be addressed in more detail in future studies. With the presently available knowledge, these fluctuations combined with transmission uncertainties across the injectors result in estimated uncertainties in injected LHC intensity of around 20-30%.

Electron cooling and space charge limits

Two key intensity limitations assumed in the model are a) electron cooling in LEIR and b) space charge in LEIR and in the SPS, as discussed in Chapter 3 and 5. Due to the longer cooling times of lighter ion species with lower charge states, fewer Linac3 injections into LEIR will be possible (for reasonable injection efficiency). The number of predicted possible injections was listed in Table 3.2, which we use as input for the Injector Model. It should be noted that the short 2024 low-intensity Mg beam test run [53] in LEIR confirmed that the given flat-bottom length is insufficient to inject and cool more than one Linac3 pulse, as predicted in Table 3.2. This limitation to a single Linac3 pulse in LEIR was also observed for the 2025 single-bunch O^{4+} pilot beam [13]. Also, assuming that Pb beams are presently limited by space charge in LEIR and the SPS, Eq.(5.96) was derived in Section 5.6.1. This expression is used to estimate the SC-limited bunch intensity of the new ion species compared to Pb.

IBS growth rates for future ion species

IBS effects were already extensively in Chapter 5. To estimate the IBS effects on other future ion species to first order, their IBS emittance growth rates $1/\tau_u$, ($u \in \{x, y, z\}$) are numerically computed with the Nagaitsev formalism model implementation in Xsuite [49, 161]. Recall that $1/\tau_u$ in each plane is a way to quantify the IBS strength for a given set of beam parameters. Growth rates depend on the machine optics, the charge state, the bunch intensity N_b, the geometric emittance ε_u and the beam energy. The values of $\varepsilon^n_{x,y}$, δ and σ are taken from from [156].

The bunch intensity N_b was chosen for each ion species to be at its SC limit from Eq. (5.96).

Although not all ions will reach the SC limit in each machine, this intensity value provides a fair comparison between species, when SC effects start coming into play. Growth rates will give a first-order estimate, although the combination with other effects as discussed in Chapter 5 may complicate the picture further. Table 6.2 contains the computed relative IBS growth rates (absolute growth rates divided by the Pb growth rates) at injection energy.

T_{rel}	He	O	Mg	Ar	Ca	Kr	In	Xe	Pb
X, LEIR	0.02	0.08	0.17	0.24	0.48	0.43	0.86	0.85	1
Y, LEIR	0.02	0.08	0.17	0.24	0.55	0.42	0.86	0.85	1
Z, LEIR	0.02	0.08	0.17	0.24	0.39	0.43	0.86	0.85	1
X, PS	0.02	0.08	0.19	0.26	0.53	0.42	1.09	1.02	1
Y, PS	0.02	0.08	0.17	0.24	0.62	0.42	0.95	0.92	1
Z, PS	0.02	0.08	0.16	0.24	0.64	0.42	0.87	0.86	1
X, SPS	0.04	0.15	0.17	0.25	0.34	0.5	0.47	0.56	1
Y, SPS	0.04	0.14	0.18	0.26	0.26	0.49	0.54	0.62	1
Z, SPS	0.04	0.16	0.11	0.21	0.22	0.51	0.03	0.26	1

Table 6.2: Relative growth rates $T_{\mathrm{rel}} = (1/\tau_u)/(1/\tau_{u,\mathrm{Pb}})$, which is the ratio of analytical Nagaitsev IBS growth rates and the corresponding values for Pb at injection energy.

In the present Pb production scheme across the ion injector chain, IBS is most important at the SPS FB segment, which accumulates 14 injections over around 48 s, compared to only a few seconds in LEIR and the immediate ramp in the PS. Hence, the impact from IBS in LEIR and PS is smaller due to this earlier acceleration. Looking closer at the SPS injection, Kr, In and Xe have growth rates only around half of that of Pb in the transverse planes. These ratios are even smaller for the lighter ions. As seen for oxygen in Chapter 5, IBS is most likely a second-order loss effect for lighter ions, and it is therefore not directly included in the Injector model at this stage.

Beam lifetimes from residual gas interactions

Chapter 4 explained charge-exchanging beam-gas interactions, where beam particles lose or capture electrons from residual gas molecules, a process leading to beam losses. These loss mechanisms can be important for imperfect vacuum conditions. The beam lifetimes from electron capture and loss processes computed using the `beam_gas_collisions` program as shown in Fig. 4.12 are condensed into Table 6.3, which here also includes values at PS extraction. Beam lifetimes in the SPS are normally not affected by these processes, as ions are normally fully stripped and only electron capture is possible, which is relatively rare are at these higher energies, yielding very long lifetimes and negligible beam-gas interactions. Note that these lifetime values are *approximate*, due to uncertainty in residual gas composition and dynamic outgassing.

The Injector Model accounts for this reduced PS transmission due to beam-gas interactions by calculating the average beam lifetime $\tau_{\mathrm{EC,\,EL}}$ over the cycle (from Table 6.3) in the PS using

`beam_gas_collisions` for the given projectile. The total lifetime $\tau_{\text{PS, total}}$ combines these lifetimes inversely: $1/\tau_{\text{PS, total}} = 1/\tau_{\text{PS, EC+EL}} + 1/\tau_{\text{PS, other}}$, where τ_{other} corresponds to about 3% losses from unknown sources not explained by beam-gas interactions, as observed for Pb^{54+}. The PS transmission is $\eta_{\text{PS}} = \exp(-t_{\text{PS, cycle}}/\tau_{\text{PS, total}})$, where $t_{\text{PS, cycle}} = 1.2$ s represents the typical interval the ion beam spends in the PS for any production scheme. 92% is still assumed to be the upper limit for the PS transmission, as in Table 6.1. Whereas no major transmission issues from beam-gas interactions are expected for the heavier proposed future ion species, it may be critical for lighter partially stripped ion species such as O^{4+} and Mg^{7+}.

$q_{\text{LEIR,PS}}$	$\tau_{\text{LEIR, inj}}$ [s]	$\tau_{\text{PS, inj}}$ [s]	$\tau_{\text{PS, extr}}$ [s]	η_{PS}
He^{1+}	160	4.0	5.4	76%
O^{4+}	130	3.3	4.6	73%
O^{5+}	120	2.8	3.8	69%
Mg^{7+}	230	5.5	7.7	82%
Ar^{11+}	370	9.1	11.9	88%
Ca^{17+}	610	25	26	92%
Kr^{22+}	280	12	17	91%
In^{37+}	150	43	54	92%
Xe^{39+}	140	36	48	92%
Pb^{54+}	69	39	47	92%

Table 6.3: Calculated beam lifetime τ (in seconds) due to EL and EC processes in LEIR (injection) and the PS (injection and extraction) for partially stripped ions, used to compute the PS transmission η_{PS}.

Note that fully stripped ions such as He^{2+} and O^{8+} have very long lifetimes in the PS, as electron loss (normally the most important effect in this machine) is not possible. All computed LEIR lifetimes exceed the typical 3.6-second operational cycle length with a large margin. The only ion species with a concern of short lifetimes are the partially stripped lighter ion species He^{1+}, O^{4+}, O^{5+} and Mg^{7+} in the PS, where beam-gas interactions could act as a potential bottleneck. This problem can be avoided for He and O with fully stripped ions through source charge state selection, but may cause radiation protection issues. It is important to emphasize that the transmission efficiency of O^{4+} beams observed during the pilot run in 2025 exhibited significant dependence on the average PS pressure conditions, which are directly influenced by the periodic sublimation process. In the absence of sublimation, transmission values typically oscillated around 50%, but demonstrated levels exceeding 70% during the initial three-hour period following sublimation events, as reflected in the data presented in Table 6.3. These findings indicate that lighter ion species will require comprehensive PS vacuum system investigations and enhancements.

6.2 Injector model results

6.2.1 Injector model baseline predictions

First, the maximum injected bunch intensity N_b in each machine at injection is calculated. For illustration, results of the *baseline* production scenario (PS splitting, PS-SPS stripping) — with and without considering the LEIR electron cooling limit — are summarized in Table 6.4. The calculations use the computational flowchart in Fig. 6.1, ion species parameter input from Table 2.1, injector parameters from Table 6.1 and the allowed LEIR injection number from Table 3.2, based on the achievements with the operational 2024 Pb production scheme.

To understand which effect limits which ion species, the “global bottleneck" in the ion injector chain is marked in bold and is underscored. SC limits the intensity in LEIR for He, Ca, In, Xe and Pb. In the SPS, SC also limits He, and Pb. The electron cooling rate in LEIR limits O, Mg, Ar and Kr. In this baseline scheme, Pb stands out with the highest number of injected charges per bunch into the LHC.

	LEIR injection (accumulated intensity before capture)			PS injection		SPS injection		LHC injection	
	No. LEIR injections	Max N_b 8 inj, ECL	SCL	Max N_b, with bunch splitting	SCL (at least)	Max N_b	SCL	Max N_b	Max charges per bunch
He	1	1.2E+12, 1.5E+11	**1.45E+11**	5.1E+10, 5.1E+10	9.6E+10	1.8E+10, 1.8E+10	**1.1E+10**	7.5E+9, 7.5E+9	1.5E+10
O	1	1.7E+11, **2.1E+10**	3.6E+10	1.3E+10, 7.4E+9	2.4E+10	4.3E+9, 2.5E+9	2.8E+9	1.9E+9, 1.7E+9	1.3E+10
Mg	1	2.1E+10, **2.7E+9**	1.8E+10	6.3E+9, 9.5E+8	1.6E+10	2.4E+9, 3.6E+8	3.0E+9	1.6E+9, 2.4E+8	2.9E+9
Ar	1	4.1E+10, **5.1E+9**	1.2E+10	4.2E+9, 1.8E+9	9.7E+9	1.7E+9, 7.4E+8	1.9E+9	1.2E+9, 4.9E+8	8.9E+9
Ca	4	1.1E+10, 5.5E+9	**5.0E+9**	1.8E+9, 1.8E+9	1.1E+10	7.6E+8, 7.6E+8	5.5E+9	5.1E+8, 5.1E+8	1.0E+10
Kr	3	1.4E+10, **5.1E+9**	6.4E+9	2.3E+9, 1.8E+9	4.5E+9	9.6E+8, 7.6E+8	8.0E+8	5.4E+8, 5.1E+8	1.8E+10
In	7	5.1E+9, 4.4E+9	**3.0E+9**	1.1E+9, 1.1E+9	3.5E+9	4.6E+8, 4.6E+8	1.2E+9	3.1E+8, 3.1E+8	1.5E+10
Xe	6	5.8E+9, 4.3E+9	**3.1E+9**	1.1E+9, 1.1E+9	3.1E+9	4.6E+8, 4.6E+8	8.8E+8	3.1E+8, 3.1E+8	1.7E+10
Pb	8	4.2E+9	**2.6E+9**	9.8E+8	9.8E+8	3.9E+8	**3.9E+8**	2.6E+8	2.1E+10

Table 6.4: Baseline ion production scenario: predicted theoretical maximum bunch intensities N_b (in number of ions) and space charge limit (SCL) at the injection energies along the injector chain. In LEIR, the maximum number of Linac3 injections is also listed, and N_b in this column represents the total accumulated intensity at injection before capture (assuming constant injection efficiency). Two values are shown for N_b: assuming in LEIR either 8 injections (default for Pb) vs the Electron-Cooling Limit (ECL) from Table 3.2. For each ion species, the **global bottleneck** is marked in bold and underlined.

6.2.2 Possible ion production scheme improvements

Production scheme optimizations are then studied to reveal potential improvements in the injected LHC bunch intensity. Some of the most realistic technical proposals — without altering already extensively optimized configurations such as the SPS optics — include:

- Omitting PS bunch splitting
- A LEIR–PS stripping stage as an alternative to the PS–SPS stripping stage
- Optimizing charge-to-mass ratio by varying charge states after stripping in Linac3
- Isotopes selection to optimize the charge-to-mass ratio

- 25 ns bunch spacing in the LHC

All these proposals come with advantages and caveats. Omitting the PS bunch splitting theoretically doubles the extracted bunch intensity, but may introduce further PS degradations and challenges (e.g. instabilities at PS transition crossing) and in addition entails the risk of hitting the SC limit at SPS injection, causing more losses and emittance blow-up. As an alternative, three extracted LEIR bunches into PS without splitting could be considered an intermediate option.

The alternative stripping foil between LEIR–PS instead of the present PS–SPS stripping stage leads to higher injected PS charge states [173], allowing for higher PS extraction energies for a given $B\rho$ from Eq. (2.1). Consequently, the SCL at SPS injection will also be higher due to higher injection energy. Previous studies have assessed Pb stripper foil yields in the CERN accelerator complex [174]. Analogously, theoretical stripper foil efficiencies for the future ion species were computed with the GLOBAL simulation code, developed at GSI based on studies of relativistic heavy ions through matter [175], as shown in Table 6.5. For Mg (added later in the studies), an efficiency similar to the neighboring light ions was assumed.

Caution should be taken with this alternative LEIR-PS stripping scenario, where a higher charge state may amplify SC effects at PS injection energy. The stripping to bare nuclei is likely to increase the angular spread (i.e. resulting in transverse emittance blow-up) and energy spread, but can be mitigated with appropriate optics (as previously done in the PS-SPS transfer line), where experimental beam quality studies are needed. In this scenario, some ion species require too low dipole magnetic fields compared to the limit discussed in Table 6.1. Different radio-frequency (RF) harmonics h and frequencies f_{RF} may also be needed for the PS, which have to be synchronized with LEIR.

Ion	Z	A	q_{LEIR}	LEIR-PS stripping efficiency
He	2	4	1	90%
O	8	16	4	90%
Mg	12	24	7	90%
Ar	18	40	11	90%
Ca	20	40	17	90%
Kr	36	86	22	87%
In	49	115	37	75%
Xe	54	129	39	50%
Pb	82	208	54	50%

Table 6.5: Theoretical LEIR-PS stripper foil efficiencies for each LEIR charge state q_{LEIR}.

Optimization of charge state and isotope has the potential to improve transmitted bunch intensities into the LHC, but requires more detailed multi-dimensional nonlinear analysis and and will be treated in Sec. 6.2.4.

As an additional option, a PS bunch spacing reduction to 50 ns is considered. In ongoing hardware feasibility studies, two potential RF upgrade schemes to enable this scheme are currently discussed: a) narrow-band, tuneable cavities in the 10-20 MHz range, and b) two new wideband Finemet cavities in the range 9.5-20.5 MHz [176]. In this case, similar bunch intensities to the baseline scenario are assumed. Combined with SPS slip stacking, this scheme results in 25 ns bunch spacing in the LHC. Alternatively, two PS bunches spaced by 50 ns can potentially avoid hardware upgrades but would lead to excessively long injection processes due to the many injections needed with very short trains.

Another alternative to improve ion beam production is higher LEIR extraction energy, which requires hardware upgrades with new power converters and leads to longer LHC filling times. However, the absence of a protective roof for LEIR may pose radiation hazards for projectile kinetic energies E_{kin} above 90 MeV/u. In contrast, E_{kin} = 72 MeV/u at LEIR extraction for present Pb^{54+} beams. This necessitates risk assessment and additional personnel protective barriers, a scenario left for future studies.

From these considerations, **five alternative operational scenarios** are formulated:

1. Baseline scenario (PS bunch splitting and PS-SPS stripping, default Pb production)
2. No PS splitting, PS-SPS stripping
3. PS splitting, but changing the stripper foil location from PS-SPS to LEIR-PS
4. LEIR-PS stripping *and* no PS splitting (combining scenario 2 and 3)
5. 25 ns bunch spacing in the LHC, but with similar bunch intensities as in Scenario 1.

In these studies, the key performance metric is the achievable nucleons per bunch injected in the LHC, a way to normalize bunch intensity between different ion species. Figure 6.2 shows the injected bunch intensities for the various scenarios, also compared to previous WG5 projections from Eq. (1.3). Previous WG5 estimates are typically higher [14], in particular for the lighter ions O, Ar and Ca. He, Mg and In were not considered in their study. For the lighter ions He, O, Mg and Ar, the single tolerated LEIR injection due to electron cooler limits discussed in Table 3.2 causes a large discrepancy compared to the WG5 results. LEIR-PS stripping looks unfeasible for He and O ions, as the dipole magnetic field B at PS injection falls below the minimum threshold B_{min} = 0.0383 T in scenarios 3 and 4. These bars are marked in magenta and require further technical studies if seriously considered. For all other ions, the required B field at PS injection safely surpasses this lower limit.

6.2.3 Comparison with 2025 oxygen pilot run data

The commissioning activities conducted during June and July 2025 using a single-bunch O^{4+} pilot beam offer valuable preliminary data for evaluating the Injector Model's performance.

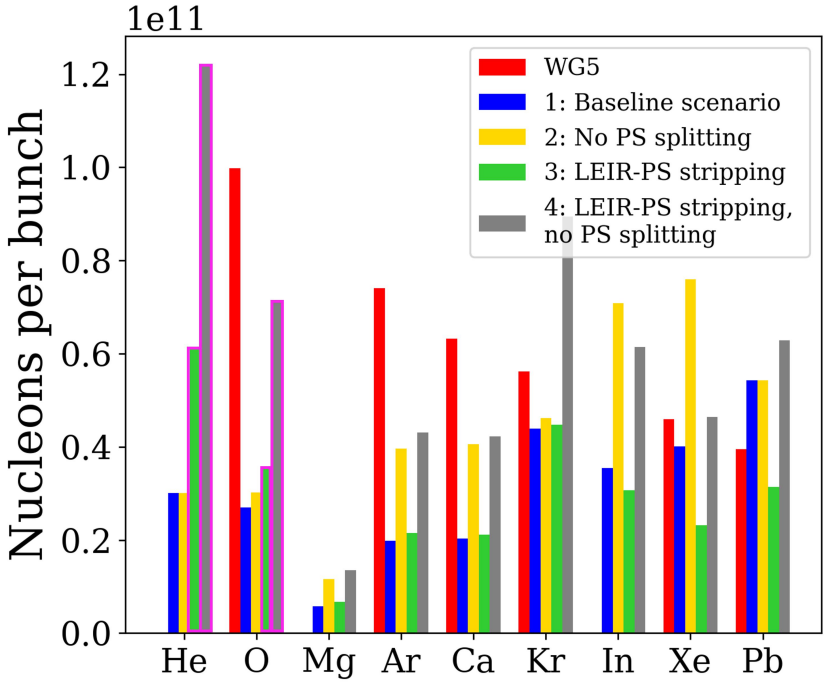


Figure 6.2: Estimated nucleons per bunch for the various scenarios, including the WG5 estimates [14] from Eq. (1.3). He and O bars with pink frames require B_{inj} in PS that presently would be too low without hardware upgrades.

While the beam characteristics and production scheme differ from standard LHC operation planned for Run 5, some meaningful comparisons can still be made. The pilot beam configuration employed in LEIR involved capturing two bunches using RF harmonic $h = 2$, with subsequent transfer of only one bunch to the PS. In the PS, the O^{4+} beam omitted the typical bunch splitting process. The electron stripping occurred during transfer to the SPS. The SPS cycle accommodated four-injections on an injection plateau of around 12 s, in contrast to the 14-injection approach over 48 s employed for $^{208}Pb^{82+}$. Given these operational differences, the most appropriate Injector Model comparison scenario was identified as Scenario 2 with no PS bunch splitting. One of the successful LHC fills on July 6$^{\mathrm{th}}$ 2025 provide representative measurements of the injector performance, as presented in Fig. 6.3.

A comparison between these experimental results and model predictions is shown in Table 6.6, with the characteristically observed 90 μA Linac3 current documented in Table 2.1. Although the Injector Model assumes a higher intensity in LEIR at injection (in particular before capture), the overall transmission efficiencies (extraction/injection ratio) demonstrates agreement between model predictions and experimental observations: LEIR shows 38% (model) versus 37% (measured), while PS exhibits 73% (model) versus 77% (measured). The experimental data reveal lower PS-SPS transfer losses compared to model assumptions. The measured bunch intensity at SPS injection falls within the model's predicted range between the maximum achievable total bunch intensity (5.0E+09) and the tolerable space charge threshold (2.8E+09,

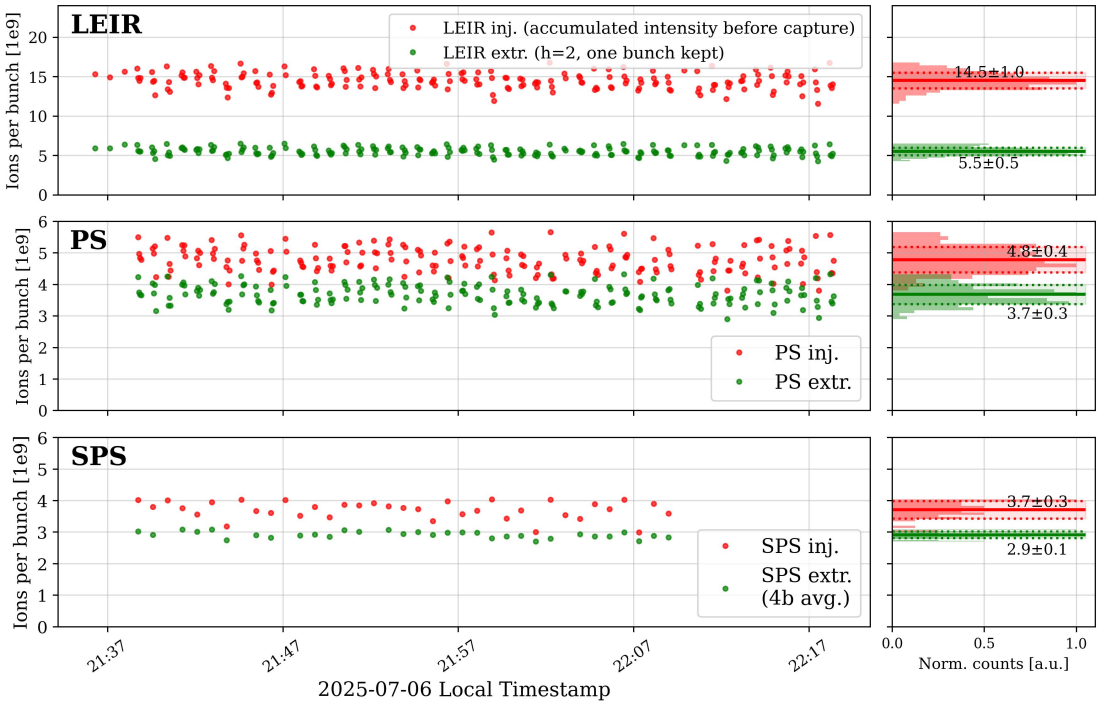


Figure 6.3: Measured oxygen bunch intensities at injection and at extraction in LEIR, the PS and the SPS during one of the LHC fills on July 6th 2025.

indicated in red). In the measurements, a loss rate of typically 1.5%/s was observed for O^{8+} beams, compared to around 0.8%/s for the Pb ion reference case. However, this was for a tune working point that was giving better beam brightness (intensity/emittance) on the short cycle used for the LHC pilot run. A test with the optimal working point for long cycles (like the one used for Pb) using the same intensity as the one mentioned in Table 6.6, showed loss rates on the order of 0.5%/s. This improved transmission compared to the Pb beam is expected from the weaker IBS effects for the lighter ions. Overall, these preliminary measurements do not reveal any fundamental gap in the model assumptions.

Table 6.6: Comparison between: a) measured single-bunch O^{4+} pilot beam intensities (July 2025) from Fig. 6.3 versus b) Scenario 2 with no bunch splitting from the Injector Model (the most similar production) scheme. "*" indicates accumulated intensity before capture at LEIR injection. The SPS space charge limit is marked in red compared to maximum injectable intensity (black).

[ions/bunch]	**LEIR inj.***	**LEIR extr.**	**PS inj.**	**PS extr.**	**SPS inj.**
Measured	1.5E+10	5.5E+09	4.8E+09	3.7E+09	3.7E+09
Inj. Model (Scen. 2)	2.10E+10	8.00E+09	7.40E+09	5.4E+09	5.0E+09 2.8E+09

6.2.4 Charge state and isotope scan

Further optimization of injected LHC bunch intensity is done by scanning the outgoing Linac3 charge state or isotope. The main advantage of a higher LEIR charge state q_{LEIR} is a) higher extraction energy both from LEIR and PS — possibly mitigating space charge effects at SPS injection — and b) faster electron cooling according to Eq. (3.6) and consequently more LEIR injections allowed than listed in Table 3.2.

For realistic projections, previous source experiments have to be considered [24, 25, 26]. Some lighter ion species can be directly produced from the source and do not need stripping after Linac3, as the q/A ratio is sufficiently high for the initial transfer lines. Successfully tested "unstripped" ions directly from the source so far include He, O, Mg, Ar, and also recently Kr^{22+} after source re-optimization.

On the other hand, the ions Ca, In, Xe and Pb require stripping after Linac3, but also the previously assumed charge state Kr^{29+} [27]. For these ion species, a model is needed to estimate the relative charge state distribution after stripping at the exit of Linac3 and derive meaningful yields. One of the most established semi-empirical formulae was postulated in 1993 by Baron, Bajard and Ricaud [177] to compute the charge state distribution after stripping through a carbon foil. Up to krypton, the alternative formula from Nikolaev and Dmitriev [178] proved sufficient, with average charge state $\bar{Q}$, standard deviation d, relativistic β and energy-dependent constant C, given by

$$\bar{Q} = Z_p \times \left(1 - C\exp(-83.275\beta/Z^{0.447})\right), \tag{6.1}$$

$$d = 0.5\sqrt{\bar{Q}\left(1-\bar{Q}/Z\right)^{1.67}}. \tag{6.2}$$

However, for the heavier elements with $Z \geq 54$ tested in the GANIL accelerator, Ref. [177] proposed a new formula to extend Baron's formula in Eq. (6.1) and (6.2) based on additional measurements

$$\bar{Q} = \bar{Q}_p \times \left(1 - \exp(-12.905 + 0.2124Z - 0.00122Z^2)\right), \tag{6.3}$$

$$d = \sqrt{\bar{Q}_p\left(0.07535 + 0.19Y - 0.2654Y^2\right)}, \tag{6.4}$$

where $\bar{Q}_p$ is given by Eq. (6.1) and $Y = \bar{Q}_p/Z$. This study uses Eq. (6.3) and (6.4). Other charge-state prediction formulae exist, such as Ref. [179]. Nonetheless, [177] remains one of the most practical and commonly used formulae, and was recently implemented numerically in the Python package `baroncs` [180] by J.Olsen.

As an example, Fig. 6.4 shows the resulting charge state distribution of Pb upon exit from Linac3. The most abundant charge state, Pb^{53+}, was excluded from operation due to high recombination rates [34]. The second-most abundant charge state, Pb^{54+}, is currently used today for standard ion physics operation. All other most abundant charge states Ca^{17+}, In^{37+}

and Xe^{39+} predicted by `baroncs` agree with the default charge states in Table 2.1. Throughout the full charge state scan in the relevant interval for each ion species, none was found to be isoelectronic with Pb^{53+} at the ionized level $3d^{10}$, and recombination is hence not expected to be a problem.

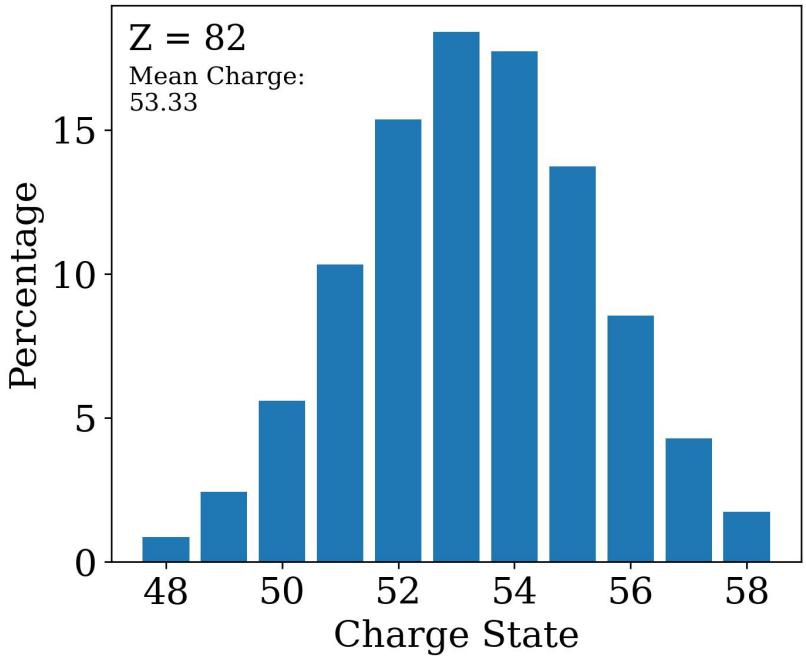


Figure 6.4: Pb charge state distribution after carbon foil stripping at 4.2 MeV/u after Linac3.

The selection of charge state has a direct impact on the transmission across the ion injector chain, but nonlinearly affects numerous superimposed effects such as stripper yield after Linac3 with Baron's formula, number of LEIR injections allowed due to electron cooling, SCL for the various machines, etc. For this reason, a full charge state scan for each ion species was performed with the Injector Model.

Figure 6.5 shows the bunch intensity N_b injected into LHC for different LEIR charge states. For example, in the baseline scenario, Xe^{38+} may offer small gains in injected LHC intensity compared to the default choice Xe^{39+}, but not for Scenario 2 (yellow curve) with no PS bunch splitting where Xe^{39+} already represents the optimum. Isotope selection may also improve the number of nucleons per bunch $\mathcal{N}_{b,0}$ into the LHC. In the second step, all stable isotopes are scanned for each ion species to optimize $\mathcal{N}_{b,0}$ for each scenario, shown in Fig. 6.6. It is assumed that the source and the injectors can handle all stable isotopes, if they can be commercially acquired. For example, looking once again at xenon, ^{126}Xe increases the injected nucleons per bunch by 3% for Scenario 2 (no PS bunch splitting) compared to the default isotope ^{129}Xe.

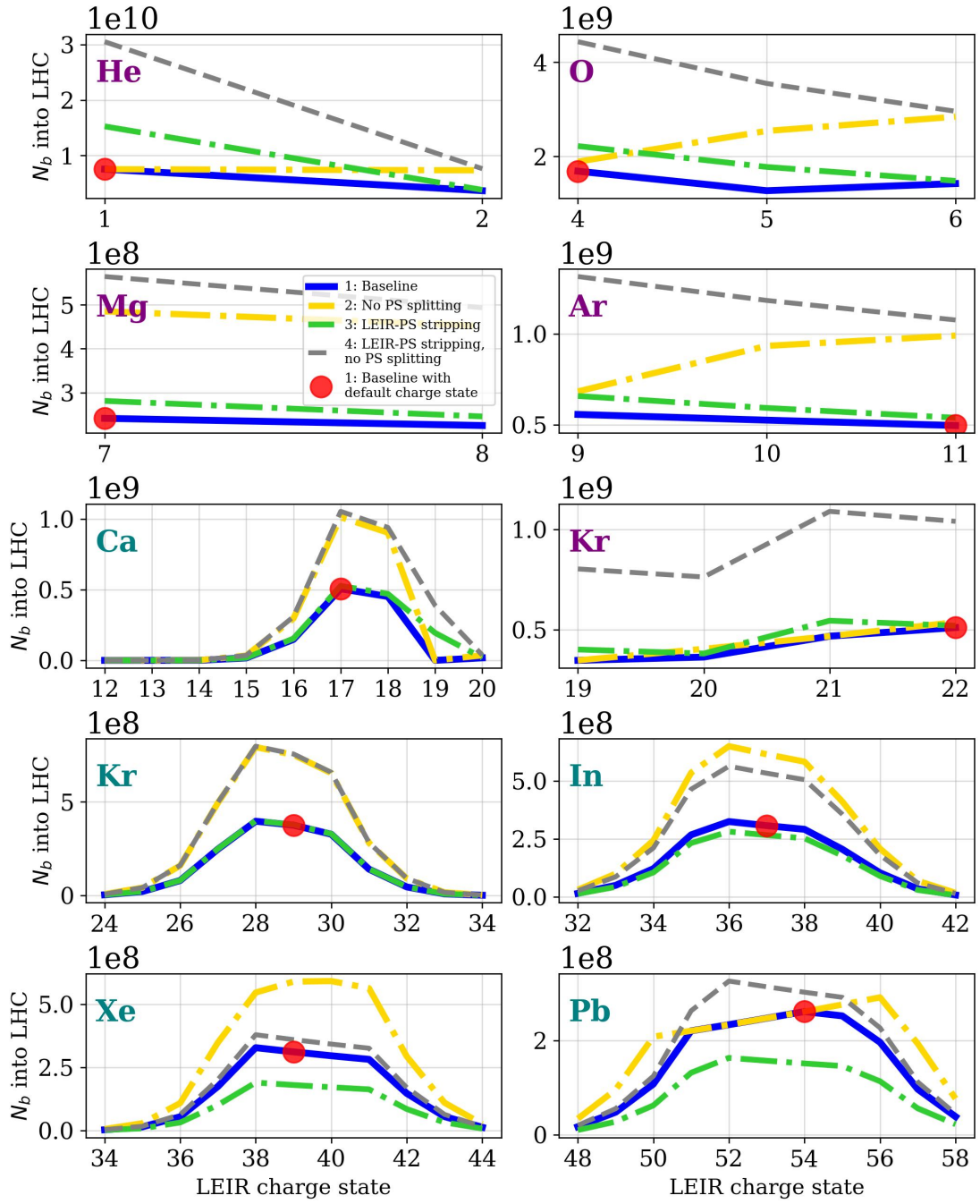


Figure 6.5: Injected ions per bunch N_b into LHC resulting from the LEIR charge state scan, for all the considered ions in the four scenarios. Purple ion labels indicate charge state scans directly produced from the source, teal ion labels indicate charge state scans produced through stripping after Linac3.

As a study case, the performance of ideal charge states and isotopes are tested in Scenario 2,

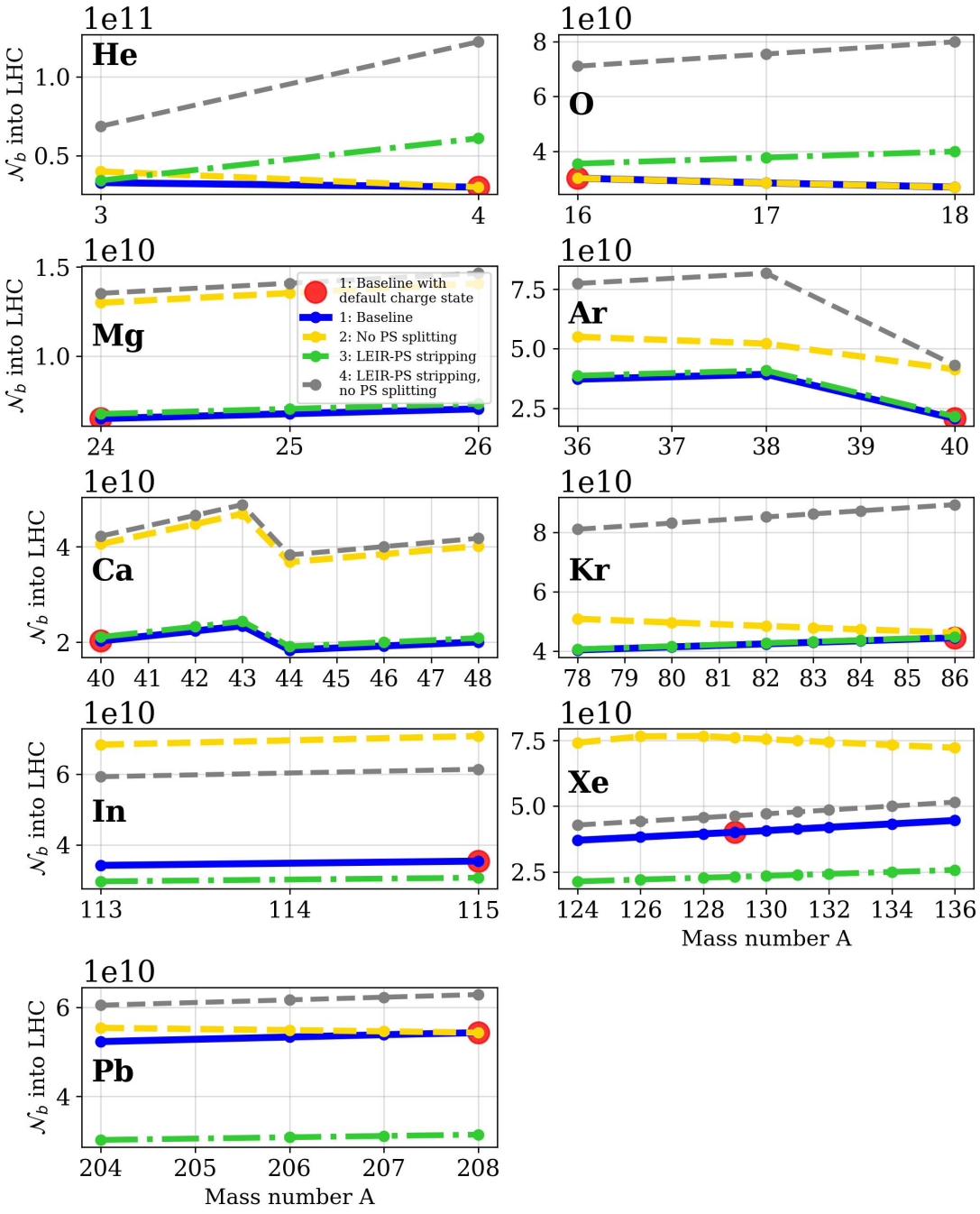


Figure 6.6: Isotope scan for all the stable isotopes of the considered ion scenarios, with resulting number of nucleons per bunch $\mathcal{N}_{b,0}$ injected into the LHC. The sudden reduction in injected LHC nucleons per bunch for heavier isotopes in e.g. Ar and Ca is explained by fewer allowed LEIR injections due to longer cooling times required.

which does not require hardware modification and is typically the best-performing, compared to the baseline Scenario 1. The condensed scan results are summarized in Table 6.7, which 1) shows the best LEIR charge state q_{LEIR} and 2) mass number A, each compared the baseline

scenario with default choices from Table 2.1. In Scenario 2, Pb^{56+} achieves 12% more nucleons per bunch than Pb^{54+}, due to a higher space charge limit at SPS injection (the global bottleneck for most Pb charge states) despite the lower stripping efficiency from Fig. 6.4.

Ion	$q_{\mathrm{LEIR}}^{\mathrm{best}}$	q_{LEIR}^{0}	$\mathcal{N}_{b,q}/\mathcal{N}_{b,0}$	A_{best}	A_0	$\mathcal{N}_{b,A}/\mathcal{N}_{b,0}$
He	1	1	1.0	3	4	1.33
O	5	4	1.35	16	16	1.0
Mg	7	7	1.0	24	24	1.0
Ar	11	11	1.0	36	40	1.33
Ca	17	17	1.0	43	40	1.16
Kr	28	22	1.46	78	86	1.10
In	36	37	1.06	115	115	1.0
Xe	39	39	1.0	128	129	1.01
Pb	56	54	1.12	204	208	1.02

Table 6.7: Ratio between injected nucleons per bunch $\mathcal{N}_{b,0}$ into the LHC for default values in Scenario 2 (no PS splitting), versus using the calculated a) best LEIR charge state q_{LEIR} and b) the best isotope with mass number A.

The charge state scan reveals whether stripping or direct source production is the most beneficial for Kr, where both options are possible. Despite a higher deliverable Linac3 current of 40 μA confirmed for Kr^{22+} from Table 2.1, the previously assumed charge state Kr^{29+} (with the assumed 25 μA) has two main advantages; the higher charge state allows for two extra injections into LEIR (at least five instead of three) and a higher SPS SCL due to higher PS extraction energy. Kr^{28+} achieves 46% more injected LHC bunch intensity than Kr^{22+}. Also, charge state optimization of In and Pb can lead to improvements. Regarding isotope scan results, some notable isotope cases stand out: ^{3}He delivers 33% more injected nucleons per bunch than ^{4}He, ^{78}Kr 10% more than ^{86}Kr and ^{204}Pb 2% more than ^{208}Pb. However, charge state selection appears more accessible and less costly than the purchase of exotic isotopes, as not all stable isotopes can be acquired at reasonable costs or implemented in the source. For instance, the natural abundance for ^{3}He is only 0.0002%, for ^{78}Kr 0.36%, for ^{124}Xe 0.095%, and for ^{204}Pb 1.4% [181]. An important remark for isotopes is that price and availability typically depend not only on abundance but also on how easily they separate.

Some optimized charge states and isotopes are not practically possible in operations, also mentioned by Ref. [24]. The key issue for some charge states is the potentially reduced stripping efficiency and hardware limitations. For instance, the Linac3-LEIR transfer line cannot handle ion charge states with a ratio $q/A < 0.25$, below which the magnets cannot bend the beam sufficiently. As previously mentioned, charge states with kinetic energies above $E_{\mathrm{kin}} > 90$ MeV/u potentially pose radiation hazards in LEIR, which normally is the case if the charge over mass ratio $q/A \approx 0.3$. For example, despite the attractive potential 35% gain of O^{5+}, this charge state reaches kinetic energies of 103 MeV/u at LEIR extraction and falls above the radiation limit. O^{6+} or any higher oxygen charge state are considered excluded without major radiation protection barriers in LEIR, despite their attractiveness. Radiation limits from

neutron production in Linac3 can also be an issue for some lighter ions.

Future source tuning and optimization can provide additional leverage. For instance, He and In currents from [24] were measured with a previous ECR source, but the new source could deliver better currents. In this same study, reduced plasma chamber lifetime with Ar lowered the peak performance in this test, meaning that realistic currents could be higher than in Table 2.1. However, some charge states of He, O, Ar, Mg and Kr are conservatively assumed to require hardware upgrades, such as additional LEIR personnel protective barriers, improved PS vacuum conditions and new power converters for the Linac3 transfer line. Further operational feasibility studies for particularly interesting charge states are encouraged.

6.3 Studies of LHC ion luminosity production

With the Injector Model set up to estimate injected bunch intensities, the achievable LHC luminosity performance has been estimated with the Collider Time Evolution (CTE) software [23, 182], and used to simulate the LHC beam and luminosity evolution for typical fills with various ion species. CTE is a particle tracking simulation code — developed and maintained by R. Bruce — including physical processes such as luminosity burn-off, IBS and synchrotron radiation damping, which has been extensively benchmarked with LHC data [23].

The development of the numerical Injector Model and subsequent studies constitute the main contribution of this thesis work, providing input for CTE beam evolution simulations (conducted by R. Bruce and N. Triantafyllou) at the LHC injection plateau for each ion species and each scenario. The full luminosity projections results and technical details are discussed in Ref. [167], but some key highlights are mentioned here. In particular, these Injector Model studies and parameter explorations were condensed into **three different performance scenarios**. Two scenarios, based on achievable injected bunch intensity into the LHC, are presented in Fig. 6.7. An additional scenario with reduced PS bunch spacing to 50 s is also explored. The three cases are the following:

- **Baseline scenario**: Bunch intensities are calculated using the present understanding of the injector limitations and the same production scheme as predicted for future Pb runs, which corresponds to the baseline scenario defined in Sec. 6.1, also represented by blue bars in Fig. 6.7. For the LHC, the assumptions are based on 2024 achievements with Pb, as discussed in detail in Ref. [167].
- **Optimistic scenario**: in more than a decade from now at the start of Run 5, new developments that improve luminosity production performance could be within reach. In this case, a few optimistic assumptions are made. Scenario 2 with no PS splitting (discussed in Sec. 6.2.2) is selected — typically is the highest-performing scenario without major hardware changes — combined with the best possible LEIR charge state from the optimization effort in Table 6.7. In addition, an extra Linac3 injection (if applicable, as the maximum is still eight) is considered for a potential LEIR electron cooling improvement,

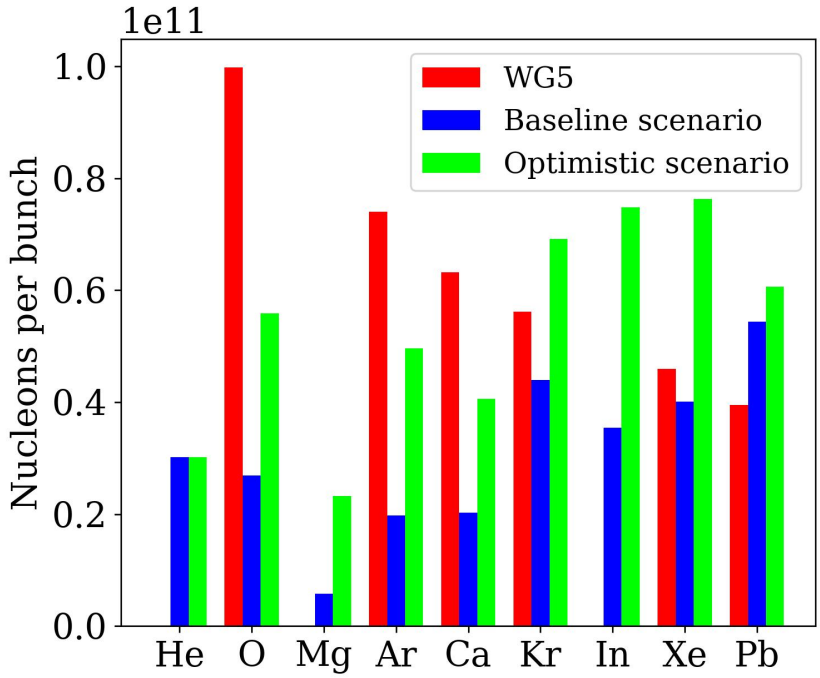


Figure 6.7: Estimated nucleons per bunch injected in LHC from WG5 versus 1) the baseline scenario from Fig. 6.2 and 2) an “optimistic" scenario with improved charge states and an additional LEIR injection, if applicable. These results were used as input for luminosity projections in Ref. [167].

except for He where the cooling time is excessively long. Possible filling schemes and LHC performance assumptions are discussed in detail in Ref. [167].

- **25 ns bunch spacing**: Based on a hypothetical future PS RF system upgrade, this scenario optimistically assumes identical bunch intensities and emittance as the baseline scenario but with more tightly spaced bunches. As in the optimistic scenario, CTE assumes a longer injection plateau, giving larger losses and emittance growth, which is simulated individually for each ion species. Otherwise, the assumptions are identical to the baseline scenario.

The baseline scenario relies on the best possible knowledge at the time of writing, with operationally well-tested configurations. On the other hand, the optimistic scenario relies on *untested configurations and concepts*, and the 25 ns scenario relies on future possible hardware upgrades that are not in the present upgrade plan – with the potential to be implemented but not to be taken for granted. Therefore, the real achievable luminosity most likely lies somewhere in between these scenarios. These scenarios assume that LHC can handle the projected higher intensities and luminosities, which needs to be tested further in feasibility studies. Table 6.8 — shown graphically in Fig. 6.8 — shows the calculated one-month integrated ion-ion luminosities $\int \mathscr{L}_{AA} dt$ and the nucleon-nucleon luminosities $\int \mathscr{L}_{NN} dt$ for the

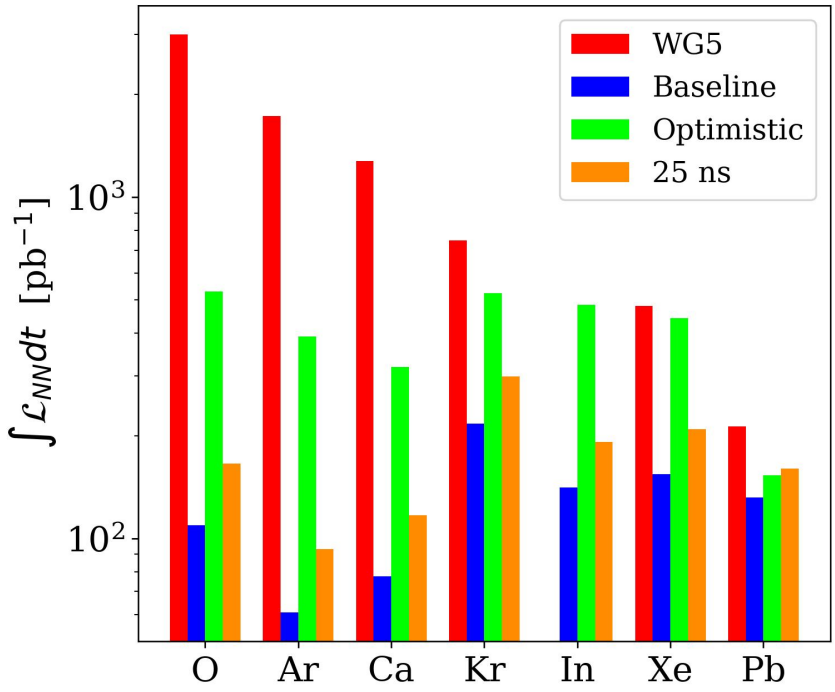


Figure 6.8: One-month integrated nucleon-nucleon luminosity $\int \mathcal{L}_{NN} dt$ from Ref. [167].

ALICE experiment; the other high-luminosity experiments ATLAS and CMS are expected to obtain similar but slightly reduced values.

In general, the computed $\int \mathcal{L}_{NN} dt$ is inferior to the WG5 results [14] for all ion species, even for the optimistic scenario. This discrepancy increases further for the lighter the ion species. The predictions from Table 6.8 show a potential gain factor in $\int \mathcal{L}_{NN} dt$ of about 4 for O in the optimistic case compared to the baseline Pb scenario, where WG5 instead suggests a spectacular 14-fold gain. The WG5 study highlighted oxygen as the most prominent candidate in terms of $\int \mathcal{L}_{NN} dt$, where the new predictions summarized in Table 6.8 instead show that

	One-month $\int \mathcal{L}_{AA} dt$ [nb^{-1}]				One-month $\int \mathcal{L}_{NN} dt$ [pb^{-1}]			
	WG5	Baseline	Optimistic	25 ns	WG5	Baseline	Optimistic	25 ns
O	11700	428.1	2070.4	648.6	2995.2	109.6	530.0	166.0
Ar	1080	38.0	244.7	58.3	1728.0	60.8	391.4	93.2
Ca	799	48.4	199.3	73.3	1278.4	77.5	318.9	117.2
Kr	123	29.4	70.9	40.3	748.3	217.5	524.5	298.2
In	-	10.7	36.7	14.5	-	141.5	485.2	192.1
Xe	28.9	9.3	26.6	12.6	480.9	154.3	443.4	209.7
Pb	4.92	3.0	3.5	3.7	212.9	131.8	153.5	160.2

Table 6.8: Projections from Ref. [167] of one-month integrated ion-ion luminosities $\int \mathcal{L}_{AA} dt$ and one-month integrated nucleon-nucleon luminosities $\int \mathcal{L}_{NN} dt$ from WG5 [14] versus the baseline, optimistic and 25 ns scenarios from this study.

no single ion species dramatically outperforms any other. Kr achieves the highest value of 217 pb^{-1} in the baseline scenario and, O has the highest value in the optimistic scenario with 530 pb^{-1}. The 25 ns scenario results mostly lie in between the baseline and optimistic scenario except for Pb, where it slightly exceeds the optimistic case.

Overall, this program development effort has established a systematic process to identify relevant beam performance-limiting effects across the CERN injectors and synthesize them into self-consistent Injector model. This approach will be important in future studies, and it can also be applied to other accelerator complexes.

6.4 Conclusions

This chapter presented studies of candidate ion species lighter than Pb, envisaged for Run 5 and beyond in the ALICE3 detector upgrade proposal. Contributions of this thesis work include calculations of deliverable bunch intensities to LHC injection, propagated through the CERN ion injector chain (source, Linac3, LEIR, PS, SPS) in the numerical Injector Model, in five principal ion beam production scenarios. Several technical proposals are investigated to improve injected LHC bunch intensities: no bunch splitting in the PS, alternative LEIR-PS stripping, new LEIR charge states and isotopes, and a reduced bunch spacing requiring an upgraded RF system in the PS. The model incorporates realistic performance-limiting effects from space charge and electron cooling in the injectors. These findings have been used as input to Ref. [167] for projections of LHC ion luminosity production, condensed into three principal production scenarios: baseline, optimistic, and 25 ns. The baseline scenario merely extrapolates the present Pb production scheme to new ion species, whereas the optimistic scenario relies on omitting the PS bunch splitting and using different LEIR charge states, and it assumes more optimistic LHC parameters. Hence, the real achievable luminosity may lie in between these scenarios.

The **main findings** include:

- Some lighter ions are limited by either the LEIR electron cooling performance (setting an upper limit on the number of Linac3 injections) and/or space charge in LEIR and the SPS.
- The new nucleon-nucleon luminosity projections are lower than the previous WG5 estimates, both for the baseline and optimistic scenario. This is particularly true for the lighter ions. This discrepancy arises from the simple WG5 power law scaling from Eq. (1.3) (not considering injector limitations), whereas numerous realistic performance-limiting effects are considered in the ion injectors.
- The 25-ns scenario offers an interesting alternative with potential 20-50% gains of nucleon-nucleon luminosity compared to the baseline scenario, but comes at the cost of longer turnaround time and increased beam degradation, which has to be studied

further. This would also require a new RF system in the PS.

- The optimistic scenario suggests gains by up to a factor 4 for some ion species (O, Kr) compared to the baseline Pb, but both this case and the 25-ns scenario result in longer turnaround time and hence more beam degradation,.

Future studies should focus on 1) experimental validations of the Injector Model with various ion species, 2) even more refined models of loss mechanisms with the full combination of space charge, IBS and tune ripples in the injectors, 3) dedicated LHC loss handling and collimation studies, 4) the operational feasibility of discussed hardware upgrades (such as stripper foils and RF systems), and of LHC filling schemes. This version of the Injector Model mainly focuses on propagating bunch intensity, but emittance is a crucial quality factor for luminosity productions and detailed emittance models for each ion species should be addressed experimentally in future studies for better estimates. Nevertheless, the hope is that these studies will provide new insights into performance-limiting factors and ion production scheme optimizations — both in the ion injectors and the LHC — giving input to target the ideal ion species for future experiments in the CERN accelerator complex.

7 Main conclusions and outlook

7.1 Study synthesis

The central goal of this thesis work is to evaluate beam dynamics limitations in the CERN ion injector chain, in order to predict and optimize the performance of future lighter ion species in the CERN accelerator complex. The performance assessment of future ion beams begins in **LEIR**, where the *electron cooling* plays a critical role in limiting the number of Linac3 injections. The simulation studies of Chapter 3 established and validated a scaling law to be used as a predictive tool for cooling times of future ion species and various charge states and isotopes. Following acceleration in LEIR, *beam interactions with residual gas molecules* in the **PS** were identified as a potential lifetime bottleneck. Chapter 4 presented dedicated gas injection experiments with beam lifetime measurements to validate a semi-empirical numerical prediction model of atomic charge-changing cross sections (electron capture and electron loss). Good agreement was found between ion beam lifetime predictions and measured lifetimes from reconstructed target pressure profiles of the injected gas. In the **SPS**, major losses and beam degradations are observed during the long injection plateau (flat bottom) accumulation segment at injection energy for Pb beams, originating from the *interplay* of *tune modulations* from power converter *ripples*, *space charge* and *intra-beam scattering* (IBS), in combination with magnet imperfections. Experimental campaigns and subsequent model validations in Chapter 5 were crucial, demonstrating that a realistic tracking model must include tune ripple adjusted with a semi-empirical transfer function to reproduce beam losses, one of the key findings from this PhD work. Findings from these individual studies were integrated into a comprehensive *Injector Model* in Chapter 6, propagating bunch intensities from Linac3 all the way to **LHC** injection, which allowed first detailed *luminosity projections* for various ion species.

The synthesis of these studies indicates that the reference future ion $^{16}O^{8+}$ has the potential to achieve a factor 4 increase in projected one-month integrated nucleon-nucleon luminosity $\int \mathscr{L}_{NN} dt$, compared to the baseline $^{208}Pb^{82+}$ case. These estimates rely on possible improvements such as omitted PS splitting, optimized LEIR charge state and optimized LHC

parameters and filling scheme. In parallel, a 25-ns bunch spacing scenario with RF system upgrades in the PS offers an interesting alternative with potential $\int \mathscr{L}_{NN} dt$ gains by up to 50%. The assumed remaining principal limiting effects in each machine for O and Pb beams are listed in Table 7.1. Experimental studies in this PhD work showed that some of these effects could be mitigated at least partially, in particular the SPS tune ripple and space charge effects, but are important to consider for any future ion species.

	Main machine limitation		
Ion	LEIR	PS	SPS
O	Electron cooling	Electron loss	Space charge, tune ripple
Pb	Space charge	No major limitation	Space charge, IBS and tune ripple

Table 7.1: Assumed dominant limitation for each machine in the CERN ion injector chain.

7.2 Major contributions of thesis work

Experimental contributions

- Contribution to commissioning a 50 Hz tune ripple compensation scheme for SPS Pb ion beams, which together with working point optimizations and upstream injector optimizations resulted in the total extracted Pb charges per cycle exceeding 130×10^{10}: more than 40% higher than the LHC Injector Upgrade (LIU) ion project objectives.
- Design and execution of dedicated SPS ion beam experiments to study the impact of controlled tune ripple, bunch intensity and transverse tunes on high-intensity $^{208}Pb^{82+}$ beams.
- Experimental benchmarking of a semi-empirical lifetime formula for charge exchange processes by using neutral gas injection to create an in-ring gas target, whose pressure profiles were reconstructed together with the PS vacuum team.

Simulation and physics modeling contributions

- Spectral characterization of the SPS tune ripple and the development of a semi-empirical frequency-dependent transfer function for the transmission line behavior of the main quadrupole magnet chain, allowing realistic tune ripple models in simulations from measured magnet currents.
- The development of a tracking simulation model for the flat-bottom SPS injection segment for Pb beams to quantitatively study the effects of magnet errors, space charge, IBS and tune ripple. The simulations showed that the combination of all these effects — rather than their summed individual effects — is indeed the main loss driver at the SPS flat bottom.

- The creation of a semi-empirical Injector Model to account for physical limitations and semi-empirical scaling laws to provide propagated ion intensities, used as input for the first comprehensive LHC nucleon-nucleon luminosity projections for a range of future ion species.

Software and code development contributions

- Convergence tests and contribution to GPU-compatibility of a kinetic IBS kick element in `xsuite/xfields`.
- Contribution to implementation and validation of a symplectic longitudinal frozen space charge kick within the `xsuite/xfields` framework, improving simulation accuracy for beams with fast synchrotron motion, a useful new community feature.
- Numerical implementation of non-Gaussian longitudinal profiles for the frozen space charge kick within the `xsuite/xfields` framework.

7.3 Future work

Refinement of existing models and further experimental campaigns

- The semi-empirical electron loss and capture model
  - Validation with additional ion projectiles across a larger energy range.
  - Ion beam lifetime measurements in a dedicated neutral gas injection set-up for a more controlled environment than the PS BGI instrument, which however requires additional hardware.
- The SPS ion flat-bottom tracking simulation model
  - More refined model of lattice non-linearities and the study of particular resonances (both excited and natural).
  - Extension of the noise compensation scheme to also reduce the 150, 300 and 600 Hz components, in addition to the 50 Hz, with subsequent simulation benchmarking studies.
  - Further investigations to better understand the measured O beam loss rates in the SPS and possible resonances excited by the machine, not yet explained by the simulation model.
  - Additional experimental comparisons with other ion species.
- The Injector Model
  - Further experimental validation of bunch intensities propagated with the model, for various ion species.

- Inclusion of emittance evolution in the injectors, which requires detailed emittance measurements across the injectors for various ion species.
- Dedicated LHC loss handling and collimation studies of lighter ion species.
- Operational feasibility studies of the possible hardware upgrades: LEIR-PS stripper foil, upgraded RF system in the PS, etc.
- Optimized LHC filling schemes for particularly interesting scenarios.

Bibliography

[1] Oliver S. Bruning, P. Collier, P. Lebrun, S. Myers, R. Ostojic, J. Poole, and P. Proudlock. *LHC Design Report Vol.1: The LHC Main Ring*. CERN Yellow Reports: Monographs. CERN, Geneva, 2004. doi: https://doi.org/10.5170/CERN-2004-003-V-1.

[2] ATLAS Collaboration. *ATLAS detector and physics performance: Technical Design Report, 1*. Technical design report. ATLAS. CERN, Geneva, 1999. URL: https://cds.cern.ch/record/391176.

[3] The CMS Collaboration. The CMS experiment at the CERN LHC. *Journal of Instrumentation*, 3(08):S08004, 2008. doi: https://doi.org/10.1088/1748-0221/3/08/S08004.

[4] The ALICE Collaboration. The ALICE experiment at the CERN LHC. *Journal of Instrumentation*, 3(08):S08002, 2008. doi: https://doi.org/10.1088/1748-0221/3/08/S08002.

[5] J. M. Jowett and C. Carli. The LHC as a proton-nucleus collider. In *Proc. of the 10th European Particle Accelerator Conference (EPAC'06)*, page 550, Edinburgh, Scotland, 2006. Paper ID: MOPLS009, URL: https://jowett.web.cern.ch/epac2006/MOPLS009Poster.pdf.

[6] J. M. Jowett et al. Proton-nucleus Collisions in the LHC. In *Proc. IPAC'13)*, page 49, Shanghai, China, 2013. URL: https://cds.cern.ch/record/1572994.

[7] R. Versteegen, R. Bruce, J. M. Jowett, et al. Operating the LHC Off-momentum for p-Pb Collisions. In *Proc. 4th Int. Particle Accelerator Conf. (IPAC'13)*, Shanghai, China, 2013. URL: https://www.um.edu.mt/library/oar/handle/123456789/27153.

[8] J. M. Jowett, R. Alemany-Fernandez, and G. others Baud. The 2016 proton-nucleus run of the LHC. In *Proc. 8th Int. Particle Accelerator Conf. (IPAC'17)*, page 2071, Copenhagen, Denmark, 2017. URL: http://accelconf.web.cern.ch/AccelConf/ipac2017/papers/tupva014.pdf.

[9] M. Schaumann et al. First xenon-xenon collisions in the LHC. In *Proc.of the 9th Int. Particle Accelerator Conf., Vancouver, Canada*, 2018. doi: https://www.doi.org/10.18429/JACoW-IPAC2018-MOPMF039.

[10] N. Fuster-Martinez, J. M. Jowett, P. Hermes, R. Bruce, D. Mirarchi, and S. Redaelli. Cleaning performance of the collimation system with Xe beams at the Large Hadron

Collider. In *Proc. of the 9th Int. Particle Accelerator Conf. (IPAC'18)*, page 176, Vancouver, Canada, 2018. doi: https://www.doi.org/10.18429/JACoW-IPAC2018-MOPMF038.

[11] M. Schaumann, R. Alemany-Fernandez, H. Bartosik, et al. First partially stripped ions in the LHC ($^{208}Pb^{81+}$). *Journal of Physics: Conference Series*, 1350:012071, 2019. doi: https://www.doi.org/10.1088/1742-6596/1350/1/012071.

[12] A. Gorzawski, A. Abramov, R. Bruce, N. Fuster-Martinez, M. Krasny, J. Molson, S. Redaelli, and M. Schaumann. Collimation of partially stripped ions in the CERN Large Hadron Collider. *Phys. Rev. Accel. Beams*, 23:101002, Oct 2020. doi: https://www.doi.org/10.1103/PhysRevAccelBeams.23.101002.

[13] R. Bruce, R. Alemany-Fernández, H. Bartosik, M. Jebramcik, J. M. Jowett, and M. Schaumann. Studies for an LHC Pilot Run with Oxygen Beams. In *Proc. 12th Int. Particle Accelerator Conf. (IPAC'21)*, pages 53–56, Campinas, Brazil, 2021. doi: 10.18429/JACoW-IPAC2021-MOPAB005. Paper ID: MOPAB005.

[14] Z. Citron et al. Future physics opportunities for high-density QCD at the LHC with heavy-ion and proton beams. In *Proc. of the Workshop on the Physics of HL-LHC, and Perspectives at HE-LHC*, Geneva, Switzerland, 2018. Technical report CERN-LPCC-2018-07. doi: https://www.doi.org/10.23731/CYRM-2019-007.1159.

[15] ALICE Collaboration. Letter of intent for ALICE 3: A next-generation heavy-ion experiment at the LHC, November 2022. arXiv:2211.02491 [hep-ex, physics:nucl-ex, physics:physics]. URL: http://arxiv.org/abs/2211.02491.

[16] Michael Benedikt, Paul Collier, V. Mertens, John Poole, and Karlheinz Schindl. *LHC Design Report Vol.3: The LHC Injector Chain*. CERN Yellow Reports: Monographs. CERN, 2004. doi: https://www.doi.org/10.5170/CERN-2004-003-V-3.

[17] E. Lopienska, 2022. The CERN accelerator complex (2022 layout), URL: https://cds.cern.ch/record/2800984/files/CCC-v2022.png. Accessed 2025-07-07.

[18] J. Coupard, H. Damerau, A. Funken, et al. LHC Injectors Upgrade, Technical Design Report, Vol. II: Ions. Technical Report CERN-ACC-2016-0041, CERN, Geneva, Apr 2016. URL: https://cds.cern.ch/record/2153863.

[19] I. Efthymiopoulos et al. Development of fragmented low-Z ion beams for the NA61 experiment at the CERN SPS. In *Proc. of the 2nd Int. Particle Accelerator Conference (IPAC'11)*, San Sebastián, Spain, 2011. JACoW Publishing. Paper ID: THPS051. URL: https://cds.cern.ch/record/1402561/files/CERN-ATS-2011-226.pdf.

[20] Shyh-yuan Lee. *Accelerator Physics (Fourth Edition)*. World Scientific Publishing Company, 2018. doi: https://www.doi.org/10.1142/11111.

[21] Bartosik, H. et al. Injectors beam performance evolution during Run 2. In *Proc. of the 9th LHC Operations Evian Workshop*, Evian, France, 2019. URL: https://indico.cern.ch/event/751857/.

[22] S. Hancock, M. Lindroos, E. McIntosh, and Mike Metcalf. Tomographic measurements of longitudinal phase space density. Technical Report CERN-PS-99-002-OP, CERN, 1999. URL: https://cds.cern.ch/record/378023.

[23] R. Bruce, M. A. Jebramcik, J. M. Jowett, T. Mertens, and M. Schaumann. Performance and luminosity models for heavy-ion operation at the CERN Large Hadron Collider. *Eur. Phys. J. Plus*, 136:745, 2021. doi: https://www.doi.org/10.1140/epjp/s13360-021-01685-5.

[24] D. Küchler and R. Scrivens. The CERN heavy ion source - present status, 2019. Presentation at the Gamma Factory Meeting. URL: https://indico.cern.ch/event/802131/.

[25] D. Küchler. Preliminary results of the source performance with krypton, 2023. Presentation at the CERN New Ions Working Group Update Symposium on deliverables D1.1 and D3.1. URL: https://indico.cern.ch/event/1304924/.

[26] Detlef Küchler. Magnesium test at the GTS-LHC ion source: preliminary results, 2024. Presentation at the CERN Future Ions WG: Mg tests results I. URL: https://indico.cern.ch/event/1421592/.

[27] R. Bruce et al. Preliminary LHC Light-Ion Scenarios for Run 5 and Beyond, 2021. Presentation LIU-Ions PS injectors Performance Coordination Meeting. URL: https://indico.cern.ch/event/1085343/.

[28] Mieczyslaw Witold Krasny. The gamma factory proposal for CERN, 2015. arXiv:1511.07794 [hep-ex] doi: https://doi.org/10.48550/arXiv.1511.07794.

[29] Gersh Itskovich Budker. An effective method of damping particle oscillations in proton and antiproton storage rings. *Soviet Atomic Energy*, 22:438–440, 1967. doi: https://www.doi.org/10.1007/BF01175204.

[30] Sergei Nagaitsev. Review of Recent Advances in Cooling Techniques. In *Proc. of the 3rd North American Particle Accelerator Conf. (NAPAC'19)*, Lansing, MI, USA, 2019. URL: https://accelconf.web.cern.ch/napac2019/talks/frxba1_talk.pdf.

[31] Gerard Tranquille. LEIR Cooler Status. In *AIP Conference Proc.*, volume 821, pages 57–64. American Institute of Physics, 2006. doi: https://www.doi.org/10.1063/1.2190100.

[32] Gerard Tranquille, Antti Kolehmainen, Marc Timmins, Benjamin Moles, Lars Jørgensen, Jean Cenede, and Alexandre Frassier. The ELENA electron cooler. Technical Report CERN-ACC-2016-280, CERN, 2016. URL: https://cds.cern.ch/record/2207345.

[33] T. Eriksson et al. AD status and consolidation plans. In *Proc. of the Int. Workshop on Beam Cooling and Related Topics (COOL'13)*, Murr, Germany, 2013. Paper ID: MOPM2HA02. URL: https://cds.cern.ch/record/1697065.

[34] Jacques Bosser, M. Chanel, C. Hill, et al. Experimental investigation of electron cooling and stacking of lead ions in a low energy accumulation ring. *Part. Accel.*, 63:171–210, 1999. Technical report CERN-PS-99-033-DI. URL: https://cds.cern.ch/record/388111.

[35] Vasilii V. Parkhomchuk and Aleksandr N. Skrinsky. Electron cooling: 35 years of development. *Physics-Uspekhi*, 43(5):433, 2000. doi: https://www.doi.org/10.1070/PU2000v043n05ABEH000741.

[36] Gersh Itskovich Budker and Aleksandr N. Skrinsky. Electron cooling and new possibilities in elementary particle physics. *Soviet Physics Uspekhi*, 21(4):277, 1978. doi: https://www.doi.org/10.1070/PU1978v021n04ABEH005537.

[37] Yaroslav S. Derbenev and A. N. Skrinsky. The Effect Of An Accompanying Magnetic Field On Electron cooling. *Part. Accel.*, 8:235–243, 1978. URL: https://cds.cern.ch/record/1107957.

[38] I. Meshkov. Electron cooling: Status and perspectives. In *Proc. of the Workshop on Beam Cooling and Related Topics*, pages 26–38, Montreux, Switzerland, 1994. CERN. Technical report CERN-94-03. URL: https://cds.cern.ch/record/398450/.

[39] V. V. Parkhomchuk. New insights in the theory of electron cooling. *Nuclear Instruments and Methods in Physics Research Section A*, 441(1-2):9–17, 2000. doi: https://www.doi.org/10.1016/S0168-9002(99)01100-6.

[40] S. Baird, J. Bosser, C. Carli, M. Chanel, et al. Measurement of the lifetime of $Pb^{52+,53+}$ and Pb^{54+} beams at 4.2 MeV per nucleon subject to electron cooling. *Physics Letters B*, 361(1-4):184–186, 1995. doi: https://www.doi.org/10.1016/0370-2693(95)01164-L.

[41] O. Uwira, A. Müller, J. Linkemann, T. Bartsch, et al. Recombination measurements at low energies with $Au^{49+,50+,51+}$ at the TSR. *Hyperfine Interactions*, 108:149–154, 1997. doi: https://www.doi.org/10.1023/A:1012694209176.

[42] Kramida, A. and Ralchenko, Yu. and Reader, J. and NIST ASD Team. NIST atomic spectra database ionization energies data, 2019. URL: https://physics.nist.gov/asd.

[43] Chet Nieter and John R. Cary. VORPAL: a versatile plasma simulation code. *Journal of Computational Physics*, 196(2):448–473, 2004. doi: https://www.doi.org/10.1016/j.jcp.2003.11.004.

[44] Andrea Latina. RF-Track Reference Manual, 2020. doi: https://www.doi.org/10.5281/zenodo.3887085.

[45] Meshkov, I. and et al. Physics guide of BETACOOL code Version 1.1. Technical Report C-A/AP/262, BNL, 2006. URL: https://www.osti.gov/servlets/purl/1061853.

[46] He Zhang et al. JSPEC2 code repository, 2024. URL: https://github.com/JeffersonLab/ElectronCooling.

[47] A. V. Fedotov, I. Ben-Zvi, V. N. Litvinenko, D. L. Bruhwiler, D. T. Abell, R. Busby, and P. Schoessow. Numerical Studies of the Friction Force for the RHIC Electron Cooler. In *Proc. of the 2005 Particle Accelerator Conf. (PAC'05)*, pages 4278–4280, Knoxville, TN, USA, 2005. doi: https://www.doi.org/10.1109/PAC.2005.1591790.

[48] Agnieszka Borucka, Davide Gamba, and Andrea Latina. Comparison of available models of electron cooling and their implementations. In *Proc. of the Int. Workshop on Beam Cooling and Related Topics (COOL'21)*, pages 74–77, 2021. URL: https://cds.cern.ch/record/2816680.

[49] G. Iadarola et al. Xsuite: an integrated beam physics simulation framework, 2023. URL: https://arxiv.org/abs/2310.00317.

[50] P. Kruyt, D. Gamba, and G. Franchetti. Advancements and applications of cooling simulation tools: A focus on X-suite. In *Proc. of the Int. Workshop on Beam Cooling and Related Topics (COOL'23)*, Montreux, Switzerland, 2023.

[51] Agnieszka Borucka, Davide Gamba, and Andrea Latina. Benchmark of e-cooling simulations with RF-Track, 2021. Techical report: CERN-ACC-NOTE-2021-0031. doi: https://www.doi.org/10.18429/JACoW-COOL2021-P1005.

[52] G. Tranquille. Electron Cooling of Pb^{54+} ions in LEIR. In *Proc. of the 11th Heavy Ion Accelerator Technology Conf. (HIAT'09)*, Venice, Italy, 2009. URL: https://accelconf.web.cern.ch/HIAT2009/papers/d-05.pdf.

[53] M. Slupecki. Outcome of the Mg^{7+} beam test and future plans. In *Proc. of the CERN Injectors Performance Panel (IPP) Meeting 21/07/2024*, 2024. URL: https://indico.cern.ch/event/1420323/.

[54] E. Waagaard, F. Ukena, J. Olsen, R. Alemany Fernández, J. Somoza, and G. Weber. Beam-Gas Interactions in the CERN Proton Synchrotron: Cross Section Measurements and Lifetime Modelling, 2025. arXiv preprint arXiv:2506.02928. doi: https://doi.org/10.48550/arXiv.2506.02928.

[55] Inga Tolstikhina, Makoto Imai, Nicolas Winckler, and Viacheslav Shevelko. *Basic Atomic Interactions of Accelerated Heavy Ions in Matter*. Springer Series on Atomic, Optical, and Plasma Physics. Springer, 2018. doi: https://www.doi.org/10.1007/978-3-319-74992-1.

[56] VP Shevelko, IL Beigman, MS Litsarev, Hiroyuki Tawara, I Yu Tolstikhina, and G Weber. Charge-changing processes in collisions of heavy many-electron ions with neutral atoms. *Nuclear Instruments and Methods in Physics Research Section B: Beam Interactions with Materials and Atoms*, 269(12):1455–1463, 2011. doi: https://doi.org/10.1016/j.nimb.2011.03.024.

[57] G Weber, MO Herdrich, RD DuBois, P-M Hillenbrand, H Beyer, L Bozyk, T Gassner, RE Grisenti, S Hagmann, Yu A Litvinov, et al. Total projectile electron loss cross sections of U^{28+} ions in collisions with gaseous targets ranging from hydrogen to krypton. *Physical Review Special Topics-Accelerators and Beams*, 18(3):034403, 2015. doi: https://www.doi.org/10.1103/PhysRevSTAB.18.034403.

[58] RL Hickok. Plasma density measurement by molecular ion breakup. *Review of Scientific Instruments*, 38(1):142–143, 1967. doi: https://www.doi.org/10.1063/1.1720515.

[59] I Hofmann. Hidif–an approach to high repetition rate inertial fusion with heavy ions. *Nuclear Instruments and Methods in Physics Research Section A: Accelerators, Spectrometers, Detectors and Associated Equipment*, 415(1-2):11–19, 1998. doi: https://doi.org/10.1016/S0168-9002(98)00512-9.

[60] Gerhard Kraft. Tumor therapy with heavy charged particles. *Progress in particle and Nuclear Physics*, 45:S473–S544, 2000. doi: https://www.doi.org/10.1016/S0146-6410(00)00112-5.

[61] Gianluigi Arduini, R. Bailey, T. Bohl, et al. Lead ion beam emittance and transmission studies in the PS-SPS complex at CERN. In *Proc. of the 5th European Particle Accelerator Conf. (EPAC'96)*, Sitges, Spain, 1996. Technical report CERN-SL-96-019-OP. URL: https://cds.cern.ch/record/308372.

[62] Felix M. Kröger, Günter Weber, Simon Hirlaender, Reyes Alemany-Fernandez, Mieczyslaw W. Krasny, Thomas Stöhlker, Inga Yu. Tolstikhina, and Viacheslav P. Shevelko. Charge-state distributions of highly charged lead ions at relativistic collision energies. *Annalen der Physik*, 534(3):2100245, 2022. doi: https://www.doi.org/10.1002/andp.202100245.

[63] Simon Hirlaender et al. Lifetime and beam losses studies of partially strip ions in the SPS ($^{129}Xe^{39+}$). In *Proc. of the 9th Int. Particle Accelerator Conf. (IPAC'18)*, 2018. doi: https://doi.org/10.18429/JACoW-IPAC2018-THPMF015.

[64] E Mahner. The vacuum system of the Low Energy Ion Ring at CERN: Requirements, design, and challenges. *Vacuum*, 81(6):727–730, 2007. doi: https://www.doi.org/10.1016/j.vacuum.2005.11.054.

[65] VP Shevelko, Yu A Litvinov, Th Stöhlker, and I Yu Tolstikhina. Lifetimes of relativistic heavy-ion beams in the High Energy Storage Ring of FAIR. *Nuclear Instruments and Methods in Physics Research Section B: Beam Interactions with Materials and Atoms*, 421:45–49, 2018. doi: https://www.doi.org/10.1016/j.nimb.2018.02.012.

[66] B. Franzke. Interaction of Stored Ion Beams With the Residual Gas. In *CERN Yellow Reports: School Proc.*, 1992. doi: https://www.doi.org/10.5170/CERN-1992-001.100.

[67] Gordon Drake, editor. *Classical Trajectory and Monte Carlo Techniques*, pages 869–874. Springer New York, New York, NY, 2006. doi: https://doi.org/10.1007/978-0-387-26308-3_58.

[68] Jörg KM Eichler. Eikonal theory of charge exchange between arbitrary hydrogenic states of target and projectile. *Physical Review A*, 23(2):498, 1981. doi: https://www.doi.org/10.1016/j.physrep.2006.11.003.

[69] VP Shevelko, O Rosmej, H Tawara, and I Yu Tolstikhina. The target-density effect in electron-capture processes. *Journal of Physics B: Atomic, Molecular and Optical Physics*, 37(1):201, 2003. doi: https://doi.org/10.1088/0953-4075/37/1/012.

[70] Jörg Eichler and Thomas Stöhlker. Radiative electron capture in relativistic ion–atom collisions and the photoelectric effect in hydrogen-like high-Z systems. *Physics reports*, 439(1-2):1–99, 2007. doi: https://www.doi.org/10.1016/j.physrep.2006.11.003.

[71] W Erb. *Umladung schwerer Ionen nach Durchgang durch Gase und Festkörper im Energiebereich 0,2 bis 1,4 MeV/u*. GSI, Darmstadt, 1978. URL: https://cds.cern.ch/record/119615.

[72] Jose Alonso and Harvey Gould. Charge-changing cross sections for Pb and Xe ions at velocities up to 4×10^9 cm/sec. *Physical Review A*, 26(2):1134, 1982. doi: https://www.doi.org/10.1103/PhysRevA.26.1134.

[73] RE Olson, RL Watson, V Horvat, and KE Zaharakis. Projectile and target ionization in MeV u-1 collisions of Xe ions with N2. *Journal of Physics B: Atomic, Molecular and Optical Physics*, 35(8):1893, 2002. doi: https://www.doi.org/10.1088/0953-4075/35/8/308.

[74] A. S. Schlachter, J. W. Stearns, W. G. Graham, K. H. Berkner, R. V. Pyle, and J. A. Tanis. Electron capture for fast highly charged ions in gas targets: An empirical scaling rule. *Physical Review A*, 27(6):3372–3374, June 1983. doi: https://www.doi.org/10.1103/PhysRevA.27.3372.

[75] V. P. Shevelko, Th. Stöhlker, H. Tawara, I. Yu. Tolstikhina, and G. Weber. Electron capture in intermediate-to-fast heavy ion collisions with neutral atoms. *Nuclear Instruments and Methods in Physics Research Section B: Beam Interactions with Materials and Atoms*, 268 (17):2611–2616, September 2010. doi: https://www.doi.org/10.1016/j.nimb.2010.06.019.

[76] G Baur, IL Beigman, VP Shevelko, I Yu Tolstikhina, and Th Stöhlker. Ionization of highly charged relativistic ions by neutral atoms and ions. *Physical Review A*, 80(1):012713, 2009. doi: https://www.doi.org/10.1103/PhysRevA.80.012713.

[77] VP Shevelko, I Yu Tolstikhina, and Th Stöhlker. Stripping of fast heavy low-charged ions in gaseous targets. *Nuclear Instruments and Methods in Physics Research Section B: Beam Interactions with Materials and Atoms*, 184(3):295–308, 2001. doi: https://www.doi.org/10.1016/S0168-583X(01)00774-1.

[78] IL Beigman, I Yu Tolstikhina, and VP Shevelko. Ionization of heavy ions in relativistic collisions with neutral atoms. *Technical Physics*, 53:547–553, 2008. doi: https://www.doi.org/10.1134/S1063784208050034.

[79] I Yu Tolstikhina, II Tupitsyn, SN Andreev, and VP Shevelko. Influence of relativistic effects on electron-loss cross sections of heavy and superheavy ions colliding with neutral atoms. *Journal of Experimental and Theoretical Physics*, 119:1–7, 2014. doi: https://www.doi.org/10.1134/S1063776114060211.

[80] R. D. DuBois, A. C. F. Santos, G. M. Sigaud, and E. C. Montenegro. Electron loss from fast heavy ions: Target-scaling dependence. *Physical Review A*, 84(2):022702, August

2011. doi: 10.1103/PhysRevA.84.022702. Publisher: American Physical Society. URL: https://link.aps.org/doi/10.1103/PhysRevA.84.022702.

[81] G. Weber. A new semi-empirical formular for total electron loss by energetic ions, 2017. 2016 Annual Report Helmholtz-Institut Jena. doi: https://www.doi.org/10.15120/GSI-2017-00708.

[82] H-P Hülskötter, B Feinberg, WE Meyerhof, A Belkacem, JR Alonso, L Blumenfeld, EA Dillard, H Gould, N Guardala, GF Krebs, et al. Electron-electron interaction in projectile electron loss. *Physical Review A*, 44(3):1712, 1991. doi: https://www.doi.org/10.1103/PhysRevA.44.1712.

[83] GD Alton, LB Bridwell, M Lucas, CD Moak, PD Miller, CM Jones, QC Kessel, AA Antar, and MD Brown. Single-and multiple-electron-loss-cross-section measurements from 20-MeV Fe 4+ on thin gaseous targets. *Physical Review A*, 23(3):1073, 1981. doi: https://www.doi.org/10.1103/PhysRevA.23.1073.

[84] Yong Peng. *Dependence of cross sections for multi-electron loss by 6 MeV/amu Xe18+ ions on target atomic number*. PhD thesis, Texas A&M University, 2004. URL: https://oaktrust.library.tamu.edu/items/820cf18d-ebc5-4f6f-8c7c-5533582827f9.

[85] WE Meyerhof, R Anholt, and Xiang-Yuan Xu. Atomic collisions with relativistic heavy ions. VII. L-and M-shell electron stripping of ions in light targets. *Physical Review A*, 35 (3):1055, 1987. doi: https://www.doi.org/10.1103/PhysRevA.35.1055.

[86] WE Meyerhof, R Anholt, Xiang-Yuan Xu, Harvey Gould, B Feinberg, RJ McDonald, HE Wegner, and P Thieberger. Multiple ionization in relativistic heavy-ion–atom collisions. *Physical Review A*, 35(4):1967, 1987. doi: https://www.doi.org/10.1103/PhysRevA.35.1967.

[87] Beam-gas collisions Github repository, 2025. URL: https://github.com/ewaagaard/Beam-gas-collisions.

[88] Bernhard Franzke. Vacuum requirements for heavy ion synchrotrons. *IEEE Transactions on Nuclear Science*, 28(3):2116–2118, 1981. doi: https://www.doi.org/10.1109/TNS.1981.4331609.

[89] RE Olson, RL Watson, V Horvat, AN Perumal, Y Peng, and Th Stöhlker. Projectile electron loss and capture in MeV/u collisions of U^{28+} with H_2, N_2 and Ar. *Journal of Physics B: Atomic, Molecular and Optical Physics*, 37(22):4539, 2004. doi: https://www.doi.org/10.1088/0953-4075/37/22/012.

[90] AN Perumal, V Horvat, RL Watson, Y Peng, and KS Fruchey. Cross sections for charge change in argon and equilibrium charge states of 3.5 MeV/amu uranium ions passing through argon and carbon targets. *Nuclear Instruments and Methods in Physics Research Section B: Beam Interactions with Materials and Atoms*, 227(3):251–260, 2005. doi: https://doi.org/10.1016/j.nimb.2004.09.005.

[91] Franz Mandl. *Statistical physics*, volume 14. John Wiley & Sons, 1991. ISBN: 978-0-471-91532-4.

[92] John Dalton. Essay IV. On the expansion of elastic fluids by heat. *Memoirs of the Literary and Philosophical Society of Manchester*, 5(2):595–602, 1802.

[93] R. L. Watson, Yong Peng, V. Horvat, G. J. Kim, and R. E. Olson. Target Z dependence and additivity of cross sections for electron loss by 6-MeV/amu Xe^{18+} projectiles. *Phys. Rev. A*, 67:022706, Feb 2003. doi: https://www.doi.org/10.1103/PhysRevA.67.022706.

[94] James Storey et al. Development of an ionization profile monitor based on a pixel detector for the CERN Proton Synchrotron, 2016. doi: 10.18429/JACoW-IBIC2015-TUPB059. URL: https://cds.cern.ch/record/2265930.

[95] James Storey et al. First results from the operation of a rest gas ionisation profile monitor based on a hybrid pixel detector, 2017. Proc. of the 6th Int. Beam Instrumentation Conf. (IBIC) 2017. doi: https://www.doi.org/10.18429/JACoW-IBIC2017-WE2AB5.

[96] M. Ady and R. Kersevan. Recent developments of Monte-Carlo codes MolFlow+ and SynRad+. In *Proc. of the 10th Int. Particle Accelerator Conference (IPAC 2019)*, page TUPMP037, Melbourne, Australia, 2019. doi: https://www.doi.org/10.18429/JACoW-IPAC2019-TUPMP037.

[97] Marton Ady. *Monte Carlo simulations of ultra high vacuum and synchrotron radiation for particle accelerators*. PhD thesis, EPFL, 2016. doi: https://www.doi.org/10.5075/epfl-thesis-7063.

[98] Harry H Ku et al. Notes on the use of propagation of error formulas. *Journal of Research of the National Bureau of Standards*, 70(4), 1966. doi: https://www.doi.org/10.6028/jres.070C.025.

[99] Frank Zimmermann. *Emittance Growth and Proton Beam Lifetime in HERA*. PhD thesis, Universität Hamburg, 1993. Report number: DESY-93-059.

[100] Y. Luo, W. Fischer, and S. White. Analysis and Modeling of Proton Beam Loss and Emittance Growth in the Relativistic Heavy Ion Collider. *Phys. Rev. Accel. Beams*, 19(2): 021001, 2016. doi: https://www.doi.org/10.1103/PhysRevAccelBeams.19.021001.

[101] H. J. Kim and T. Sen. Beam Simulation of the SPS. In *Proc. LHC-CC11 Symposium*, 2011. URL: https://indico.cern.ch/event/149614/contributions/191529/attachments/150842/213584/lhc-cc11-11-14-2011.pdf.

[102] Fanouria Antoniou et al. Emittance Growth in Coast in the SPS at CERN. In *J. Phys.: Conf. Ser.*, volume 1067, page 022008. IOP Publishing, 2018. doi: https://www.doi.org/10.1088/1742-6596/1067/2/022008.

[103] H. L. Bradt and B. Peters. The Heavy Nuclei of the Primary Cosmic Radiation. *Phys. Rev.*, 77(1):54, 1950. doi: https://www.doi.org/10.1103/PhysRev.77.54.

[104] G. D. Westfall, L. W. Wilson, P. J. Lindstrom, H. J. Crawford, D. E. Greiner, and H. H. Heckman. Fragmentation of Relativistic Fe 56. *Phys. Rev. C*, 19(4):1309, 1979. doi: https://www.doi.org/10.1103/PhysRevC.19.1309.

[105] Lembit Sihver, Mattias Lantz, M. Takechi, A. Kohama, A. Ferrari, F. Cerutti, and T. Sato. A Comparison of Total Reaction Cross Section Models Used in Particle and Heavy Ion Transport Codes. *Adv. Space Res.*, 49(4):812–819, 2012. doi: https://doi.org/10.1016/j.asr.2011.11.029.

[106] John David Jackson. *Classical Electrodynamics*. John Wiley & Sons, 1998.

[107] Karlheinz Schindl. Space charge - introduction. *CERN Document Server*, March 1999. doi: 10.5170/CERN-2005-004.285. Technical report CERN-PS-99-012-DI. Publisher: CERN. URL: https://cds.cern.ch/record/384395.

[108] S. Kheifets. Potential of a Three-Dimensional Gaussian Bunch. Technical Report PETRA Note 119, DESY, 1976.

[109] M. Bassetti and George A. Erskine. Closed Expression for the Electrical Field of a Two-Dimensional Gaussian Charge, 1980. Number: ISR-TH-80-06. URL: https://cds.cern.ch/record/122227.

[110] Foteini Asvesta. *Space Charge and Lattice Driven Resonances at the CERN Injectors*. PhD thesis, CERN, June 2021. Number: CERN-THESIS-2020-344. URL: https://cds.cern.ch/record/2771289.

[111] R. W. Hockney and J. W. Eastwood. *Computer Simulation Using Particles*. CRC Press, Boca Raton, March 2021. doi: https://www.doi.org/10.1201/9780367806934.

[112] G. Franchetti and I. Hofmann. Modeling of Space Charge Induced Resonance Loss. *AIP Conf. Proc.*, 642(1):260–262, December 2002. doi: https://www.doi.org/10.1063/1.1522641.

[113] Adrian Oeftiger et al. Review of CPU and GPU Faddeeva Implementations. *Proc. 7th Int. Particle Accelerator Conf. (IPAC'16), Busan, Korea*, page WEPOY044, 2016. doi: https://www.doi.org/10.18429/JACoW-IPAC2016-WEPOY044.

[114] S. Y. Lee, G. Franchetti, I. Hofmann, F. Wang, and L. Yang. Emittance Growth Mechanisms for Space-Charge Dominated Beams in Fixed Field Alternating Gradient and Proton Driver Rings. *New J. Phys.*, 8:291–291, November 2006. doi: https://www.doi.org/10.1088/1367-2630/8/11/291.

[115] Johan Bengtsson. *Non-Linear Transverse Dynamics for Storage Rings With Applications to the Low-Energy Antiproton Ring (LEAR) at CERN*. PhD thesis, Lund U., 1988. Thesis number 10.5170/CERN-1988-005. URL: https://repository.cern/records/hc82y-bq702/preview/CERN-88-05.pdf.

[116] S. Machida. Space-Charge-Induced Resonances in a Synchrotron. *Nucl. Instrum. Methods Phys. Res. A*, 384(2-3):316–321, 1997. doi: https://www.doi.org/10.1016/S0168-9002(96)00884-4.

[117] G. Franchetti and I. Hofmann. Particle Trapping by Nonlinear Resonances and Space Charge. *Nucl. Instrum. Methods Phys. Res. A*, 561:195–202, June 2006. doi: https://www.doi.org/10.1016/j.nima.2006.01.031.

[118] G. Franchetti, O. Chorniy, I. Hofmann, W. Bayer, F. Becker, P. Forck, T. Giacomini, M. Kirk, T. Mohite, C. Omet, A. Parfenova, and P. Schütt. Experiment on Space Charge Driven Nonlinear Resonance Crossing in an Ion Synchrotron. *Phys. Rev. Accel. Beams*, 13: 114203, November 2010. doi: https://www.doi.org/10.1103/PhysRevSTAB.13.114203.

[119] Hannes Bartosik. Challenges in Understanding Space Charge Effects. Challenges in Understanding Space Charge Dynamics. *Proc. 61st ICFA Advanced Beam Dynamics Workshop on High-Intensity and High-Brightness Hadron Beams*, 2018. doi: https://www.doi.org/10.18429/JACoW-HB2018-MOA1PL01.

[120] Giuliano Franchetti, Simone Gilardoni, Alexander Huschauer, Frank Schmidt, and Raymond Wasef. Space Charge Effects on the Third Order Coupled Resonance. *Phys. Rev. Accel. Beams*, 20(8):081006, 2017. doi: https://www.doi.org/10.1103/PhysRevAccelBeams.20.081006.

[121] Hannes Bartosik and Sofia Kostoglou. Transverse Nonlinear Effects. *CERN Yellow Reports: Proc. Joint Universities Accelerator School (JUAS)*, 3:385, 2024. doi: https://www.doi.org/10.23730/CYRSP-2024-003.385.

[122] G. Franchetti, I. Hofmann, M. Giovannozzi, M. Martini, and E. Metral. Space Charge and Octupole Driven Resonance Trapping Observed at the CERN Proton Synchrotron. *Phys. Rev. ST Accel. Beams*, 6:124201, December 2003. doi: https://www.doi.org/10.1103/PhysRevSTAB.6.124201,.

[123] T. Chen and S. Peggs. The Driven Pendulum, and E778 Tune Modulation. In *Proc. 1989 IEEE Particle Accelerator Conf.: Accelerator Science and Technology*, pages 1343–1345 vol.2, 1989. doi: https://www.doi.org/10.1109/PAC.1989.73443.

[124] A. Chao et al. Experimental Investigation of Nonlinear Dynamics in the Fermilab Tevatron. *Phys. Rev. Lett.*, 61:2752–2755, December 1988. doi: https://www.doi.org/10.1103/PhysRevLett.61.2752.

[125] T. Satogata and S. Peggs. Is Beta Modulation More or Less Potent Than Tune Modulation? In *Conf. Record of the 1991 IEEE Particle Accelerator Conf.: Accelerator Science and Technology, May 6-9, 1991, San Francisco, California*, page 476. IEEE, 1991. URL: https://epaper.kek.jp/p91/PDF/PAC1991_0476.PDF.

[126] Sofia Kostoglou. *Noise Effects in the Large Hadron Collider (LHC) and Its High-Luminosity Upgrade (HL-LHC)*. PhD thesis, Natl. Tech. U., Athens, 2020. URL: https://cds.cern.ch/record/2743602.

[127] Roderik Bruce. *Beam Loss Mechanisms in Relativistic Heavy-Ion Colliders*. PhD thesis, Lund U., 2009. URL: https://cds.cern.ch/record/1246025.

[128] Fanouria Antoniou. *Optics Design of Intrabeam Scattering Dominated Damping Rings*. PhD thesis, CERN, March 2014. Thesis number CERN-THESIS-2012-368. URL: https://cds.cern.ch/record/1666863.

[129] Parthena Stefania Papadopoulou. *Bunch Characteristics Evolution for Lepton and Hadron Rings Under the Influence of the Intra-Beam Scattering Effect*. PhD thesis, University of Crete, 2019. URL: https://cds.cern.ch/record/2745710.

[130] S. Papadopoulou, F. Antoniou, T. Argyropoulos, M. Hostettler, Y. Papaphilippou, and G. Trad. Impact of Non-Gaussian Beam Profiles in the Performance of Hadron Colliders. *Phys. Rev. Accel. Beams*, 23:101004, October 2020. doi: 10.1103/PhysRevAccelBeams.23.101004.

[131] Michail Zampetakis. *Numerical Models and Interplay of Intrabeam Scattering With Incoherent Effects for High Brightness Circular Accelerators*. PhD thesis, University of Crete (UOC), 2024. doi: https://www.doi.org/10.12681/eadd/57683.

[132] C. Bernardini, G. F. Corazza, G. Di Giugno, G. Ghigo, J. Haissinski, P. Marin, R. Querzoli, and B. Touschek. Lifetime and Beam Size in a Storage Ring. *Phys. Rev. Lett.*, 10:407–409, May 1963. doi: 10.1103/PhysRevLett.10.407.

[133] James D. Bjorken. Intrabeam Scattering. *Part. Accel.*, 13:115–143, 1983. No: FERMILAB-PUB-82-47-THY. URL: https://cds.cern.ch/record/140304/files/p115.pdf.

[134] A. Piwinski. Intra-Beam-Scattering, 1974. doi: https://www.doi.org/10.5170/CERN-1992-001.226.

[135] Sergei Nagaitsev. Intrabeam Scattering Formulas for Fast Numerical Evaluation. *Phys. Rev. ST Accel. Beams*, 8:064403, June 2005. doi: https://www.doi.org/10.1103/PhysRevSTAB.8.064403.

[136] P. Zenkevich, O. Boine-Frankenheim, and A. Bolshakov. A New Algorithm for the Kinetic Analysis of Intra-Beam Scattering in Storage Rings. *Nucl. Instrum. Methods Phys. Res. A*, 561:284–288, June 2006. doi: https://www.doi.org/10.1016/j.nima.2006.01.013.

[137] F. Antoniou Et Al. Transverse studies with ions at SPS flat bottom. *CERN Proc.*, page 145 Pages, December 2017. doi: https://www.doi.org/10.23727/CERN-PROCEEDINGS-2017-002.145.

[138] M. Martini. Intrabeam Scattering in the ACOL-AA Machines. Technical Report CERN-PS-84-9-AA, SCAN-0009244, 1984. Publication Title: CERN Document Server. URL: https://cds.cern.ch/record/151638.

[139] K. L. F. Bane, H. Hayano, K. Kubo, T. Naito, T. Okugi, and J. Urakawa. Intrabeam Scattering Analysis of Measurements at KEK's Accelerator Test Facility Damping Ring. *Phys. Rev. ST Accel. Beams*, 5:084403, August 2002. doi: https://www.doi.org/10.1103/PhysRevSTAB.5.084403.

[140] M. Conte and M. Martini. Intrabeam Scattering In The CERN Anti-Proton Accumulator. *Part. Accel.*, 17:1–10, 1985. URL: https://cds.cern.ch/record/457572.

[141] F. Antoniou and F. Zimmermann. Revision of Intrabeam Scattering With Non-Ultrarelativistic Corrections and Vertical Dispersion for MAD-X. Technical report, CERN, Geneva, 2012. Technical report CERN-ATS-2012-066. URL: https://cds.cern.ch/record/1445924.

[142] Frank E. Harris. *Mathematics for Physical Science and Engineering: Symbolic Computing Applications in Maple and Mathematica.* Academic Press, 2014. ISBN: 978-0-12-801000-6.

[143] Sabir Umarov, Constantino Tsallis, and Stanly Steinberg. On a q-Central Limit Theorem Consistent With Nonextensive Statistical Mechanics. *Milan J. Math.*, 76(1):307–328, 2008. doi: https://doi.org/10.1007/s00032-008-0087-y.

[144] K. Smedley, A. Jayasuriya, C. Christiansen, and R. Shafer. Ripple Distribution in Magnet Strings of Super Collider [SSC]. *IEEE Trans. Nucl. Sci.*, 41(4):1364–1370, 1994. doi: https://doi.org/10.1109/23.322914.

[145] P. Burla, D. Cornuet, K. Fischer, P. Leclère, and F. Schmidt. Power Supply Ripple Study at the SPS. Technical report, CERN, Geneva, 1994. Technical report CERN-SL-94-11-AP. URL: https://cds.cern.ch/record/263879.

[146] Verena Kain, Ewald Effinger, Fabio Follin, Francesco Velotti, Matthew Fraser, Michael Schenk, Nico Madysa, and Pablo Andreas Arrutia Sota. Slow Extracted Spill Ripple Control in the CERN SPS Using Adaptive Bayesian Optimisation. *JACoW IPAC*, 2024: TUPS55, 2024. doi: https://www.doi.org/10.18429/JACoW-IPAC2024-TUPS55.

[147] Hannes Bartosik and Frank Schmidt. Studies on Tune Ripple. *Proc. 4th ICFA Mini-Workshop on Space Charge*, 2019. URL: https://indico.cern.ch/event/828559/contributions/3528378/attachments/1938914/3214441/2019.11.05_SC_and_ripple.pdf.

[148] Jacques Laskar, Claude Froeschlé, and Alessandra Celletti. The Measure of Chaos by the Numerical Analysis of the Fundamental Frequencies. Application to the Standard Mapping. *Physica D: Nonlinear Phenomena*, 56(2-3):253–269, 1992. doi: https://doi.org/10.1016/0167-2789(92)90028-L.

[149] CERN. Super Proton Synchrotron Optics Repository. URL: https://gitlab.cern.ch/acc-models/acc-models-sps.

[150] Hart William, Jack E. Kemmerly, and Steven M. Durbin. *Engineering Circuit Analysis*. McGraw-Hill Higher Education, 2007. ISBN: 978-1-119-50195-4.

[151] Elias Waagaard. FMA Ions Simulation Tool. GitHub repository, 2025. URL: https://github.com/ewaagaard/fma_ions. Accessed: September 5, 2025.

[152] Elias Walter Waagaard, Reyes Alemany Fernandez, Hannes Bartosik, Roderik Bruce, and Felix Soubelet. Expanding the CERN ion injector chain capabilities: new beam dynamics simulation tools for future ion species. *JACoW*, IPAC2024:MOPC08, 2024. URL: https://cds.cern.ch/record/2904667.

[153] Hans Grote, Frank Schmidt, Laurent Deniau, and Ghislain Roy. The MAD-X program (Methodical Accelerator Design) version 5.08.01: User's reference manual, 2021. URL: http://madx.web.cern.ch/.

[154] P. Zisopoulos, E. Maclean, J. Dilly, K. Paraschou, and M.Hostettler. Towards operational optics measurements with ac dipole excitations in the cern sps. In *Proc. 16th Int. Particle Accelerator Conf. (IPAC'25), Taipei, Taiwan*, page WEPM108. JACoW Publishing, Geneva, Switzerland, 2025.

[155] P Castro. *Luminosity and Beta Function Measurement at the Electron-Positron Collider Ring LEP*. PhD thesis, Valencia U., 1996. URL: https://cds.cern.ch/record/316609.

[156] Isabelle John and Hannes Bartosik. Space Charge and Intrabeam Scattering Effects for Lead-Ions and Oxygen-Ions in the LHC Injector Chain, 2021. Technical report CERN-ACC-NOTE-2021-0003. URL: https://cds.cern.ch/record/2749453.

[157] Gianluigi Arduini, A. Faus-Golfe, and Frank Zimmermann. Measurements and Modelling of Nonlinear Chromaticity and Detuning With Amplitude at 26 GeV, 2001. Technical report SL-Note-2001-030-MD. URL: https://cds.cern.ch/record/702665.

[158] Gianluigi Arduini, Frank Zimmermann, A. Faus-Golfe, N. Iida, and R. Tomás. 2002 Nonlinear Optics Measurements and Modelling for the SPS at 26 GeV, 2003. Technical report AB-Note-2003-025-MD. URL: https://cds.cern.ch/record/693938.

[159] Hannes Bartosik. *Beam Dynamics and Optics Studies for the LHC Injectors Upgrade*. PhD thesis, TU Vienna, 2013. URL: https://cds.cern.ch/record/1644761.

[160] Xsuite official website. URL: https://xsuite.readthedocs.io/.

[161] Felix Soubelet, Hannes Bartosik, Sofia Kostoglou, Konstantinos Paraschou, Michail Zampetakis, and Giovanni Iadarola. Development of Numerical Tools for Intra-Beam Scattering Modelling. *JACoW IPAC*, 2024:MOPS37, 2024. doi: https://www.doi.org/10.18429/JACoW-IPAC2024-MOPS37.

[162] E. Waagaard. Status of the New IBS Module of Xsuite. In *Proc. 38th DL2 LHC Luminosity Meeting*, 2023. URL: https://indico.cern.ch/event/1281509/.

[163] Hannes Bartosik, Simon Albright, Angoletta, et al. The LHC Injectors Upgrade (LIU) Project at CERN: Ion Injector Chain. In *Proc. 8th Int. Particle Accelerator Conf. (IPAC'17)*, 2017. doi: http://dx.doi.org/10.18429/JACoW-IPAC2017-TUPVA020.

[164] E. Waagaard, H. Bartosik, F. Soubelet, and K. Paraschou. Investigating Ion Beam Loss Mechanisms at the SPS Flat Bottom. In *Proc. 16th Int. Particle Accelerator Conf. (IPAC'25), Taipei, Taiwan*, page WEPM092. JACoW Publishing, Geneva, Switzerland, 2025.

[165] R. Bruce et al. Exceeding High-Luminosity LHC Performance Targets During the 2024 Pb-Pb Ion Run. In *Proc. 16th Int. Particle Accelerator Conf. (IPAC'25), Taipei, Taiwan*, page TUBN3. JACoW Publishing, Geneva, Switzerland, 2025.

[166] M. Slupecki. Update on Ion Readiness in the Injectors. In *Proc. LHC Injector and Experimental Facilities Committee (IEFC) Meeting 18/10/2024*, 2024. URL: https://indico.cern.ch/event/1464610/.

[167] E. Waagaard, R. Bruce, H. Bartosik, R. Alemany Fernández, J.M. Jowett, and N. Triantafyllou. Charting the Luminosity Capabilities of the CERN Large Hadron Collider With Various Nuclear Species. *Nucl. Instrum. Methods Phys. Res. A*, 2025. Under submission.

[168] Elias Waagaard. Injector model simulation tool. GitHub repository, 2025. URL: https://github.com/ewaagaard/injector_model. Accessed: September 5, 2025.

[169] Elias Waagaard and Hannes Bartosik. Exploring Space Charge and Intra-beam Scattering Effects in the CERN Ion Injector Chain. In *Proc. of the 68th ICFA Advanced Beam Dynamics Workshop on High-Intensity and High-Brightness Hadron Beams (HB'23)*, pages 515–518, Geneva, Switzerland, 2024. doi: https://doi.org/10.18429/JACoW-HB2023-THBP23.

[170] Hannes Bartosik, R Alemany, Theodoros Argyropoulos, Thomas Bohl, Heiko Damerau, Verena Kain, Giulia Papotti, Giovanni Rumolo, A Saa Hernandez, and Elena Shaposhnikova. Recent beam performance achievements with the Pb ion beam in the SPS for LHC physics runs. In *Proc. 10th Int. Particle Accelerator Conf. (IPAC'19), Melbourne, Australia*. JACoW Publishing, Geneva, Switzerland, 2019. doi: 10.18429/JACoW-IPAC2019-MOPGW069.

[171] G. Rumolo. LIU Ion Beam Parameters Table, 2017. Report number LIU-PM-ES-0004 v.2. URL: https://edms.cern.ch/ui/file/1420286/2/LIU-Ions_beam_parameter_table.pdf.

[172] M Mackowiak-Pawlowska. Addendum to the NA61/SHINE proposal: Request for light ions beams in run 4, 2023. NA61/SHINE Collaboration. Technical report CERN-SPSC-2023-022. URL: https://cds.cern.ch/record/2867952.

[173] F. Kröger et al. Optimization of the stripper foil material and thickness for the Gamma Factory, 2019. Presentation at the Gamma Factory Meeting. URL: https://indico.cern.ch/event/802131/.

[174] Felix M Kröger, Günter Weber, Simon Hirlaender, Reyes Alemany-Fernandez, Mieczyslaw W Krasny, Thomas Stöhlker, Inga Yu Tolstikhina, and Viacheslav P Shevelko. Charge-state distributions of highly charged lead ions at relativistic collision energies. *Ann. Phys.*, 534(3):2100245, 2022.

[175] C Scheidenberger and H Geissel. Penetration of relativistic heavy ions through matter. *Nucl. Instrum. Methods Phys. Res. B*, 135(1-4):25–34, 1998. doi: https://doi.org/10.1016/S0168-583X(97)00639-3.

[176] CERN. PS RF cavities for 50 ns ion bunch spacing - user specification for the study phase, 2025. Functional specification CPS-A-ES-0001 v. 2.1. URL: https://edms.cern.ch/document/3233949/2.1. Accessed: September 5, 2025.

[177] E Baron, M Bajard, and Ch Ricaud. Charge exchange of very heavy ions in carbon foils and in the residual gas of GANIL cyclotrons. *Nucl. Instrum. Methods Phys. Res. A*, 328 (1-2):177–182, 1993. doi: https://doi.org/10.1016/0168-9002(93)90622-O.

[178] VS Nikolaev and IS Dmitriev. On the equilibrium charge distribution in heavy element ion beams. *Phys. Lett. A*, 28(4):277–278, 1968. doi: https://doi.org/10.1016/0375-9601(68)90282-X.

[179] G Schiwietz and PL Grande. Improved charge-state formulas. *Nucl. Instrum. Methods Phys. Res. B*, 175:125–131, 2001. doi: https://doi.org/10.1016/S0168-583X(00)00583-8.

[180] J. Olsen. Baroncs simulation tool. GitHub repository, 2024. URL: https://github.com/jako4295/baroncs. Accessed: September 5, 2025.

[181] FG Kondev, Meng Wang, WJ Huang, S Naimi, and G Audi. The NUBASE2020 evaluation of nuclear physics properties. *Chin. Phys. C*, 45(3):030001, 2021. doi: https://doi.org/10.1088/1674-1137/abddae.

[182] R. Bruce, J. M. Jowett, M. Blaskiewicz, and W. Fischer. Time Evolution of the Luminosity of Colliding Heavy-Ion Beams in BNL Relativistic Heavy Ion Collider and CERN Large Hadron Collider. *Phys. Rev. ST Accel. Beams*, 13:091001, Sep 2010. doi: https://doi.org/10.1103/PhysRevSTAB.13.091001.

Elias Waagaard

Rue de Lausanne 81, 1202, Geneva, Switzerland
+39 334 915 59 42
elias.waagaard@gmail.com
Date of birth: May 12th 1997 **Nationality:** Swedish



PhD candidate in physics with a passion for computational modelling of complex systems, numerical optimization, machine learning techniques and experimental benchmarking. Eager to tackle interdisciplinary challenges with new technology.

Professional experience

Sep 2022 – Aug 2025 **Doctoral researcher in accelerator physics** – CERN, Switzerland
- Developed Python simulation models of **ion beam dynamics** effects in the Xsuite toolkit: space charge, intra-beam scattering, and residual gas interactions. Conducted benchmarking measurements.
- Contributed to implementing a **50 Hz noise compensation** scheme for the Super Proton Synchrotron (SPS) power converters, which partly enabled the 2024 Pb ion beams to **exceed targets by 40%.**
- Developed a **semi-empirical numerical prediction model** – the Injector Model – for future ion species requested by the ALICE3 detector upgrade at CERN, from source to the detector.

Sep 2021 – Aug 2022 **Technical student** (part of my Master's thesis) – CERN, Switzerland
- Built a **numerical optimization toolkit** for the SPS injection kicker magnet system, which reduced harmful injection oscillations by up to 70%.
- Developed a **magnet surrogate model** with a **neural network** for offline optimization.
- Conducted project to deploy an SPS magnet system **reinforcement learning** agent.

Jul – Aug 2021 **CERN summer student** – CERN, Switzerland
- Developed a numerical correction scheme for resonances in the Large Hadron Collider (LHC).

Jan – Dec 2020 **Student researcher –** FREIA Laboratory, Uppsala University, Sweden
- Studied **vacuum arc** behaviour for high-field cryogenic copper electrodes for the CLIC project.
- Upgraded GUIs of the laboratory control system.
- Developed and benchmarked a **cryogenic code** for helium liquefaction (part of my Bachelor's thesis).

Jul – Aug 2019 **Erasmus trainee** – Istituto Nazionale di Fisica Nucleare (INFN), Turin, Italy
- Developed numerical analysis tools for the ALICE collaboration.

Jun – Aug 2016 **Trainee through the Research Science Institute (RSI) summer school** – MIT, Boston, USA
- Developed numerical gravitational lensing models.

Education

2022 – 2025 **PhD in Accelerator Physics –** EPFL & CERN, Switzerland
Thesis title: "Beam Dynamics Limitations for Future Ions in the CERN Injector Complex".
Supervisors: Prof. Mike Seidel (EPFL) & Dr. Hannes Bartosik (CERN).

2020 – 2022 **Master's Programme in Particle and Nuclear Physics –** Uppsala University, Sweden
GPA: 4.9/5.0. Graduated with 25 extra ECTS credits. *Supervisors*: Prof. Volker Ziemann & Dr. Francesco Velotti.

2017 – 2020 **Bachelor's Programme in Physics –** Uppsala University, Sweden
GPA: 4.9/5.0. Graduated with 30 extra ECTS credits.

Relevant skills, software and certificates

Software and numerical analysis
- Linux, Microsoft Windows
- Git and Continous Integration
- Python and PyData ecosystem: numpy, matplotlib, pandas, scipy, seaborn, etc.
- Python libraries in optimization and ML: pytorch, gym (RL), pymoo (multi-objective optimization), scikit-learn
- High-Throughput Computing usage with HTCondor software (CPU/GPU)
- MATLAB
- ROOT data analysis framework (C++)
- MADX: accelerator lattice design

Scientific Python package development
- FMA_ions (creator): Python-based particle tracking program with space charge, intra-beam scattering and tune ripple
- Beam-gas-collisions (creator): emulates beam interactions with residual gas
- injector_model (creator): numerical model of future ion beam intensities at CERN
- Xsuite (contributor to several modules): CERN beam dynamics simulation toolkit
- SPS kicker magnets numerical toolkits (creator)

Courses & certificates
- **Master & PhD-level:** Plasma physics, Numerical methods for particle transport modelling, Advanced accelerator physics
- **Udemy:** Python Reinforcement Learning; SQL Programming Basics; Leadership/Project Management; Entrepreneurship and Business

Selected publications and proceedings

- E. Waagaard et al. (2025). Charting the luminosity capabilities of the CERN Large Hadron Collider with various nuclear species. *Nuclear Instruments and Methods in Physics Research Section A* (submitted).
- E. Waagaard et al. (2025). Beam-gas interactions in the CERN Proton Synchrotron: Cross section measurements and lifetime modelling. *arXiv preprint arXiv:2506.02928*
- E. Waagaard et al. (2025). Investigating Lead Ion Beam Loss Mechanisms at the Super Proton Synchrotron Flat Bottom. *16th International Particle Accelerator Conference (IPAC2025) Proceedings.*
- E. Waagaard et al. (2023). Designing a new CERN SPS injection system with numerical optimization. *14th International Particle Accelerator Conference (IPAC2023) Proceedings*.
- E. Waagaard & V. Ziemann (2022). Emittance Growth of Kicked and Mismatched Beams Due to Amplitude-Dependent Tune Shift. *Phys. Rev. Accel. Beams 25, 054001*.
- E. Waagaard & E. H. Maclean (2022). A Response Matrix Approach to Skew-Sextupole Correction in the LHC at Injection. *13th International Particle Accelerator Conference (IPAC2022) Proceedings*.

Invited talks

- Speaker at the "5th ALICE Upgrade Week 2024".
- Speaker at the "CERN Machine Learning and Data Analytics Community Forum".

Selected workshops

- "5th ICFA Beam Dynamics Mini-Workshop on Machine Learning for Particle Accelerators", CERN (2025).
- "Challenges and perspective in computational modelling for fusion reactors", EPFL (2024).

Teaching and supervision experience

- **Joint Universities Accelerator School (JUAS) Tutor** for numerical accelerator design workshop (Jan – Feb 2024).
- **EPFL teaching assistant** for Master-level course "Introduction to particle accelerators" (Sep – Dec 2023).
- **Co-supervisor** of CERN Master thesis student Jakob Olsen. Coordinated his numerical physics project (Sep – Dec 2023).
- **Supervisor** of CERN high-school intern Gregor Wein. Organized physics project and study visits (Apr 2023).

Volunteering, leadership and extracurricular activities

2024 - 2025	**Technology scout** for Positron Ventures, scouting early-stage deep tech scientist entrepreneurs in Europe.
Apr 2024	Selected as one out of 30 participants among 120+ applicants to the 2024 **Sciencepreneurship Summer School**: Sustainability & AI, at EPFL/ETH. Won 2nd award for best final project pitch.
2022 - today	**Outreach collaborator** with Sweden's Industrial Liaison Office (ILO) **Big Science Sweden** to promote student opportunities at CERN, with inspirational lectures and video content production.
2022 - today	Official **CERN guide** for public accelerator tours and **Junior Liaison Officer** for head-of-state visit.
2021 – 2022	**Student representative** at the Physics Master's Programme at the Uppsala University – gave inspirational introductory lectures and served on international programme evaluation panel.
2020 – 2021	**Board president** of the Gästrike-Hälsinge Student Nation, Uppsala. 2000 members, €700k annual budgets.
2018	**Camp counsellor** at the Space Summer School, KTH, Stockholm – arranged field trips, activities, experiments and presentations for a group of 30 nationally selected high school students.
2016 – 2018	**Vice president** of the Swedish Astronomical Youth Association – coordinated local associations, organised national conferences and led strategic work for ~4500 members.

Awards and honours

- **Inspiration Award** 2024 at the Swedish Big Science Forum, Lund, for my outreach work for students in Sweden
- **Leman Scholarship** 2017 – 2021 from the Uppsala University for academic achievements (€10 000 annually)
- **Honorary Prize** 2019 from the Mathematical Society of Uppsala for top marks in multiple mathematics courses
- **Third Award** in the category "Physics and Astronomy", Taiwan International Science Fair 2018, Taipei
- **K. T. Li Special Award**, Intel International Science and Engineering Fair (ISEF) 2017, Los Angeles
- **First award**, Swedish Federation of Young Scientists' Science Fair 2017, Stockholm
- Scholarship for the **Research Science Institute (RSI) Summer School** 2016 at MIT, Boston
- National Swedish scholarship to attend the **European Southern Observatory (ESO) Astronomy Camp** 2015

Language skills

- **Swedish** – native speaker
- **English, French, Italian** – professional proficiency
- **German** – advanced
- **Spanish** – intermediate

Additional certificates

- **CMAS two-star advanced diving certificate** – diving down to 40 meters (2021)
- **Bilingual Canadian high school diploma** – exchange year in Jonquière, Quebec, Canada (2014/15)